Delving Into Massive Stars: The Colliding Wind Binaries, Relations and Various Interferometric Radio Observations

by

FARRAH DILLA ZAINOL

A thesis submitted to the University of Birmingham for the degree of

DOCTOR OF PHILOSOPHY

Astrophysics and Space Research Group

School of Physics and Astronomy

College of Engineering and Physical Sciences

University of Birmingham

October 2021

Abstract

Massive stars are rare and possess strong winds that provide feedback mechanisms to the interstellar medium. They are usually found in binary or multiple systems, which complicates the wind interaction between stars. This work has primarily involved massive stars, focusing on the colliding-wind binary at radio wavelengths as well as other wavelengths, such as the X-ray. A new Güdel-Benz style relation uncovered in an archival sample of massive stars suggests a positive correlation between X-ray and radio luminosities.

Several new radio observations of the archetypal colliding-wind binary WR140 at low and high frequencies have been made using the currently available radio interferometers. The low frequencies radio observations using the upgraded broad bandwidth Giant Metre Radio Telescope at $0.3 - 1.4$ GHz revealed that WR140 has a thermal spectrum, a vital baseline to disentangle the non-thermal emission in future works. The high-frequency radio observation of WR140 at 22 GHz to observe the colliding wind region closer to apastron was unsuccessful due to the high rms of the East Asia VLBI Network.

We introduced the Distributed Radio Emission Measure model to capture the shape of the non-thermal radio emission spectra from various archival WR140 radio data. The outcomes of the model indicate that the radio emission from the wind collision region is the result of a distributed emission measure, where the line-of-sight has travelled across different regions. The radio emission measure is large at apastron consistent with thermal emission and progressively small leading up to periastron, revealing the non-thermal emission region, coherent with the observational radio data.

To my late mom,

Jamilah Md. Som

Acknowledgements

Throughout the writing of this thesis, I have received a great amount of support, encouragement as well as considerate guidance. I would first like to thank my supervisor, Dr. Ian Stevens for his tireless help, for being a good listener to my problems, and whose expertise was invaluable in the formulation of the research topic. His support and endless motivations have always been an inspiration for me to keep moving forward.

I would like to acknowledge my WR140 collaborators led by Mike Corcoran for their wonderful discussions. I would particularly like to single out my gratitude to the uGMRT team namely Prof C.H. Ishwara-Chandra and Dr. Ruta Kale for their insights and discussions. In addition, I am thankful to the EAVN team particularly to Jiang Wu and Kiyoaki Wajima for their endless help and assistance.

I would like to express my sincere gratitude to my funders, the MARA Scholarships (the Malaysia government's global scholarship programme) as well as partial group funding from Prof. William Chaplin. Without them I wouldn't be able to be part of this incredible journey to conduct my research at UoB.

In addition, I am grateful to my officemates, in particular, Riccardo Buscicchio, Amit Ubhi and Joe Bentley for their endless support and encouragement throughout my studies mentally and emotionally. I would also like to thank Jyortirmoy Dey for his immeasurable and tireless help throughout my PhD journey. Not to forget, from the IT department, David Stops, for his computing support and providing all sorts of solutions to my computing problems.

I would like to thank my family and friends for all the unconditional support in this very intense academic journey. I'd like to thank Nadia Samsudin for providing me endless support and encouragement in deliberating over my too many problems, especially during this pandemic time and to Marisa Fo'ad who always be my number one supporter. I would also like to thank all my close Malaysian friends who studied abroad, especially the ones from UoB - they have always been my go-to support

bubble, providing a distraction to rest my mind outside of my research. Finally, I would like to thank my husband, Alif Ahmad for his immense understanding, my only daughter Eva Rose for her forgiveness on missing a huge part of her toddler life for this Ph.D thesis and to my father, Zainol Mohamad, for always believing in me in every aspect from the beginning. Not to forget, to Meena who provides me with happy distractions especially during the lockdown period. The support that I had received was entirely great for this bittersweet journey.

Preface

This thesis is based on research carried out at the School of Physics and Astronomy, University of Birmingham under the supervision of Dr. Ian R. Stevens between October 2017 and July 2021. The thesis consists of two introduction chapters, five main chapters and one conclusion. These main chapters were written as separate research papers to be published in peer-reviewed journals namely the *Monthly Notices of the Royal Astronomical Society* (MNRAS). The studies presented in the main chapters of this thesis are the work of the author, but were done together with several co-authors, mentioned below.

Chapter 3 *A Güdel-Benz Type Relations for Massive Stars* - This chapter was written by the author in collaboration with Dr. Ian R. Stevens. The paper is to be submitted to MNRAS.

Chapter 4 *A Reinterpretation of the Variable Radio Emission from the Colliding Wind System WR140*– This chapter was planned and written by the author with the help from Dr. Ian R. Stevens. The paper is to be submitted to MNRAS.

Chapter 5 *Low Frequencies New Observations of WR140 using the uGMRT*– This chapter was written by the author in collaboration with Dr. Ian R. Stevens and the WR140 collaboration led by Dr. Michael F. Corcoran (P.I: Farrah Zainol, Project Code: 37_005). The paper is to be submitted to MNRAS.

Chapter 6 *High Frequency New Observation of WR140 using the EAVN*– This chapter was written by the author in collaboration with Dr. Ian R. Stevens and the WR140 collaboration led by Dr. Michael F. Corcoran (P.I: Farrah Zainol, Project Code: a2003a). The paper is to be submitted to MNRAS.

Chapter 7 *The Low-Frequency Observation of WR146 using the Legacy GMRT*– This chapter was written by the author in collaboration with Dr. Ian R. Stevens.

The paper is to be submitted to MNRAS.

Miscellaneous The author appeared as a co-author on *The Orbit and Stellar Masses of the Archetype Colliding-Wind Binary WR140* (Thomas J.D., et al. MNRAS, 2021, 504, 5221). The author is involved in the WR140 collaboration and was actively involved in the discussion for this paper but did no data analysis.

Contents

List of Figures

List of Tables

1 | The Physics of Massive Stars

"My whole entry into astronomy started from a spiritual place."

–Carolyn Porco.

Chapter Summary

In this first chapter, I briefly discuss the formation, life, and death of massive stars, as well as their importance to the structure of the universe we live in today. A brief discussion of the winds of massive stars and the complexities of the wind interaction in binary star systems is provided. Then, I discuss the emission from other wavelength, specifically at X-ray. Finally, I provide a brief discussion on the radio emission from massive stars and the effects of the wind clumping.

1.1 Massive Stars

Massive stars are distinguished from lower mass stars by their ultimate fate. The vast majority of lower mass stars will eventually fade away as white dwarfs. In contrast, all massive stars with initial masses ranging from $8M_{\odot}$ and $150M_{\odot}$ form an iron core that collapses into neutron stars, while stars with masses $< 20M_{\odot}$ will collapse into proto-neutron stars (Dexheimer and Schramm, 2008). The lower limit of massive

stars is $\sim 8M_{\odot}$, however, is not entirely fixed, since the concept of a massive star derives from the stars that undergo helium burning and then carbon burning in their non-degenerated stellar cores. The exciting possible outcomes of massive star evolution are core-collapse supernova explosion, gamma-ray burst (GRB), or for a very massive star, into a black-hole.

The evolution of massive stars is very rapid, hence massive stars have short lives, usually between $3-35$ Myr (see Fig. 1 from Crowther (2012)) compared to our Sun ($\sim$12 Gyr). Massive stars create heavier elements in their core, such as silicon, while low mass stars cannot produce such metal. Low mass stars ($<2M_{\odot}$), can get helium-burning at their core, producing carbon. However, the core temperature can never get high enough (up to 600 million K) to start fusing carbon into heavier elements, while massive stars core can. These elements produced in massive core lie in an onion-like structure of layers of different chemical composition with the heaviest element being at the core, separated by shell-burning sources (see Fig. 1.1). Typical massive stars have convective cores where the chemical composition can be assumed uniform at all times, while the stellar envelope has more or less the original composition when the star was formed. Some massive stars do not retain their original composition (i.e. their hydrogen envelope), such as Wolf-Rayet stars (hereafter WR stars), which have lost most or all the hydrogen layer via their strong stellar winds exposing their helium core (McClelland and Eldridge, 2016). In addition, many massive stars existed in binary systems (Sana et al., 2012; Kobulnicky et al., 2014) (see section 1.3), so they suffered from the mass-transfer during the Roche-lobe overflow (RLOF) process, where the primary star loses most of its hydrogen envelope, while the secondary star gains mass and spins up (Hurley et al., 2002).

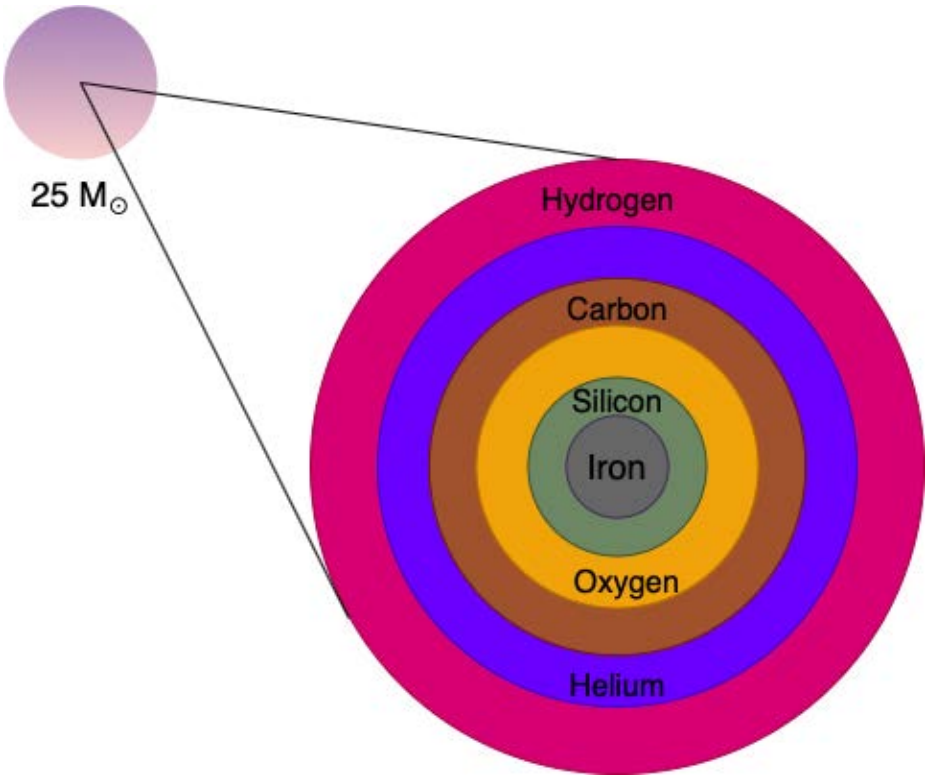

Figure 1.1: A typical $25M_{\odot}$ massive star has onion-like layers with many elements laying on top of each other, with the heaviest located at the core. Massive stars begin to burn heavier elements in order to keep the star from collapsing due to the gravitational force. As the iron has been generated at the core, this cross-section diagram is at a stage just before a massive star explodes. Massive stars can generate heavy elements via nucleosynthesis, such as the triple-alpha process, in which three helium elements fuse to form a carbon. Heavier elements than carbon, such as oxygen, can be created from the proton capture process. The nucleosynthesis process is repeated to produce a variety of heavier elements, including magnesium, silicon, and, iron.

1.1.1 The Classification of Massive Stars

One of the critical parts in the stellar evolution is stellar classification, where the massive stars are positioned at the top left region of the Hertzsprung-Russell diagram (hereafter HR diagram). The HR diagram was named after the Danish and American astronomer who independently worked on the versions of the diagram in the twentieth century (Russell, 1914). This diagram became an important reference to the astronomers studying stars, specifically stellar evolution.

Massey (2003) reported that for every 20 $M_{\odot}$ O-star in the Galaxy, there should be about a hundred thousand solar-type stars. This report was in consensus with the mass distribution of stars characterised by the Initial Mass Function (IMF, Salpeter 1955) given by $N \propto M^{-2.35}$, where N is the number of stars at a given mass, M. From the scaling, massive stars are rare.

O-stars are categorised as the most massive, where they can go up to 130 $M_{\odot}$. The effective temperatures range between 30 000 K to 50 000 K while a few O-type stars can get as high as $T_{eff} > 50\ 000$ K such as HD 269810 (O3-star) in NGC 2029 of the Large Magellanic Cloud (LMC) that has $T_{eff} = 52\ 500$ K and a mass of $130 M_{\odot}$ (Zacharias et al., 2012). Meanwhile, their bolometric luminosities range at a staggering $10^4 - 10^6 L_{\odot}$. O-stars are considered young as they entered into the main sequence immediately after their birth. Their average lifetime is the shortest in the main sequence which is about 1 – 5 Myr (Martins et al., 2005). The stellar winds from these stars are strong and can reach supersonic with the terminal velocities, v_{∞} range between $1500 - 4000$ km s^{-1} contributing to mass loss rates, $\dot{M}$ of $10^{-6} - 10^{-5} M_{\odot}\mathrm{yr}^{-1}$ (Lamers and Leitherer, 1993).

The next category in line for massive stars are the B type stars where their mass range from 2 – 16 $M_{\odot}$ and have T_{eff} between 10 000 K – 30 000 K with v_{∞} between $200 - 2000$ km s^{-1}. Their $\dot{M}$ range between $10^{-8} - 10^{-6} M_{\odot}\mathrm{yr}^{-1}$ (Lamers and Leitherer, 1993) while their average lifetime is between 12 – 30 Myr with bolometric

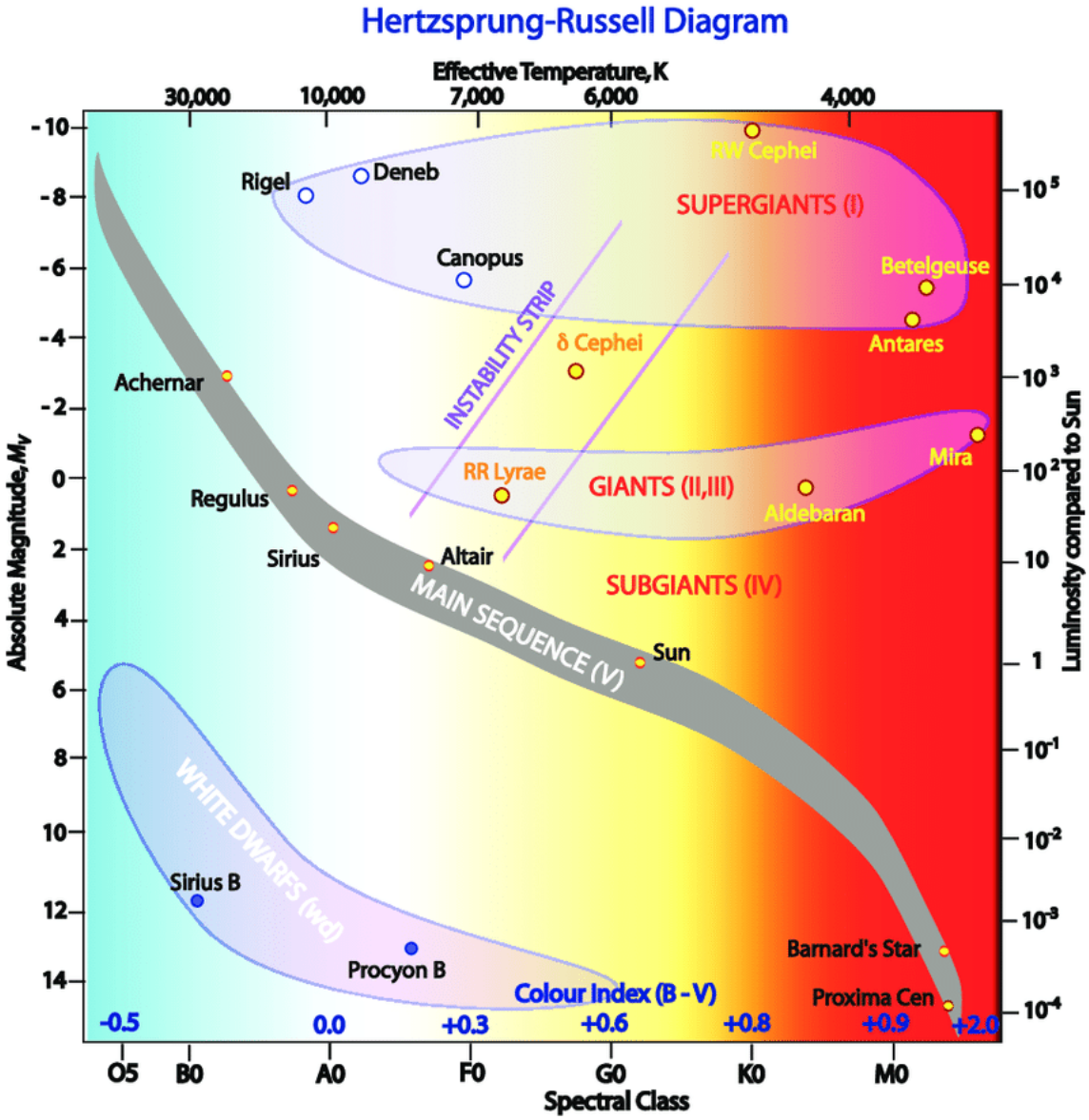

Figure 1.2: This Hertzsprung-Russell diagram shows the absolute magnitude along the left axis and the luminosity compared to the Sun along the right axis. The spectral class was indicated at the base of the diagram while the effective temperature is illustrated at the top. The grey band runs across the diagram represents the main sequence stars where the massive stars are positioned at the top left corner. Image credit: R. Hollow, CSIRO.

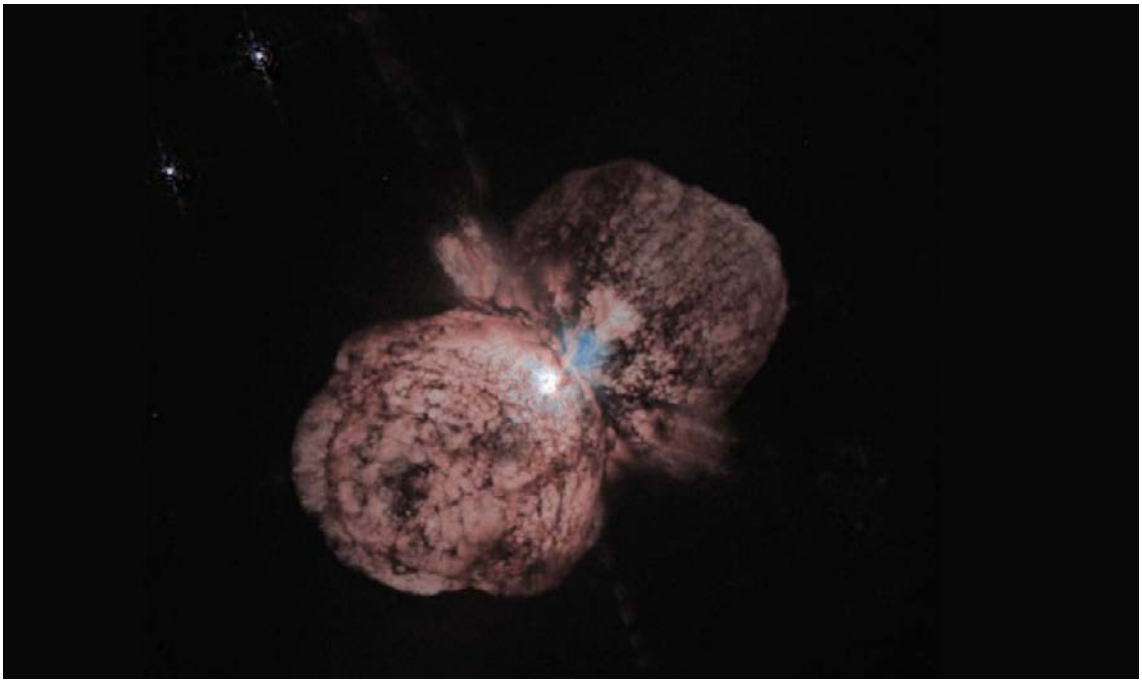

Figure 1.3: The Hubble Space Telescope image of the η Carinae. A huge amount of materials has been ejected and can be seen in the form of two giant lobes and an equatorial disk in the course of its evolution. These materials will then contribute to the "feedback" mechanism at that region. Image credit : from Jon Morse (University of Colorado) & NASA.

luminosities of $25 - 10^4 L_\odot$.

Luminous Blue Variables (hereafter LBVs), are another class of stars that evolve from OB stars. These stars are very luminous and are known to be unstable supergiant or hypergiant stars with very dense but slow winds to shed mass. They occasionally produce abnormal outbursts that can be mistaken for supernovae. An example of an LBV is η Carina, which is the most luminous binary in our galaxy and had a major outburst in 1837 (See Fig. 1.3). η Carina is an important massive binary system for which the colliding wind shock has been well studied (Corcoran et al., 2017; Hamaguchi et al., 2018). For stars that have an initial mass between $20 - 25\ M_\odot$, the LBVs are usually their final stage before exploding as a supernova, but higher mass stars evolve into LBVs before transitioning into Wolf-Rayet stars.

WR stars are rare, and as of this writing, Oct 2021, there are around 667 cat-

alogued WR stars maintained online by Paul Crowther[1]. WR stars have three sub-types which are classified according to their main spectral type of the main composition which are WN(Nitrogen), WC(Carbon) and WO(Oxygen) (Van Der Hucht, 2001). The range of WR sub-type are WN types (WN2 - WN11), WC types (WC4 - WC9) and WO types (WO1 - WO4) where the full list is in Van Der Hucht (2001), in their Table 2 (along with their references within the paper). These classifications are further divided according to their temperature, luminosity and magnitude. WR stars is a normal phase of evolution from massive stars typically for stars with masses $> 20M_{\odot}$ and when they have or nearly used up their hydrogen to start burning helium. The life time of massive stars when they are in WR phase is short which is around 0.4 Myr (Groh et al., 2014) before ending their life as a supernova (see Fig. 1.6).

1.1.2 The Formation of Massive Stars

Stars, regardless of their mass, are formed from cold molecular gas and dust, which are often found in giant molecular clouds where the gravitational force overcomes internal pressure. Massive stars are mostly created in clusters, but knowledge of their processes of formation remain limited since they are relatively rare, form rapidly, and often are heavily clouded by dust (Zinnecker and Yorke, 2007). But from some observations made in our Galaxy, the regions where the massive stars form have very high surface density, high total pressure and cold temperature ($\Sigma \sim 1$ g cm^{-2}, $P/k \sim 10^8 - 10^9$ K cm^{-3}, $T = 10 - 20$K) (McKee and Tan, 2003). Crowther (2012) stated that there was an empirical correlation between the maximum stellar mass and cluster mass. In low mass clusters, such as the ρ Oph ($\sim$100 $M_{\odot}$), there are barely any massive stars, but in Orion Nebula Cluster ($\sim 2000M_{\odot}$), θ^1 Ori C with a mass about $40M_{\odot}$ can be found. NGC 3603 (see Fig. 1.4), located at ~ 6.9 kpc, with a mass of $\sim 10^4 M_{\odot}$, hosts a number of stars which are more than $100M_{\odot}$ including

[1]http://pacrowther.staff.shef.ac.uk/WRcat/Description.php

Figure 1.4: Image of the NGC 3603 region with the field of view of $[3.37' \times 3.37']$ obtained in near-IR filter bands with the ISAAC instrument using the ANTU telescope (VLT). Due to the relatively low dust at NIR, UV-radiating OB-stars that ionise the nebula can be studied at visible and near-infrared (NIR) wavelength. From ESO and Stolte et al. (2004); Brandner et al. (2000).

the highest massive double-eclipsing binary star HD 97950A1 (Schnurr et al., 2008).

The major issue with the formation of massive stars is the radiation pressure exerted by massive stars on the surrounding dust and the gas core (e.g.,Yorke and Sonnhalter (2002); Krumholz and McKee (2005)). The review paper by Beuther et al. (2006) referred to the two methods to solve this problem. The first approach is accretion-based star formation. Many variations have been included in this method, such as accretion disks, increasing accretion rates in turbulent cloud cores, accretion through the evolving hypercompact HII region, and many more. Contrary to this, the second approach is based on the observational fact that massive stars often form at the core of dense stellar clusters ($\sim 10^8$ pc^{-3})(Bally and Zinnecker, 2005). The second approach mentioned by Beuther et al. (2006) is more dramatic in which the protostars undergo physical collisions and merge by avoiding the effect of radiation

pressure.

Tan et al. (2014) reported a less dramatic approach of two main classes of accretion; Core Accretion and Competitive Accretion. In Competitive Accretion, without going through a phase of being in a massive coherent core, the material is drawn more chaotically from a broader region of the clump. Massive stars are formed under the initial conditions of self-gravitation in Core Accretion. They are subject to relatively ordered collapse through the central disk to form a single star or a small-N multiple.

A simple yet informative diagram (see Fig. 1.5) about the evolution of stellar cores at different masses by Gary A. Glatzmaier, University of California, Santa Cruz, gives some insights about the evolutionary path of stars. Understanding the evolution of massive stars is crucial as these stars can enter more complicated stages (see Section 1.1.3) before they end their life with a bang.

1.1.3 The Short and Complicated Evolution of Massive Stars

Massive stars have a brief lifetime, therefore the luminosity can become an indicator of how rapid the star uses its fuel since it is a measure of the star energy output. For massive stars, we can conduct approximate analysis using the information on the proportionality of the mass of fuel available and the luminosity to estimate the lifetime of a star by ($L \propto M^{\alpha}$), where $\alpha = 3.5$ (Phi, 1999). The scaling can be written as:

$$L = L_{\odot} \left(\frac{M}{M_{\odot}} \right)^{3.5} , \tag{1.1}$$

and the approximation of the lifetime, τ can be further estimated by:

$$\tau \sim 10^{10} \left(\frac{M_{\odot}}{M} \right)^{2.5} yr \, . \tag{1.2}$$

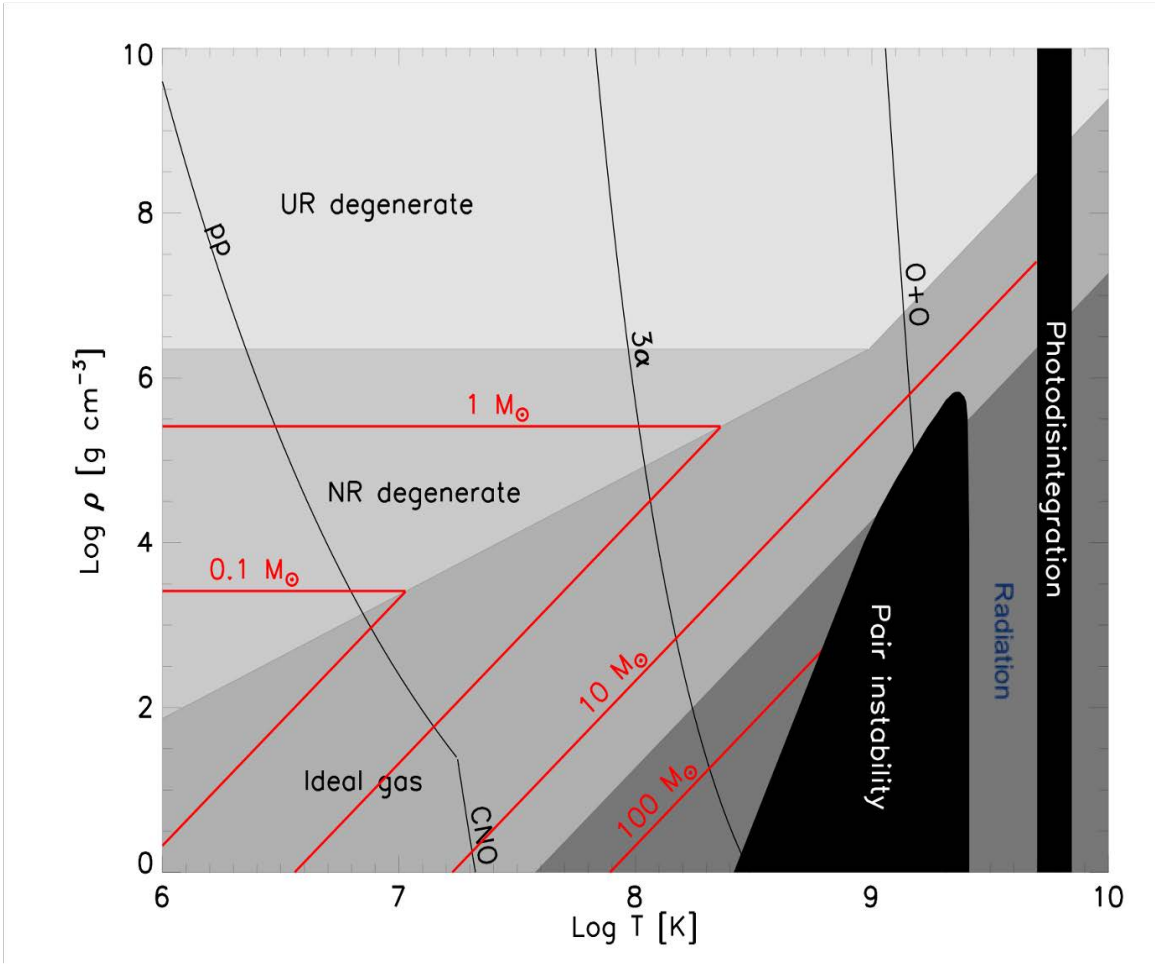

Figure 1.5: The evolution of the stellar cores on the log T and log ρ plane for a number of stellar core masses. The shades of the grey regions show the form of pressure which are the radiation, ideal gas, non-relativistic and relativistic degenerate gas. The solid black areas represent the instability regions, namely the pair-instability and photodisintegration, where the star becomes unstable. These simple evolutionary tracks show that most of the stars starts off from the ideal gas at the bottom left except for the very massive star ($100M_{\odot}$). As the mass is constant (not accounting for any mass-loss), the stars should more or less follow the red solid path according to their mass. The transition into a degenerate state is unlikely for high-mass stars (see the evolutionary tracks for $10M\odot$), but instead, it enters the next line of nuclear burning. It first burns carbon and contracts, then burns oxygen, and some more contraction occurs and then burns silicon. The star has to continue going up on its mass evolution track once the silicon is burned to iron. The high mass stars will eventually reach the photodisintegration instability strip, and the star becomes dynamically unstable. The star would either collapses into a black hole, or explodes as a supernova, leaving a neutron star behind. Image credit: Gary A. Glatzmaier, University of California, Santa Cruz.

This means that massive stars with 40 $M_{\odot}$ have a lifetime of $\sim$ 0.9 Myrs compared to the Sun $\sim$ 12 Gyrs. In that short time, they have to undergo a lot of complicated nucleosynthesis processes and shed a huge amount of mass to make them evolve off from the main sequence and turn into different types and subtypes before ending their lives as supernovae.

Their evolution depends heavily on their mass at Zero Age Main Sequence (ZAMS) and their metallicity, Z. Parameters X, Y and Z, defines the stellar composition as:

$$X + Y + Z = 1.00 \ , \tag{1.3}$$

where X = mass fraction of hydrogen, Y = mass fraction of helium, and Z = mass fraction of all the remaining chemical elements. The metallicity, Z, is used to describe the abundance of the elements present in an object or environment that are heavier than hydrogen and helium and so, for any elements that fit in this category, astronomers will refer them as "metals". For our Sun, the values for $X_{\odot}$ is 0.7381, $Y_{\odot}$ is 0.2485 and $Z_{\odot}$ is 0.0134. For massive stars, the metallicity affects the mass-loss rate by $\dot{M} \propto Z^{\alpha}$, where $\alpha = 0.69 \pm 0.10$, (Vink et al., 2001) which dictates the evolution. Low metallicity stars lose less mass than high metallicity stars. In the early universe, Z was low and hence massive stars lose less mass at higher redshift. A recent simulation by Regan et al. (2020) found more than 20 very massive stars (VMS) ranging from $1000 M_{\odot}$ to $6000 M_{\odot}$ in the early galaxies. These findings are significant because these VMS will end their lives as a population of black holes with masses ranging from $300 M_{\odot}$ to $10^4 M_{\odot}$ which will eventually coalesce into bigger intermediate mass black holes that will be detected by LISA.

Groh et al. (2014) presented high-resolution evolution models (CMFGEN) for a non-rotating 60 $M_{\odot}$. From their findings, the evolutionary track for this star is the following:

O3 I (ZAMS) $\rightarrow$ O4 I (mid H-core burning) $\rightarrow$ hot LBV (end H-core burning) $\rightarrow$

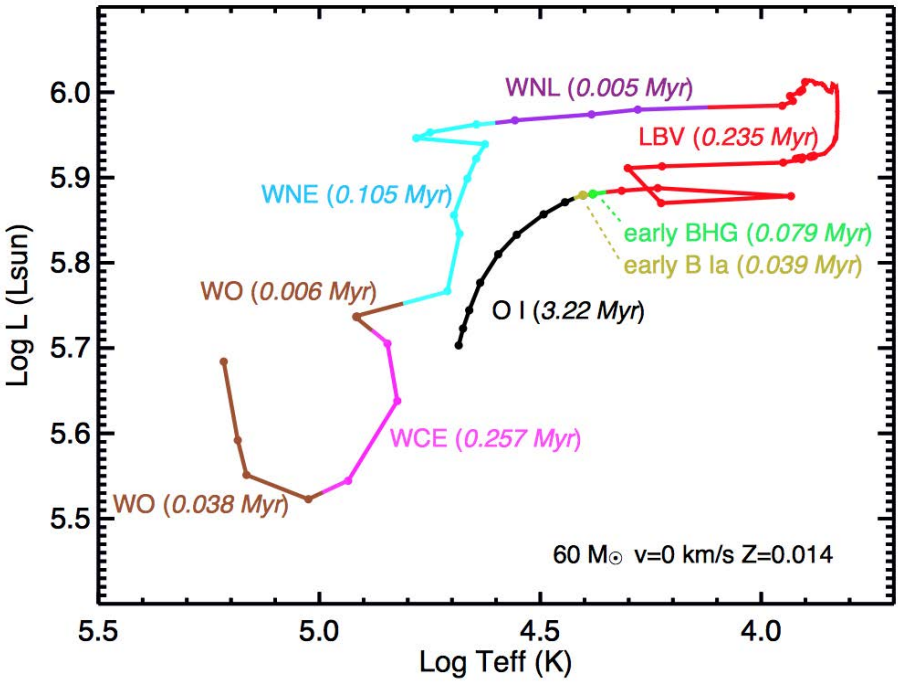

Figure 1.6: CMFGEN model for a non-rotating 60 $M_\odot$ massive stars with $Z_\odot$ = 0.014 and the standard $\dot{M}$. The total lifetime of the star is just 3.727 Myr. The star spend most of its lifetime as an O-star and only spend around 0.9 Myr as a WR star. At the LBV stage, the star has the highest luminosity and temperature. From Groh et al. (2014).

cool LBV (start He-core burning) → WNL → WNE → WC (mid He-core burning) → WO (end He-core burning until core collapse).

From Fig. 1.6, the total lifetime of the star is just 3.727 Myr. The star spends most of its lifetime as an O-star and only spends around 0.9 Myr as a WR star.

If the star is in a binary (and most are (Sana et al., 2012), see Section 1.3), mass-transfer between stars can occur during their evolution. This will complicate the evolution even more. Massive stars in a binary system are essential for forming black-holes. These black-hole systems can then be detected with the present gravitational wave detectors like *LIGO*. Abbott et al. (2016) reported a detection that was the result of the merger of two massive $\sim 30 M_\odot$ black holes (gravitational-wave event GW150914). The stars in this system are believed to have initial masses of $40 - 100 M_\odot$ and metallicity of 0.1 $Z_\odot$. During their evolution, the stars lose mass by

their winds and they also interact through mass-transfer and a common envelope phase.

1.1.4 The Role of Massive Stars

Massive stars serve as "cosmic engines" through their strong stellar winds and intense radiation fields. Their role can be radiative with the radiation mostly in the UV and hot gas emitting in X-rays. They also have an important role in heating the interstellar medium (ISM) and hence shaping star-formation regions from their radiative feedback (e.g., Kennicutt (2005); Geen et al. (2015); Kim et al. (2017)). Massive stars have various mechanical roles in the universe such as stellar winds, colliding winds from the binary stars system, supernovae and gamma-ray bursts that are driving the galactic outflows and turbulence such as the major eruption by the η Carina in 1837 (see Fig. 1.3) and a study from Agertz et al. (2013) that suggested the Wolf-Rayet winds have significant contribution to the energy of the ISM. Massive stars have intense radiations and take on a leading role during the epoch of re-ionisation of the universe. Massive stars are also useful cosmic probes. Astronomers can use the light of massive stars from a distant galaxy and inferred the properties of stellar populations nearby at high red-shift to explore more on the transformation of the universe. Abel et al. (2002) performed a simulation of the formation of the "first-star" at high red-shift, $z = 18.2$ (at the end of the simulation output) where there are nearly zero metal abundances. Unfortunately, from their simulation, the final mass of the star is uncertain because the calculation is stopped when the optical depth become significant. Fig. 1.7 shows their "first-star" image near to the end of the simulation. The center of the object is formed from very small density fluctuations that merge to larger objects (see their Fig. 1 for more images on the simulation outcomes).

Massive stars are important as they can produce heavier elements such as silicon

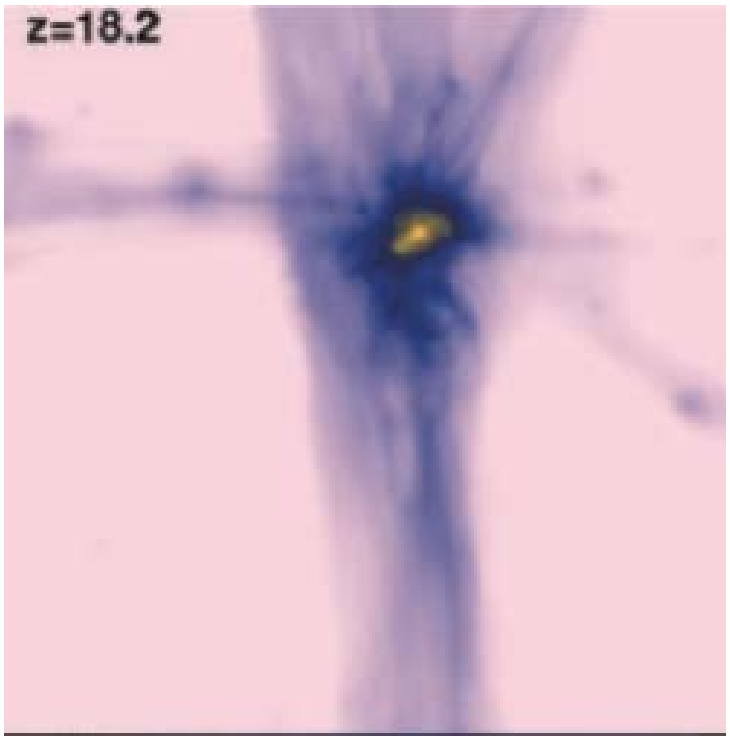

Figure 1.7: The simulation of the formation of the "first-star" at $z = 18.2$ with nearly zero metal abundances. The center of the object form from very small density fluctuations that merge to larger objects. Massive stars in the early universe is the most likely explanation for the re-ionisation of the universe. From Abel et al. (2002).

and iron. These metals which are more massive than hydrogen and helium are created from repeated nucleosynthesis process in a star. For massive stars, the hydrogen burning stage utilises the CNO cycle instead of the 'p-p' chain for low mass stars. The CNO cycle requires a higher core temperature and uses carbon as a catalyst to produce helium. The carbon in the CNO cycle was not being used up but instead returned to be used again. At this stage, stars start producing heavier elements and releasing numerous photons to cause significant radiation pressure, which helps support the star against gravity. For heavier stars, additional bi-cycle loop happened when ^{16}O capture another proton to produce ^{16}O,^{17}O and ^{17}F. The cycle is repeated to produce elements such as magnesium, silicon and eventually iron until the fuel is exhausted. This repeated shell burning fusion is to balance huge gravitational force to prevent the stars from collapsing. When the gravitational contraction increases, so does the temperature of the core. The star will undergo different nuclear reaction producing heavier elements (e.g. Woosley and Heger (2007) and the references therein). Once the iron core is formed, the system will require energy in oppose to producing energy. The layers start to abruptly collapse in preparation for the supernova (refer to Fig. 1.5).

1.2 The Winds of Massive Stars

The origin of radiatively driven stellar winds theory for early-type stars has been explained in a detailed manner by Castor, Abbott and Klein, (1975), hereafter CAK. Here in this section, we will briefly describe the two significant snapshots of the mechanisms namely the "continuum" radiation and line-driven winds. To derive the mass-loss rate, we will start with the mass continuity equation:

$$\frac{\partial \rho}{\partial t} + \nabla \cdot (\rho v) = 0 \,. \tag{1.4}$$

For simplicity, we assumed that the wind flow is at steady state $\frac{\partial \rho}{\partial t} = 0$. Hence this becomes

$$\nabla \cdot (\rho v) = 0 \,. \tag{1.5}$$

Assuming a spherical symmetry, the wind flows radially outwards, hence $\frac{\partial}{\partial \theta} = 0$ and $\frac{\partial}{\partial \varphi} = 0$. The mass continuity equation becomes

$$\nabla \cdot (\rho v) = \frac{1}{r^2} \frac{d}{dr} \left(r^2 (\rho v)_r \right) = 0 \,. \tag{1.6}$$

Solving Eqn. 1.6, gives us the first major equation from CAK which is the mass conservation equation:

$$\dot{M} = 4\pi r^2 \rho v(r) = \text{constant}, \tag{1.7}$$

where $\dot{M}$ is the mass-loss rate, ρ is the wind density, r is the distance from the centre of the star, and $v(r)$ is the wind velocity at a radius r.

To describe the radiatively driven wind, we will start with the momentum balance equation from CAK:

$$v \frac{dv}{dr} = -\frac{GM_*}{r^2} + \frac{\sigma_e L}{4\pi r^2 c}[1 + M(t)] - \frac{1}{\rho} \frac{dp_g}{dr} \,, \tag{1.8}$$

where M_* is the mass of star, p_g is the pressure, c is the speed of light, σ_e is the mass scattering coefficient of the free electrons (in the order of 0.4 cm^2/gm) and L is the luminosity of star. The second term on the right represents the total radiation force and has two components. The $M(t)$ term is termed the force multiplier and represents the line force and the other term is the force due to "continuum" processes (namely electron scattering). The first term on the right is the gravitational force, and the third term is the gas pressure force. Both of these terms have small effects compared to the radiation force. The first component of the radiation force is the "continuum" radiation where this force utilises the electron scattering process. In this mechanism, where there are free-free ionised particles, the photon interacts

with the electron, imparting momentum, and making them move, hence dragging the proton along and away from the source. This radiation force also depends on the Eddington Limit, (L_{edd}) where the radiation force and the gravitational force are in equilibrium. The Eddington Limit, L_{edd} is given by:

$$\frac{\sigma_T L_{edd}}{4\pi r^2 c} = \frac{GM_* m_p}{r^2} \text{ or } L_{edd} = \frac{4\pi G M_* m_p c}{\sigma_T} , \tag{1.9}$$

where m_p is the mass of proton and σ_T is the Thomson electron scattering constant ($\sigma_e = \sigma_T/m_H, \sigma_T \approx 6.65 \times 10^{-25}$ cm^2). From Eqn. 1.9, we can say that high luminosity stars will have higher radiation force attribute to the "continuum" radiation. This attribution towards the total radiation force, however, is not large compared to the second component of the term, which is the force multiplier $M(t)$ that represent the line-driven force.

The main mechanism of line-driven wind is the photon being absorbed by the atom. Elements such as carbon and oxygen will have a few different ionisation states such as C^{3+}, C^{4+}, O^{2+}, O^{3+} etc. With more complex species in massive stars namely iron, it offers a lot more ionisation states. Electrons with the energy from the photons are excited into different ionisation states and atoms with higher energy will accelerate away from the source. The excitation of the electron is temporary, and they will jump down to the original ionisation level by re-emitting photons. When the atom accelerates away from the source with higher energy, they are capable of absorbing photons that have slightly higher energy than the previous absorption. Hence the atom is now blue-shifted towards the observer. These absorptions occur at many ionisation levels with different species, making the atom move away or flow out from the stars with a stronger and dominant force. The evidence of this mechanism can be observed with a P Cygni profile. The schematic diagram for multiple scattering of photons in a stellar wind powered by the principle of radiative line-driven winds is illustrated in Fig. 1.8.

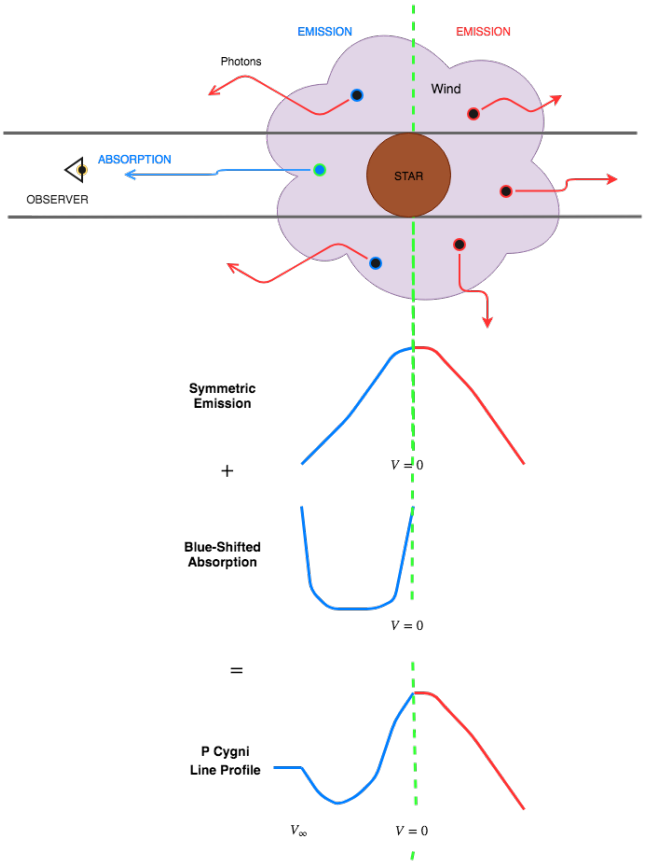

Figure 1.8: Top panel: The absorption of photons by the atom takes place everywhere within the extended atmosphere of the star. Bottom panel: The symmetric broadened emission line from the region close to the star where the gases are very hot. The absorption that occurs in the direction of the observer gives the blue-shifted component. The red-shifted part of the line profile is associated with the re-emission of photons. The combination of emission line and blue-shifted absorption component give the distinguish P Cygni line profile.

1.2.1 The Effects of Stellar Winds On the Evolution of Single Massive Stars

Most stars possess the outflow of gas from the surface, i.e., the stellar wind. For example, the solar wind from the Sun is about 400 km s^{-1} in all directions, and the mass-loss rate of the Sun $\sim 2 \times 10^{-14}$ $M_{\odot}yr^{-1}$. For massive stars, the wind plays a significant role as the terminal velocity, v_{∞} for a typical O-star reached supersonic $\sim$ 3000 km s^{-1} hence the contributing mass-loss rates, $\dot{M} \sim 10^{-6} - 10^{-5} M_{\odot}yr^{-1}$ (Lamers and Leitherer, 1993). Due to the high mass-loss rates, this factor will eventually determine massive stars' further evolution, pre-supernovae structure, and their end fate, making it essential to study the stellar winds of massive stars.

A detailed study to investigate the evolution of single non-rotating massive stars was conducted by Renzo et al. (2017) using the open-source stellar evolution code (MESA) (see Fig. 1.9 for the evolutionary tracks). Parameters such as the linear wind efficiency scale factors, η that account for the clumpiness of the winds, and various wind scheme "recipes" with various combinations of mass-loss algorithms have been applied to solar metallicity massive stars with a mass range from 15 - 35$M_{\odot}$. They concluded that massive stars evolve differently with different treatments of mass-loss applied to the star. They also implied that the specifics of mass-loss treatment could bias the outcome of precise calculations of core-collapse supernova and the predictions of neutron star and black hole formation with potential consequences for gravitational wave astronomy.

For even more massive stars (70$M_{\odot}$ - 140$M_{\odot}$), the stronger stellar wind can change the star's structure by stripping the entire hydrogen-rich envelope, hence further reducing the total mass of the star (Woosley, 2017).

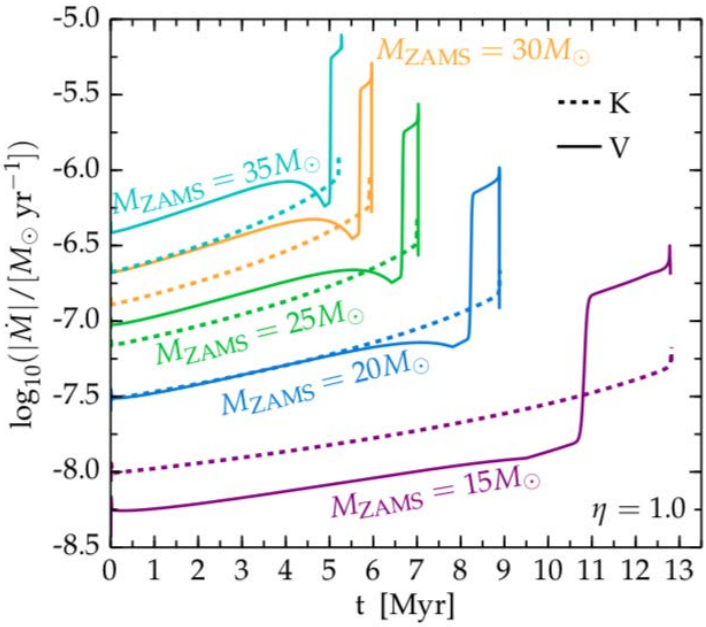

Figure 1.9: Mass loss rate with the wind efficiency $\eta = 1$ for different initial mass at ZAMS. The solid and dashed curves are simulated using the V (Vink et al. 2000, 2001) and K (Kudritzki et al. 1989) mass-loss algorithm. The simulations ended when $T_{eff} = 15\,000$ K threshold as this effective temperature was assumed to divide the cool and hot phases of massive stars. This value also was chosen because the radiation pressure peaks between 10 000−15 000K due to the iron recombination. Image credit: Renzo et al. (2017).

1.2.2 The Wolf-Rayet Wind Momentum Problem

An interesting anomaly arises from WR stars that is potentially defying the law of physics will be highlighted here. The radiative energy of a star which is the total energy radiated away is given by the bolometric luminosity, L_{BOL}, while the kinetic energy driven by the stellar winds is given by:

$$L_{kin} = \frac{1}{2}\dot{M}v_{\infty}^{2}\,, \tag{1.10}$$

where the $\dot{M}$ is the mass-loss rate and v_{∞} is the terminal velocity of the wind. The radiative momentum of a single photon is given by:

$$p = \frac{h\nu}{c}\,, \tag{1.11}$$

where h is the Planck constant, ν is the frequency and c is the speed of light. The total number of photons from the star can be estimated by:

$$N_{photon} = \frac{L_{BOL}}{h\nu_{mean}}\,, \tag{1.12}$$

where ν_{mean} is the mean frequency of the photons from the star. Simplifying Eqn. 1.11 and 1.12, gave us the total stellar radiative momentum, P_{rad} in the form of $P_{rad} = L_{BOL}/c$. On the other hand, the mass momentum, $P_{kinetic}$ is given by $P_{kinetic} = \dot{M}v_{\infty}$. If we take the ratio of kinetic energy to L_{BOL} for an O-star such as the ζ Pup that has the properties of $L_{BOL} \sim 3.11 \times 10^{32}\,W$, $\dot{M} \sim 2.22 \times 10^{17}$ kg s^{-1} and $v_{\infty} \sim 2250$ km s^{-1}, the calculated ratio is less than 1 as follows:

$$\frac{(1/2)\dot{M}v_{\infty}^{2}}{L_{BOL}} = 0.0018. \tag{1.13}$$

If we then take a ratio of $P_{kinetic}$ upon P_{rad}, the calculated ratio is 0.48 which is still below 1. But, if we repeat the same calculation for a WR star, such as WR140

where the properties are $L_{BOL} \sim 2.06 \times 10^{32}\ W$, $\dot{M} \sim 1.27 \times 10^{18}$ kg s^{-1} and $v_\infty \sim 3.00 \times 10^{6}$ m s^{-1} , the result for the ratio of kinetic energy to L_{BOL} is:

$$\frac{(1/2)\dot{M}v_\infty^2}{L_{BOL}} = 0.0273\,, \tag{1.14}$$

but, the ratio of radiative momentum is:

$$\frac{P_{kinetic}}{P_{rad}} = 5.54\,. \tag{1.15}$$

This is termed as the Wolf-Rayet Wind Momentum Problem (WR-WMP), and the solution has been a matter of much debate. Brown et al. (2004) suggested that the solution to the WR-WMP is due to a mixture of clumping in the wind and multiple scattering. A paper by Hamann et al. (2019) has recalculated the $P_{kinetic}/P_{rad}$ for 55 Galactic WN stars as listed in their Table 1 (column 14), where most of the ratio values are less than 10 (still more than 1), and for some of the star such as WR36 and WR110, their wind momentum to the radial momentum ratio are more than 20. Clumping in the wind tends to reduce the inferred mass-loss rate (which in turn lessens the discrepancy in the problem), whereas multiple scattering delivers more momentum to the wind per emitted photon which also reducing the problem but both of these solutions were concluded to be too simplistic by Brown et al. (2004).

1.3 Binary Interaction in Massive Stars Evolution

Almost all of the stellar evolutionary pathways have often used models that usually involve single stars. Unfortunately, the belief that each star is single is incorrect. A lot of research has shown in recent years that most stars are in binary systems e.g., Sana et al. (2012); Kobulnicky et al. (2014). Sana et al. (2012) reported that massive O-stars have binary fractions of nearly 100% in young, massive star-forming regions, with more than 70% of these stars likely to undergo a binary interaction

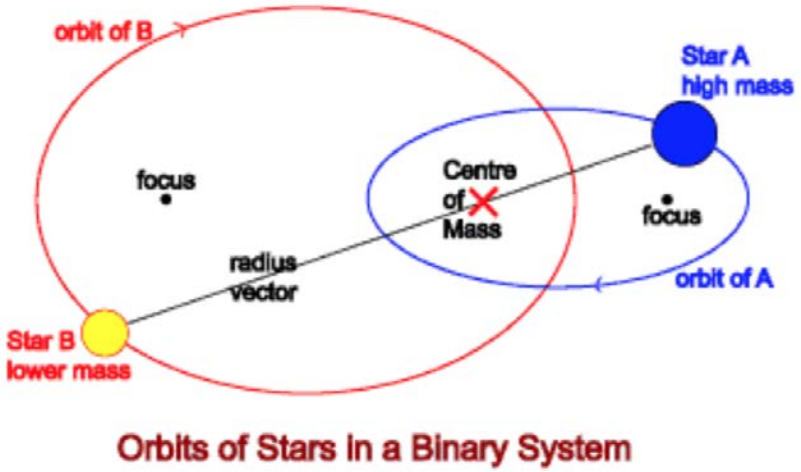

Figure 1.10: The two stars in binary system share a point called a common focus, which is the barycenter of the system and orbit. Binary systems that have strongly elliptical orbits will have eccentricity, e, closer to 1 and near 0 if the orbits are more circular. An example of high eccentricity massive binaries is the WR140, with $e = 0.8993$ (Thomas et al., 2021). Image Credit: `https://www.atnf.csiro.au/outreach//education/senior/astrophysics/binary_intro.html`

that will alter their evolutionary path.

A binary system is one in which two stars are gravitationally bound to each other, orbiting around a common centre of mass, called the barycentre (see Fig. 1.10. For astronomers, binary stars are important as not only for the stars mass determination but also binary stars will affect the evolution of the star, especially if the stars are massive. Binary orbital periods and distances differ significantly. Some binary systems are classified as "close binaries" where the binary separation is ≤ 10 AU so the material on the surface can be exchanged (e.g., γ^2 Velorum, $a = 1.2$AU (North et al., 2007) and WR123, $a = 1.2$ AU (Richardson et al., 2017)). In contrast, others have orbital periods of hundreds of years, such as WR146 system with an orbital period of more than 550 years (Gunawan et al., 2003). Regardless, for being wide or close binaries, massive stars evolution will be different from single massive stars.

There are strong observational indications that binaries are significant such as the discovery of the gravitational waves from massive black holes mergers (Abbott

et al., 2020). Unfortunately, many studies only used single-star models. For example, the merging neutron star GW170817 where the study used only single-star models (e.g., Blanchard et al. 2017, Murguia-Berthier et al. 2017), but the observed GW transients were formed by a binary star.

An insightful study by Eldridge (2020) using the Binary Population and Spectral Analysis (BPASS) code has shown many different evolutionary pathways that are not possible with single-star stellar models. From Fig. 1.11, 189 BPASS evolutionary tracks of the theoretical HR diagram are overlaid with single-star evolutionary tracks for 10, 20, and $40 M_{\odot}$. Sequence models are experiencing Roche-Lobe Overflow (RLOF) and Common Envelope Evolution (CEE). Some models undergoing mergers and others take paths that lie in between those two instances. Models undergoing RLOF and CEE can now lose their hydrogen envelope to form Wolf-Rayet (WR) stars which was impossible without binary interaction. From single-star models, these stars are unable to lose their hydrogen envelopes through stellar winds and usually explode as red supergiants.

Most massive stars possess strong stellar winds, and they usually exist in a binary system. When we have these stars in the binary system, we will have colliding winds in the binaries. It is widely believed that binarity (including the intrinsic wind-wind interaction) is the main cause of excess infrared and radio luminosity of WR-binaries as compared to single WR-stars. The evolutionary effects of binarity on stellar evolution in a close system may assist the stripping of WR stars of its H-envelope as suggested by Eldridge (2020). Additionally, the X-ray radiation attenuation that could not be explained by a single-star system could be caused by the colliding winds in a binary system (e.g., (Corcoran et al., 2011)).

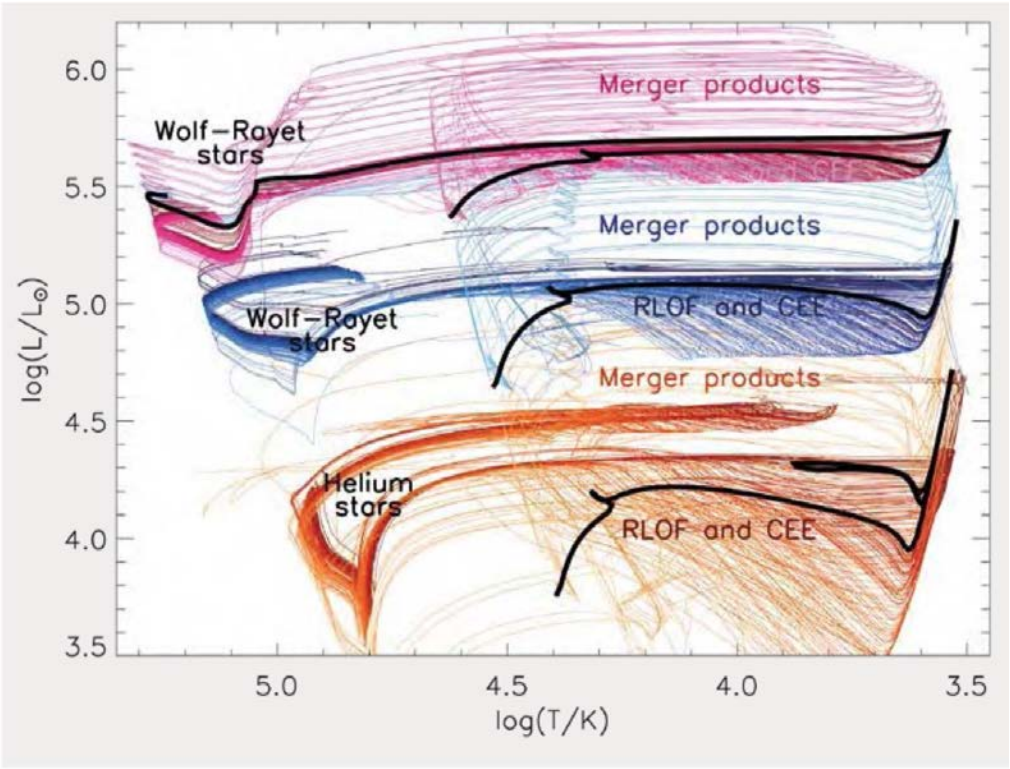

Figure 1.11: A theoretical HR diagram shows the evolution tracks of $10M_{\odot}$, $20M_{\odot}$, and 40 $M_{\odot}$ stars in orange, blue, and magenta lines. The thick black lines represent the single-star tracks, while the coloured tracks are for the 189 BPASS primary-star evolution tracks at mentioned masses at solar metallicity. The coloured tracks showed a variety of evolutionary paths such as merger products, RLOF and CEE. From this diagram, stars ranges between 8 and 25 solar masses can lose their envelope to become WR stars, whereas not in single-star models. Image credit: Eldridge (2020).

1.4 X-ray Emission from Massive Stars

The X-ray emission from a single massive star is generally from the internal shocks of the powerful wind, driven by the radiation forces on the stellar surface (Rauw et al., 2015). In typical cases, early-type stars have soft X-ray spectra and a temperature of $kT \sim 0.5\,\mathrm{k}eV$. But if much higher quality spectra used, hard X-ray emission can be observed with a temperature range of $kT \sim 2.0$ keV (e.g., Oskinova et al. (2007); Corcoran et al. (2011)).

Abundant metals in the wind are very capable of absorbing soft X-rays. For example, emission lines for heavy elements can be detected in ζ Pup using the *Chandra* Spectrometer as shown in Fig. 1.12 by Cassinelli et al. (2001). Cohen et al. (2010) has fitted emission lines in the high-resolution *Chandra* grating spectrum emission line for the materials from the ζ Pup. For example, the Ne X, the X-ray line profile shows that Lyα line is blue-shifted due to more absorption of the materials on the far side of the star (see Fig. 1.13).

The instabilities of line-driven winds are capable of producing X-ray emission from massive stars. Owocki et al. (1988) suggested that the outer winds possess strong reverse shocks implying that the line-driven wind is not smooth and these perturbations grow prominently with radius following the power-law shape of the steady, homogenous wind. There are many complex dynamical structured wind models investigating the "clump", such as the hydrodynamical model by Feldmeier et al. (1997) (see Fig. 1.14), but as far as we know, these internal shocks can dramatically increase the temperature of the winds to 10^7 K where the X-ray emission can be observed.

For a very eccentric binary system such as WR140 (eccentricity, $e = 0.8993 \pm 0.0013$, orbital inclination, $i = 119.070°$ (Thomas et al., 2021)), which consists of a WC7 and an O5 star, the X-rays comes from the wind-wind collision region peaking

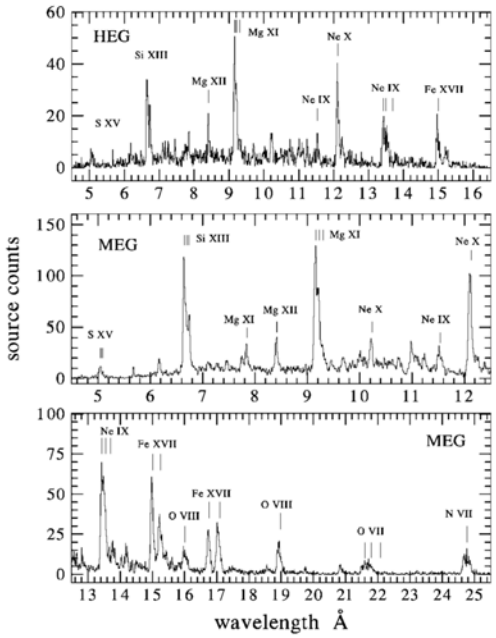

Figure 1.12: The *Chandra* High-Energy Transmission Grating Spectrometer (HETGS) emission line of a single star ζ Pup. Emission lines for heavy elements such as Mg, Si, Ne and O clearly can be seen (Cassinelli et al., 2001).

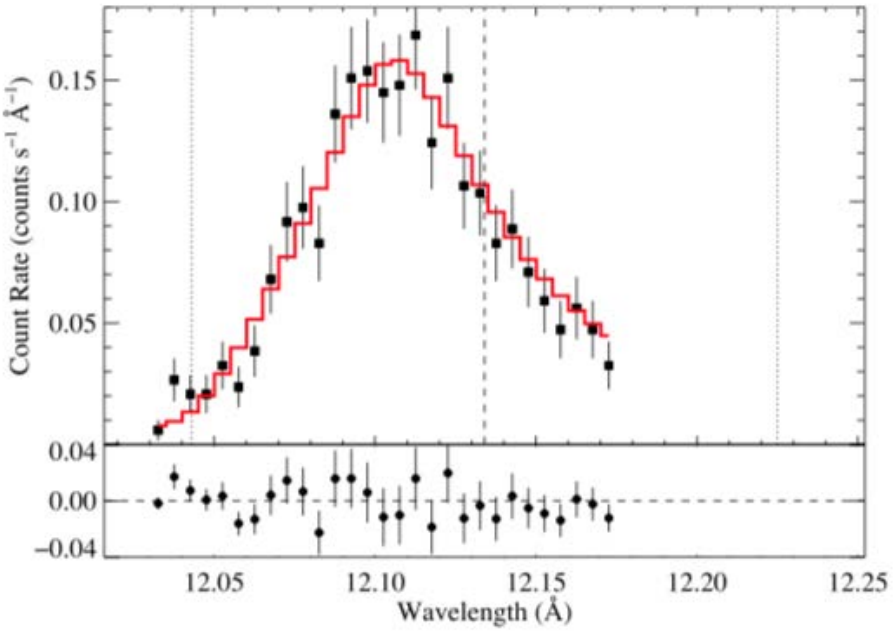

Figure 1.13: The emission line profile model fitting of Ne X from ζ Pup clearly shows that the Lyα line has been blue-shifted and has asymmetry line profile because of the materials on the far side of the star has been more absorbed (Cohen et al., 2010).

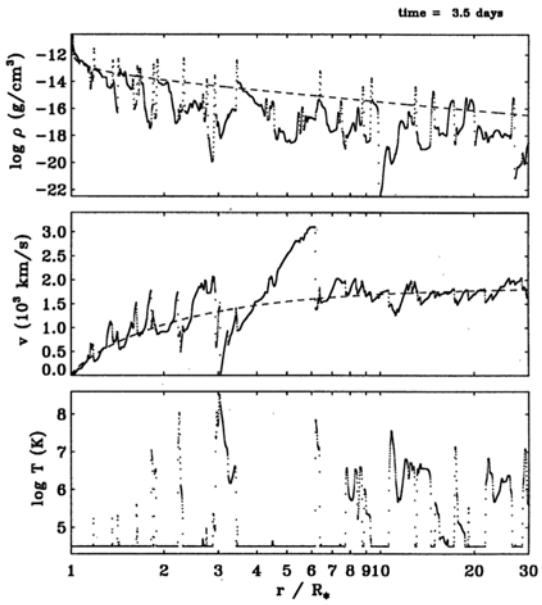

Figure 1.14: The time-dependent hydrodynamical model of dynamical wind structure by Feldmeier et al. (1997) suggested that the wind collision is inhomogeneous and have strong shocks which producing the X-ray emissions.

near the periastron passage. WR140 lightcurve observed by the *Rossi X-ray Timing Explorer, (RXTE)*, shows a strong absorption dip closer to the periastron indicating that the materials being absorbed by the thick wind of the WC7 star (Corcoran et al., 2011) (See Fig. 1.15).

1.5 Radio Emission from Massive Stars

The first massive star detected at radio wavelengths was the LBV star, P Cygni at 6 cm ($S_\nu = 9\pm2$ mJy) and at 3 cm ($S_\nu = 15\pm3$ mJy) by Wendker et al. (1973). The first WR star was detected also by Wendker et al. (1973) was the WR 136 while the first O-type star detected by radio wavelengths was the ζ Pup by Morton and Wright (1978). The radio emission intensity is measured in units of flux density, S_ν, as a function of frequency, ν and usually expressed in unit Jansky where 1 mJy $= 10^{-29}\,\mathrm{Wm^{-2}Hz^{-1}} = 10^{-26}\mathrm{ergs^{-1}cm^{-2}Hz^{-1}}$. Fig. 1.16 shows the HR diagram for stars detected as radio stars. Massive stars such as the Wolf-Rayet and O-stars

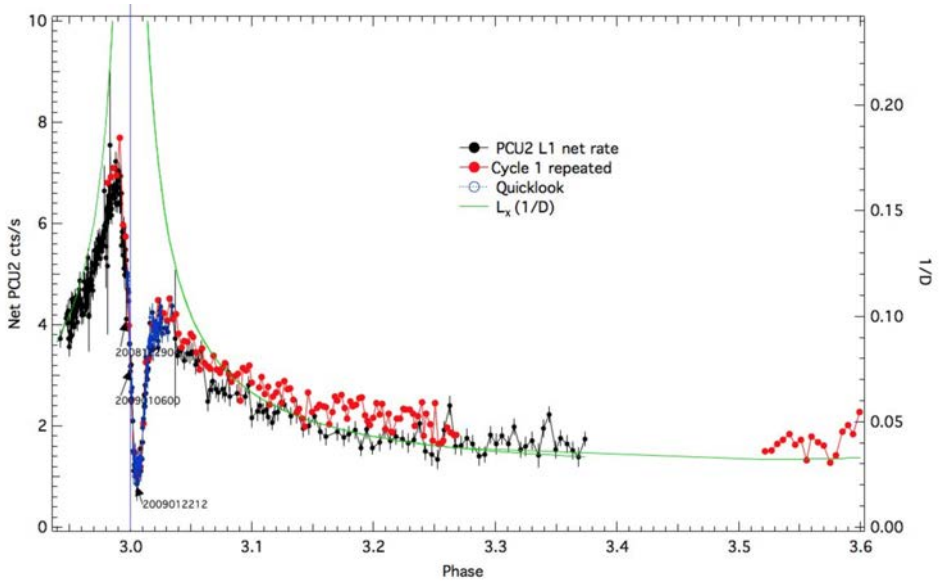

Figure 1.15: A strong dip can be seen from WR140 lightcurve where the materials from the O-star has been absorbed by the thick wind of WC7 at periastron. The green line shows the X-ray luminosity which scales as $L_X \propto 1/D$, where D is the separation between two stars. From: Corcoran et al. (2011).

were positioned at the top left region of this HR diagram indicating that these hot stars are excellent radio stars.

1.5.1 Free-Free Emission

Radio emission in massive stars is due to the thermal and non-thermal processes in stellar winds. A non-thermal radiation source comes from any charged particles namely electron at the relativistic speed, accelerated by the magnetic field. Fig. 1.17 shows the mechanism of synchrotron emission from a binary star system. On the other hand, the counterpart of that synchrotron radiation, i.e. non-thermal, is the free-free emission where the charged particles accelerated by an electric field in local thermal equilibrium (LTE). It is important to remember that this free electron is not being absorbed by the ion but only deflects with other charged particles hence it is termed "free-free" because it is a free particle both before and after the interactions. The thermal emission from this process is continuous and has a brightness temperature roughly at 10^4 K (Wright and Barlow, 1975).

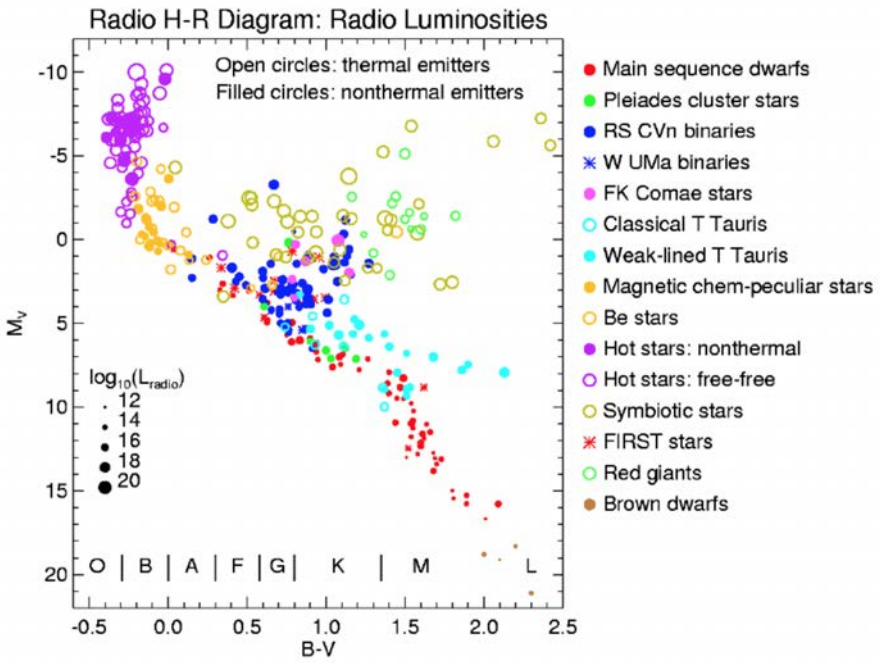

Figure 1.16: The colour coded radio detection of various types of stars. Hot stars such as the Wolf-Rayet and the O-stars were positioned at the top left corner of the diagram (purple circles - fill and no-fill). Image Credit: Stephen White, http://www.astro.umd.edu.

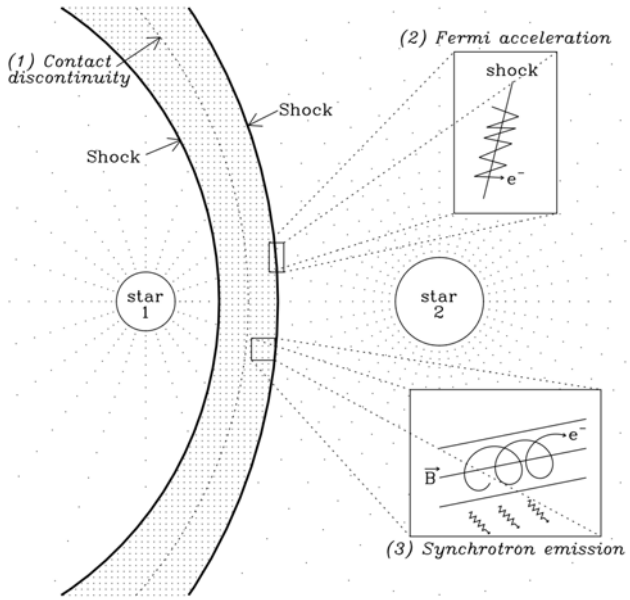

Figure 1.17: Synchrotron emission from colliding winds. (1) The winds of both components collide, creating a narrow band of contact discontinuity. (2) Repeatedly reflected, the Fermi acceleration brings the electrons to relativistic speeds. (3) Synchrotron radiation is emitted when the electrons spiral in the magnetic field at relativistic speed (Blomme, 2011).

It is useful to approximate a 'black body' radiation to our source so that the intensity, I_ν of the source is given by the Planck function as:

$$I_\nu = B_\nu(T) = \frac{2h\nu^3}{c^2}\frac{1}{e^{\frac{h\nu}{k_\mathrm{B}T}} - 1} \,. \tag{1.16}$$

For radio photons, where the frequency, ν is much less energetic, $h\nu \ll k_B T$, the term $(\exp(h\nu/kT) \simeq 1 + h\nu/kT)$, hence Eqn. 1.16 becomes the Rayleigh-Jeans approximation:

$$B_\nu(T) \approx \frac{2\nu^2}{c^2} k_\mathrm{B} T \,. \tag{1.17}$$

From this limit, astronomers will be able to observe infrared/radio sources at the tail of Rayleigh-Jeans. The Kirchhoff relation in the thermodynamic equilibrium system is given by:

$$j_\nu = \kappa_\nu B_\nu(T) \,, \tag{1.18}$$

where j_ν is the emissivity coefficient as a function of frequency and κ_ν is the opacity as a function of frequency. The ratio j_ν/κ_ν is called the *source function* or more commonly used as the flux density, S_v. In the Planck function, S_v is termed as $S_\nu = B_\nu$ and scales with frequency, ν as $S_\nu \propto \nu^\alpha$.

The flux density very much depends on the opacity of the medium. If we think about a beam of radiation from a distant point source (e.g., a star), passing through a cloud, the intensity of the source, I_ν changes as the radiation travels across the material of gas with the thickness $\mathrm{d}s$, given by the form of the Equation of Radiative Transfer:

$$\frac{\mathrm{d}I_\nu}{\mathrm{d}s} = j_\nu - k_\nu I_\nu \,. \tag{1.19}$$

If we consider the simplest case where there is no emission from the cloud; $j_\nu = 0$, the Eqn. 1.19 has a solution:

$$I_\nu = I_\nu(0) \exp\left\{-\tau_\nu\right\} \,, \tag{1.20}$$

where the total opacity, τ_ν is given by the integral of $-\kappa_\nu$ along the line of sight given by:

$$\tau_\nu = \int_{\rm los} -\kappa_\nu ds \, . \tag{1.21}$$

But the more general solution where $j_\nu \neq 0$ is given by:

$$I_\nu = I_\nu(0) \exp\{-\tau_\nu\} + B_\nu \left(1 - \exp\{-\tau_\nu\}\right) \, , \tag{1.22}$$

where the first term is the original intensity from the point source and the second term is associated with the emission from the cloud. From Eqn. 1.22, if τ_ν is large, $I_\nu = S_\nu(B_\nu)$ where it scales with frequency as $S_\nu \propto \nu^2$. At low frequency, the cloud of gas will have a large optical depth to free-free radiation and become optically thick, photons cannot escape easily and emit like a blackbody. Next, if τ_ν is small, $I_\nu = S_\nu \tau_\nu$. The opacity scales as $\kappa_\nu \propto \nu^{-2.1}$. So at high frequency, the cloud is nearly transparent as:

$$S_\nu \propto \frac{2kT\nu^2}{c^2}\tau_\nu \propto \nu^{-0.1} \, . \tag{1.23}$$

From Mezger and Henderson (1967), the free-free opacity, τ_{ff} can be expressed as:

$$\tau_{ff} \approx 3.28 \times 10^{-7} T^{-1.35} \nu^{-2.1} EM \tag{1.24}$$

where the temperature, T is in units of 10^4 K, ν is the frequency in GHz and EM is the radio emission measure in pc cm^{-6}.

For O-stars, the radio emission is a mixture of optically thick from the inner regions and optically thin from the outer regions and as a result, the spectral shape is intermediate between the thin and thick region. In the radio regime, as shown in Fig. 1.18, the spectral index of the free-free emission by a wind of a typical O-star is closer to +0.6 than to +2. Fig. 1.19 shows the total radio emission for a typical O-star consists of the thermal component and non-thermal component of the star scale with frequency, ν.

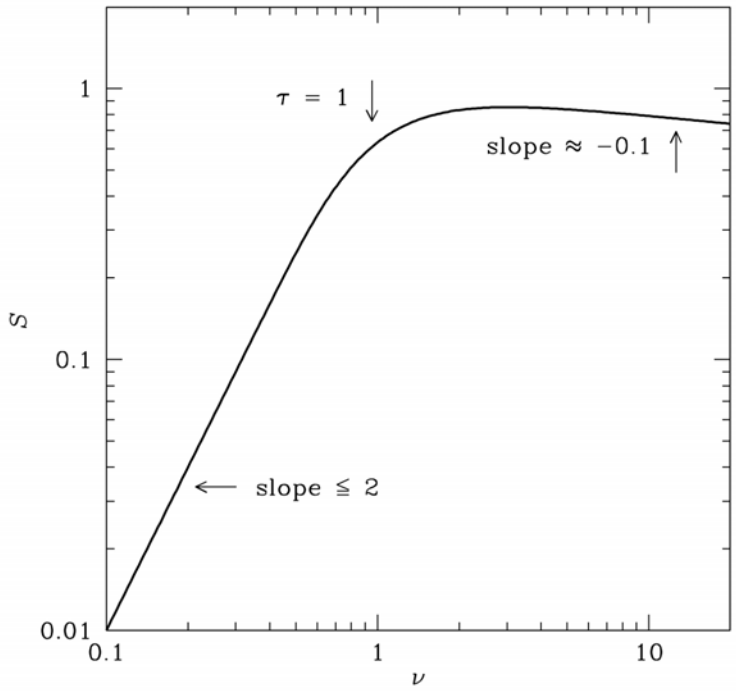

Figure 1.18: At low frequencies, with the slope (known as the spectral index) equal to 2, the source is blackbody, while at higher frequencies, the spectral index is negative (≈ -0.1) because the opacity coefficient, κ scales as $\kappa(\nu) \propto \nu^{-2.1}$. So, at high frequencies the cloud of materials is optically thin. Image Credit: https://www.cv.nrao.edu.

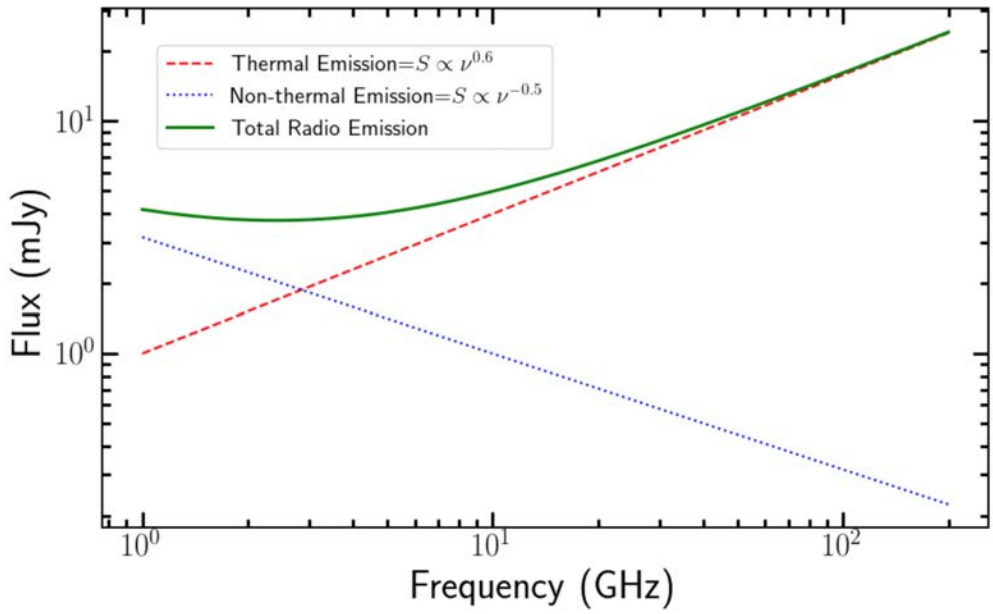

Figure 1.19: The radio emission model represents the total observed radio flux with the thermal and non-thermal component. The numbers in this model are from simple assumptions and not from the real observation data.

From Wright and Barlow (1975), the radio and infrared regions of the spectrum where $h\nu \ll kT$, can be expressed as:

$$S_v = 23 \cdot 2 \left(\frac{\dot{M}}{\mu v_\infty} \right)^{4/3} \frac{\nu^{2/3}}{D^2} \gamma^{2/3} g^{2/3} Z^{4/3} \,, \tag{1.25}$$

where $\dot{M}$ is the mass-loss rate in $M_\odot \mathrm{yr}^{-1}$, D is in kpc, v_∞ is in km s^{-1}, ν is in Hz and g is the Gaunt factor. From Eqn. 1.25, $S_v \propto \nu^{2/3}$ and further flatten to $S_v \propto \nu^{+0.6}$ in the radio region. From Wright and Barlow (1975), the effective radius of the emitting region is given by:

$$R(\nu) = 2 \cdot 8 \times 10^{28} \gamma^{1/3} g^{1/3} Z^{2/3} T^{-1/2} \left(\frac{\dot{M}}{\mu v_\infty \nu} \right)^{2/3} \mathrm{cm} \,, \tag{1.26}$$

where T is in K, $\dot{M}$ is the mass-loss rate in $M_\odot \mathrm{yr}^{-1}$, v_∞ is in km s^{-1} and ν is in Hz. From Eqn. 1.26, the effective radius of the emitting region, $R(\nu)$ scales with frequency, ν as:

$$R(\nu) \propto \nu^{-2/3} \,, \tag{1.27}$$

therefore, we are able to see much deeper into the wind at higher frequencies, such as with ALMA. At this depth, we might see where the wind is accelerating. Fig. 1.20 shows an illustration of stellar wind with different regions at different penetration frequencies. For example, for a massive star with a mass-loss rate, $\dot{M} \sim 10^{-5} M\odot/yr$, $v_\infty = 2000$ km/s at 1 kpc observed at 100 GHz, the radio flux, $S_\nu \sim 2$ mJy and the effective radius, $R(\nu) \sim 1.7$ AU which is very close to the optical photosphere.

1.6 The Effects of Wind Clumping

Many stellar atmosphere models adopted smooth wind prescriptions for simplification. Still, the line-driven stellar winds of massive stars are expected to be unstable and clumped, as discussed by Owocki et al. (1988). Abbott et al. (1981) examined

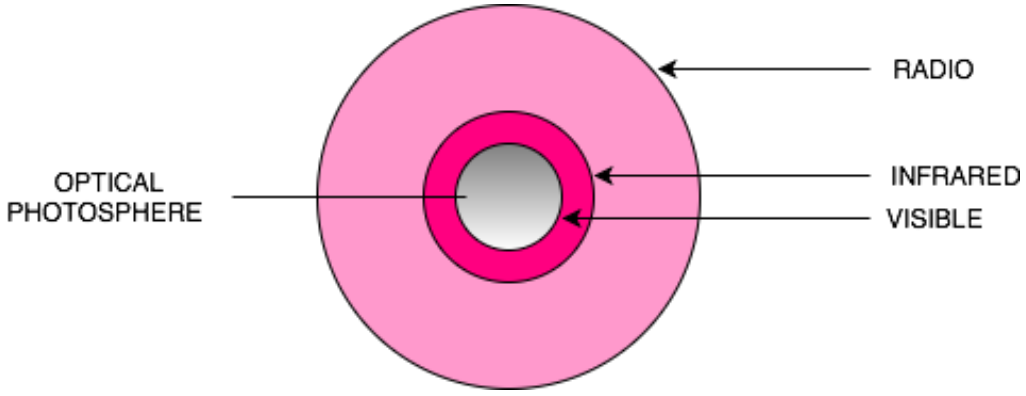

Figure 1.20: An illustration of the stellar wind with different observing regions. As the frequency increases, the effective radius of the star becomes smaller, and we will eventually see the optical photosphere of the star. Hence, if we use higher frequency facilities such as ALMA, we can see deeper into the stellar wind.

the effects of clumping in the wind on the mass-loss rate derived from the thermal radio emission and summarise that clumping leads to an increase in the radio emission for a given mass-loss rate. The effects of 'microclumping' and 'macroclumping' have been discussed in detail by Oskinova et al. (2007).

The term 'microclumping' refers to the wind clumps that are optically thin with the basic assumption that the clumps are smaller than the photons' mean free path. On the other hand, 'macroclumping' refers to the clumps that are optically thick or optically thick at some frequencies.

The clumping factor, f_{cl} and the volume filling factor, f_V (from Abbott et al., 1981; Runacres and Owocki, 2002; Daley-Yates et al., 2016) can be expressed by:

$$f_{cl} = \frac{1}{f_V}, \tag{1.28}$$

where for a clumped wind, $f_{cl} > 1$ and $f_V < 1$, while for the unclumped wind, $f_{cl} = 1$ and $f_V = 1$. If we assume the degree of clumping is constant at each radius of the wind, from Abbott et al. (1981), the radio flux scales as:

$$S_\nu \propto \dot{M}^{4/3} \times f_{cl}^{2/3}. \tag{1.29}$$

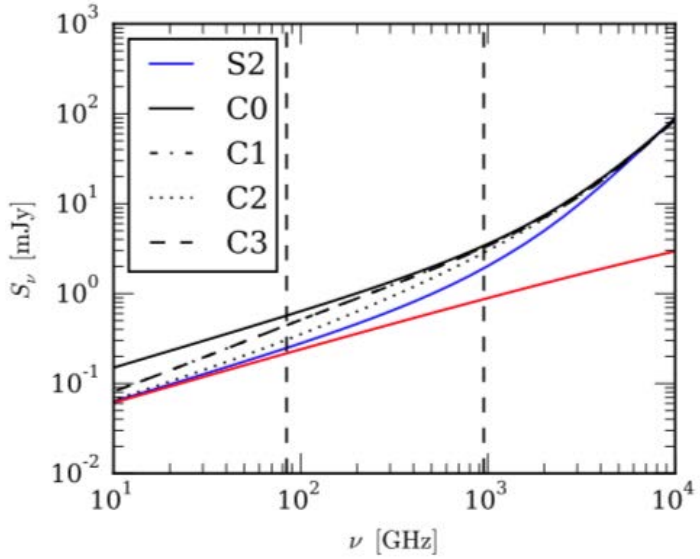

Figure 1.21: The plot shows several numerical wind models across three decades of frequency. The red line shows the thermal radio emission from Wright and Barlow (1975). The black non-solid lines (C1-C3) represents various wind clumped models. The solid blue line (S2) represents a no-clumping wind model, while the solid black line (C0) represents a smooth wind model (uniform clump). Generally, we can see that wind clumping pushes up the expected spectral flux inferring that the mass-loss rate will be overestimated (Daley-Yates et al., 2016).

From Eqn. 1.29, we can see that if the clumping is constant throughout the wind, the flux derived from the thermal emission will be raised uniformly across all wavelengths for a specific mass-loss rate. Consequently, clumping means the inferred mass-loss rate will be lower for the same observed flux, as shown in in Fig. 1.21, hence affecting the evolutionary path of massive stars.

2 | Introduction to Radio Astronomy

"Radio astronomers are aware in the back of their minds that if there are other civilisations out there in space, it might be the radio astronomers who first pick up the signal."
–Jocelyn Bell Burnell.

Chapter Summary

This chapter includes an overview of radio astronomy's history as well as a look into the radio sky. I consider the different radio telescopes available and focus on the diverse capabilities of the current radio interferometry. Finally, I give an overview of the software and applications used by today's radio astronomers to analyse radio data.

2.1 A Brief History of Radio Astronomy

The nature of our atmosphere is truly incredible. As illustrated in Fig. 2.1, it is transparent to some wavelength, but opaque to others. Harmful electromagnetic waves, such as gamma rays and ultraviolet waves, can not reach the ground while visible lights, radio, and certain infrared waves can. The atmosphere of the radio

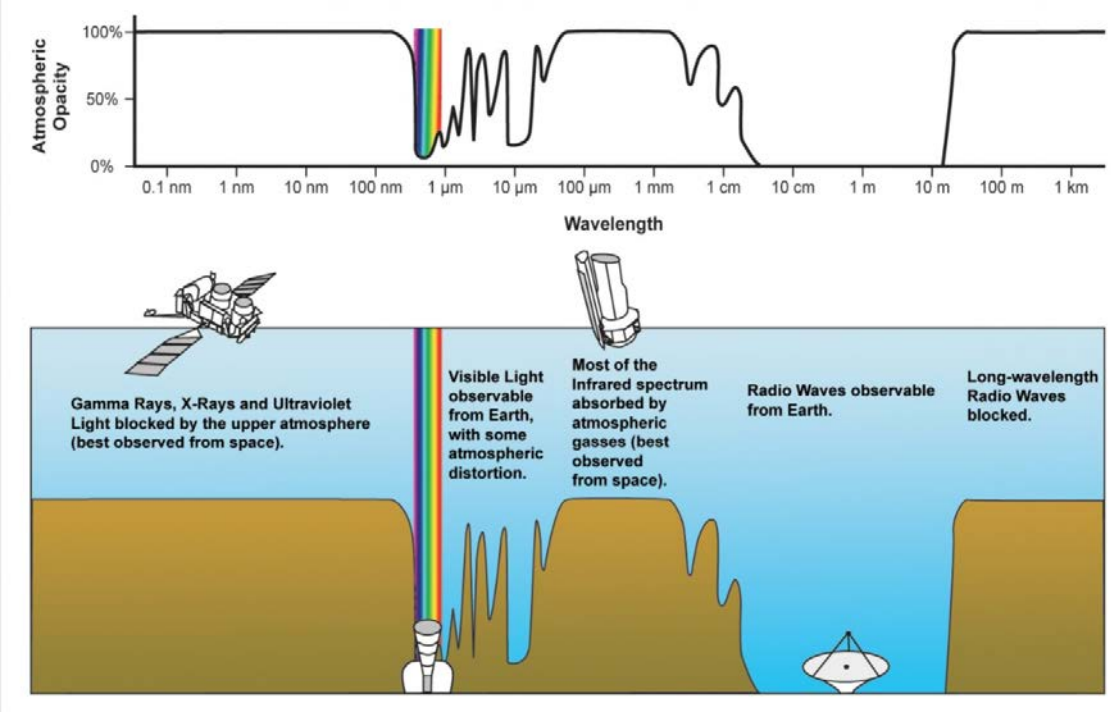

Figure 2.1: The atmospheric electromagnetic transparency graph shows a few openings where it is suitable to place telescopes on the ground. For some windows such as X-ray, UV and part infrared, the observations are best conducted from space because the atmosphere is opaque. Image credit: `http://coolcosmos.ipac.caltech.edu`

window is transparent to any radiation, and it ranges between 30 cm and 10 m. To our advantage, astronomers can place the radio telescope on the ground with significant modifications to the built, as the photon energy is much less than the visible.

Radio waves as an astronomical source were first detected from the centre of Milky Way in 1933 by Karl Jansky. Working at a wavelength of 14.5 metres, three distinct signals were detected where one of them was coming from the centre of the Milky Way (Jansky, 1933). Although did not receive any Nobel Prize, his name is now used widely as the unit for flux density, "Jansky" ($1\text{Jy} = 10^{-26} W/m^2/Hz$). The first true radio astronomer that set the stage for the rise in radio astronomy was Grote Reber where he built a 9 m parabolic reflector in 1937 in his backyard, at Wheaton, Illinois as shown in Fig. 2.2. He conducted the first sky survey at radio frequencies (3300 MHz, 900 MHz and 160 MHz) and only successful on the third

attempt in 1941. For the first time, the existence of Cassiopeia A and Cygnus A has been resolved as individual sources, where Cas A being a supernova remnant and Cyg A is a radio galaxy (Reber, 1944).

Martin Ryle, a British astronomer, worked on airborne radar antennas during the World War II, built the first multi-element interferometer in 1946. In 1955, he published interferometric radio observations to produce early catalogues for radio sources. He led the Third Cambridge Catalogue of Radio Sources (3C) (Edge et al., 1959) with various Cambridge interferometers at $80 - 200$ MHz.

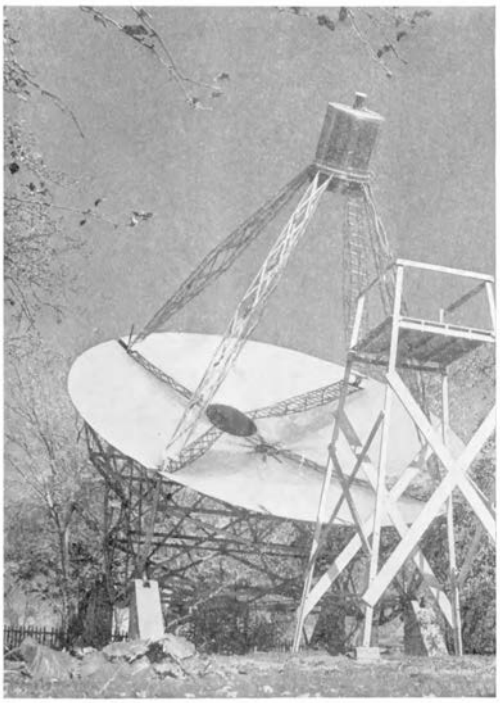

Figure 2.2: The 9 meter parabolic reflector telescope built in Wheaton, Illinois for the first sky survey at 160 MHz (Reber, 1944).

2.2 The Radio Sky

The sky looks majestic with many stars of different brightness. Away from the city lights, we could see the Milky Way's faint band, the illumination of billions of stars making up our Galaxy. Fig. 2.3 shows the optical image of the Milky Way across a

quiet sky in a remote area of East Malaysia, Sabah, located on the island of Borneo. From Fig. 2.3, we can see familiar stars such as λ and γ Sagittarius, as well as a band of darkness made out of dust blocking our view of the galactic plane. Radio waves have a long wavelength that is not scattered by dust particles. This property enables us to image and study varieties of unique structures in the galactic plane.

Figure 2.3: The optical image of The Milky Way with familiar stars (γ and λ Sagittarius) taken from a remote area in Sabah, Malaysia . Image credit: Emma Zulaikha's private collections, April 2020.

Witnessing the night sky through 'radio eyes' seems very similar to the optical unaided eyes shown in Fig. 2.4, but the dots are not real stars. Many strong radio sources are optically weak or invisible, and most bright stars are undetectable at radio wavelengths. A typical radio emission for Wolf Rayet star is $\sim$ 1 mJy at 4.8 GHz (for example, WR125 at 4.8 GHz using the VLA interferometer, $S_\nu = 1.18 \pm 0.06$, Cappa et al. 2004). The majority of the point-like objects in Fig. 2.4 are extremely luminous radio galaxies or Active Galactic Nuclei (AGN)s billions of light-years away.

Figure 2.4: The 4.85 GHz view of the radio sky about 45 degrees across the NRAO site in West Virginia. This composite image depicts the sky as seen from the 'radio eyes'. The dots scattered throughout the sky are not real stars, but distant, active radio galaxies. Image credit: `https://public.nrao.edu/gallery/`

Fig. 2.5 shows an image from a radio interferometer located in Western Australia called the Murchison Widefield Array (MWA). This image is a part of the GaLactic and Extragalactic All-sky MWA survey (GLEAM). We can see that the galactic plane is not dark, but glowing with synchrotron radiation with many compelling features. The radio colours in this image are not false, but demonstrate a range of radio frequency where red is the lowest, blue is the highest, and green is the frequencies in between. Also, from the inset of this Milky Way image, unique features like radio jets from a galaxy (purple box), shell-like bubbles of the supernovae remnants (SNR) (blue box), and the ionised regions all over bright stars (orange box) can be seen, whereas undetectable in visible light.

A higher resolution image of the galactic plane by a radio interferometer called MeerKAT, consisting of 64 antennas in the Northern Cape of South Africa, is shown in Fig. 2.6. Here, we can see details and deep images of SNRs bubbles, the Radio

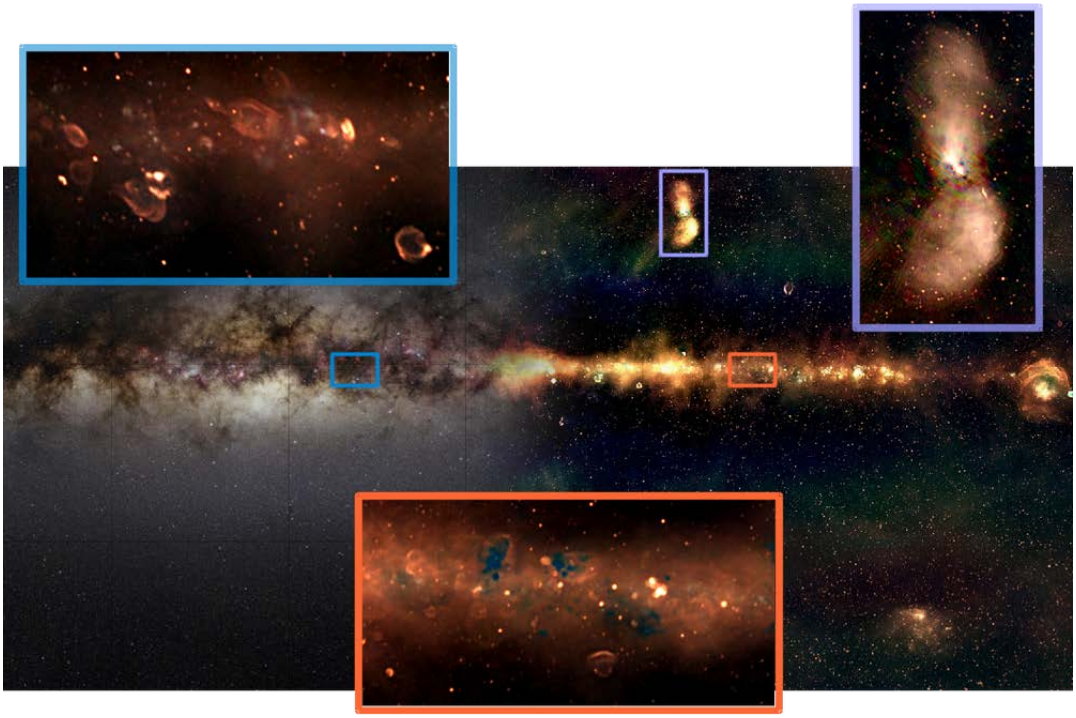

Figure 2.5: The image of the galactic plane taken by GLEAM survey. The Milky Way as seen from the visible light on the left to the radio light as seen by GLEAM on the right. Features like supernovae bubbles (blue box), radio jets (purple box) and ionised gas (orange box) can be seen. The dots scattered in this image by GLEAM are not stars but distant active radio galaxies. Image credit: Dr. Natasha Hurley / Curtin University, International Centre for Radio Astronomy Research.

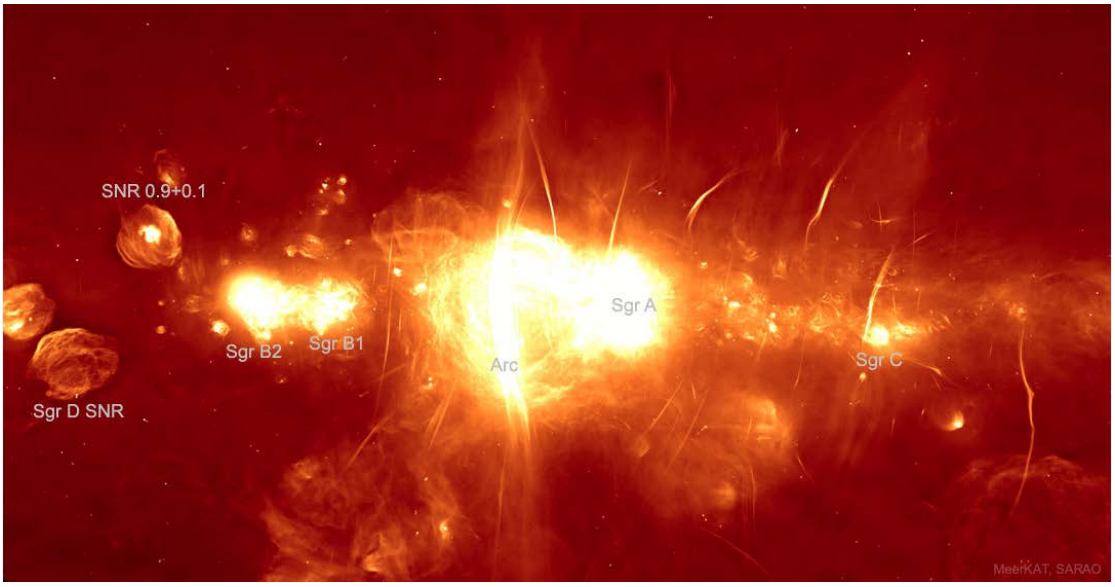

Figure 2.6: A deep and detailed image of The Galactic Centre at 2 degrees across imaged by the MeerKAT array. This image shows the galactic centre is an interesting and an active place with various features like SNR bubbles, the Radio Arc and many filamentary threads. Image credit: `https://apod.nasa.gov/apod/ap190708.html`

Arc and numerous filamentary threads.

Closer to home, the Sun is a bright radio source, while other planetary bodies are undetectable by reflected solar radiation at radio wavelengths. However, a planet like Jupiter also emits a strong non-thermal emission due to synchrotron radiation emitted by relativistic electrons trapped in Jupiter's magnetic field.

2.3 The Radio Telescope : Single Dish versus Interferometers

A single-dish telescope is preferable to an interferometer for certain observations and vice versa. The fundamental difference between a single-dish telescope and interferometric instruments is the range of angular scale sizes to which they are sensitive. For practical purposes, consideration must be given to the complexity of the interferometer instrumentation and, to some degree, the user software package's learning complexity, which allows single-dish telescopes to be a realistic option in a given

project or experiment. However, the challenge of maintaining sufficient amplitude stability in single-dish instruments make the interferometric instruments taking the lead. A combination of single-dish and an interferometry array is necessary for some observations. Therefore, since they are complementary, most of the next-generation telescopes working in the mm and sub-mm parts of the spectrum can benefit from using both single-dish radio telescopes and interferometers. This subsection addresses the advantages and drawbacks of single-dish telescopes and interferometers.

Due to the weight and stability of the single-dish telescope, large parabolic dishes usually were built in a karst depression on the ground, such as the 305 m Arecibo telescope in Puerto Rico and the latest Five Hundred Meter Aperture Spherical radio Telescope (FAST), in the Dawodang depression, Guizhou, China. The FAST telescope has superseded the previous largest radio telescope (Arecibo) by providing more flexibility having an 'active surface' with the maximum working aperture up to 300 m at one time (see Fig. 2.7). This telescope works by having the receiver to illuminate a circle of 300 m when held in the correct parabolic shape and not spherical as claimed. Hence, the collecting area and resolution power are a lot less than expected (Li and Pan, 2016). Regardless, both of these single-dish telescopes have a large collecting area that will be very useful to observe the deep sky.

To obtain a higher image resolution, one must build a gigantic telescope than the current FAST. Unfortunately, this is quite an engineering challenge and impractical to construct. Furthermore, enormous telescopes will be too heavy and unsteerable. To date, large, steerable telescope dishes are up to 100 m, such as the 76 m Lovell telescope located in Jodrell Bank, Manchester, UK and the 100 m Effelsberg telescope, in Bad Münstereifel, Germany. Therefore, moving forward, radio interferometers usually become the primary choice for astronomers.

In order to benefit the advantages of higher resolution and a large collecting area, smaller single-dish telescopes are integrated into radio interferometers. The e-

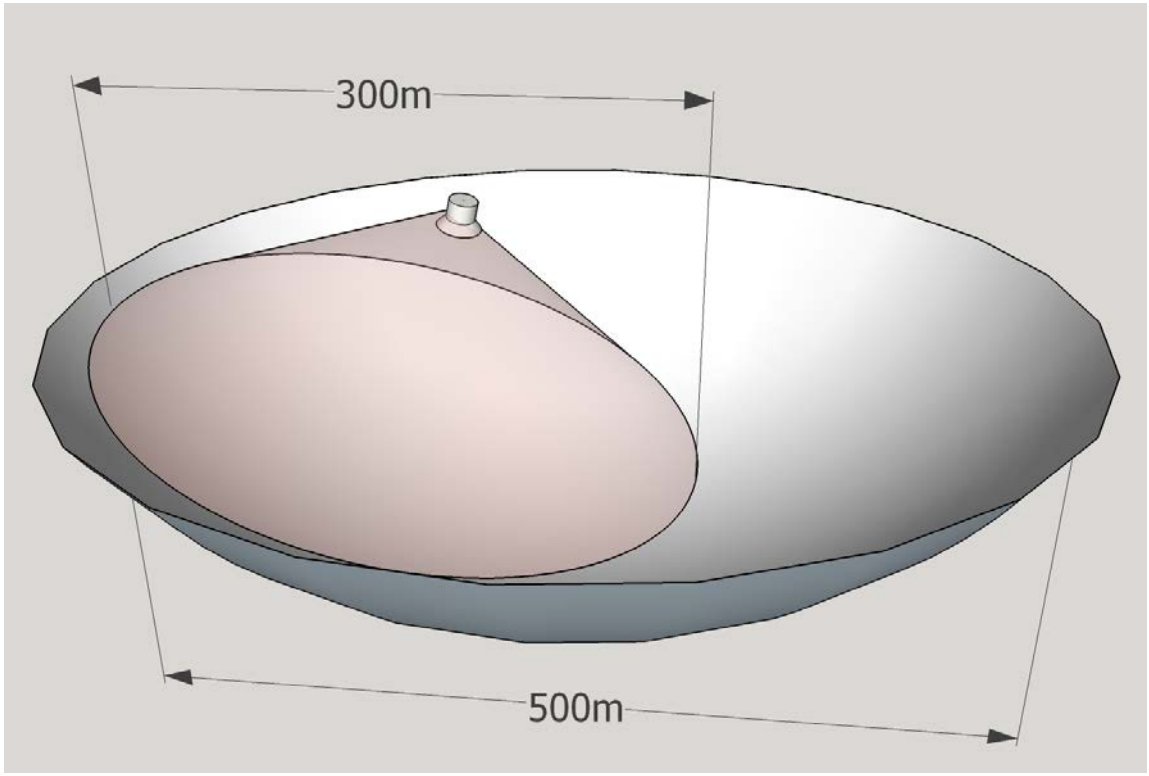

Figure 2.7: FAST has an 'active surface' where the 500 meter diameter is illuminated up to 300 meters at one time, providing more flexibility. Image credit: Phoenix7777 `https://commons.wikimedia.org/w/index.php?curid=51795209`.

Table 2.1: Comparison between single-dish telescope and interferometer regarding their collecting area and resolution power.

Aspect	*FAST*	*JVLA*
Collecting Area	70600 m^2	13254 m^2
Resolution power at 1.4 GHz	3.0 arcmin	1.45 arcsec

MERLIN radio array is an example of active radio interferometers across the United Kingdom. It consists of seven radio telescopes, spanning at 217 km, linked to the Jodrell Bank Observatory via a new optical fibre network. The Jansky Very Large Array (JVLA) is another premier radio interferometer located in Socorro, New Mexico. It includes 27 radio antennas, where each of the element is 25 metres in diameter in a Y–shaped configuration. Each element can be moved along the specific track for maintenance or can be changed to a different configuration for a specific duration in a year. The resolution of an interferometer is given by:

$$R \approx \frac{1.22\lambda}{D} \tag{2.1}$$

where D is the distance of the longest baseline. Comparing the two leading telescopes from both categories as in Table 2.1, we can see clearly that both methods are rather complimentary and the decision on choosing the method depends on the project aims.

2.4 Radio Interferometer

2.4.1 Array Design

The science waiting to be solved motivates the design of radio telescope arrays across the globe. Arrays with the best resolution and sensitivity would be the perfect tool for the scientist to work with, but they are typically limited to organisations or

countries' financial resources. In order to maximise the array capabilities, the chosen design must adapt to many factors, such as the weather and geography. Arrays like ALMA and VLA have the ability to change their array configuration in order to have u-v coverage varieties, whereas others like the uGMRT have a fixed design.

The key advantage of the interferometer is each element, and each radio station can be connected across countries to form a Very Long Baseline Interferometer (VLBI) through the correlator. VLBI is an international collaboration that has made it possible for more extensive use of radio stations in a country. With an improved baseline and enhanced collecting area, better resolution and sensitivity can be accomplished where it is typically impossible alone. Several active VLBI networks are already in operation including the Very Long Baseline Array (VLBA) in the United States and the European VLBI Network (EVN). The EVN telescopes are located primarily in Europe and Asia. Telescope stations in East Asia have collaborated to have their own East Asia VLBI Network (EAVN) spanning across Japan, China and Korea. This network is expanding rapidly as more countries in the region will join this collaboration, such as Thailand, Indonesia and Malaysia.

Fig. 2.8 shows the current, active EVN stations and the new under-construction stations. There are at least 22 active stations primarily located in Europe and Asia. Based on the 'open-skies' hours available at each station, astronomers worldwide have the opportunity to access EVN as an 'open-skies' facility. EVN also offers 3 to 4 different observing frequencies based on the chosen antennas.

The EVN can also extend their array by integrating with other arrays such as the UK e-MERLIN interferometer. The coverage of the EVN-MERLIN array in this extended mode ranges from a few tens to several thousands of kilometres, increasing the sensitivity of the network[1].

[1]The information about the various radio interferometers are available at the NRAO website-https://science.nrao.edu.

Figure 2.8: The map shows the EVN current participating and under-construction radio stations. Yellow/Red: current operational EVN stations, Blue/Red: existing telescopes soon to be EVN stations and Pink/Purple: non-EVN stations that have participated in EVN observations. Image credit: `http://old.evlbi.org`.

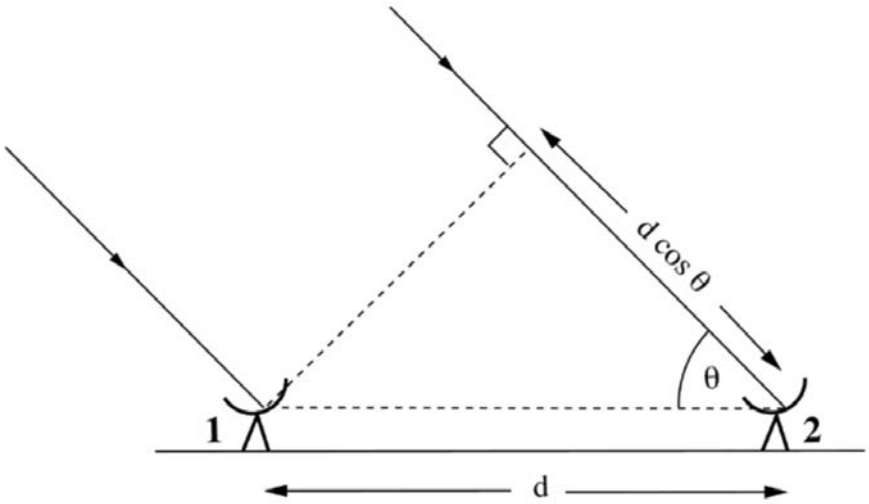

Figure 2.9: The basic radio interferometry with two elements separated by a baseline, d. The signal from the source in parallel to the elements will produce the geometrical delay, τ_g given by a simple trigonometry, $d\cos\theta$. Image credit: `http://www.astro.wisc.edu/sparke/book/ch5figs/fig5.jpg`.

2.4.2 Baselines and The u-v Plane

The chase for better resolution has been the ultimate goal for using interferometry technique. Start from linking many smaller single-dish elements into several different configurations, to incorporating larger dish telescopes in an array. To explain how the radio interferometry works, we start with the simplest case, where we consider two single-dish telescopes separated by a large distance, observing the same astronomical object as shown in Fig. 2.9. In order to obtain the information of the target source, the radio signal from each element is transformed electronically and then combined to produce an interference pattern. From Fig. 2.9, the geometrical delay, τ_g is given by:

$$\tau_g = d\cos\theta\,, \tag{2.2}$$

where d is the longest baseline of the array configuration. Depending on the number of elements in an array, there are several configurations that the array can provide. The maximum resolution of an array will be based on the most extended configuration baseline.

The resolution of an interferometer can also be improved by increasing the number and distance between telescopes. The number of baselines in an array, correlates with the number of telescopes, N by:

$$\frac{N(N-1)}{2} \,. \tag{2.3}$$

Increasing the number of baselines will greatly improve the sensitivity of an array incorporating the rotation of the Earth. Instead of making larger single-dish elements and incorporate them into the array, the next major arrays keen towards lighter and smaller elements for their mobility.

The u-v plane is used to evaluate the resolution of the image by their density coverage and the declination. As shown in Fig. 2.10, the u-v plane is the projection of the position of the elements in the array configuration as the Earth rotates. For an example, VLA antennas are arrayed along the three arms of a Y-shape with a maximum arm length of 21 km and the longest baseline roughly around 40 km.

The "full-track" observation being made spanning over 12 hours, while a "snapshot" only covers several minutes. The u-v coverage will be filled with long lines indicating higher density sampling along the arms while the short breaking lines indicating the "snapshots". Fig. 2.11 shows the example of the u-v plane full coverage with different angles of declination.

2.4.3 ALMA: The Sub-mm Observations

In the heart of the Atacama Desert, specifically the Chajnantor Plateau, the Atacama Large Millimeter/submillimeter Array (ALMA) is a collaboration between the National Radio Astronomy Observatory (NRAO), the Japan National Astronomical Observatory (NAOJ) and the European Southern Observatory (ESO) to study light and signals from the coldest objects in the Universe. ALMA operates at wavelengths

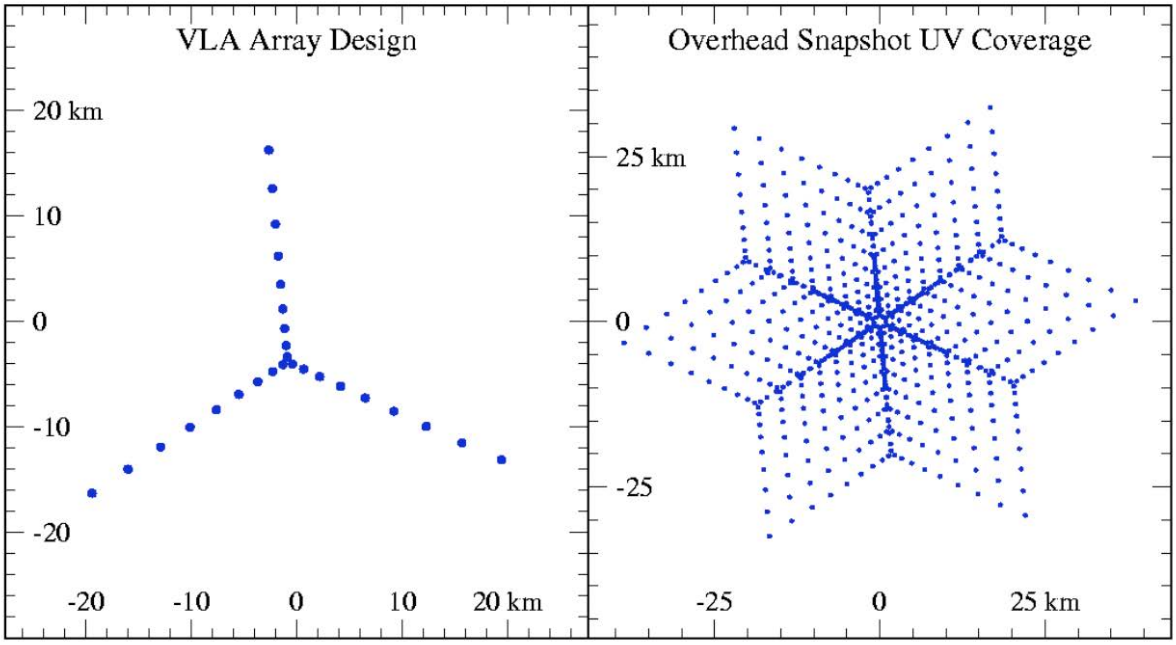

Figure 2.10: The u-v coverage of the A-configuration. Left Panel: The position of the antennas on the ground arrayed along the three arms. Right Panel: The overhead snapshot of the u-v coverage. Image credit: `https://www.strw.leidenuniv.nl/radioastronomy/lib`.

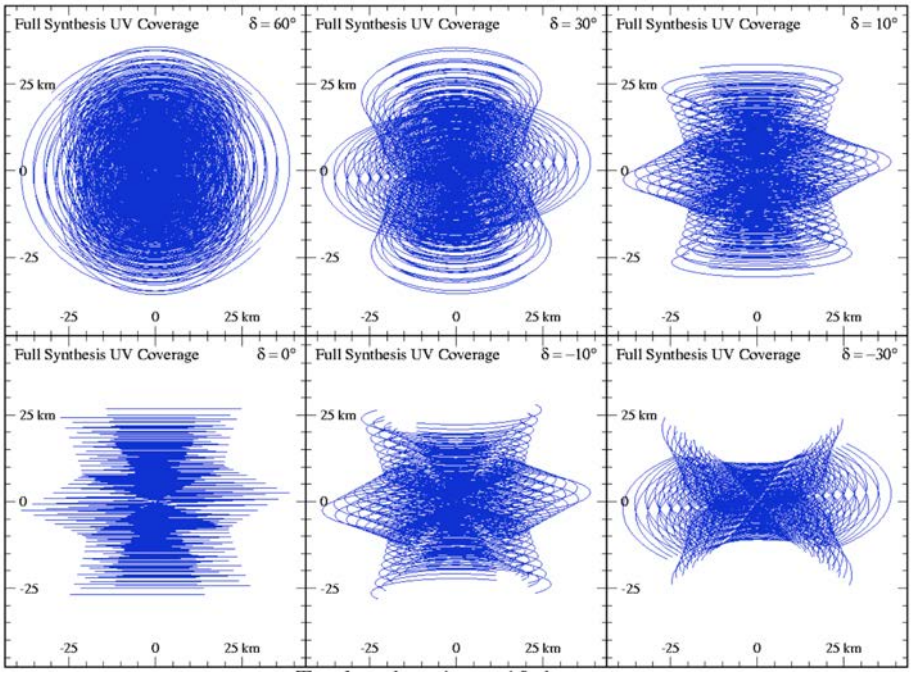

Figure 2.11: The full u-v coverage of A-array with the track elevation >10 degrees for different declination, $\delta = 60°$ to $-30°$. Image credit: `https://www.strw.leidenuniv.nl/radioastronomy/lib`.

Table 2.2: To date, eight receiver bands have already seen the first light. Band 1 and 2 might be added in the future[1].

ALMA Band	Wavelength Coverage (mm)	Frequency (GHz)	First light
1	$6.0 - 8.5$	$35 - 50$	TBD
2	$3.3 - 4.5$	$65 - 90$	TBD
3	$2.6 - 3.6$	$84 - 116$	2009
4	$1.8 - 2.4$	$125 - 163$	2013
5	$1.4 - 1.8$	$163 - 211$	2016
6	$1.1 - 1.4$	$211 - 275$	2009
7	$0.8 - 1.1$	$275 - 373$	2009
8	$0.6 - 0.8$	$385 - 500$	2013
9	$0.4 - 0.5$	$602 - 720$	2011
10	$0.3 - 0.4$	$787 - 950$	2012

[1] `https://www.eso.org/public/unitedkingdom/teles-instr/alma/receiver-bands/`.

between the infrared light and radio waves; hence it is known as the mm and sub-mm observations.

ALMA is a revolutionary international project because this array has unparalleled sensitivity and better resolution than the current arrays in the sub-mm region. ALMA was built at a high altitude (5000 m above the sea level) and on a dry site with stable weather conditions. ALMA observation bands were specifically chosen to suit the significant absorption of water and oxygen as shown in Fig. 2.13.

In total, ALMA consists of 66 antennas (for a typical antenna see Fig. 2.12); fifty-four 12-meter diameter and twelve 7-meter diameter. Similar to the JVLA, ALMA's array configuration is not fixed. Transporter trucks, specifically built for this purpose will be able to move these high-precision antennas between different pads without losing the precision mechanism. The Morita Array, also known as the Atacama Compact Array (ACA), is made up of twelve 7-meter antennas and four 12-meter antennas in which the components are clustered together to act as a single telescope. This particular array will enhance ALMA's ability to map large-scale and extended structures as well as measuring the radio intensity very precisely.

ALMA can observe at many different frequency bands and in different physical

Figure 2.12: ALMA antennas at the Array Operation Site (AOS) located in the Central Cluster. There are a total of 118 foundations where the antennas are located, extended over 32 km in diameter for 66 antennas. Notice that the highly polished reflective surface that enable the sub-mm observation. Image Credit: Carlos Padilla - AUI/NRAO.

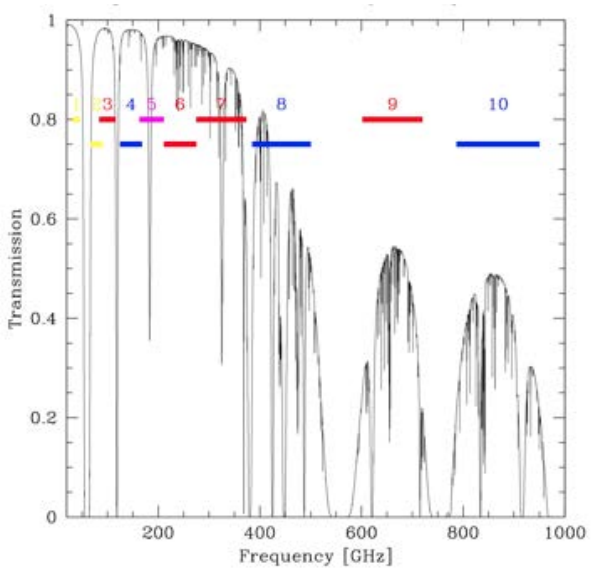

Figure 2.13: ALMA atmospheric transmission and the ALMA receiver bands. The observation bands were specifically chosen to suit the significant absorption of water and oxygen. The absorption for water is at 22.2, 183, 325, 380, 448, 475, 557, 621, 752, 988, and 1097 GHz and for oxygen is at $50 - 70$ GHz and 118 GHz. Image Credit: `astrobites.org`.

configurations, with longer baselines providing higher resolution (at a given frequency). The maximum baseline of the array is at 16 km. Every ALMA antenna is equipped with detectors that are highly sensitive radio receivers, and each type of the receiver is sensitive to a specific 'band' (see Table 2.2). Every ALMA band has a national developer of its own (e.g. band 6 created by NRAO). Therefore, each band has its particular scientific observation, depending on their research objectives.

2.4.4 The Upgraded Giant Metre Radio Telescope (uGMRT)

The upgraded Giant Metre Radio Telescope (uGMRT) is located in Maharastra state, north of Pune, India. This radio interferometry facility consists of 30 fully steerable parabolic dishes, each with a 45-meter diameter. The uGMRT array has a basic Y-shaped configuration, with 14 antennas located in the central region while the rest of the antennas are spread out along three arms as shown in Fig. 2.14. Unlike the VLA, this array is a fixed interferometer with the shortest baseline of $\sim$ 100 m, and the most extended baseline is up to 25 km (Swarup et al. 1991). Each element was placed carefully in a not so aligned position to increase the u-v coverage.

The central square consists of 14 antennas in a 1 km square region. As shown in Fig. 2.15, the antennas were positioned randomly but close together to produce a compact array at the centre. The short baselines from this array will enable the detection and imaging extended sources.

The uGMRT has an inventive design, using light-weight wire mesh for the telescope surface to minimise costs and reduce the high wind forces in the region. The wire mesh is unevenly distributed with smaller grids at the centre and gradually larger grids outwards (see Fig. 2.16).

This facility enabled the low-frequency radio observation to be made with high sensitivity due to the large collecting area. The upgraded GMRT has receivers in

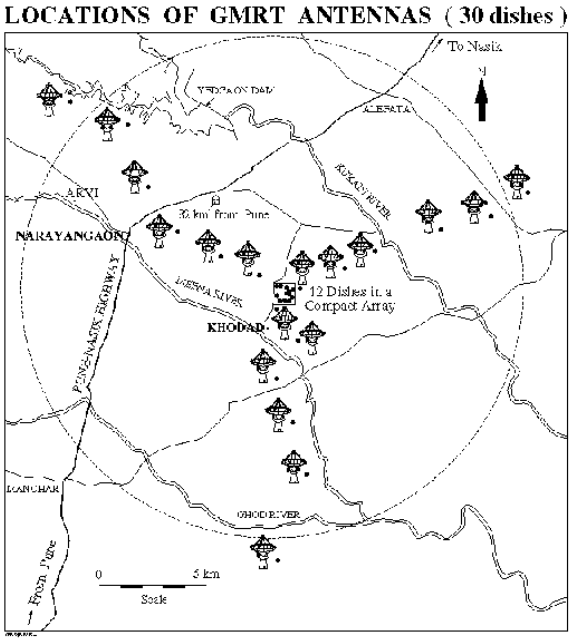

Figure 2.14: The location of the 30 GMRT antennas in Maharastra. As seen in the diagram, nearly half of the antennas were placed in the central region, while the rest of the antennas were spread out in a 'Y'- shaped. Image Credit: `http://www.gmrt.ncra.tifr.res.in/gmrt_hpage/Images/Diagrams/yarray.gif`.

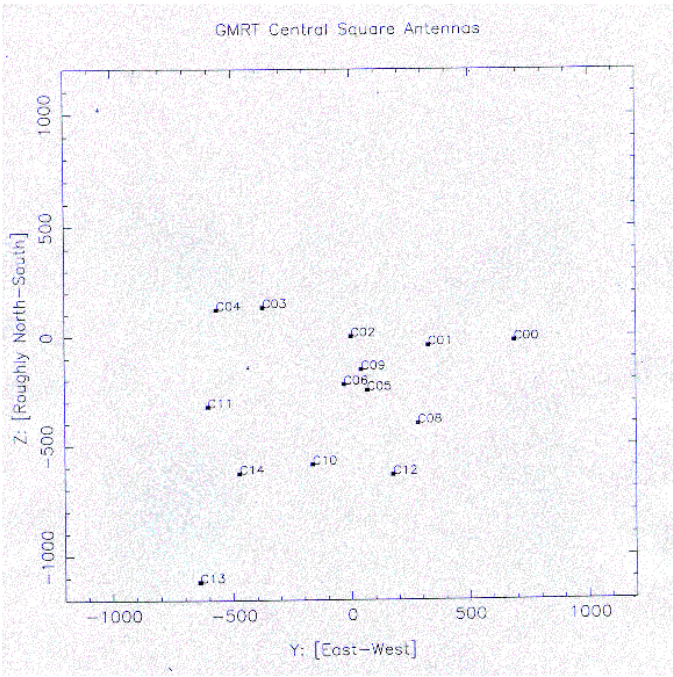

Figure 2.15: The location of the 14 GMRT antennas at the central square. The compact array were located in a small region, up to 1 km square. Image Credit: `http://www.gmrt.ncra.tifr.res.in/gmrt_hpage/Images/Diagram1`.

Figure 2.16: The light-weight wire mesh is used to lower the wind forces and to cut the cost on building the array. This is the C02 antenna picture taken by the author in the central square with two other antennas at the background (C03 & C04).

5 bands, covering the frequency ranges from 0.3–1.5 GHz. The new broadband receivers were installed and successfully tested in 2017. It offers a much broader bandwidth (200 - 400 MHz) compared to the legacy narrower bandwidth of 32 MHz (Gupta et al., 2017). The new system parameters are shown in Table 2.3.

When we compare the legacy narrow band GMRT to the upgraded GMRT, the new upgraded array offers much better sensitivities. Fig. 2.17 shows the comparison of current and future radio interferometers' continuum sensitivities for a 9 hours on-source integration. The figure demonstrates GMRT, VLA, JVLA, uGMRT, LOFAR, MeerKAT, ASKAP, and SKA-1-Mid sensitivities for various parts of the spectrum in which these facilities work. As can be seen, before the SKA's Phase-1 advent, uGMRT will be the most sensitive interferometer in the world at frequencies between 250–1500 MHz. The low-frequency SKA-1 is located in Australia; hence many sources in the northern hemisphere will not be able to be observed using the SKA-1-Mid but will be covered by the uGMRT.

Table 2.3: The upgraded GMRT system parameters (Gupta et al. 2017).

	Frequency (f, MHz)			
	Band 2	Band 3	Band 4	Band 5
Frequency range (MHz)	$120-250$	$250-500$	$550-850$	$1050-1450$
Total system temperature (K)	$760-200$	$165-100$	$105-100$	$80-75$
Primary beam (arc min)	$152^*(185/f)$	$70^*(375/f)$	$37^*(700/f)$	$27^*(1250/f)$
Antenna gain (K/Jy/antenna)	0.33	0.38	0.35	$0.28-0.22$
Synthesized beam (arcsec)				
Whole array	$17^*(185/f)$	$8^*(375/f)$	$4^*(700/f)$	$2^*(1250/f)$
Central square	$343^*(185/f)$	$174^*(375/f)$	$87^*(700/f)$	$45^*(1400/f)$
Sensitivity				
RMS noise in image (μJy)*,**	190	50	40	45

*For 30 antennas and average $T_{\rm sys}$ over the band.
** For 10 min integration and 100MHz bandwidth.

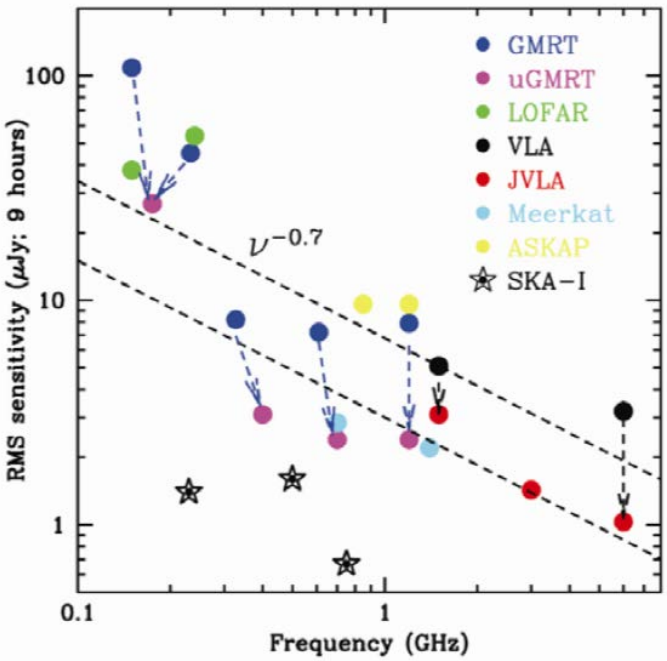

Figure 2.17: The comparison of existing and future radio inteferometers. A typical extragalactic source flux density with power-law behaviour is shown as the dashed lines. uGMRT will be the most sensitive radio array before the SKA-1, where it is now at the construction phase (2018-2023). Image Credit: Gupta et al. (2017).

2.4.5 East Asia VLBI Network (EAVN)

The future of radio interferometry is progressively revolving around VLBI. The rapid development of technology and increasing interest in science in the East Asia region leading to more radio telescope stations are being built. This movement encourages many collaborations between countries in the name of science. VLBI offers control and flexibility. In terms of control, the single-dish telescope is managed by the country's organisation so that the local scientist and the government can focus on their scientific goals. These telescope stations also can take part in the much larger consortium and contribute to a more significant international science project.

The full current EAVN network consists of 19 telescopes located in Japan, China and Korea. Subject to the telescopes being used by the observer, there are four possible frequency coverages which are at 6.7 GHz, 8 GHz, 22 GHz and 43 GHz. The data is being correlated by KASI (Korea) and SHAO (China). The individual stations have been taking data since 2009. Still, the EAVN has only recently started the open-use program from the second half of 2018 with the maximum observation time of 100 hours at 22 GHz and 43 GHz inclusive with only nine telescopes. In the recent round, the maximum open-use observation time increased to 500 hours (first half of 2020) with an increase in the participation of eleven telescopes from the previous nine, thus increasing their sensitivity. Fig. 2.18 shows the position of the radio telescopes in EAVN network. There are 12 stations in Japan, 4 stations in China and 3 stations in Korea with the main observing wavelength is at centimetre with several other potential telescopes due to join the network.

There are campaigns to encourage astronomers, scientists and governments from East Asia region such as from Thailand, Malaysia and Indonesia to join the VLBI network as these countries are geographically in between the Oceania VLBI group and the current EAVN networks. The overall collecting area of EAVN will be much better in the future when the FAST telescope in China joins the array with several

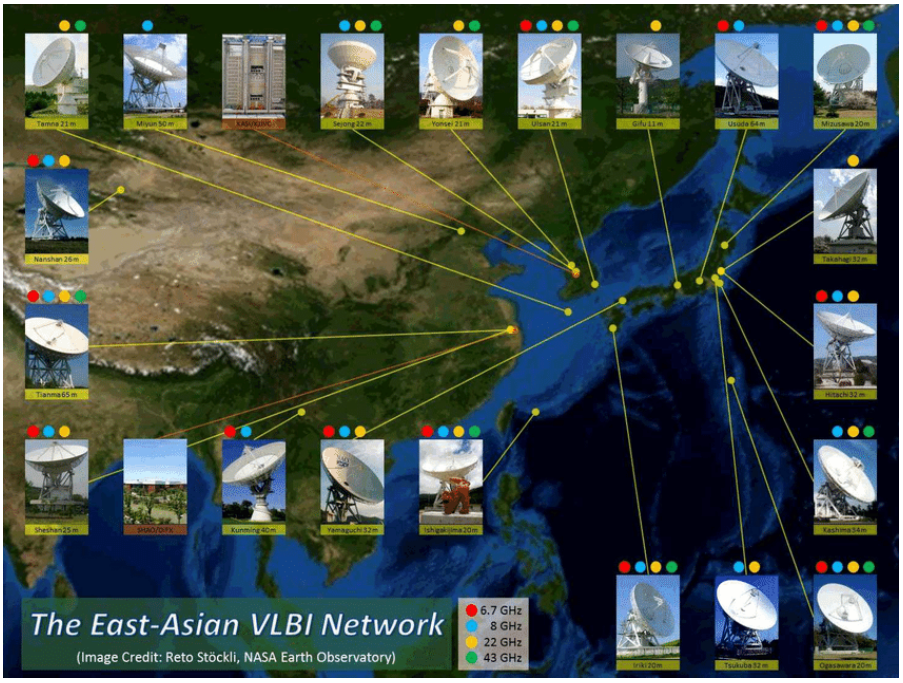

Figure 2.18: The map shows the current telescopes that are actively being used (yellow) and potential radio telescopes (brown) that will be used in EAVN network. Image credit: Asada et al. (2017).

other under-construction radio telescopes such as the 40 metres Thai National Radio Telescope (TNRT), the 32-m Jatiluhur Radio Telescope in Indonesia and the 13-m UM-XMUM-SHAO Radio Telescope in Jelebu, Malaysia.

2.5 Radio Data Reduction

2.5.1 Astronomical Image Processing System (AIPS)

AIPS is a radio data reduction package based on the programming language FORTRAN. For over 30 years, AIPS has been used to image radio data; it is therefore a very stable package. A stable data reduction package is vital for the data analysis and radio imaging process. As a result, many astronomers still prefer to use AIPS and wait until the new CASA reduction package is more stable, particularly for older individual telescopes participating in EAVN. Some telescopes, such as the

uGMRT, offer the flexibility to analyse their data in both packages. Scientists operating specific arrays around the globe are responsible for developing a specific routine based on their telescope specifications for migration from AIPS to CASA. This task is challenging, but it can be done. So, in order to avoid wasting precious observational hours, some telescope stations are using AIPS as their preferred data reduction package.

All of the data reduction processes in this thesis were performed using CASA, with the exception of the EAVN data where it was reduced in AIPS.

2.5.2 Common Astronomy Software Application (CASA)

CASA is the next generation of post-processing radio telescopes data after Astronomical Image Processing System (AIPS). Although AIPS is still currently being used by astronomers worldwide, many scientists have been motivated to switch to CASA because it provides many advantages. This package is designed by an international group of scientists under the guidance of the National Radio Astronomical Observatory (NRAO).

CASA infrastructure is based on the C++ tools under the iPython interface. As the iPython being a more favourable programming language to date, it enables many improvements on the CASA tasks, especially the useful, user-friendly GUI. On top of that, many beneficial algorithms are easily applied by calling the name of the algorithm in the Python script. Because of this flexibility, many scientists are motivated to develop the CASA software further, making this package more robust and producing better radio images.

An essential feature of CASA that is vital for new radio astronomers and also for the old one is the details of each CASA task are very well documented and maintained by the NRAO. They included several examples and tutorials, depending on the objective of the end-user. As more radio telescope stations are being built, the

effective diameter of the interferometers increases, and also, the size of the radio data that needs to be processed. CASA is competent in handling massive data. A typical dataset from GMRT 4 hours observation, will produce 50 GB of data pre-processed. Usually, the data reduction process will gradually decrease the amount of data as we flagged many unwanted data such as the RFIs and non-functional antennas to about 30 GB. However, at the same time, during the process, astronomers will duplicate many Measurement Sets (MS), so that the data can be processed simultaneously, leading to a vast data handling process by CASA. Premium radio telescopes, such as the SKA, will have an enormous amount of data that needs to be analysed, and scientists believe that CASA will be able to handle it.

2.5.3 CASA Data Reduction Sequence

This subsection will briefly explain the data reduction process using CASA tasks. Generally, the data reduction processes are the same using any radio data reduction package, such as AIPS and MIRIAD. The flexibility of the tasks offered by CASA making this package more in-favour in the future.

Depending on which radio telescope is being used, whether it is an interferometer or a single-dish radio telescope, the raw data received by the Principal Investigator (PI) will be accustom to the telescope. In order for CASA to be able to 'read' the data, the raw data from the telescope need to be converted to a 'Measurement Sets' file (ms).

Most of the telescope's raw data is a Flexible Image Transport System (FITS) file, and it is readable in AIPS. To read the data in CASA, every telescope has unique tasks to perform the conversion. For example, raw data from uGMRT is recorded in `lta` format and needed a few tasks before it is readable in CASA. PI has to perform `listscan`, `gvfits` and then converted to ms file in CASA using `importgmrt`. Once the data is in ms file, it can be loaded to perform the initial inspection using the

task `listobs`. This task is essential for the PI to check the information about the observation, especially regarding the antennas, calibrators and the target source.

One of the most useful tools in CASA is the `plotms`. This interactive tool enables the user to plot various data tables such as the $u-v$ coverage, antennas and amplitudes. Beyond this function, `plotms` can perform `flagdata` tasks interactively while keeping the tab on flagged data. So, this task is a useful tool to check if any task performed by the user has correctly taken place, and it is used throughout the reduction process.

Flagging is required several times in the data reduction process. A python script inside the CASA environment can be used to call the `flagdata` function. Typically, the P.I performs the initial flagging, which is to delete the first spectral channel (spw), flag the first and last records of all scans using `quack` mode, and eliminate data from non-functional antennas.

Calibration is the next major task. There are several calibrations to perform, such as density, bandpass, gain and delay. Density calibration is carried out using the `setjy` task. This function utilised the latest standard CASA database flux calibrator which is the 2017 Perley-Butler catalogue.

Other listed calibrations were performed to get the final calibration table which was then transferred to the target source using the `applycal` method. Once the target source is calibrated, task `mstransform` is used to separate the target so that we only work with the specific source. At this stage, additional flagging may be performed on the data to eliminate the remaining outlier, depending on the objective of the science.

CASA utilised a user-friendly GUI invoked by the task `tclean` to process radio images. The `tclean` algorithm consist of two major processes – Gridding and Deconvolution. The first step in `tclean` is to perform inverse of Fast Fourier Transform (FFT) to create a 'dirty map'. The gridding process involved the $u-v$-data arranged

on a grid. Depending on the source, several different weightings for the grids can be applied. Weighting like `Briggs` can vary between `natural` where generally gives more weights to short baselines and `uniform` to long baselines.

`tclean` minor cycle consists of a deconvolution process (i.e. the process of cleaning the 'dirty image'). This process involves repeated steps of subtraction collections of 'dirty beams' from the 'dirty image' until a certain number of iterations achieved. Several deconvolver solutions are available in CASA to be applied, such as the basics 'Hogbom' [Hogbom, 1974] and the latest multi-scale multi-frequency synthesis 'mtmfs' [Rau and Cornwell, 2011].

Self-calibration is an iterative process where if there is enough flux, the model from the previous `tclean` can be used to calibrate the data. The corrected data is then imaged, and this process is repeated until there is no improvement can be seen. The data reduction sequence using CASA are summarised in Fig. 2.19.

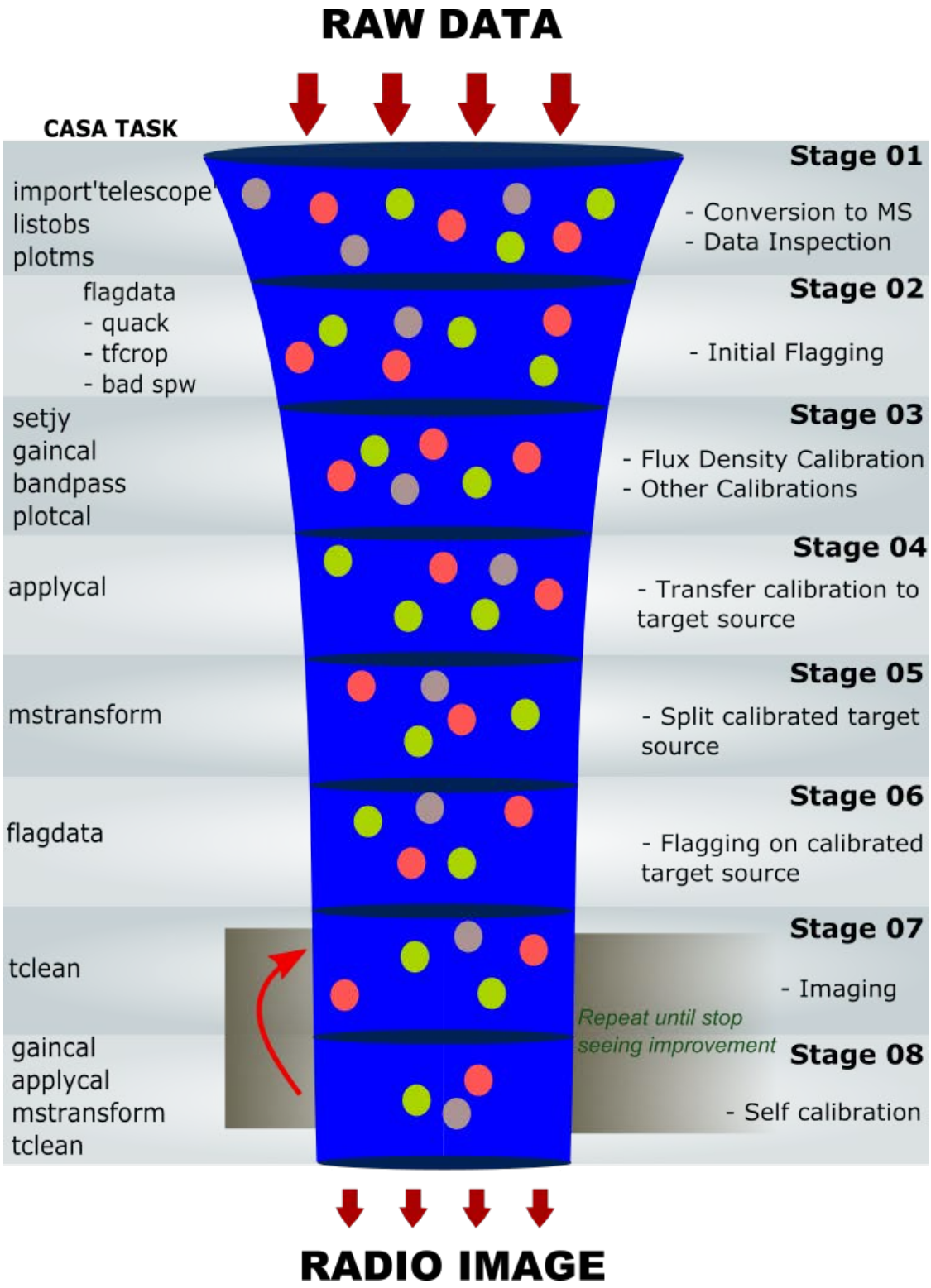

Figure 2.19: The sequence of radio data reduction using CASA software package. The funnel diagram indicates that the amount of data decreases as the process continue. For a typical 4 hour GMRT observation, the data is reduced roughly from 50 GB to 30 GB.

3 | A Güdel-Benz Type Relations for Massive Stars

"We have peered into a new world and have seen that it is more mysterious and more complex than we had imagined. Still more mysteries of the universe remain hidden. Their discovery awaits the adventurous scientists of the future. I like it this way."
–Vera Rubin (1997)

Chapter Summary

In this chapter, we look at the relationship between X-ray and radio luminosities to explore a new Güdel-Benz style relationship for massive stars. We address the physics of X-ray and radio emission from massive stars, as well as the Güdel-Benz relation for low-mass stars and other related relations in other types of objects. There are theoretical reasons to believe that a correlation between the X-ray and radio luminosities of massive star should exists. Early-type stars are both X-ray and radio emitters, and the emission at both wavelengths is believed to be due to processes within the stellar winds, specifically the free-free radio emission and thermal X-ray emission. We gathered and presented an archival sample of 53 X-ray and radio-emitting massive stars from two spectral classes, Wolf-Rayet and OB-stars.

In addition, we investigated and highlighted some advantages and issues with the IDL `FITEXY` and a Bayesian approach to linear regression, `LINMIX` fitting packages. We discuss the results obtained with `LINMIX`, which suggests a new positive correlation between the X-ray and radio luminosities from both spectral classes that is in agreement with the expected theoretical value.

3.1 Introduction

Massive stars are marked by their stellar winds. These winds are an important component of the observational characteristics of massive stars at a number of different wavelength bands. In the context of this chapter, wind emission is believed to be responsible for both the X-ray and radio emission in massive stars.

Previously, a strong correlation has been noted for the X-ray and radio flux for low-mass stars (where both the radio and X-ray emission is believed to be related to coronal emission and probably to magnetic activity). This relationship was first noted by Güdel et al. (1993) and is usually referred to as the Güdel-Benz relation, hereafter referred to as the G-B relation. Here, we are investigating whether there is a similar G-B relation for massive stars - namely the OB stars and Wolf-Rayet (WR) stars. We are not claiming that the origin of the G-B like relation for massive stars is the same as for low-mass stars, nor that it even has the same slope, but merely that there is such a correlation between X-ray and radio emission for massive stars.

In this chapter, we will briefly review the G-B relation for low-mass stars, and other similar relations in other types of objects in Section 3.2. We discuss the physics of X-ray and radio emission from massive stars in Section 3.3. In Section 3.4, we describe the theoretical reasoning why we would expect to see a G-B type relation in massive stars. In Section 3.5 we present the literature sample for X-ray and radio emitting massive stars. In Section 3.6, we compare and discuss the issues and advantages of the IDL `FITEXY` and `LINMIX` fitting packages on our simulated data

and in Section 3.7 we present the results and investigate their significance.

3.2 The Güdel-Benz Relation For A Variety of Objects

Güdel and Benz (1993) summarised X-ray and radio properties of several classes of magnetically active stars and produced an empirical relation between time-averaged radio luminosities, L_R and X-ray luminosities, L_X. The quantity L_R mostly refers to 6 cm wavelength and exceptionally to 3.6 cm. By using the VLA X-band and ROSAT data, a linear correlation between L_R and L_X was found for active cool stars to be $L_X/L_R = 10^{15.5\pm0.5}$ (Güdel and Benz, 1993).

For low-mass stars, in general, radio emission and X-rays serve as diagnostics of coronal energy release. Using X-rays, it will be possible to trace the presence of hot and dense plasma trapped in closed coronal magnetic fields. On the other hand, radio observations are to probe both thermal atmospheric components from the chromosphere to the corona, and populations of non-thermal, accelerated electrons, typically in low-density, open or closed coronal magnetic fields (Forbrich et al., 2011).

The G-B relation also extends to objects like the active galactic nuclei (AGN). In an optically selected sample of nearby low-luminosity AGN, Panessa et al. (2007) discovered a similar linear radio to X-ray relation. Selection effects and incompleteness are still present in this study, so, according to Laor and Behar (2008), a significant portion of the objects may be affected by X-ray absorption, which cannot be adequately corrected for. Using the radio-quiet Palomar–Green quasar sample, Laor and Behar (2008) found a significant correlation between the radio luminosity (L_R) and X-ray luminosity (L_X) of accretion disks in radio-quiet quasars with $L_R \sim 10^{-5} L_X$.

Lü et al. (2015) also extended the study of the G-B like relation to the gamma-ray bursts. They discovered that GRBs show a $L_R - L_X$ relationship with a slope

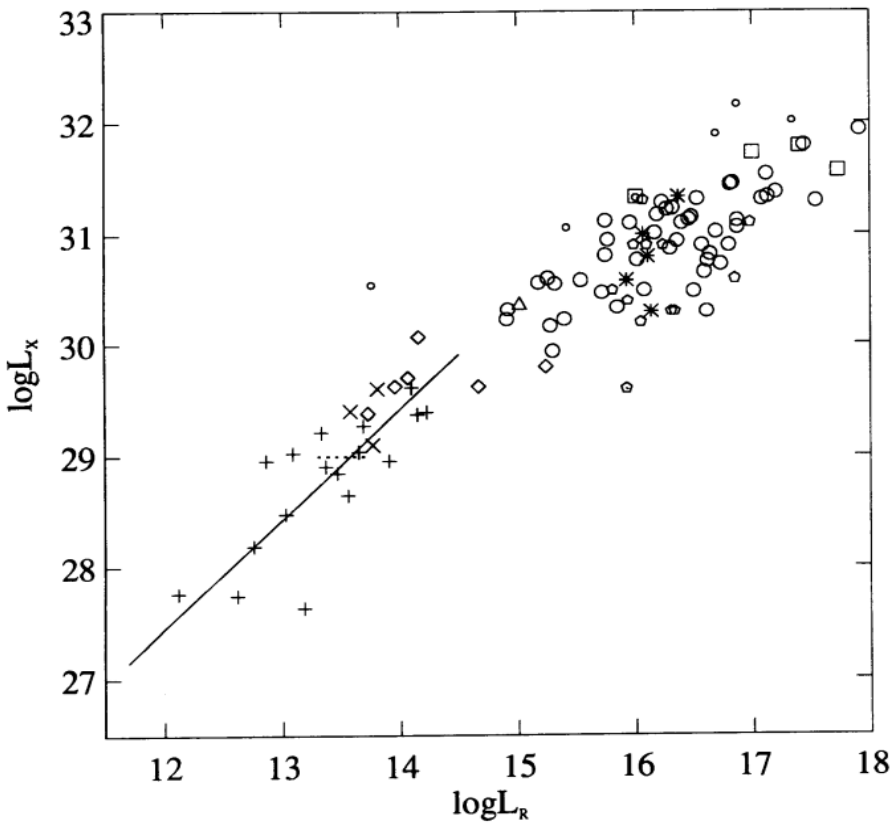

Figure 3.1: The relationship between radio luminosity and X-ray luminosity of different classes low-mass stars. From Güdel and Benz (1993).

Key to the symbols and references:
(*pluses*) dM(e) stars (Güdel and Benz, 1993; Güdel et al., 1993);
(*crosses*) dK(e) stars (Güdel, 1992);
(*diamonds*) BY Dra binaries (Güdel and Benz, 1993; Güdel et al., 1993);
(*large circles*) RS CVn binaries (Drake et al., 1989, 1992);
(*small circles*) RS CVn binaries with two giants ((Drake et al., 1989, 1992);
(*triangles*) AB Dor (Kurster et al., 1992; Lim, 1992);
(*asterisks*) Algos (Hjellming et al., 1972; Umana et al., 1991; White and Marshall, 1983; McCluskey and Kondo, 1984);
(*squares*) FK Com stars (Slee et al., 1987; Bedford et al., 1985; Ambruster et al., 1992; Phillips, 1992; Drake et al., 1990);
(*pentagons*) PTTS.
The solid line is a fit to the M dwarfs.

of 1.1, as $L_R \propto L_X^{1.1}$.

3.3 Physics of the X-ray and Radio Emission for Massive Stars

3.3.1 Radio Emission

Radio observations have provided evidence of high level coronal activity for many low-mass stars, either in the form of strong flares, or "quiescent" radiation. Steady radio emission is commonly attributed to gyrosynchrotron radiation of mildly relativistic electron gyrating in magnetic field. The radio wavelength range provides access to synchrotron radiation from relativistic electron populations (Güdel, 2002).

The thermal radio emission from massive stars is due to the free-free emission originating from the ionised stellar wind. As addressed by Panagia and Felli (1975), Wright and Barlow (1975) and many other authors, thermally emitting ionised stellar wind emits the radio flux with a characteristics spectrum of $S_\nu \propto \nu^{+0.6}$.

Some massive stars are also well known non-thermal emitters and are associated with binarity, as catalogued by De Becker (2007). The non-thermal radio emission is caused by the shock accelerated electrons gyrating in the magnetic field. According to Chapman et al. (1999), the percentage of WR stars that are non-thermal emitters is about 40%. In addition, Van Loo et al. (2006) investigated the possibility of a single-star to be a non-thermal emitter on the typical O-star, Cyg OB2 No.9. A model was created that included several shocks in the stellar wind for the O-star, and particularly for the shock jump velocity, they were inspired by the hydrodynamical model developed by Runacres and Owocki (2005). Unfortunately, the model could still not explain the star observational data, which casts considerable doubt on the single-star hypothesis, which then leads to the implication of most non-thermal radio

emitters, especially the Wolf-Rayet and O-stars, are colliding-wind binaries (CWBs), (Van Der Hucht, 1992).

3.3.2 X-ray Emission

The X-ray emission from low-mass stars has a variety of sources. These include collimated outflows, accretion hotspots and stellar coronae. For massive stars, the X-ray emission is believed to be produced in the stellar winds resulting from several kinds of shocks produced either by very strong winds driven by the star's radiation (Babel and Montmerle, 1997), by the head-on collision between winds that have been magnetically channelled by the star's magnetic field, or by wind collisions in a binary system in which each star has a wind (ud-Doula and Nazé, 2016). For more elaborate explanations regarding the X-ray emission from massive stars, please refer to Section 1.4.

3.4 The Expected Güdel-Benz Relation for Massive stars

In this section, we continue our investigation into the possibility of the existence of a physical relationship between the radio and X-ray luminosities of two spectral classes of massive stars, namely the Wolf-Rayet, and OB-stars.

For single O-stars, the X-ray luminosity scales linearly with bolometric luminosity has been empirically established by X-ray satellites since *Einstein* as $L_X/L_{bol} \approx 10^{-7}$ (Pallavicini et al., 1981). However, the popular model where the X-rays are produced by the instability-generated shocks embedded in the stellar wind predict a steeper scaling with the mass-loss rate, $\dot{M}$. From Owocki et al. (2013), L_X scales as $L_X \sim \dot{M} \sim L_{bol}^{1.7}$ if the shocks are radiative. They also mentioned that for radiative shocks, L_X scales as $L_X \propto (\dot{M}/v_\infty)^{1-m}$, where m is the 'mixing exponent'. If the exponent is $m \approx 0.4$, then the X-ray luminosity $L_X \sim \dot{M}^{0.6} \sim L_{bol}$ where it matches

the empirical scaling.

Many papers have investigated the relation between L_X and L_{bol} for massive stars. A study involving hot single O-stars from *Chandra* Carina Complex Project by Nazé et al. (2011) concluded that their results of L_X-L_{bol} relation is found to be $\log(L_X/L_{bol}) = -7.26$, with a dispersion of 0.21 dex. A study on the same region using XMM-Newton by Antokhin et al. (2008) determined a value of $\log(L_X/L_{bol}) = -6.58 \pm 0.79$. According to Nazé et al. (2011), the difference in their values is attributable to different reddening laws and bolometric luminosities assigned to the O-stars in their studies.

Using XMM-Newton, Sana et al. (2006) discovered a much lower scatter of L_X-L_{bol} relation ($\log(L_X/L_{bol}) = -6.91 \pm 0.15$) based on a relatively small sample of 12 O-stars in the open cluster NGC 6231. Nazé (2009) concluded a study with about 300 X-ray counterparts from Galactic OB stars all-sky catalogue by Reed (2003). From the study, the ratio of X-rays luminosity to bolometric luminosity is $\log(L_X/L_{bol}) = -6.45 \pm 0.51$. Another extensive analysis using *Chandra*–ACIS by Rauw et al. (2015) revealed that the ratio between X-ray luminosity and bolometric luminosities of O-stars in Cyg OB2 is $\log(L_X/L_{bol}) = -7.2 \pm 0.2$ and for WR stars is $\log(L_X/L_{bol}) = -8.8 \pm 0.2$. A more recent study utilising the Galactic O-Star Spectroscopic Survey (GOSS) and the catalogue of X-ray sources detected by the XMM-Newton, Gómez-Morán and Oskinova (2018) found that the peak of the distribution of their sample is $\log(L_X/L_{bol}) = -6.6 \pm 0.4$.

Now, consider an O-star with a luminosity, L_{bol}. From the results of Howarth and Prinja (1989) - their Equation (18), with 95% confidence limit:

$$\log\left(\dot{M}/M_{\odot}\mathrm{yr}^{-1}\right) = 1.69\log(L_*/L_{\odot}) - 15.41 \pm 0.13. \tag{3.1}$$

From Eqn. 3.1, we can estimate a mass-loss rate, $\dot{M}$ as:

$$\dot{M} = 6.78 \times 10^{-73} L_{bol}^{1.69}, \tag{3.2}$$

with a scatter in $\dot{M} = \pm 0.13$ in log, L_{bol} in erg/s and $\dot{M}$ in $M_{\odot}$/yr.

From Wright and Barlow (1975), we assume that the radio emission is thermal where the radio luminosity, L_R scales with $\dot{M}$ as:

$$L_R \sim \dot{M}^{\frac{4}{3}}. \tag{3.3}$$

For the X-ray emission, from Pallavicini et al. (1981) and others, (see the literature above), we assume it is thermal (see earlier values) with the ratio value of:

$$\frac{L_X}{L_{bol}} \approx 10^{-7}. \tag{3.4}$$

From Equation 3.2, 3.3 and 3.4, we have $L_R \sim L_{bol}^{2.25}$ or $L_R \sim L_X^{2.25}$, so that we can write the X-ray luminosity in terms of radio luminosity as:

$$L_X \sim L_R^{\alpha}, \tag{3.5}$$

with $\alpha = 0.44$. The mass-loss rate can be estimated from the radio flux density, S_ν, as from Lamers and Leitherer (1993):

$$S_\nu = 2.32 \times 10^4 \left(\frac{\dot{M} Z}{v_\infty \mu} \right)^{4/3} (\gamma g_{ff} \nu)^{2/3} D^{-2}, \tag{3.6}$$

where Z is the rms ionic charge, γ is the ratio of electron to ion density, μ is the mean weight per ion, ν is the frequency, D is the distance in kpc, S_ν is the radio

flux in mJy and g_{ff} is the Gaunt factor, where it can be approximated by:

$$g_{ff} = 9.77\left(1 + 0.13\log\left(\frac{T_e^{3/2}}{Z\nu}\right)\right) \tag{3.7}$$

with ν in Hz.

From Eqn. 3.6 and 3.7, if we assume that the wind is fully ionised, with the terminal velocity $v_\infty = 2000$ km s^{-1} which is appropriate for O-stars, so that $\mu = 1.339$, $\gamma = 1.105$, $Z = 1.149$, $T_e = 20000$ K, in such a way that $g_{ff} = 5.57$, the relation can be written as:

$$L_X = 2.063 \times 10^{25} L_R^{0.44} \tag{3.8}$$

with L_X in erg s^{-1} and L_R in erg s^{-1} Hz $^{-1}$.

It is difficult to detect a single WR star that is responsible for the observed level of X-ray emission, (e.g. for single WC star (Oskinova et al., 2003) & for WO star - see Oskinova et al. (2009)). The X-ray emission from WR stars most probably due to their O-type companion resulting from a wind-wind interaction zone. Rauw et al. (2015) reported the analysis of the *Chandra*-ACIS data in the young association of Cyg OB2 where WR 144 responsible for a very low value of ($\log(L_X/L_{bol}) = -8.8 \pm 0.2$), suggesting that hot plasmas exists far out in the wind. Ignace et al. (2000) and Oskinova (2005) also reported that the L_X/L_{bol} relation for WR stars were not observed as the $L_X/L_{bol} \approx 10^{-7}$ trend for O-stars.

3.5 The X-ray and Radio Sample of Massive Stars

We have collected X-ray and radio fluxes from the literature for our sample of massive stars, specifically Wolf-Rayet, O-type and early B-type stars. These results are presented in Table 3.1 and Table 3.2.

We have only included stars with detections in both wavebands (a future study

could include upper limits). We have in general used more recent results when available. In particular, at X-ray energies, where XMM-Newton or Chandra results are available, we use those in preference to *ROSAT* or *EINSTEIN*. Some of the stars are variable in one or both wavebands, and there, we have used the brightest. We exclude the archetypal WR140 because it is an extremely variable system with a highly eccentric orbit. Refer to Chapter 4 and 5 in this thesis, and others (e.g., White and Becker (1995)).

Regarding the assumed distances, we have used *GAIA DR2* distances where available (42 out of 52 stars). In a number of cases, the *GAIA DR2* values are not available because the star is too bright or the value is erroneous (i.e. negative), and in this case we have assumed previous literature values.

For radio observation, we recorded two fluxes, S_ν, at two different frequencies, 4.8 GHz and 8.4 GHz. The data was retrieved from several papers and archives as shown in Table 3.1 for Wolf-Rayet stars and Table 3.2 for OB stars. For the radio flux, the majority of the data is at 4.8 GHz, but a small number of stars only have data at 8.4 GHz (18 out of 52 stars). To include stars with a detection at 8.4 GHz in the analysis, we have estimated a 4.8 GHz flux for these stars, assuming that the radio emission is thermal in nature (that is with the spectral slope of +0.6). We note that assuming +0.6 spectral slope means that for these stars, the assumed 4.8 GHz flux is a factor 0.71 lower than the 8.4 GHz flux.

To obtain the observational luminosity from the flux density, we use:

$$L_R = 1.197 \times 10^{18} D_{kpc}^2 S_\nu \tag{3.9}$$

where the radio luminosity L_R is measured in erg s^{-1} Hz $^{-1}$, D_{kpc} is the assumed distance of the star in kpc and S_ν is the radio flux density in mJy. The distance used in 26 WR stars and 14 OB stars has been updated using the new data release from *GAIA DR2* (Rate and Crowther, 2020).

For X-ray fluxes, we have always assumed the flux to be the unabsorbed flux, corrected for ISM absorption. In our case study, the relation that we want to investigate can be written as:

$$log_{10}\, L_X = \alpha\, log_{10}\, L_R + b \tag{3.10}$$

where α is the slope and b is the normalisation. We also noted with an asterisk that some of the stars in our catalogues are non-thermal emitters as listed by De Becker (2007).

3.5.1 Wolf-Rayet Stars

We have recorded data for 29 Wolf-Rayet stars for this study. We incorporated the spectral types of the WR stars, the radio fluxes that were originally available from the literature, the corresponding radio luminosity and X-ray luminosity updated with the new *GAIA DR2* distances whenever it is available, along with the original references for the catalogue and the telescope used (see Table 3.1).

3.5.2 O-Stars and Early B-stars

We collected data for 22 individual O-stars and one early B-stars (Cyg OB2 No.12) from various papers and catalogue as shown in Table 3.2. We also included the spectral class of the stars and also the radio fluxes at two frequencies, as in WR stars. We struggled to obtain much more X-ray observation data for early B-stars compared to a good radio sources reported because not many X-ray observations have been done for early B-stars.

B supergiants have slower winds, with $v_\infty \sim$ a few hundred km s^{-1} rather than $\sim$ 1500 - 3000 km s^{-1}. For example, the Luminous Blue Variables (LBVs) such as P Cygni and Eta Car has a slow wind $\sim$ 300 km s^{-1} compared to WR stars ($\sim$ 3000 km s^{-1}). The mass-loss rate for these LBVs is about $10^{-3} M_\odot$ yr^{-1} (including

the historical eruptions) while about $10^{-5} M_{\odot}$ yr^{-1} from the WR stellar wind alone, (Smith, 2017). When a highly supersonic wind passes through a shock, the post-shock temperature scales as v^2, where v is the wind velocity (from the Rankine-Hugoniot condition). LBVs are typically not very bright X-ray sources, except where the LBV star is in a binary system and the X-rays are produced by colliding winds, such as in Eta Carinae and Cyg OB2 No.12. For example, the very bright and nearby LBVs such as P Cyg or AG Car are not detected at all in X-rays, with the implied values of $\log(L_X/L_{bol}) = -9.4$ for P Cygni, (Nazé et al., 2012), while Eta Car on the other hand, is an extremely bright and variable X-ray source with the X-ray luminosity, $L_X = 7 \times 10^{35}$ ergs s^{-1}) with a companion that has a very fast and powerful wind (Corcoran et al., 2000).

For main-sequence B-stars, they have weaker winds, less luminous, have lower L_{bol} and hence, less X-ray luminous. Even though B-stars are more common than O-stars, and the closest ones will tend to be nearer; the wind strength falls off very rapidly as we move from B0 to B3/B4 stellar classes (Krtička, 2014), hence the struggle to obtain many more X-ray observation data for the early type B-stars.

Table 3.1: The X-Ray and Radio Emission Catalogue for Wolf-Rayet Stars.

WR No	Spectral Class	Distance (kpc)	S_ν 4.8 GHz (mJy)	S_ν 8.4 GHz (mJy)	Ref	L_R (erg/s)	L_X (erg/s)	Ref
1	WN4b	3.50	0.47 ± 0.10		B82V	18.84 ± 0.09	32.85 ± 0.17	P95R
5	WC6	3.28		0.20 ± 0.03	C04V	18.36 ± 0.07	31.11 ± 1.25	I00R
6	WN4b	2.43	1.48 ± 0.03		C00V	19.02 ± 0.01	32.32 ± 0.02	P95R
*11	WC8 + O7.5III-V	0.26	2.90 ± 0.40		A86V	17.37 ± 0.06	31.70 ± 0.05	P95R
12	WN8h	7.99		0.51 ± 0.06	C04V	19.54 ± 0.05	33.24 ± 0.23	P95R
48a	WC8ed +..	2.27	2.02 ±0.3		H12A	19.10 ± 0.07	34.15 ± 0.20	T19C
*79a	WN9ha	2.24	0.90 ± 0.14		A86V	18.73 ± 0.07	32.14 ± 0.15	S10X
86	WC7 (+BOIII-I)	2.86	0.50 ± 0.07		A86V	18.69 ± 0.06	31.75 ± 0.24	P95R
88	WC9	3.92		0.26 ± 0.05	C04V	18.63 ± 0.08	33.05 ± 0.18	P95R
89	WN8h + abs	3.73	0.60 ± 0.10		C04V	19.00 ± 0.07	32.92 ± 0.28	P95R
93	WC7 + 07-9	1.87	0.90 ± 0.19		A86V	18.58 ± 0.09	33.10 ± 0.14	P95R
100	WN7b	4.55		0.47 ± 0.05	C04V	19.02 ± 0.05	32.81 ± 0.16	I00R
*104	WC9d + B0.5V (+VB)	4.11		0.54 ± 0.06	C04V	18.99 ± 0.05	32.44 ± 0.22	P95R
*105	WN9h	1.82	4.39 ± 0.15		C04V	19.24 ± 0.02	32.27 ± 0.35	I00R
110	WN5-6b	1.66	0.96 ± 0.10		B82V	18.50 ± 0.05	32.59 ± 0.29	P95R
111	WC5	1.72	0.33 ± 0.10		B82V	18.07 ± 0.13	31.08 ± 0.11	P95R
115	WN6o	0.48	0.40 ± 0.09		A86V	17.04 ± 0.10	32.10 ± 0.22	P95R
120	WN7o	1.57		0.40 ± 0.04	C04V	18.02 ± 0.04	32.73 ± 0.29	I00R
*125	WC7ed + O9 III	4.09	1.18 ± 0.06		C04V	19.37 ± 0.02	32.49 ± 0.53	I00R
133	WN5o + O9I	1.95		0.36 ± 0.03	C04V	18.16 ± 0.04	33.07 ± 0.06	P95R
134	WN6b	1.85	0.80 ± 0.10		A86V	18.52 ± 0.05	31.66 ± 0.21	P95R
136	WN6b(h)	2.06	1.60 ± 0.20		D80V	18.91 ± 0.05	31.28 ± 0.25	P95R
*137	WC7pd + O9	2.25	0.37 ± 0.08		B82V	18.35 ± 0.09	31.79 ± 0.07	P95R
138	WN5o + B..	2.72	0.60 ± 0.10		B82V	18.73 ± 0.07	32.58 ± 0.11	P95R
139	WN5o + O6 III-V	1.36	0.28 ± 0.08		B82V	17.79 ± 0.12	32.63 ± 0.06	P95R
145	WN7o/CE + ..	1.53	0.98 ± 0.15		B82V	18.44 ± 0.07	32.55 ± 0.21	P95R
*146	WC6 + O8	1.10	41.6 ± 0.38		H17V	19.77 ± 0.02	33.53 ± 0.01	Z17X
*147	WN8(h) + B0.5V	0.65	35.30 ± 0.13		A86V	19.25 ± 0.002	31.76 ± 0.23	P95R
156	WN8h	4.79		1.06 ± 0.03	C04V	19.41 ± 0.01	32.22 ± 0.32	P95R

A86V: (Abbott et al., 1986) VLA; B82V: (Bieging et al., 1982) VLA; D80V: (Dickel et al., 1980) VLA;C04V: (Cappa et al., 2004) VLA; P95R: (Pollock et al., 1995) ROSAT; I00R: (Ignace et al., 2000) ROSAT; S10X: (Skinner et al., 2010) XMM; H17V: (Hales et al., 2017); Z17X:(Zhekov, 2017) XMM; H12A:(Hindson et al., 2012) ATCA; T19C: (Townsley et al., 2019) CHANDRA. (*Asterisk*): Non-Thermal radio emitting WR stars as listed by De Becker (2007).

Table 3.2: The X-Ray and Radio Emission Catalogue for O-stars and early B-stars

Name	Spectral Class	Distance	S_ν 4.8 GHz	S_ν 8.4 GHz	L_R	Ref	L_X	Ref
		(kpc)	(mJy)	(mJy)	(erg/s)		(erg/s)	
*HD 93129A	O2If*+O3.5V	3.09	5.60 ± 0.03		19.81 ± 0.002	B06A	33.97 ± 0.12	B06X
*HD 150136	O3.5If*+O6V+..	1.06	5.57 ± 0.03		18.87 ± 0.002	B06A	32.65 ± 0.09	S05C
*HD 93250	O3.5V((f+))	2.75		1.36 ± 0.17	19.04 ± 0.05	L95A	33.23 ± 0.003	G11X
HD 66811	O4 I(n)f	0.40	1.64 ± 0.07		17.50 ± 0.02	B03A	32.42 ± 0.21	C89E
HD 190429A	O4 If+	2.17		0.28 ± 0.03	18.15 ± 0.02	S98V	33.25 ± 0.33	C89E
HD 15570	O4If+	2.51		0.11 ± 0.03	17.87 ± 0.12	LL93	32.39 ± 0.30	R16X
*CD−47 4551	O5If	1.83	2.98 ± 0.05		19.08 ± 0.01	B06A	31.73 ± 0.09	B06R
*CygOB2 #9	O5If+	1.45	0.89 ± 0.05		18.35 ± 0.02	B12E	33.76 ± 0.002	C14X
*HD 15558	O5III(f)+O7V	2.15	0.50 ± 0.10		18.44 ± 0.09	B89V	32.50 ± 0.01	R16X
HD 210839	O6I(n)fp	0.62	0.40 ± 0.25		17.26 ± 0.28	S07V	32.60 ± 0.32	C89E
*CygOB2 #8A	O6Ib(n)(f)+ O5.5III(f)	1.80	0.73 ± 0.05		18.45 ± 0.03	B10V	33.90 ± 0.002	N12X
*HD 124314	O6V(n)((f))	1.81	4.14 ± 0.20		19.21 ± 0.02	B06A	32.02 ± 0.09	B06R
*CygOB2 #5	O7Ia+Ofpe/ WN9	1.65	2.48 ± 0.08		18.91 ± 0.01	W98V	33.75 ± 0.004	C14X
HD 24912	O7.5III(n)((f))	0.73		0.169 ± 0.03	16.88 ± 0.08	S07V	32.14 ± 0.30	N14X
HD 151804	O8Iaf	1.63	0.40 ± 0.10		18.10 ± 0.11	B89V	32.72 ± 0.30	C89E
HD 47129	O8I+O7.5III	1.58		0.208 ± 0.015	17.64 ± 0.031	K17J	32.87 ± 0.01	N14X
HD 37043	O9III+B7IV	0.50		0.046 ± 0.02	16.09 ± 0.14	LL93	32.10 ± 0.22	C89E
HD 57061	O9II+B2V	1.50		0.35 ± 0.03	17.92 ± 0.04	LL93	32.82 ± 0.25	C89E
HD 149757	O9.5Vnn	0.17		0.18 ± 0.02	15.74 ± 0.05	LL93	31.48 ± 0.29	C89E
HD 36486	O9.5II+B0III	0.50		0.30 ± 0.01	16.90 ± 0.01	LL93	32.57 ± 0.21	C89E
HD 30614	O9.5Ia	0.73	0.29 ± 0.04		17.27 ± 0.06	S07V	32.55 ± 0.29	C89E
HD 37742	O9.5Iab+B1IV+B0III	0.41		1.104 ± 0.015	17.20 ± 0.006	K17J	32.39 ± 0.01	N09X
CygOB2 #12	B5 Ia-0	1.80	3.94 ± 0.07		19.18 ± 0.01	W98V	33.82 ± 0.01	C14X

B06A: (Benaglia et al., 2006) ATCA; L95A: (Leitherer et al., 1995) ATCA; B03A: (Blomme et al., 2003) ATCA; S98V: (Scuderi et al., 1998) VLA; LL93: (Lamers and Leitherer, 1993); N12X: (Nazé et al., 2012) XMM; B89V: (Bieging et al., 1989) VLA; B01A: (Benaglia et al., 2001) ATCA; S07V: (Schnerr et al., 2007) VLA; B10V: (Blomme et al., 2010) VLA; W98V: (Waldron et al., 1998) VLA; B01X: (Benaglia et al., 2001) XMM; B01R: (Benaglia et al., 2001) ROSAT; G11X: (Gagné et al., 2011) XMM; C89E: (Chlebowski et al., 1989) EINSTEIN; R16X: (Rauw and Nazé, 2016) XMM; N14X: (Nazé et al., 2014) XMM; C14X: (Cazorla et al., 2014) XMM; N09X: (Nazé, 2009) XMM; K17J: (Kurapati et al., 2016) JVLA. (*Asterisk*): Non-Thermal radio emitting O-type stars as listed by De Becker (2007).

3.6 Monte Carlo Modelling and Fitting of Simulated L_X:L_R data

There are many fitting packages available in the Python library, such as the `polyfit1d`, `curve_fit` and `Orthogonal Distance Regression` (ODR). The main challenge to fitting our data is that both axes have observational errors while the existing common python packages work when the error is established on Y-axis only. A program in IDL called the `FITEXY` (Press et al., 1992)[1] does linear least-squares fitting in one dimension when both the data axes have errors. It does not account for the case when one axes has an intrinsic spread.

An interesting program called `LINMIX_ERR.pro` in IDL by Kelly (2007) utilised a Bayesian approach to account for measurement errors in linear regression of astronomical data. The routine has been tested with the real astronomical data for the dependence of X-ray photon index, Γ_X on L_{bol}/L_{Edd} for Radio-Quiet Quasars (RQQs). Kelly (2007) concluded that `LINMIX_ERR.pro` outperformed other linear regression fitting packages but they are still 'statistically acceptable'. In this study, we use a Python port for `LINMIX` by Josh Meyers[2].

This section compares the results from `LINMIX` and another commonly used program, `FITEXY`, on synthetically generated data. We randomly generated a large number of realisations of $L_X : L_R$ and fit them with both `LINMIX` and `FITEXY` and highlight some of the issues with the fitting.

We have generated synthetic $L_X : L_R$ data (designed to roughly represent the expected $L_X : L_R$ correlation) for a sample of N_* stars, and a number of realisations, N_{real}. We did this in several steps:

[1]The IDL version of *FITEXY* that we use here is available at: https://idlastro.gsfc.nasa.gov/ftp/pro/math/fitexy.pro.

[2]The `LINMIX` GitHub repository available at https://github.com/jmeyers314/linmix.

1. We randomly generated values of L_{bol} in the range of $\log_{10}(L_{bol}/L_{\odot}) = [4.5 - 6.5]$, appropriate for O-stars. While a more sophisticated sampling of the luminosity function would be possible, we adopted a simple approach (especially given the strong dependence of L_R on L_{bol}).

2. From this, we generated a value of $\dot{M}$ from the Howarth and Prinja (1989) relationship. See Eqn. 3.2.

3. We randomly generated a wind terminal velocity where we assumed a mean value of $v_{\infty} = 1500$ km s^{-1}, with a normally distributed scatter, $\sigma_v = 300$ km s^{-1}. Again, a more sophisticated prescription could be used, but we regarded this simple approach as sufficient to highlight the advantage of `LINMIX`.

4. From these values of $\dot{M}$ and v_{∞}, we generated a radio flux, S_{ν}, from Wright and Barlow (1975) and Lamers and Leitherer (1993), (see Eqn. 3.6), and hence, we estimated L_R, noting that $L_R = 4\pi D^2 S_{\nu}$, with D is the distance (so that the distance is not required).

   For the calculation of S_{ν} and L_R, using the appropriate values for O-stars, we assumed solar abundance material, H is fully ionised and He is singly ionised, so that $\mu = 1.339$, $Z = 1.149$, $\gamma = 1.105$, $g_{ff} = 5.57$ (appropriate for $\nu = 4.8$ GHz) and $T_e = 20000$ K.

5. We then calculated an X-ray luminosity, assuming that $L_X/L_{bol} = 10^{-7}$, with a normally distributed intrinsic scatter of σ_{int}. We investigated the effect of different values of σ_{int} on the accuracy of the `LINMIX` and `FITEXY` fitting.

6. Given the above inputs, the true underlying slope used to generate these realisations is $\alpha = 0.44$ (see Section 3.4).

7. We assumed uniform measurement errors in both L_X and L_R of 0.2 dex (which we designated as σ_X and σ_R) and we added those to our values of L_X and L_R.

The size of the error-bars for the real sample is of course very variable and a constant value of 0.2 dex is chosen purely for convenience.

Having generated such a realisation of the L_X:L_R relation, we fitted the resulting realisation with the IDL software `FITEXY` (Press et al., 1992), and the Python migrated package `LINMIX` (Kelly, 2007). We assumed $N_* = 20$ (representative of our sample of OB stars presented here) and $N_{real} = 1000$. In our results we focused on the mean value of the slope $\bar{\alpha}$ and the dispersion in the slope (σ_α) from the N_{real} realisations. The results are presented in Table 3.3 for both `FITEXY` and `LINMIX`.

3.6.1 `FITEXY` and `LINMIX` Results and Discussions

For low values of σ_{int} in `FITEXY`, the input slope of $\alpha = 0.44$ is recovered, but for larger values of σ_{int} (specifically when $\sigma_{int} > \sigma_X$), the fitted slope tends to be systematically biased to higher values (see Fig. 3.2). The corresponding reduced χ^2 is about 1 when σ_{int} is small, but becomes much larger when $\sigma_{int} > \sigma_X$. This is because the effective errors have been underestimated, due to the intrinsic scatter (Tremaine et al., 2002). The fitting program `FITEXY` has failed to recover the true value of the slope ($\alpha = 0.44$), especially when $\sigma_{int} > \sigma_X$. From Fig. 3.2 the shift can clearly be seen as the intrinsic scatter, σ_{int} increases. The fitted results for both `FITEXY` and `LINMIX` are listed in Table 3.3 for comparison.

For `LINMIX`, we found that the input slope is basically recovered for all values of σ_{int}, demonstrating that this package is better at fitting linear models where there is an intrinsic scatter to the data. From Fig. 3.3, we noted that the dispersion of the slope, σ_α increases as σ_{int} increases.

As noted earlier, from Nazé (2009), the likely uncertainty in the $L_X : L_{bol}$ relationship is in the range of $0.3 - 0.5$ dex for O-stars and larger for B-stars. Consequently, given the range in sizes of the errors in our sample, using `FITEXY` may well result in biases in the fitted parameters. For this reason, we need to adopt a more

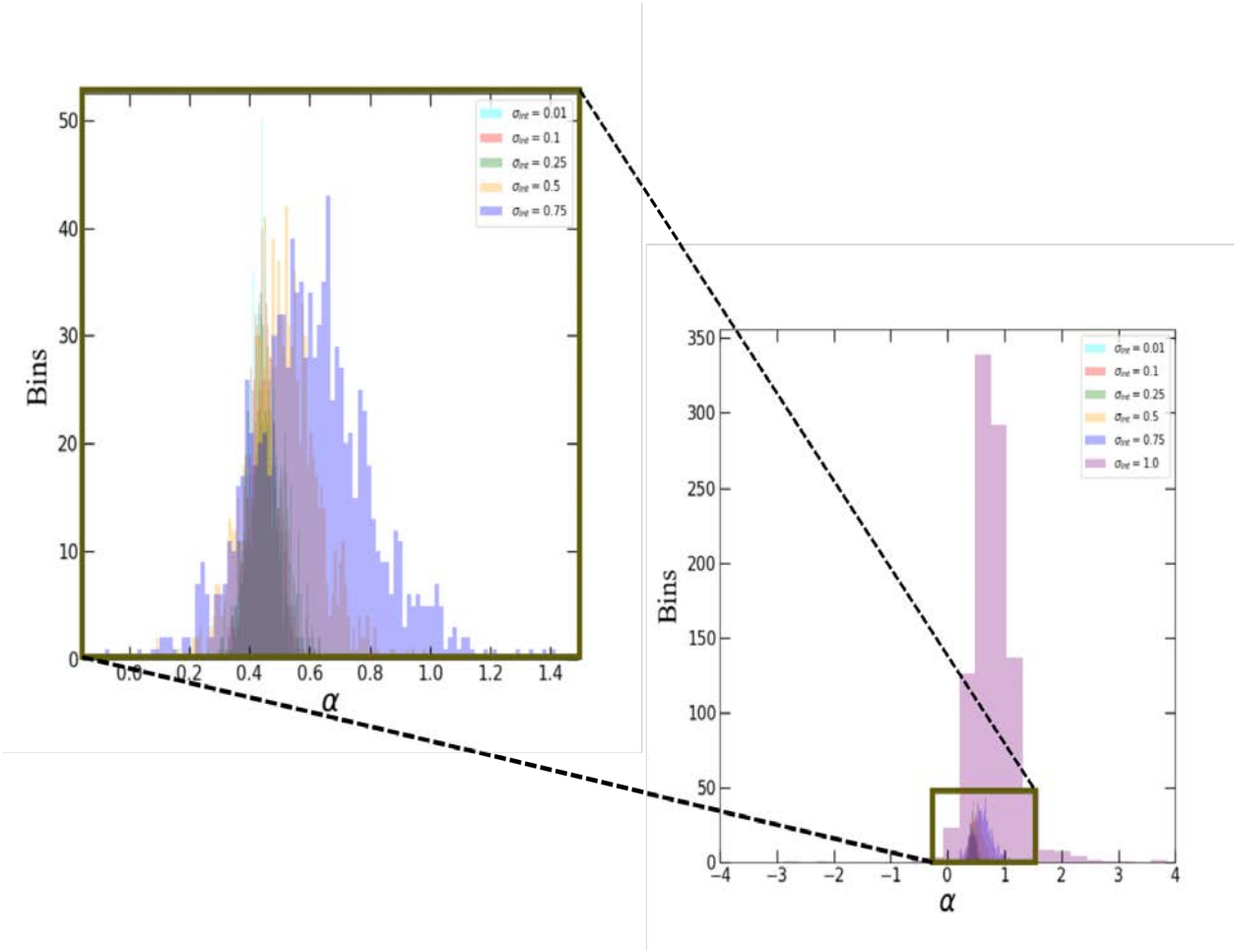

Figure 3.2: Histogram of `FITEXY` fitted slope at various intrinsic scatter, σ_{int} for 1000 realisations of simulated data. The number of bins for each σ_{int}, has been set to $N_{bins} = 100$. Left panel: With increasing σ_{int}, the mean slope, $\bar{\alpha}$, has shifted to higher values, along with the larger scatter in the fitted slope, σ_α. The right panel of Fig. 3.2 depicts the excessive dispersion when the intrinsic sigma, σ_{int} is set to 1.0. The remaining intrinsic scatter bins are visible in the centre of the histogram (zoomed in to the left panel).

Table 3.3: Fitting parameters for the `FITEXY` and `LINMIX` modelling on the simulated data. σ_{int} is the intrinsic scatter in the L_X : L_{bol} relation used to generate the synthetic data, $\bar{\alpha}$ is the mean fitted slope for the realisations and σ_α is the scatter in the fitted values of α.

	FITEXY		LINMIX	
σ_{int}	$\bar{\alpha}$	σ_α	$\bar{\alpha}$	σ_α
0.01	0.44	0.04	0.44	0.05
0.1	0.44	0.04	0.44	0.05
0.25	0.45	0.06	0.44	0.07
0.5	0.51	0.11	0.44	0.11
0.75	0.61	0.19	0.44	0.16
1.0	0.85	1.65	0.44	0.21

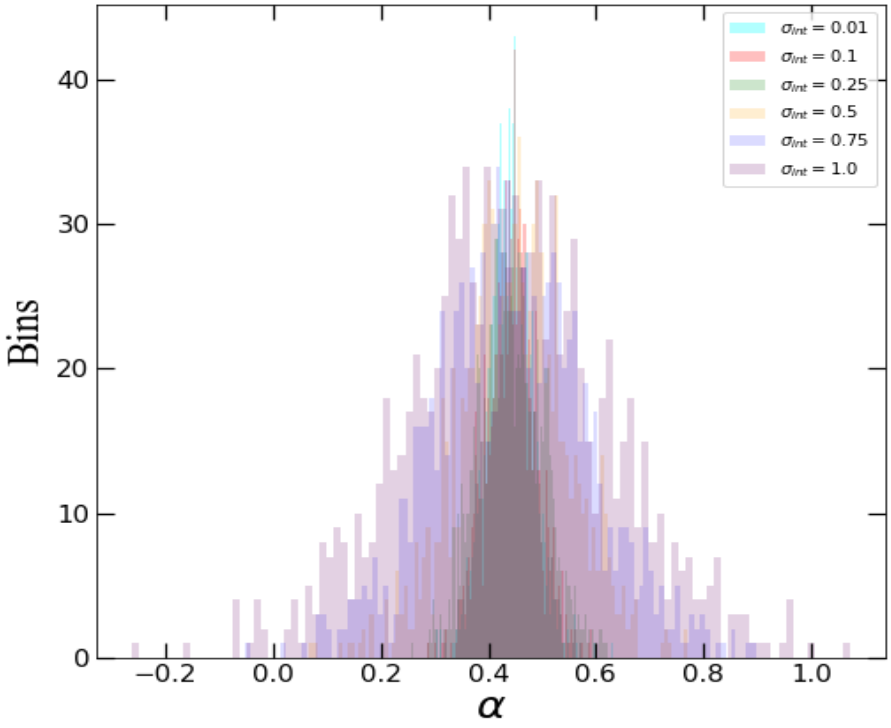

Figure 3.3: Histogram on `LINMIX` fitted slope at various σ_{int} for the simulated data. `LINMIX` recovered the mean slope value, $\bar{\alpha} = 0.44$. The dispersion of the slope, σ_α increases as the intrinsic scatter, σ_{int} increases. Please refer to Table 3.3 for all the mean values.

rigorous numerical method - namely `LINMIX` which can account for this intrinsic scatter. In the next subsection, we investigate the `LINMIX` outputs to understand the package better.

3.6.2 `LINMIX` Analysis

We generated a larger sample size of 100 simulated stars with intrinsic scatter, $\sigma_{int} = 0.01$ and an error of 0.1 dex in both the x and y directions to better understand the additional parameters available in `LINMIX` package.

The regression in `LINMIX` assumed:

$$\eta = \beta + \alpha * \xi + \epsilon, \tag{3.11}$$

with

$$X = \xi + Xerr, \tag{3.12}$$

$$Y = \eta + Yerr. \tag{3.13}$$

where the β is the regression normalisation, α is the slope and ϵ is the intrinsic random scatter about the regression with mean zero and variance $sigsqr$. $Xerr$ and $Yerr$ are the measurement errors in X and Y respectively. We fitted the simulated star sample with 10000 MCMC iterations and the main outputs is displayed in Table 3.4 and Fig. 3.4. From the `LINMIX` fitting outputs, $sigsqr = 0$ is essentially no scatter, while $sigsqr = 1$ being the most scatter. $corr = 0$ is weakly correlated and $corr = 1$ being strongly correlated.

Table 3.4: The main output from `LINMIX` fitting package featuring the slope, α, normalisation, β, the variance of the intrinsic scatter, *sigsqr*, and the *corr* is the linear correlation coefficient between ξ and η on simulated star sample to better understand the `LINMIX` package outputs.

Parameters	Values
α	0.441 ± 0.009
β	24.41 ± 0.16
sigsqr	0.018 ± 0.004
corr	0.986 ± 0.003

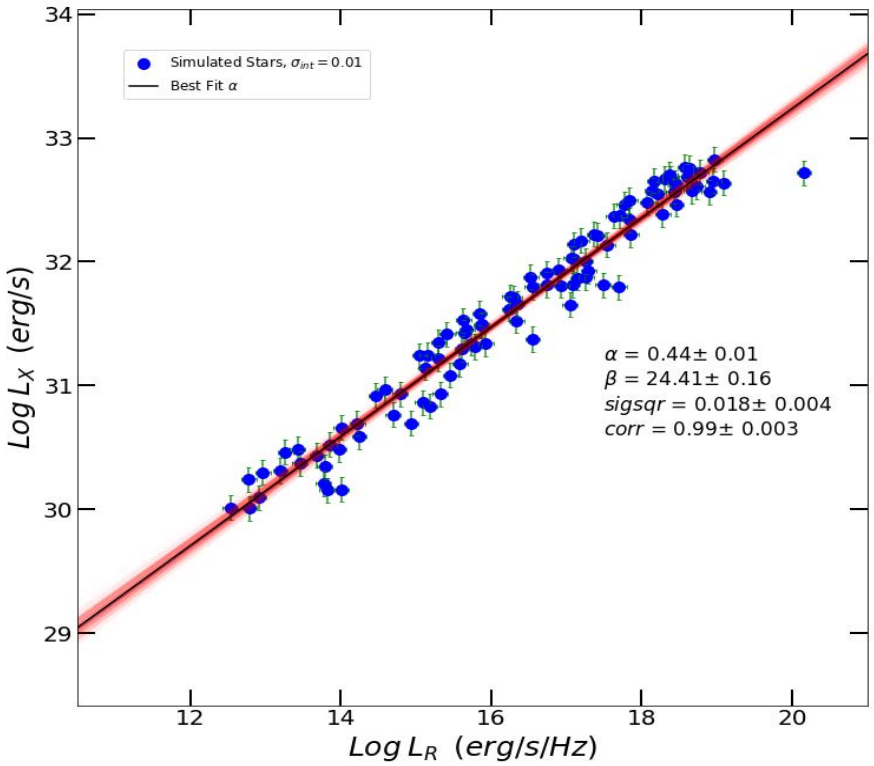

Figure 3.4: Larger sample fittings on L_X : L_R simulated massive stars to better understand the `LINMIX` package outputs. From the fitting, the slope, $\alpha = 0.44 \pm 0.01$ is recovered which is basically the theoretical value. The $sigsqr = 0.018 \pm 0.004$ indicates a very small intrinsic random scatter about the regression. A strong correlation between L_X and L_R can be seen with the coefficient, $corr = 0.99 \pm 0.003$.

3.7 Results and discussions for the WR and OB Star Archives Sample

We used the Bayesian linear regression routine `LINMIX` to calculate the best-fit slope, α, the error of the slope, and the variance of the intrinsic scatter, *sigsqr* of our $L_X : L_R$ relationship for both our spectral classes, WR star and OB star. `LINMIX` uses the Markov chain Monte Carlo (MCMC) method and uses random draws from the posterior distribution. This routine was initially developed in the IDL environment before being ported to Python (as discussed in Section 3.6). The results for the data sample in Table 3.1 and Table 3.2 are plotted in Fig. 3.5 and Fig. 3.6 for the separate category of spectral class and for the overall massive stars data sample.

From the theoretical value, we should expect a positive correlation with a slope of $\alpha = +0.44$ between L_X and L_R for massive stars (see Section 3.4). Fittings from both star samples, WR-stars and OB-stars, demonstrated compelling positive correlations. Both of these stars samples have a slope of $\alpha = +0.38$, but the WR-stars depict more scatter, as shown by the slope error of ± 0.23 and higher variance of intrinsic scatter, $sigsqr = 0.49 \pm 0.17$. The OB-stars have less scatter data and therefore have a lower slope error of ± 0.13 and a slightly lower variance of intrinsic scatter, $sigsqr = 0.45 \pm 0.16$. As shown in Fig. 3.5, we included darker and lighter gold bands to represent the 1σ and 2σ ranges of the slope from the mean slope plotted in a black solid line. The theoretical slope is still well within the 1σ confidence interval in both cases, suggesting a positive agreement with the observational data samples.

We proceed and combine all our sample stars and repeat the fitting routine to find the best-fit slope for the L_X and L_R correlation over both samples. As shown in Fig 3.6, the best-fit slope is $\alpha = 0.32 \pm 0.13$. The error from the overall sample is smaller than both of the previous categories due to a greater sample size, and the

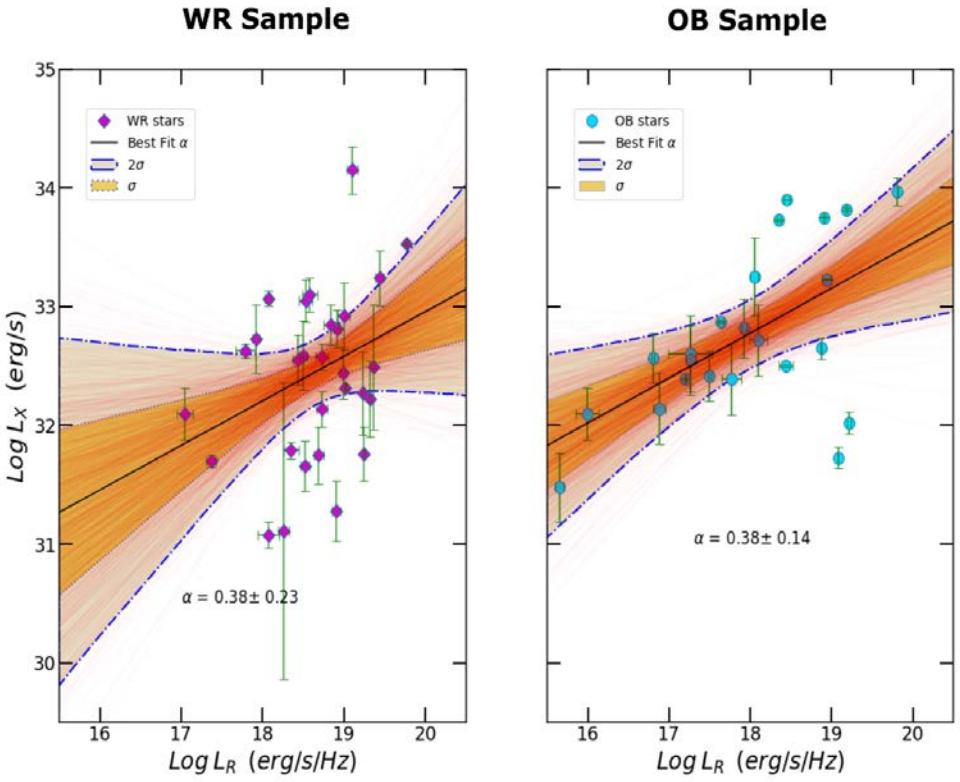

Figure 3.5: The X-ray and radio luminosity correlation for WR and OB sample. The data was fitted with `LINMIX` package utilising a Bayesian approach. Left panel: The WR data (purple diamond) with their measurement error bars are shown. The black line is the best-fit slope, $\alpha = 0.38 \pm 0.23$. Right panel: The OB data (turquoise circle) with their measurement error bars are shown. The black line is the best-fit slope, $\alpha = 0.38 \pm 0.14$. For both panels, the darker gold bands shows the slope at 1σ from the best-fit slope (mean slope) while the lighter gold bands are at 2σ. The slope was plotted by a thin red solid line for every 10 realisations. A greater scatter in the WR-stars sample can be seen by a larger dispersion of the slope.

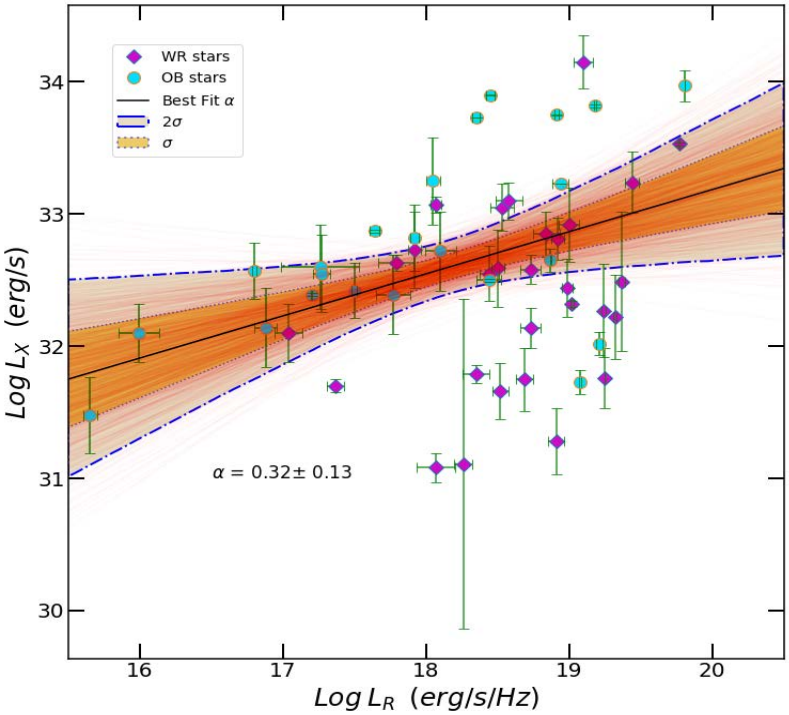

Figure 3.6: The X-ray and radio luminosity correlation for the combined sample fitted with `LINMIX` package. The WR data (purple diamond) with their error bars are more scattered at the bottom of the best-fit slope while more OB data (turquoise circle) are located at the top. The best-fit slope over WR and OB star sample is $\alpha = 0.32 \pm 0.13$ as shown in solid black line. The error of the slope is smaller than both of the previous categories due to a greater sample size. The theoretical expected slope ($\alpha = 0.44$) is still within the error of the best-fit slope suggesting a positive agreement with the theory.

theoretical expected slope is still within the error of the best-fit observational slope.

We compare the normalisation, β, variance of the intrinsic scatter, *sigsqr* and the correlation coefficient, *corr* for our overall sample. The fitting output parameters are recorded in Table 3.5. Our star samples represent systems with single stars and known colliding wind binary system. From Fig. 3.6, there is more WR data at the bottom of the best-fit slope, while there is more OB data scatter at the top. We noted that the overall best-fit slope is slightly flattened from both previously individually fitted categories but still within the error of the expected theoretical

Table 3.5: The comparison of the best-fit slope, α, intrinsic scatter, ϵ and correlation coefficient, *corr* for WR-stars, OB-stars, and the combined massive stars sample.

Star	WR	OB	ALL
α	0.38 ± 0.23	0.38 ± 0.14	0.32 ± 0.13
β	25.45 ± 4.20	26.00 ± 2.53	26.81 ± 2.43
sigsqr	0.49 ± 0.17	0.45 ± 0.16	0.49 ± 0.12
corr	0.33 ± 0.19	0.54 ± 0.17	0.35 ± 0.14

slope. This figure also shows that the O-stars are X-ray brighter for the same radio luminosity than WR stars.

3.8 Conclusions

In this chapter, we have considered the relationship between X-ray and radio luminosities for an archival sample of massive stars based on the known correlations between mass-loss rates, bolometric and radio luminosities, and the empirical relationship between X-ray and bolometric luminosities.

In both of the star samples (WR star and OB star), we discovered positive correlations of $L_X : L_R$ relationship. The expected slopes were within the error of the fitted slope. The correlation is much stronger in OB-stars than in WR-stars which is related to the fact that WR-stars have a higher variance of intrinsic scatter.

For the overall massive star sample, the fitted slope (within error) agrees with the theoretical slope and the slope error has decreased due to the larger sample size. The slope has slightly flatten which may be due to the fact that O-stars are X-ray brighter for the same radio luminosity as WR stars.

In conclusion, we have quantified a new relationship between the X-ray and radio luminosities for massive stars, as a high mass analogy of the Güdel-Benz relationship for low-mass stars.

4 | A Reinterpretation of the Variable Radio Emission from the Colliding Wind System WR140

"There's something really beautiful about science, that human beings can ask these questions and can answer them. You can make models of nature and understand how it works."
–Margaret J. Geller.

Chapter Summary

The WR140, a classic colliding-wind binary, is introduced in this chapter. The radio emission from this CWB is affected by the system's orbital position. To display the radio spectra, we present radio data collected from various archives in a new way. The data was undertaken using various radio interferometers such as the VLA, VLBA and WSRT at frequency ranges from 1.5 GHz to 22 GHz. Depending on the frequency, the non-thermal radio emission from WR140 generally increases as the system approaches periastron and then drops dramatically just before the periastron. Next, we introduce a simple yet effective Distributed Radio Emission Measure (DREM) model to capture the essence of the radio spectra. We fit the model param-

eters to our radio data and display the radio emission measure profile as a function of phase. The radio emission measure decreases at roughly around $\phi \sim 0.88$ before increases sharply just before the periastron where the line-of-sight enters the dense WC7 wind. Finally, we compare the radio emission measure with the X-ray emission measure and discuss the outcomes.

4.1 Introduction

Massive stars, either Wolf-Rayet (WR) or OB stars, have dense, ionised stellar winds, with mass-loss rates in the range of $\dot{M} \sim 10^{-7}-10^{-4}$ $M_\odot$ yr^{-1} and terminal velocities of $v_\infty \sim 500-4000$ km s^{-1}. Massive stars are often in binary or multiple systems with other massive stars. Commonly, both stars possess strong winds and the winds will collide. Systems with such events are called the Colliding Wind Binaries (CWBs). CWBs in massive stars offers varieties of physics across the spectra. These winds contain a tremendous amount of energy and are important drivers to the feedback processes within star clusters or starburst galaxies (Leitherer et al., 1999).

Many massive stars are detectable radio sources at GHz frequencies (fluxes for the brighter objects are up to a few mJy), and their radio emission is usually characterised as being either *thermal* or *non-thermal* in nature, depending on whether the radio spectral index is positive or negative. The winds are free-free emitters and the resulting thermal spectrum (which has contributions from both optically thin and optically thick regions) has a positive spectral index, with $\alpha \sim +0.6$, where the radio flux scales as $S_\nu \propto \nu^\alpha$. This thermal emission has been a key approach of estimating mass-loss rates (White and Becker, 1995). For example, the most popular massive star, η Carinae, probably the brightest thermal emitter, shows a powerful radio emission of 0.7 Jy at 9 GHz observed by the Australian Telescope (AT) (White et al., 1994).

Many massive stars also show non-thermal (NT) emission, with the NT com-

ponent having a flat or negative spectral index. This is believed to be synchrotron emission, generated by electrons accelerated by shocks within the winds (De Becker, 2007). In general, NT emission suffers from the free-free absorption in the wind at low frequency, thus we normally only see the thermal component. In the case of the classic colliding-wind binary, WR140, the NT emission was detected using the high resolution VLBA observations at higher frequencies around the phase, $\phi = 0.7 - 0.9$ (Dougherty et al., 2005), before it disappeared just before the periastron due to the absorption.

4.2 WR140 - The Archetypal Colliding Wind Binary System

WR140 is a remarkable colliding wind binary, comprising of a WC7 Wolf-Rayet star and an O5 companion star with a highly eccentric orbit ($e \sim 0.9$) of period 7.94 years at 1.7 kpc. Both stars possess fast, radiatively driven winds (terminal velocities of ~ 3000 km s^{-1}).

WR140 has been categorised as a *particle-accelerating colliding-wind binary (PACWB)* rather than just a non-thermal emitter to accurately describe the mechanisms. WR140 is the only CWB that displays radio synchrotron radiation and non-thermal hard X-rays at the same time (De Becker and Raucq, 2013).

At IR wavelengths, WR140 undergoes a dramatic rise in flux around periastron (see Fig. 4.1), followed by a gradual decline. This episodic IR rise by WR140 is due to the carbon dust formation around periastron (Williams, 2011a). The close association of this dust producing event with periastron remains a mystery, but it is believed to be associated with the wind-wind collision. Recently, Lau et al. (2020) used the Binary Population and Spectral Synthesis (BPASS) model, incorporating the `DustEM` SED models stated that the dust production of carbon-rich WR binaries

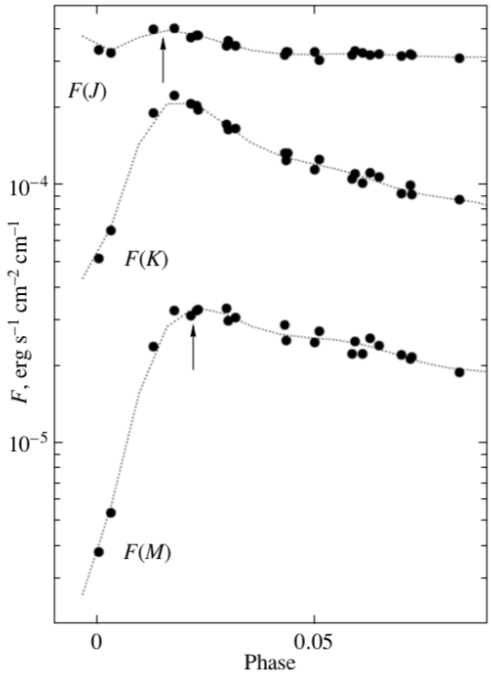

Figure 4.1: The flux variation versus the phase of WR140 near the periastron. The data was obtained in Band J (1.25 μm), K (2.2 μm) and M (5 μm) with the 1.25 m telescope at the Crimean Laboratory of the Sternberg Astronomical Institute. The arrows indicate the maxima at respective bands. The flux increment is quite dramatic; nearly a factor of 10 as can be seen in the figure (Taranova and Shenavrin, 2011).

(WC) was related to the orbital period. Hence, WR140 system is the popular choice to study dust formation.

The X-ray emission from WR140 varies strongly throughout the orbit, with a strong peak in emission close to the periastron passage. Post periastron, the X-ray emission drop steeply, followed by a quick recovery in emission level (Corcoran et al., 2011).

Fig. 4.2 shows an astonishing comparison between the radio emission and the X-ray flux of WR140. The 2 cm radio emission was observed during the year 1985-1993 cycle using the VLA. The orbital period is 7.94 years. The X-ray 2-10 keV flux was obtained by the *RXTE*. The phase increases counterclockwise, where the periastron is at 0 AU. From Fig. 4.2, closer to the periastron, both X-ray and radio flux indicate minima when the wind collision region (WCR) is viewed through the WC7 wind.

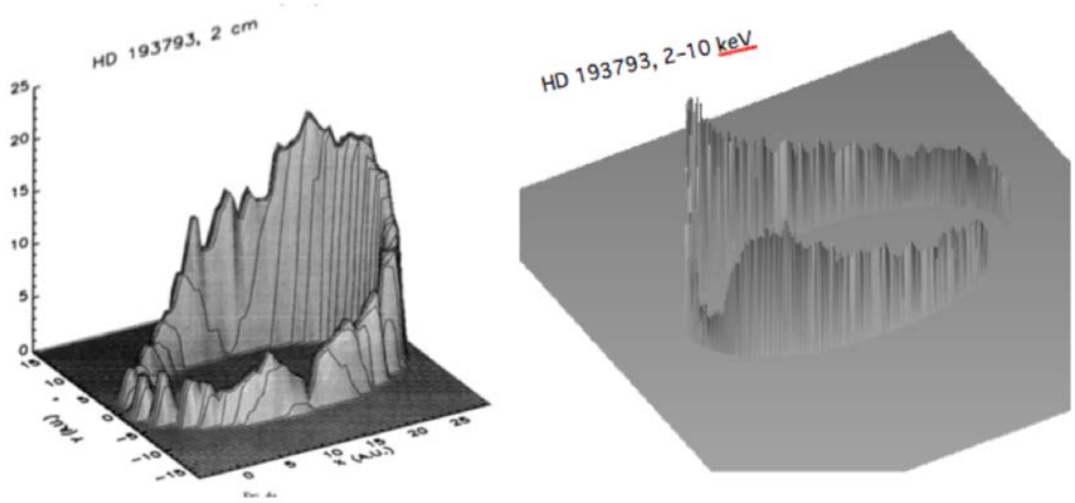

Figure 4.2: The comparison of the orbital variation of WR140 (7.94 years) between the radio emission at 2 cm taken from White and Becker (1995) using the VLA telescope and the 2−10 keV X-ray flux from *RXTE* data (Corcoran et al., 2011). The phase increases counterclockwise with the periastron is at 0 AU. The radio emission peaked around $\phi \sim 0.7$ while the X-ray emission is still increasing. Post periastron, the radio emission is increasing gradually while the X-ray emission recovered quickly after the dip at periastron.

By looking closely, the X-ray flux is still rising while the radio emission decreases gradually and is at a minimum approaching the periastron. Post periastron, the X-ray emission recovered quickly while radio emission was taking a slow increase. The 2 cm radio emission peaked around $\phi = 0.7$, where the WC7 star has moved behind the wind collision region.

Going down the frequency, the radio emission appears to stay longer at a thermal state with a steeper rise closer to periastron compared to a gradual increase at a higher frequency before a sharp decline just before the periastron (White and Becker, 1995).

The WR140 radio emission comes from two sources – thermal radio emission predominantly from the Wolf-Rayet stellar wind and highly variable non-thermal radio emission (synchrotron radiation) from the wind collision region (WCR). The striking variation in the emission from the system encompasses a wide range of physics (Pittard and Dougherty, 2006). At lower frequencies, several absorption processes

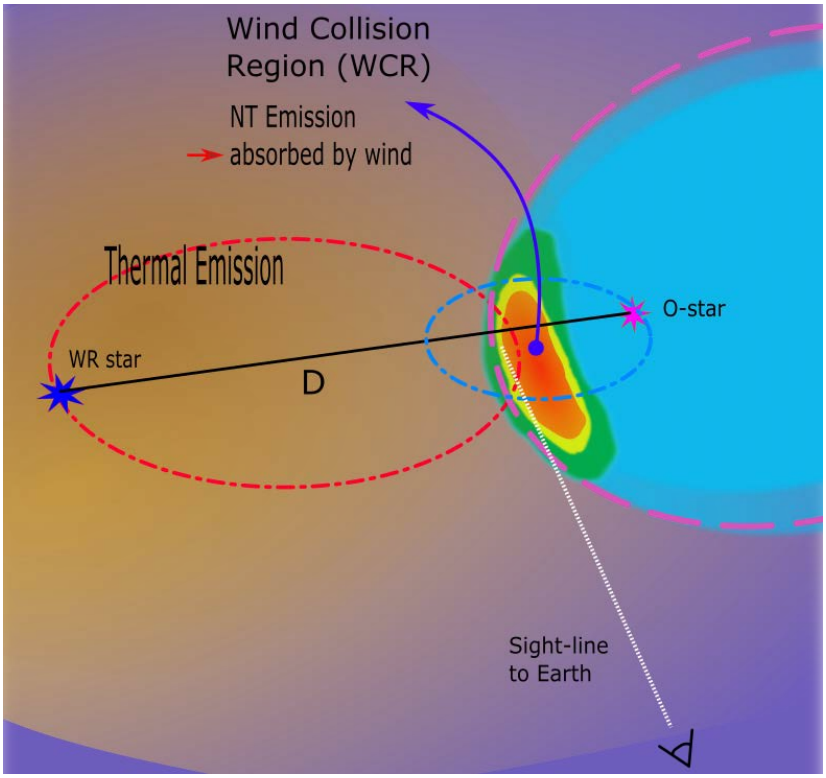

Figure 4.3: The author's illustration on WR140 approaching apastron. The WC7-star is in front of the wind collision region (WCR) so that the observer's line-of-sight encounters the denser WC7 wind where most of the NT emission suffered the free-free absorption.

affect the radio emission. Most of the processes vary as the stellar separation *(D)* changes. The influence of the Razin effect, Synchrotron Self-Absorption (SSA) and Coulombic cooling increases as the stellar separation decreases. Predominantly, the free-free absorption by the stellar wind will come into play as the generally rising NT emission will eventually turn-over at lower frequencies.

4.3 WR140 Previous Data

There were several radio observations performed to observe WR140 at frequencies ranges from 1.5 GHz to 22.0 GHz. Williams et al. (1990) and Williams et al. (1994) made the observations using the Westerbork Synthesis Radio Telescope (WSRT) at 8.4, 15.0, and 15.0 GHz. The radio observations from White and Becker (1995) using

the VLA offers a valuable dense coverage around the orbital period ~ 8 years at the same frequencies observed by Williams et al. (1994). The first high-resolution radio observations of WR140 were taken utilising the Very Large Baseline Array (VLBA) by Dougherty et al. (2005), covering the phases closer to the periastron ($\phi = 0.65$-0.98). These observations included the high-frequency observation of WR140 at 22.0 GHz. As shown in Fig. 4.4, WR140 shows some impressive variations from 1.5 to 22.0 GHz. The main feature that can be seen is that the radio emission rises up to a peak when approaching periastron (depending on the frequency), before falling again just before the periastron ($\phi = 1$). These previous radio data observations were combined (see Fig. 4.4(C)) to give a fuller and denser WR140 lightcurve.

In order to explain the radio data of WR140, White and Becker (1995) suggested a model with a disk using the free-free opacity to describe the radio peak closer to $\phi = 0.7$. The authors proposed a lower free-free opacity as the O-star moves through the disk closer to $\phi = 0.7$. But, this model was admitted to be too simple by the authors and needs a more sophisticated model to explain the radio data.

From the detailed VLBA radio observation closer to the periastron by Dougherty et al. (2005), the radio emission from the wind collision region (WCR) is the result of a distributed emission measure, where the line-of-sight to the WCR has travel across different regions between the WR and O-star. As a result, the emission will be a combination of both optically thick and thin emission. The authors also had a contradicting opinion with White and Becker (1995) about the stellar wind free-free opacity suggesting that the O-star wind opacity is of utmost concern and not the WR-star.

A very detailed and complicated hydrodynamical model is proposed by Pittard and Dougherty (2006), hereafter PD06, in an attempt to fit the radio data at $\phi = 0.837$ with various parameters. They begin with a 2D hydrodynamic simulation of a wind-wind collision. To generate the NT emission, they assumed a

distribution of non-thermal electrons. They calculated the free-free absorption from the hydrodynamic models in a self-consistent manner. The intrinsic extent of the assumed radio emission is shown in their Figure. 16, and is a bit bigger than the orbital separation.

The flattening effect at the low-frequency region of the radio spectra observed in the DREM model introduced in this chapter (in Section 4.5) is due to varying levels of free-free absorption from an extended emission region, and the same effect is intrinsically included in the PD06 modelling. The DREM model, on the other hand, is fairly simple in principle and does not require highly complex computational and radiative transfer modelling to fit a single radio spectrum at a specific orbital phase (and even then, PD06 have a number of physical parameters that are not well determined).

4.4 Simple Emission Measure Model

The emission measure is commonly used to parameterise the optical depth, τ. Remember that τ is the integral of $-\kappa$ along the line of sight, $\tau = -\int_{\rm los} \kappa \, ds$, where κ is the absorption coefficient which describe the characteristics of absorbing material. τ can be expressed as:

$$\tau = -\int_{\rm los} \kappa ds \propto \int \frac{n_{\rm e} n_{\rm i}}{\nu^{2.1} T^{3/2}} ds \approx \int \frac{n_{\rm e}^2}{\nu^{2.1} T^{3/2}} ds \, . \tag{4.1}$$

Emission measure is often used in X-ray to describe the Brehmsstrahlung radiation where the energetic electron goes past the positively charged nuclei and will accelerate strongly. The acceleration of these electrons will emit radiation. In radio, this process is called the free-free emission where the charged particles pass each other with high velocity and accelerate to produce radiation. The emission measure (EM) depends on the density of particles squared. Assuming that the wind of WR140 sys-

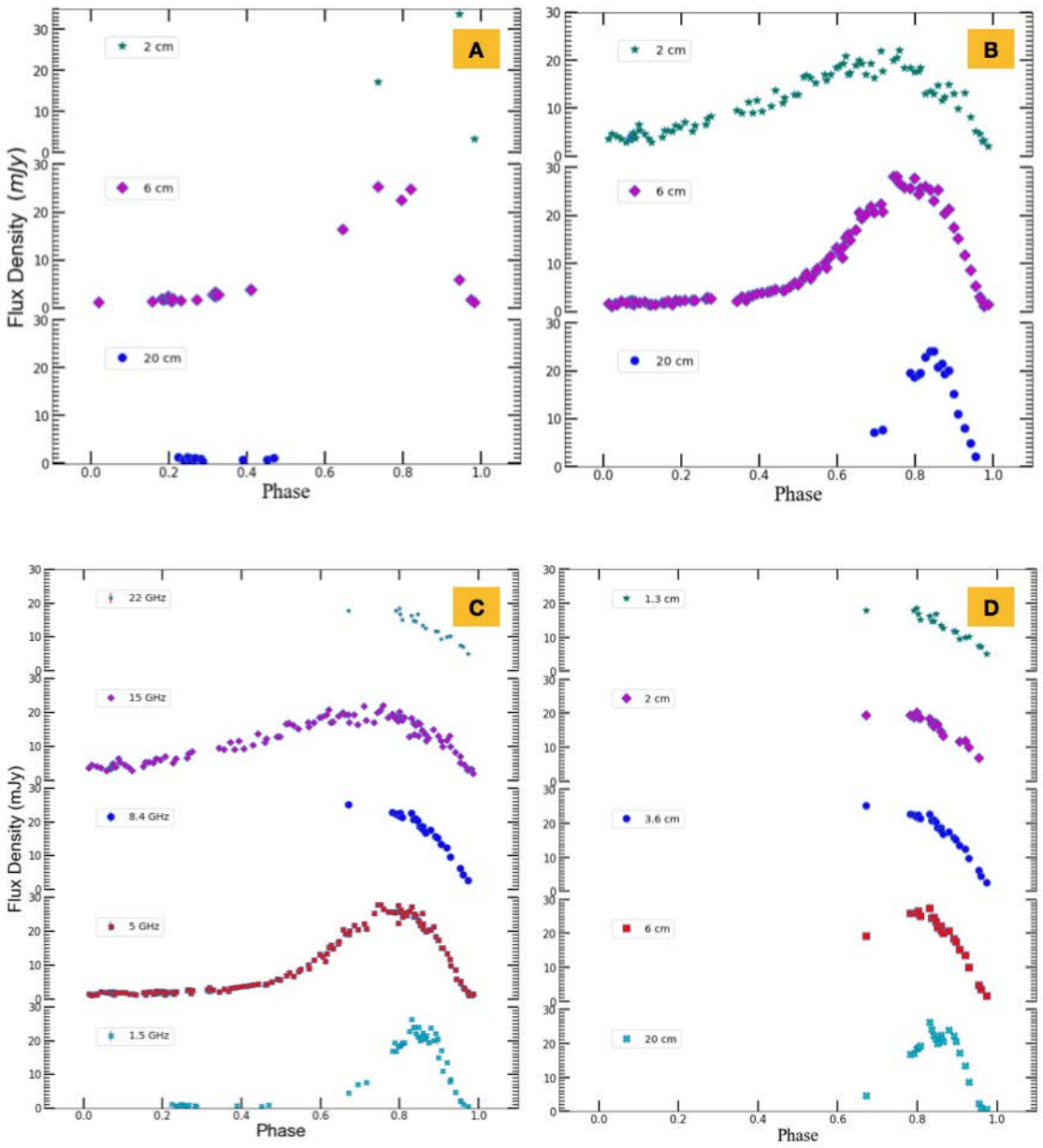

Figure 4.4: The radio emission from WR140 at several wavebands (1.5, 5, 8.4, 15 and 22 GHz) during the orbital cycle between 1978.56 and 2000.89. [This is more than one orbital cycle] Periastron passage occurs at $\phi = 0$. (A) The data taken from Williams et al. (1990) and Williams et al. (1994). (B)- Data from White and Becker (1995), and (D) from Dougherty et al. (2005). The combined data was shown in panel (C). The data has been reproduced using the updated WR140 period, P (days) = 2895.68, (Thomas et al., 2021). This data illustrates the extreme variability of WR140, with a large rise in flux around phases between $\phi = 0.65 - 0.85$ depending on the frequency. Take note that one point of the data at 2 cm (22 GHz) was omitted in the combined data due to being an outlier.

tem is completely ionised, $n_{\rm e} \sim n_{\rm p}$, thus the density $\propto n_{\rm e}^2$. If we observe the emission along the line of sight, the emission measure can be defined as:

$$EM \equiv \int_{\rm los} n_{\rm e}^2 \, ds. \tag{4.2}$$

Because the absorption coefficient, κ is proportional to $n_{\rm e} n_{\rm p} \approx n_{\rm e}^2$, from Eqn. 4.1, the optical depth, τ is proportional to EM. EM gives information about the amount of particles that should encounter the free-free process in unit of pc cm^{-6}.

The radio emission from WR140 consists of a mixture of both optically thick and thin region of the cloud. The radio flux variation of WR140 comes from two sources of emission:

1. Thermal radio emission from WR stellar wind.
2. Production of synchrotron radiation/non-thermal in the wind collision region (WCR).

From both of these sources, in terms of the orbital phase, ϕ, the radio flux can be expressed as:

$$S_\nu(\phi) = S_{th} \left(\frac{\nu}{\nu_0}\right)^{+0.6} + S_{NT}(\phi) \left(\frac{\nu}{\nu_0}\right)^{\alpha} e^{-\tau_{ff}(\phi)}. \tag{4.3}$$

where $S_\nu(\phi)$ is the total observed flux, S_{th} is the thermal flux, S_{NT} is the non-thermal flux, ν is the observed frequency, ν_0 is the frequency at 1 GHz and τ_{ff} is the free-free optical depth given by:

$$\tau_{ff} = \left(CT^{-1.35}\right) \nu^{-2.1} EM \tag{4.4}$$

where C is a constant given by 3.014×10^{-2}, and T is the temperature of the cloud.

The first term of the model is the *thermal* component where the radio flux scales as $S_\nu \propto \nu^\alpha$ while the second term of the model is dedicated to the *non-thermal* component of the radio emission.

In order to calculate the thermal component of the radio flux variation, we col-

Table 4.1: The radio data taken from Dougherty et al. (2005) at $\phi = 0.974$. At this particular phase, the data is regarded as the thermal component of WR140 as the spectrum exhibit a positive spectral index, α. We fitted the data to a form of $S_\nu \propto \nu^\alpha$ using several Python fitting packages. See Fig. 4.5 for the final `curve_fit` thermal fittings.

Frequency (GHz)	Flux (mJy)	σ Flux (mJy)
1.5	0.62	0.07
4.9	1.66	0.05
8.4	2.64	0.06
15.0*	3.30*	0.30*
22.0	5.00	0.11

* Data taken from White and Becker (1995) due to the point was not being observed by Dougherty et al. (2005).

lected the radio data from Dougherty et al. (2005) at $\phi = 0.974$ shown in Table 4.1. From the radio observation made by Dougherty et al. (2005), the radio flux at 15.0 GHz was not being observed, so a value from White and Becker (1995) at the phase of $\phi = 0.975$ is being used.

The radio flux was fitted to scale $S_\nu \propto \nu^\alpha$ using several fittings packages in Python, namely `curve_fit`, `polyfit1d`, and `Orthogonal Distance Regression (ODR)`. `curve_fit` and `polyfit1d` package gave the same value after fittings while the `ODR` gave a slightly different fitting value but with a huge error. We chose the value from the `curve_fit` as the fitting package returned smallest error and utilises the power law function definition while fitting the data. The best-fit graph is shown in Fig. 4.5. At phase $\phi = 0.974$, the spectrum have a best-fit spectral index of $\alpha = +0.724 \pm 0.04$ and the thermal flux of $S_{ther} = 0.538 \pm 0.131$ mJy. The spectral index value is noted to be a little steeper than the theoretical value $\sim +0.6$, but this value is consistent with the published value from Dougherty et al. (2005) and the thermal emission component by the WR stellar winds in WR146 system which scales as $S_\nu \propto \nu^{+0.78}$ (Williams et al., 1996).

The non-thermal component of the spectra can be calculated by subtracting the thermal spectra (at $\phi = 0.974$) from the total flux assuming the thermal emission is

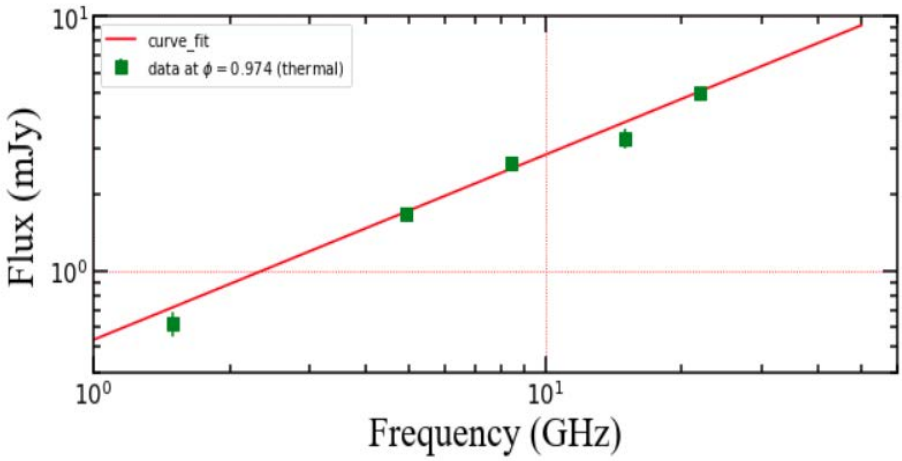

Figure 4.5: The radio data at $\phi = 0.974$ plotted on a log axis. The best-fit line is drawn on the graph in red solid line. Note that some of the errors are smaller than the data marker. From the `curve_fit`, the best-fit value of the spectral index, $\alpha = +0.724 \pm 0.04$ and the value of the thermal flux, $S_{ther} = 0.538 \pm 0.131$ mJy. The spectral index, α is consistent with the published value from Dougherty et al. (2005) indicating that the radio spectra at $\phi = 0.974$ is thermal.

constant throughout the orbit. We utilised the wealth of WR140 data at different frequencies in Fig. 4.4(C) to obtain the NT radio spectra, shown in Fig. 4.6. The NT component for each radio flux is given by:

$$S_{NT}(\phi) = S_\nu - C\nu^\alpha, \tag{4.5}$$

where $C = 0.538$ mJy and $\alpha = +0.724$.

To display the NT radio spectra in a useful way, we plotted the NT spectra as a function of frequency at each observed phase where the data is available from Dougherty et al. (2005), as shown in Fig. 4.7. The focused phases range from $\phi = 0.670$ to $\phi = 0.974$, where radio spectra at $\phi = 0.974$ represents the thermal radio spectrum.

In order to better portray the NT radio emission, we plotted the NT radio data at $\phi = 0.954$ just for convenience, as this phase is the last NT phase before $\phi = 0.974$, which is thermal. The single emission measure model is plotted against the NT data as presented in Fig. 4.8, but it fails to fit the data, especially at low frequencies.

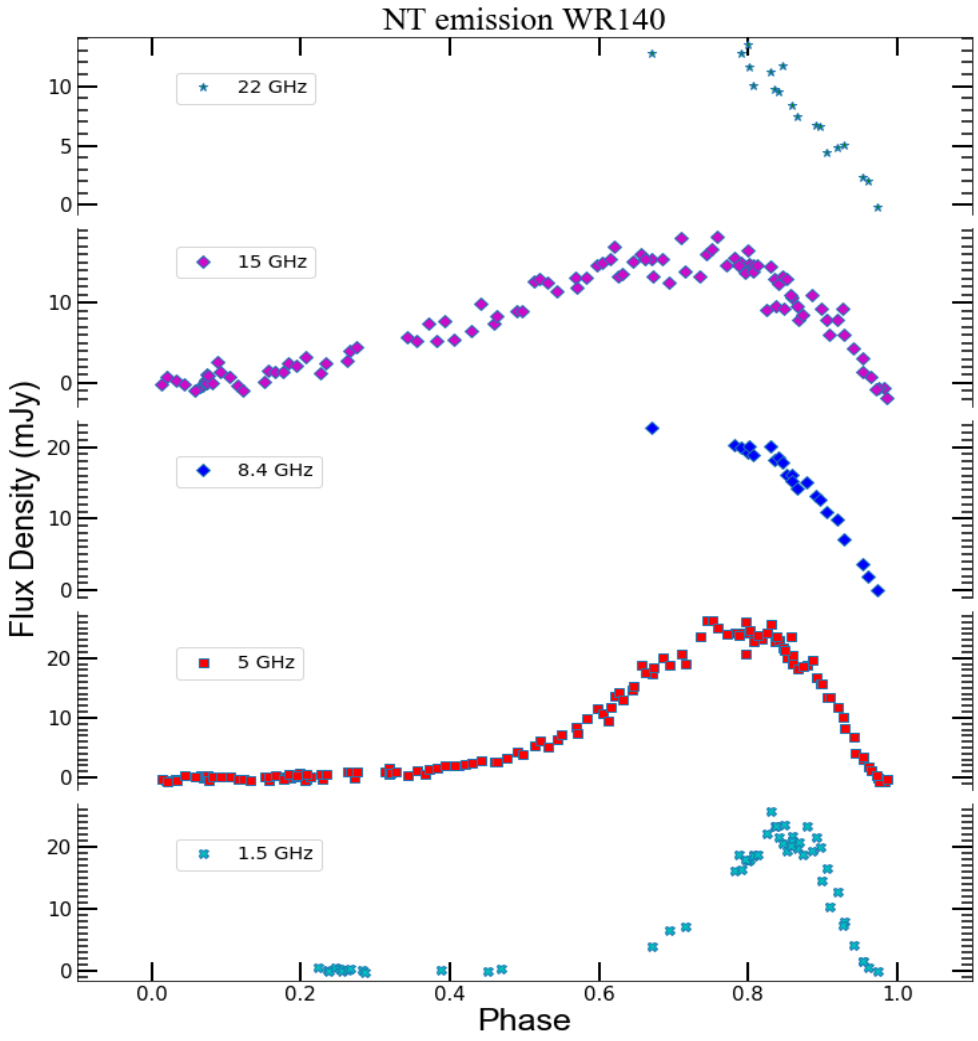

Figure 4.6: The synchrotron emission was extracted from the total flux by subtracting the thermal component ($S_{ther} = 0.538\,\nu^{+0.724}$ (mJy)). The thermal emission was assumed to be constant throughout the orbit. The non-thermal flux was observed at 1.5, 5.0, 8.4, 15.0, and 22.0 GHz. Fuller data points can be seen at 5.0 and 15.0 GHz, also when approaching the periastron compared to the scarcity of data somewhere at apastron.

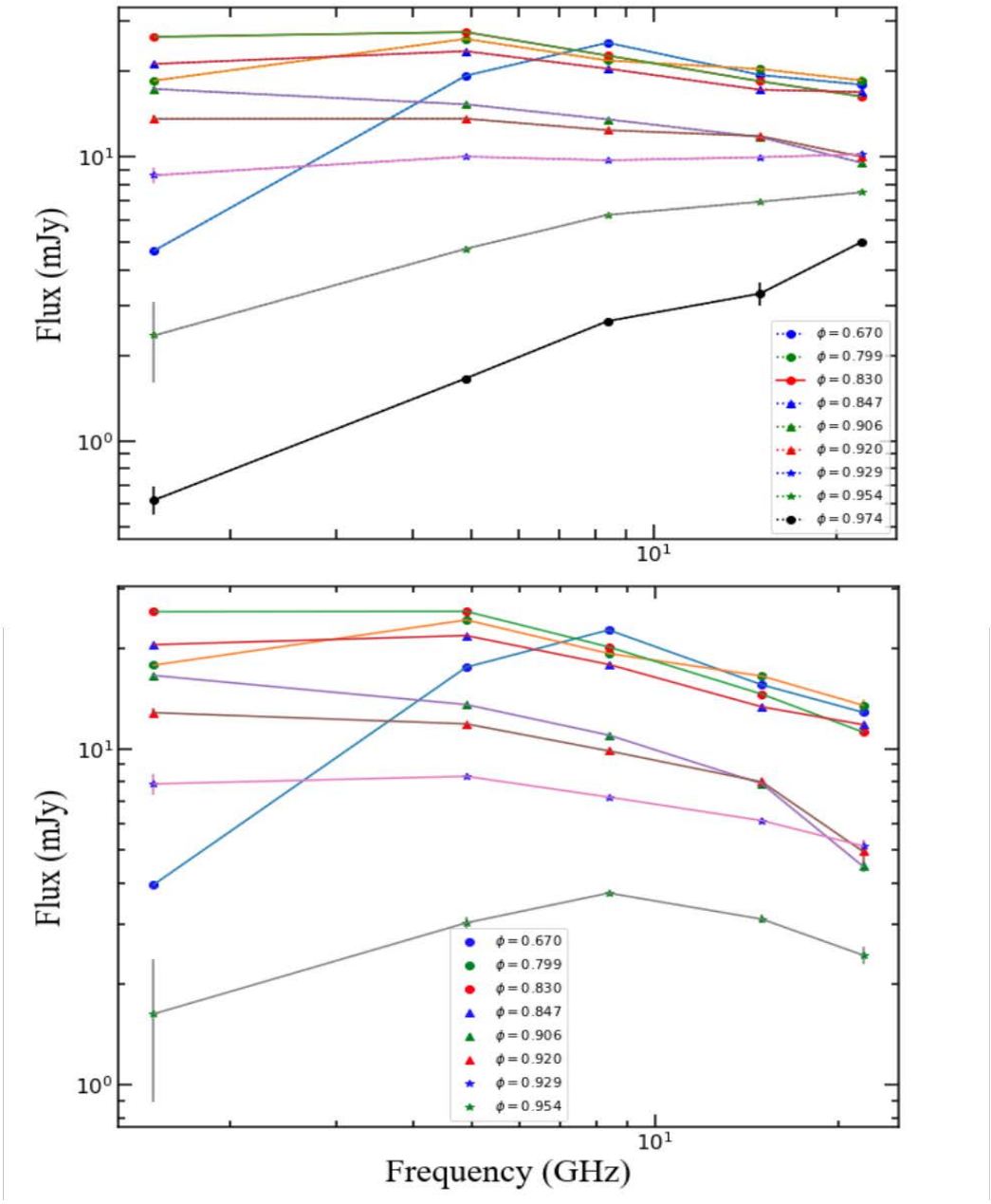

Figure 4.7: Top panel: The observed radio flux at 1.5, 4.9, 8.4, 15.0, and 22.0 GHz at several different phases ranging from $\phi = 0.670$ to $\phi = 0.974$. These observed radio data were taken from Dougherty et al. (2005). The radio spectra at $\phi = 0.974$ were assumed to be thermal as the spectral index, $\alpha \sim +0.7$. The radio data at 15.0 GHz was not observed by Dougherty et al. (2005), so we took the data from White and Becker (1995) at a similar phase $\sim \phi = 0.975$.
Bottom panel: The non-thermal spectra at different observed phase ($\phi = 0.670$ to $\phi = 0.954$) obtained by subtracting the thermal spectra from the power law fittings ($S_{ther} = 0.538\,\nu^{+0.724}$). The thermal component is assumed to be constant throughout the orbit.

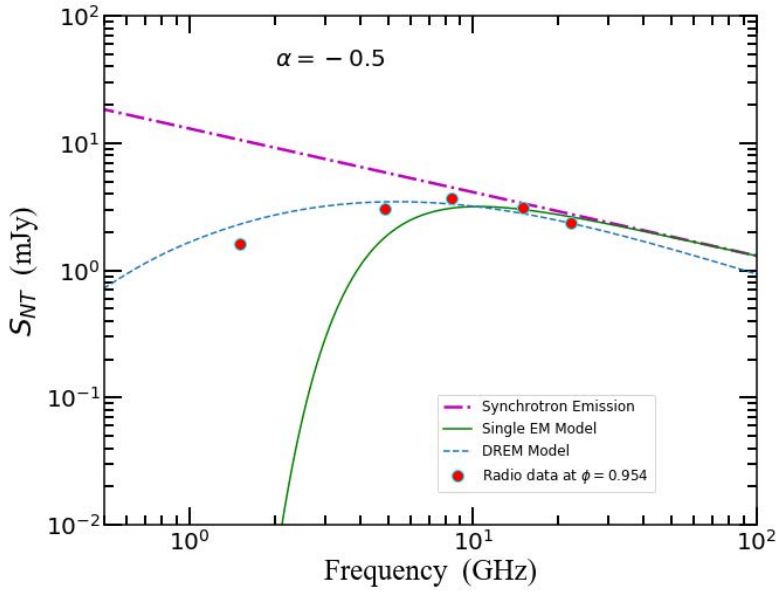

Figure 4.8: The comparison of the single Emission Measure (EM) Model in the solid green line and the Distributed Radio Emission Measure (DREM) Model in the dotted blue line. As can be seen from the figure, the DREM model can fit the radio data better especially at lower frequencies. The purple dash-dot line represents the synchrotron emission with the spectral index, $\alpha = -0.5$.

Therefore, we introduced the Distributed Radio Emission Measure (DREM) model to better capture the NT spectral shape.

4.5 The DREM Model

The DREM model is slightly different from the single emission measure model. DREM model regards the non-thermal emission coming from the wind collision region (WCR) as normally distributed where the centre of the WCR emits higher non-thermal flux as shown in Fig. 4.9. From the high-resolution VLBA observation by Dougherty et al. (2005), the WCR is resulting from a distributed emission measure. The lines-of-sight traverse different areas, as illustrated in the cartoon drawing (Fig. 4.9). The lines-of-sight to the apex (LOS2) may be thick, but there are a considerable amount of thin emissions coming from the downstream flow of

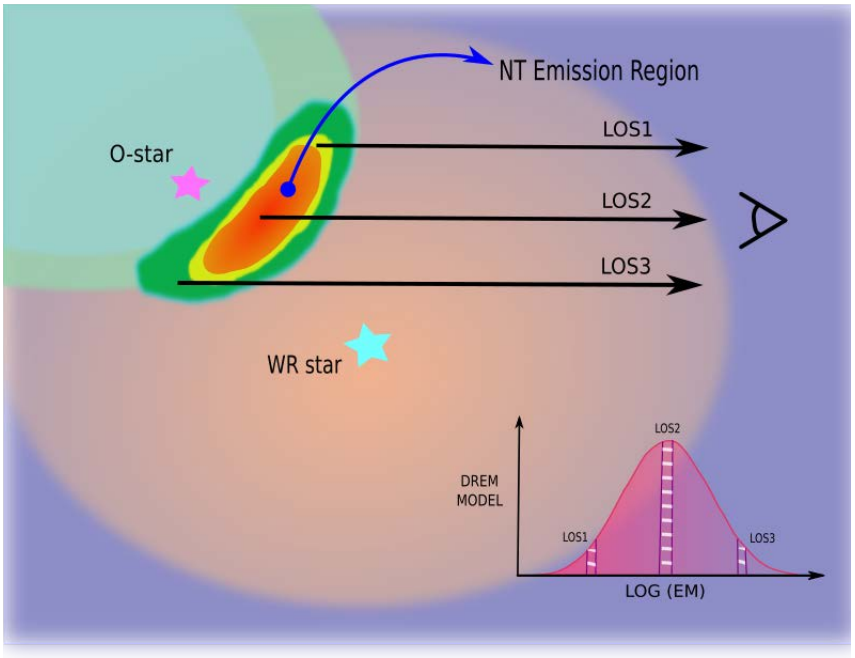

Figure 4.9: The author's illustration on the non-thermal emission region between the two star in WR140 system with different lines-of-sight traverse different areas. The radio emission measure is assumed to be normally distributed with the highest EM value originated from the centre of the WCR.

the winds (e.g. LOS1 & LOS3). Hence, the emission from the WCR is a mixture of both optically thin and thick emission.

The DREM Model consists of four parameters: the radio flux when there is no absorption is happen given by S_0, the spectral index, α, the mean emission measure, EM and the standard deviation of the emission measure, σEM. The DREM model can be expressed as:

$$S_0 \left(\frac{\nu}{\nu_0}\right)^{\alpha} e^{-\tau_{ff}}, \tag{4.6}$$

where the free-free opacity, τ_{ff} is given by:

$$\tau_{ff} = \left(CT^{-1.35}\right) \nu^{-2.1} EM. \tag{4.7}$$

To capture the spectral shape and explain the radio spectra, the DREM model needs to be fitted to the non-thermal radio data. There were several fitting routines performed in attempt to fit the data such as `curve_fit`, `polyfit` and `lmfit`. However,

Table 4.2: The best-fit values for each DREM model parameter at each observed phase was determined using the Markov chain Monte Carlo (MCMC) method and by searching the minimum χ^2 using a mesh grid search. Some of the minimum χ^2 values are large due to very small errors on the observation data.

Phase (ϕ)	S_0 (mJy)	α	EM	σEM	Minimum χ^2
0.670	636.2	−1.14	8.48	0.68	270
0.799	540.0	−1.08	8.47	1.03	115
0.830	523.9	−1.13	8.39	1.08	38
0.847	537.0	−1.18	8.39	0.98	85
0.857	307.0	−1.10	8.10	1.04	0.65
0.865	299.0	−1.13	8.10	1.95	4.07
0.885	188.1	−1.03	7.76	1.07	95.61
0.897	205.0	−1.06	7.92	0.92	1.54
0.906	200.3	−1.11	7.96	0.98	62
0.920	212.5	−1.11	8.13	0.99	27
0.929	200.5	−1.13	8.35	0.98	37
0.954	205.4	−1.28	8.78	0.77	2.12

these packages have failed to fit the data accurately because of the lack of available data points against the number of parameters.

As an alternative, the Markov chain Monte Carlo (MCMC) method was used together with the manual search of the minimum χ^2 in a mesh grid. We have successfully fitted the NT radio data and the best-fit values for the DREM model's parameters are listed in Table 4.2 together with the minimum χ^2 values obtained for every observed phase. For the clarity, the best-fit DREM model for each observed phase is plotted with their corresponding NT radio spectra as depicted in Fig. 4.10. There are only 12 observed phases that have all the 5 different frequencies due to the lack of radio observations at high frequency, specifically at 22 GHz.

4.6 Discussions

As detailed in Section 4.4 the thermal flux was calculated using $S_{ther} = 0.538\,\nu^{+0.724}$ where it assumed to be constant throughout the orbit. To obtain the non-thermal flux from the WR140 light curves as shown in Fig. 4.4 (C), the thermal component

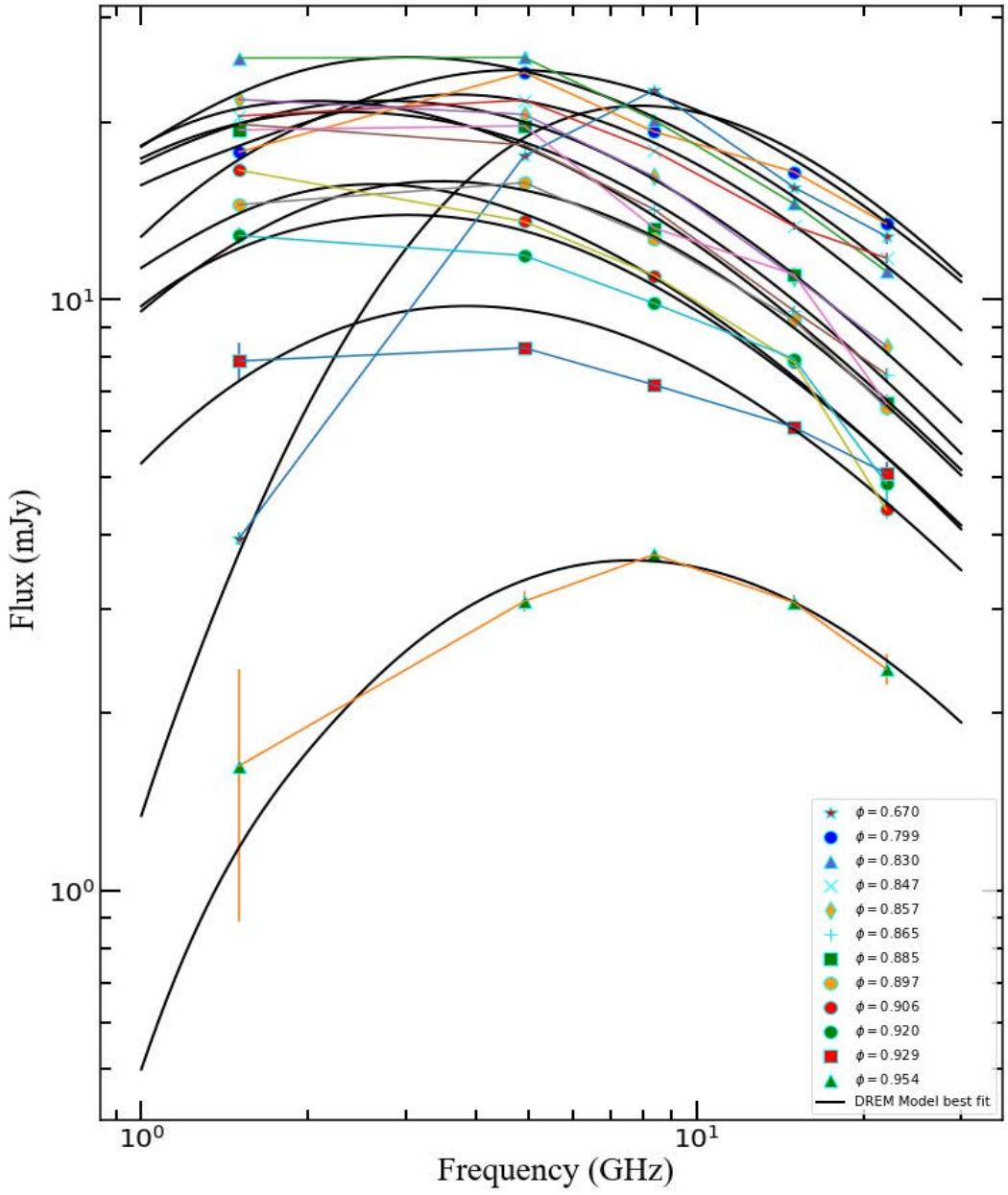

Figure 4.10: The black solid line indicates the DREM model best-fit at several observed phase. The minimum value of χ^2 was determined using the grid searching method in Python. The value of each χ^2 from every observed spectra was shown in Table 4.2.

was subtracted from the total flux. The full non-thermal emission light curves at frequencies 1.5, 4.9, 8.4, 15.0, and 22.0 GHz were displayed in Fig. 4.6. The non-thermal emission displayed involved data from Dougherty et al. (2005), White and Becker (1995), Williams et al. (1994); Williams et al. (1990). The non-thermal emission shows a fuller and denser emission throughout the orbit.

From the non-thermal emission of WR140, we calculated the spectral index for every possible frequency ratio to be able to observe the pattern and the relationship between the phase and the spectral index as shown in Fig. 4.11. The spectral index was calculated using:

$$\alpha = \frac{log(S_{\nu_1}/S_{\nu_2})}{log(\nu_1/\nu_2)}. \tag{4.8}$$

From Fig. 4.11, the spectral index, α for the available frequency ratio $\alpha^{4.9}_{15.0}$ and $\alpha^{4.9}_{1.4}$ are generally positive at lower phases, indicating the source is faint, the wind is thick, thus emitting thermal emission. As the stars move closer to the periastron, the spectral index becomes more negative, and its at its minimum around $\phi = 0.85$ before it rises sharply. The negative spectral index implies that the wind is optically thin, allowing the majority of the NT emission to escape and be detected.

In order to investigate the relationship between the spectral index, α and the mean radio emission measure, EM, synthetic spectra were generated due to the lack of data at other phases. We generated synthetic data at lower frequencies, namely at 8.5, 4.9, and 1.5 GHz, due to the denser light-curves. We repeated the same method of calculating the spectral index using Eqn. 4.8. The spectral index as a function of the mean emission measure was plotted in Fig. 4.12. At lower mean emission measure, the spectral index shows negative numbers as the emission from the WCR becomes more non-thermal, i.e. optically thin wind. As the mean emission measure increases, the spectral index turns positive as the source becomes faint due to the thick wind.

From the best-fit parameters listed in Table 4.2, we plotted the mean radio

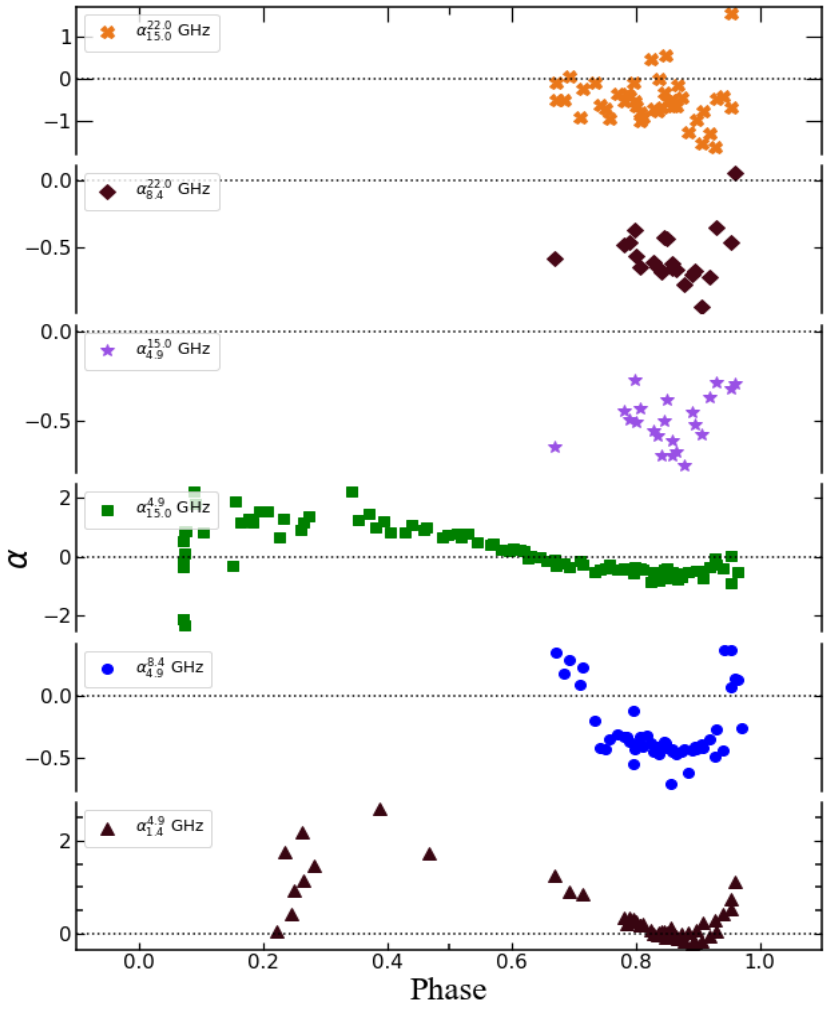

Figure 4.11: The spectral index, α versus the phase of WR140. The spectral index is positive at the lower phase, indicating that the source is faint, the wind is thick, thus emitting thermal emission. Approaching periastron, the spectral index becomes more negative, at its minimum around $\phi = 0.85$ and rises sharply right before periastron at $\phi = 1$.

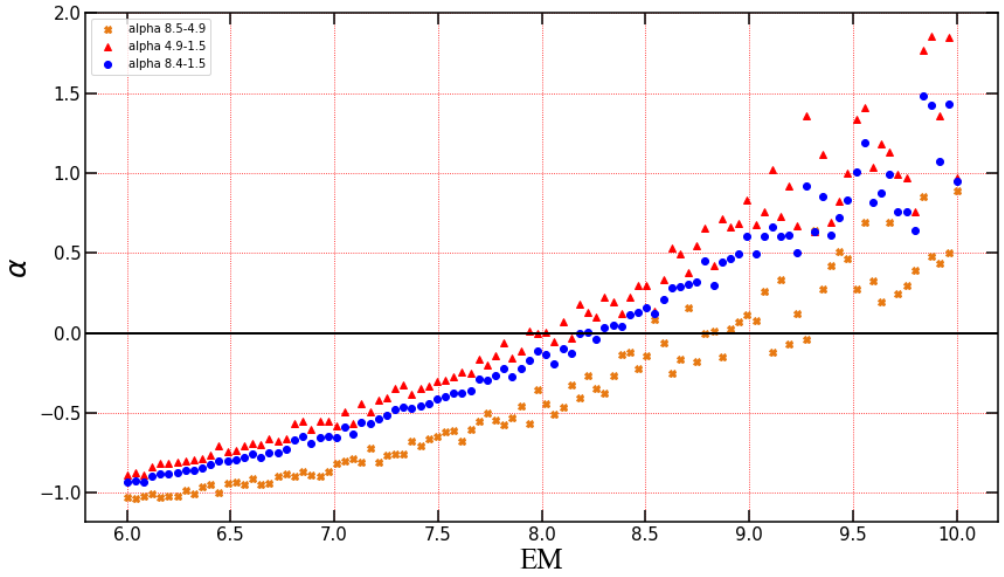

Figure 4.12: The Relationship between Emission Measure and Spectral Index calculated from the DREM model. The ratios for spectral index calculated were for the lower frequencies due to the denser data points. From this diagram, as EM increases, the α changed from negative to positive.

emission measure, EM as a function of phase depicted in Fig. 4.13. The emission measure exhibits high values at lower phases, indicating that the wind is dense and the source is faint. Here, the NT emission suffers from free-free absorption, and the radio flux is just thermal. The EM begins to fall at $\phi \sim 0.83$ and reaches its lowest point around $\phi \sim 0.88$. The low radio EM values imply that the wind is thin and most of the NT emission escapes. The less-dense wind is associated with the WC7 conjunction, which occurs when the WC7-star is behind the O-star so that the line-of-sight encounters less dense wind from the O-star. As the orbit progresses, the radio EM rise sharply as the line-of-sight encounters the dense unshocked wind of the WR-star.

A 3D smoothed particle hydrodynamical simulation of WR140 by Chris Russell from Pollock A.M.T. et al. 2021, ApJ, submitted (see Fig. 4.14), has shown that the observer's line-of-sight will start to see a less dense wind originating from the O-star at 500 days ($\phi = 0.827$) before the periastron. Here, the NT radio emission will

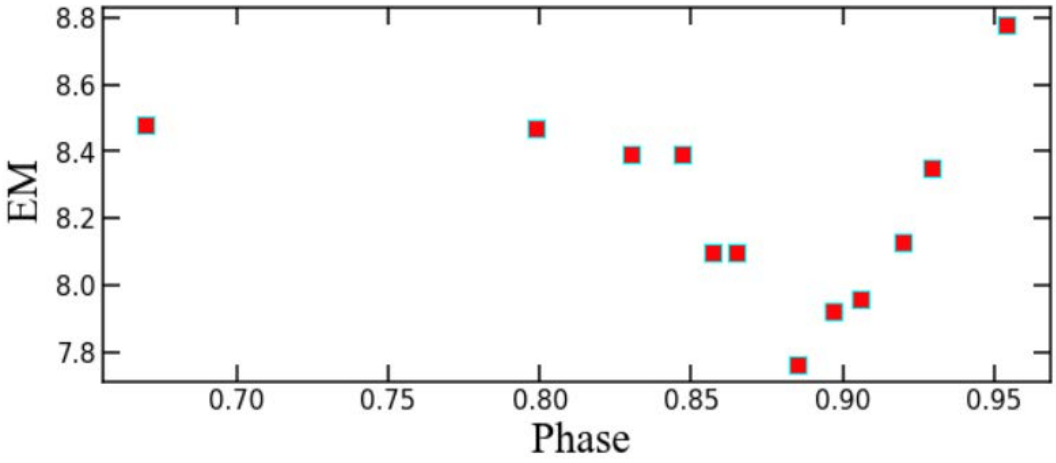

Figure 4.13: The DREM model has successfully fitted the NT radio data to present the mean emission measure, EM as a function of phase. Radio EM starts at a large value at lower phases when the radio flux is just thermal. As the orbit progresses, the radio EM dipped around $\phi = 0.88$ indicating that the line-of-sight encounter less-dense O-star wind. Approaching the periastron, the radio EM rises rapidly making the NT emission suffer huge absorption by the thicker wind from the WR-star. This result is in agreement with the NT emission region observation using the high-resolution VLBA by Dougherty et al. (2005) where the NT emission region can no longer be detected after $\phi = 0.954$.

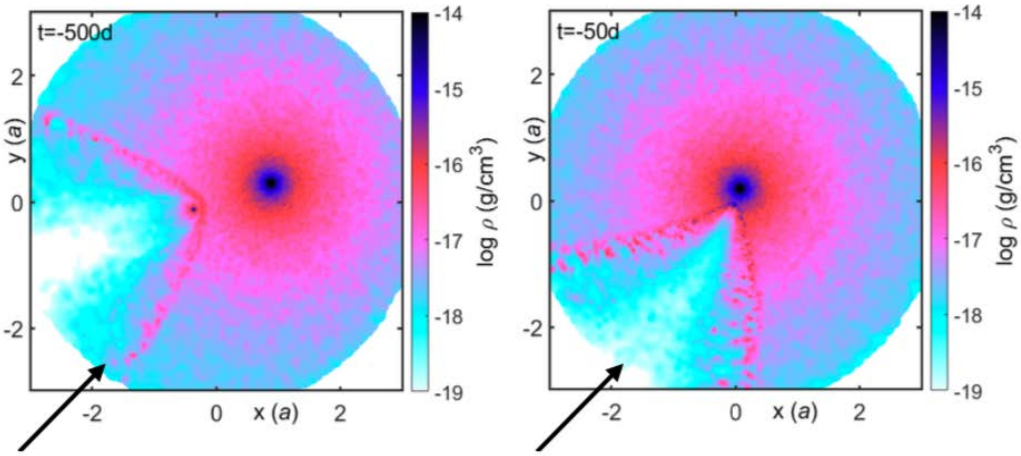

Figure 4.14: Left Panel: The line-of-sight indicated by the black arrow encounters the shocked wind at 500 days before the periastron, which is at $\phi = 0.827$. Right panel: We look through the thinner wind originating from the O-star 50 days prior to the periastron ($\phi = 0.983$) shortly before the line-of-sight re-encounter a dense shocked region where the X-ray column, N_H is significant, and radio EM will be very large and block all the NT emission from the WCR. From: Pollock et al. (2021).

mostly escaped the cloud of materials as the radio EM is low. At 50 days prior to the periastron ($\phi = 0.983$), the line-of-sight starts to pass through the dense shocked wind where the X-ray N_H column is significant, and at this time in the orbit, the radio EM will be very large and block all the NT emission from the WCR.

4.6.1 X-ray Column Density

The X-ray column, N_H is defined as:

$$\mathrm{N_H} \equiv \int_{\mathrm{los}} n_{\mathrm{H}}\, dx, \tag{4.9}$$

where n_{H} is the number density of atoms in cm^{-2} along the line of sight, x in cm while the radio EM is defined as:

$$EM \equiv \int_{\mathrm{los}} n_{\mathrm{e}}^2\, dx, \tag{4.10}$$

where n_{e} is the electron number density in cm^{-3} along the line of sight, x in pc.

Approaching periastron, the WCR will be behind the Wolf-Rayet star, and the X-ray column (see Fig. 4.15) is large (around 5×10^{23} cm^{-2}). At a phase of $\phi = 0.954$ (which corresponds to around 133 days before periastron) the radio EM is seen to be rising very sharply (Fig. 4.13), but the X-ray column is still indistinguishable from the interstellar absorption ($< 4.6 \times 10^{21}$ cm^{-2}). Assuming a co-located point source emission region for X-ray and NT radio emission (which we know is not to be the case in terms of a point source, but we do so for simplicity), for a line-of-sight with an impact parameter a to the WR star, the radio emission measure, will scale as $EM \propto 1/a^3$ while the X-ray column will have $N_H \propto 1/a$. Based on these scalings, the radio EM rises much more rapidly than N_H as the periastron is approached, as seen in Fig. 4.15 and 4.13.

WR140 is potentially an excellent laboratory for monitoring the simultaneous rise

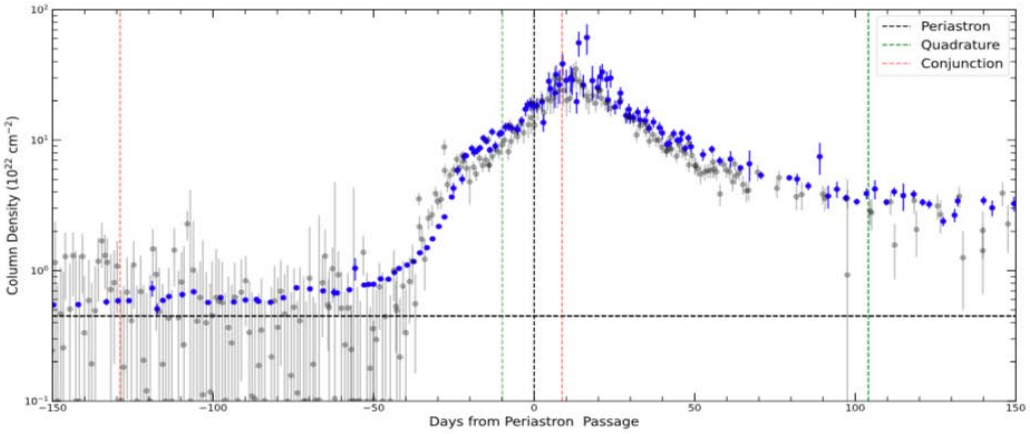

Figure 4.15: X-Ray column density as a function of phase (in days) taken from Pollock et al. (2021) their Figure 7. The grey circles are the observations from the *RXTE*, blue circles are from *Swift XRT* and the green circles are from the *NICER*. The horizontal dash line represents the interstellar medium column, $N_H = 4.6 \times 10^{21}$ cm^{-2}. The X-ray column is indistinguishable from the interstellar medium column prior to the periastron ($< \phi = 0.948$) and only starts to rise at 50 days before the periastron ($\phi = 0.983$). However, compare to the radio EM in Fig. 4.13, the emission measure starts rising around $\phi = 0.88$.

of the radio EM and X-ray N_H, which will tell us a lot about the wind structure and clumping as the dependence on clumping differs for X-ray and radio absorption - the X-ray is a sum over n (Eqn. 4.9), while for the radio EM is a sum over n^2 (Eqn. 4.10). However, due to the large radio EM closer to the periastron, we will need higher frequency radio observations through periastron so that we can still measure the radio EM at the same epochs as we can measure the X-ray column.

4.7 Conclusions

This chapter has collected WR140 archives radio data observed using various radio interferometers at frequency ranges from 1.5 GHz to 22 GHz. We analysed the data by subtracting the thermal component from the total radio flux to obtain the NT radio spectra. We introduced a simple yet effective Distributed Radio Emission Measure (DREM) model to fit the NT radio spectra. We have successfully fit the

model parameters to our radio data and display the radio emission measure profile as a function of phase. The radio emission measure starts to decrease at around $\phi \sim 0.83$ and reached its minima at $\phi \sim 0.88$. Here, the NT emission region was detected by the VLBA as the observer sees through the less-dense wind from the O-star. Then, the radio EM increases sharply just before periastron, where the line-of-sight enters the dense WC7 wind. We also compared the radio EM with the X-ray column density and found that the radio EM starts to rise earlier than the X-ray column as the orbit progresses. As confirmed by Dougherty et al. (2005), the NT emission is blocked because the radio EM will be very large at periastron and will no longer be detected. In the future, we will need higher frequency radio observations to compare the radio EM with the X-ray column to and through the periastron in order to analyse the wind structure of WR140.

5 | Low Frequencies New Observations of WR140 using the uGMRT

"Computers can't find the unexpected, but people can when they eyeball the data."

–Debra Fischer.

Chapter Summary

We present new results for new uGMRT observations of the archetypal colliding wind binary WR140. These observations were taken in November 2019, at a phase of $\phi = 0.367$ (about 3 years after the most recent periastron event and 1 year before the apastron passage) and are the most sensitive low-frequency observations of WR140. The observations were in uGMRT Band 3, 4 and 5 and covered a frequency range of $0.3 - 1.45$ GHz. We analysed the results, and the resulting spectrum is consistent with thermal emission, with a slope of $\alpha = +0.59 \pm 0.06$, where the radio flux scales as $S_\nu \propto \nu^\alpha$. We also discuss the broadband thermal spectrum of WR140.

5.1 Introduction

Massive stars are often found in binary or multiple systems with other massive stars, where the strong winds of both stars collide, which is known as the Colliding Wind Binaries (CWBs). These winds are extremely energetic and are critical drivers of feedback processes within star clusters or starburst galaxies (Leitherer et al., 1999). The high mass-loss rate of these massive stars ($\dot{M} \sim 10^{-7} - 10^{-4}$ $M_{\odot}$ yr^{-1}) is due to the fact that they have dense, ionised stellar winds with terminal velocities of $\nu_{\infty} \sim 500 - 4000$ km s^{-1}. The winds are free-free emitters, resulting in a positive spectral index of $\alpha \sim +0.6$ for the thermal spectrum which includes contributions from both optically thin and optically thick regions. This thermal emission has been used extensively in calculating mass-loss rates (Wright and Barlow, 1975).

Non-thermal (NT) emission (synchrotron emission), is produced by electrons accelerated by shocks inside the winds in many massive stars, with the NT component having a flat or negative spectral index. A schematic representation of the composite thermal and non-thermal radio spectrum of a massive star is demonstrated in Fig. 5.1. In this diagram, the NT emission suffers from the free-free absorption in the wind at high frequency region. So, low-frequency observations is the ideal place to study thermal emission.

There are relatively few observations of massive stars at < 1.4 GHz. The review by Benaglia (2010) listed only 1 OB star with such a detection (Cyg OB2 No. 8 by Gunawan et al. (2003)). 3 OB stars have been serendipitously detected at 610 MHz, during a GMRT observation of the Cyg OB2 region by Marti et al. (2007) which were the Cyg OB2 No.5, No.9 and No.12, with fluxes of ~ 1 mJy. The GMRT has also detected WR146 and WR147 at low frequencies, along with the O supergiant, BD+43 3654 (Brookes, 2016).

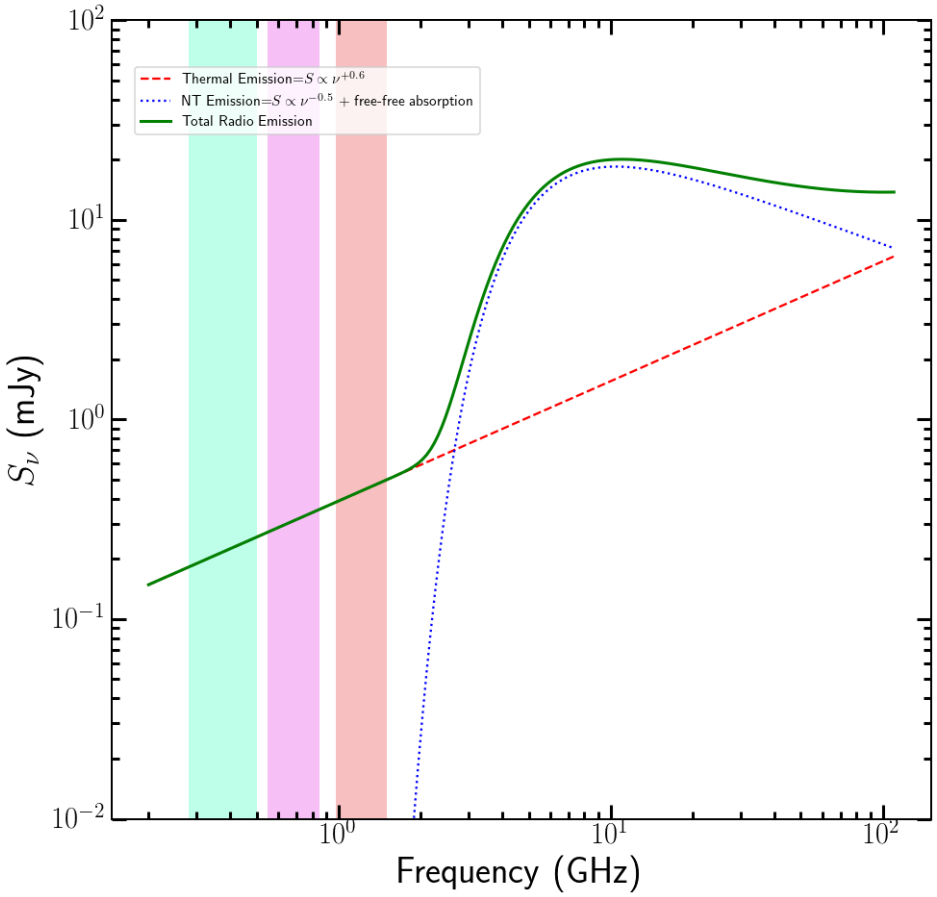

Figure 5.1: A schematic representation of the thermal and NT radio spectrum of WR140. The NT emission from the wind collision region undergoes free-free absorption in the stellar winds. This means that the low-frequency portion of the spectra may be the best place to see just thermal emission from the WR wind. The uGMRT bands are illustrated by the colour strips as such: band 3 (turquoise), band 4 (pink) and band 5 (coral).

5.1.1 WR140

WR140 is a phenomenal colliding wind binary, and comprises a WC7 Wolf-Rayet star and an O5 companion star with a highly eccentric orbit ($e \sim 0.8993$) with a period of 7.9 years. From SIMBAD, WR140 system in J2000 coordinates is (α = 20 20 27.98, δ = +43 51 16.29) and is located at 1.64 kpc, (Thomas et al., 2021). Refer to Table 5.1 for the assumed WR140 system parameters. Both stars have fast radiatively driven winds ($\nu_\infty \sim 3000$ km s $^{-1}$). WR140 is a prolific dust producer around periastron passage (Williams, 2011a) and a detailed study of this dust production will be undertaken with NASA's James Webb Space Telescope (JWST) around the next periastron passage in 2024 (ERS Program No. 1349 - PI Ryan Lau). WR140 radio emission comes from two sources – thermal radio emission predominantly from the Wolf-Rayet stellar wind and highly variable non-thermal radio emission (synchrotron radiation) from the wind collision region (WCR). For more WR140 details, please refer to Section 4.2.

There were several radio observations performed to observe WR140 including the in-depth studies by White and Becker (1995), hereafter WB95, and Dougherty et al. (2005). WB95 monitored the star for the full 8-year cycle with the VLA, and the observations show huge variations, with the radio emission rising sharply close to (but before) periastron ($\phi = 0$). As the stars moved closer, the wind collision increases in strength, and the NT emission also increases. Dougherty et al. (2005) reported a high-resolution VLBA observations covering the phases closer to the periastron at 22.0 GHz (K-band), 8.4 GHz (X-band) and 1.67 GHz (L-band) where the NT emission was coming from the WCR located between the two stars and the NT region is observed to move as the orbit progressed. Another radio observations by the Westerbork Synthesis Radio Telescope (WSRT) in the Netherlands were observed by Williams et al. (1990) and Williams et al. (1994) at the same frequencies observed by White and Becker (1995). The WR140 light-curves from these studies

Table 5.1: WR140 Basic System parameters.

Parameter	Value	Unit	Ref.
System:			
Primary spectral type	WC7p		S11
Secondary spectral type	O5		S11
Distance	$d = 1.64^{+0.11}_{-0.09}$	kpc	RC20-I
Distance	$d = 1.67 \pm 0.03$	kpc	M11 + F11
Distance	$d = 1.518 \pm 0.021$	kpc	T21
Semi-major axis	$a = 8.922 \pm 0.067$	mas	T21
Eccentricity	$e = 0.8993 \pm 0.0013$		T21
Orbital Inclination	$i = 119.07 \pm 0.88$	$\circ$	T21
Period	2896.35 ± 0.20	days	M11 + F11
Period	2895.00 ± 0.29	days	T21
Wind-Momentum Ratio	$\eta = 0.039 \pm 0.016$		F11
Wind-Momentum Ratio	$\eta = 0.02$		PD06
Primary Wolf-Rayet Star:			
$T_{\rm eff1}$	70000	K	W11
v_{∞_1}	2860	km s^{-1}	W90
R_{WR}	2	$\mathrm{R}_\odot$	W90
M_{WR}	10.31 ± 0.45	$\mathrm{M}_\odot$	T21
$\dot{M}_{1.3kpc}$	5.3×10^{-5}	$\mathrm{M}_\odot\mathrm{yr}^{-1}$	W90
$\dot{M}_{1.85kpc}$	4.3×10^{-5}	$\mathrm{M}_\odot\mathrm{yr}^{-1}$	PD06
$\dot{M}_{1.67kpc}$	3×10^{-5}	$\mathrm{M}_\odot\mathrm{yr}^{-1}$	F11
Secondary O-star:			
$T_{\rm eff2}$	35000	K	W11
v_{∞_2}	3100	km s^{-1}	SG01
R_O	26	$\mathrm{R}_\odot$	W90
M_O	29.27 ± 1.14	$\mathrm{M}_\odot$	T21
$\dot{M}_{1.85kpc}$	8×10^{-7}	$\mathrm{M}_\odot\mathrm{yr}^{-1}$	PD06
$\dot{M}_{1.67kpc}$	1×10^{-7}	$\mathrm{M}_\odot\mathrm{yr}^{-1}$	F11

* S11: Shenavrin et al. (2011), F11: Fahed et al. (2011), M11: Monnier et al. (2011), T21: Thomas et al. (2021), W11: Williams (2011b), RC20-I: Rate and Crowther (2020), W90: Williams et al. (1990), SG01: Setia Gunawan et al. (2001), PD06: Pittard and Dougherty (2006).

were plotted in Fig. 5.2 showing the frequency dependent variations as a function of phase. Various previous data of WR140 has been discussed in Section 4.3.

None of these studies considered the low-frequency domain; hence this study is the start of a program to monitor WR140 through the key bits of the next cycle leading up to and through the periastron in 2024. The uGMRT observations utilise the new broadband receivers in band 3 (260-500 MHz), band 4 (550-850 MHz) and band 5 (980-1500MHz). The uGMRT campaign will be supplemented with high-frequency VLBI observations at 22 GHz using the East Asian VLBI Network (EAVN) (see Chapter 6).

5.2 The new uGMRT Observations

We conducted the new WR140 low-frequency observations (P.I. Zainol), with the upgraded Giant Metre Radio Telescope (uGMRT), located in Maharastra state, near Pune, India. This radio interferometry facility consists of 30 fully steerable parabolic dishes, each with a diameter of 45 m. The uGMRT array has a basic Y-shaped configuration, with 14 antennas located in the central core region and 16 antennas in the three arms. The shortest baseline is about 100 m and the longest baseline is about 25 km (Gupta et al., 2017). The uGMRT has receivers in 5 bands, covering the frequency region from 0.3–1.5 GHz. Please refer to Section 2.4.4 for more details regarding the uGMRT.

The observations were performed on November 18th and 19th, 2019, with the new broadband receivers, which offers a much broader bandwidth (200 to 400 MHz) compared to the legacy narrow-band setup of 32 MHz bandwidth (Gupta et al., 2017).

The observation spanned over two days, in order to accommodate the 'up-time' of WR140 at the uGMRT. We used a bandwidth of 200 MHz for band 3 and 400 MHz

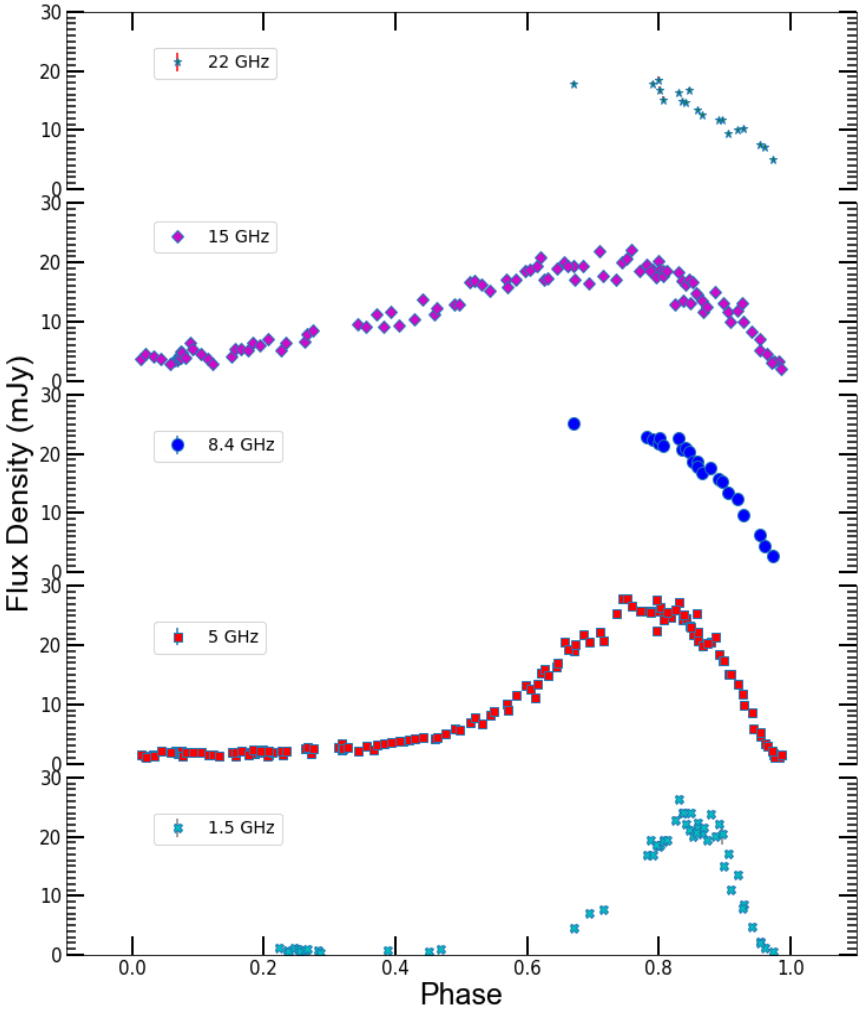

Figure 5.2: The radio emission of WR140 at several wavebands (1.5, 5, 8.4, 15 and 22 GHz) during the orbital cycle between 1978.56 and 2000.89 (please note that is more than one orbital cycle). Periastron passage occurs at $\phi = 0$. The data was taken from Williams et al. (1990), Williams et al. (1994), White and Becker (1995), and Dougherty et al. (2005). The phase for each data point was recalculated using the recent WR140 period (2895.00 $\pm$0.29 from Thomas et al. (2021)). This data illustrates the extreme variability of WR140, with a large rise in flux around $\phi = 0.5 - 0.9$.

Table 5.2: Details of the uGMRT observations of WR140. The observation was spread into two days to accommodate the 'up-time' of WR140. For Band 3, 3C286 was used as it was the only flux calibrator available.

Band	Date	Time (IST)	Bandwidth (MHz)	Duration	Flux Cal	Phase Cal
3	18-Nov-2019	14:00-17:00	200	3 hours	3C286	2052+265
4	18-Nov-2019	18:00-22:00	400	4 hours	3C48	2052+265
5	19-Nov-2019	16:00-20:00	400	4 hours	3C48	2052+265

for band 4 and band 5. For flux and bandpass calibrations, we use the usual 3C48 for band 4 and band 5 while 3C286 for band 3. The flux calibrator was scanned for 30 minutes in each band. 2052+265 was observed as the phase calibrator throughout the whole observation across all three bands to correct for phase and amplitude variations. The phase calibrator was scanned for 8 minutes after every 35 minutes observation of WR140. The summary of the observations is shown in Table 5.2.

A standard routine of data reduction using the Common Astronomy Software Application (CASA) package was implemented to produce continuum spectra. The data in each broadband was carefully flagged to remove bad spectral channels and bad baselines due to Radio Frequency Interference (RFIs). The clean calibrated data from each band was split into sub-bands with the central frequencies at 0.36, 0.44, 0.60, 0.70, 1.15, 1.22, 1.30 and 1.38 GHz. Each sub-bands were imaged separately, implementing a standard imaging routine such as spectral channels averaging, further flagging, and several iterations of self-calibrations to improve the quality of the image and correct for the phases.

5.3 Results of the New uGMRT Observations

The uGMRT observed WR140 at JD 2458806.5 and this corresponds to the orbital phase of $\phi = 0.367$ as shown in Fig.5.3, where we will see mostly through the thick WC7 wind. The orbital phase of the observations is calculated using the new orbit

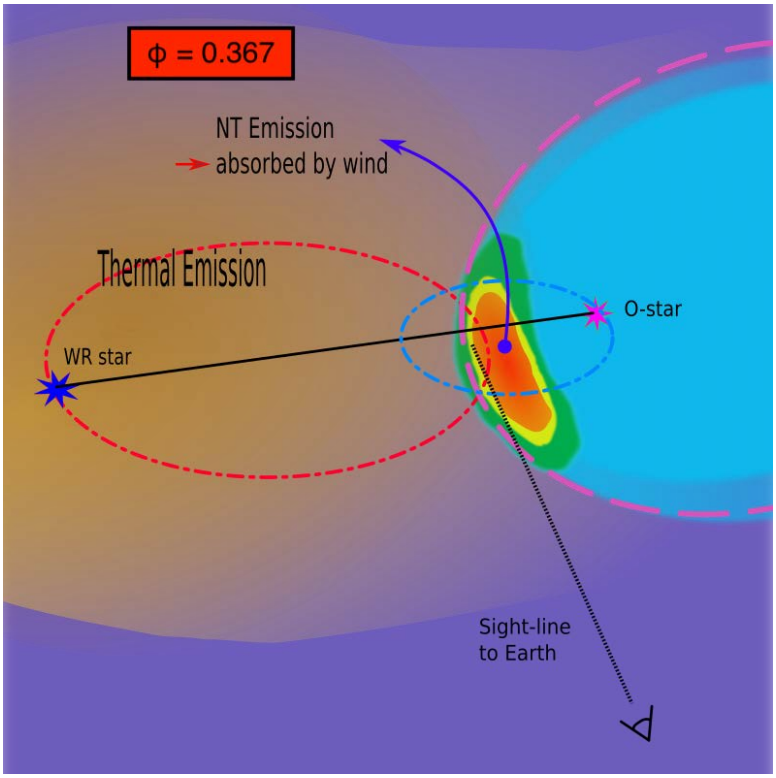

Figure 5.3: An illustration of WR140 system at $\phi = 0.367$, when the observations were made, where the line-of-sight is mostly seeing through the WC7 stellar wind. Also shown are the relative orbits of the WR and O-star. The location of the NT emission associated with the wind collision region (WCR) are shown as the 'bow-shaped' in between the two stars. The phase, $\phi = 0.367$, is about 3 years after the most recent periastron event and 1 year before the upcoming apastron passage.

from Thomas et al. (2021). This paper updated the orbit of WR140 using the new CHARA optical interferometric observations and optical spectral observations. The assumed period of WR140 is now 2895.00 ± 0.29 days, and the eccentricity is 0.8993 ± 0.0013.

For each sub-bands, the integrated flux was obtained from CASA Gaussian Fit procedure assuming the target is a point source. These values of the uGMRT observations and the corresponding bandwidth were presented in Table 5.3 with the noted uncertainty are the rms of the images. The images of these results are shown in Fig. 5.4. The contours are following $-1, 1, 1.4, 2, 2.8, 4, 5.6, 8, 11.3 \times 3\sigma$ except for the image at 0.70 GHz – $\times\sigma$. These new images indicate a clear detection at Band 4 and Band 5 and a noisier image at Band 3 which is the image of WR140 at

Table 5.3: The integrated flux of WR140 observed using the upgraded GMRT.

Frequency (GHz)	Flux (μJy)	Bandwidth (MHz)
0.36	362 ± 154	80
0.44	453 ± 178	80
0.60	516 ± 50	100
0.70	610 ± 40	100
1.15	733 ± 62	78
1.22	759 ± 60	78
1.30	860 ± 65	78
1.38	923 ± 61	78

the longest wavelength up to date.

To find the best-fit spectral index, α for our data, we performed a fitting routine using `curve_fit` from `scipy.org` package in Python. From the fitting, we obtained the value of $\alpha = +0.59 \pm 0.06$ as shown in Fig. 5.5, which is close to the theoretical value, $\alpha \sim +0.6$. From this value, we imply that we are seeing the thermal part of the emission.

5.4 Discussion

We included other WR140 data points that have been observed at radio wavelength at its thermal state as shown in Fig. 5.6 and Fig. 5.8. We also performed a fitting routine to obtain the spectral index, α and compare them with our results. From Fig. 5.6, the 3 data points were taken at the closest phase with our observation ($\sim$ 0.4). The slope for these points is $\alpha = +1.13 \pm 0.01$ and the best-fit for α including our data points is $\alpha = +1.02 \pm 0.02$ which is steeper than the expected value.

We then compared our uGMRT points with results from the high-resolution VLBA observation of WR140 by Dougherty et al. (2005). From their VLBA results which covered orbital phases of $\phi = 0.671$ to $\phi = 0.974$ and at 5 different frequencies

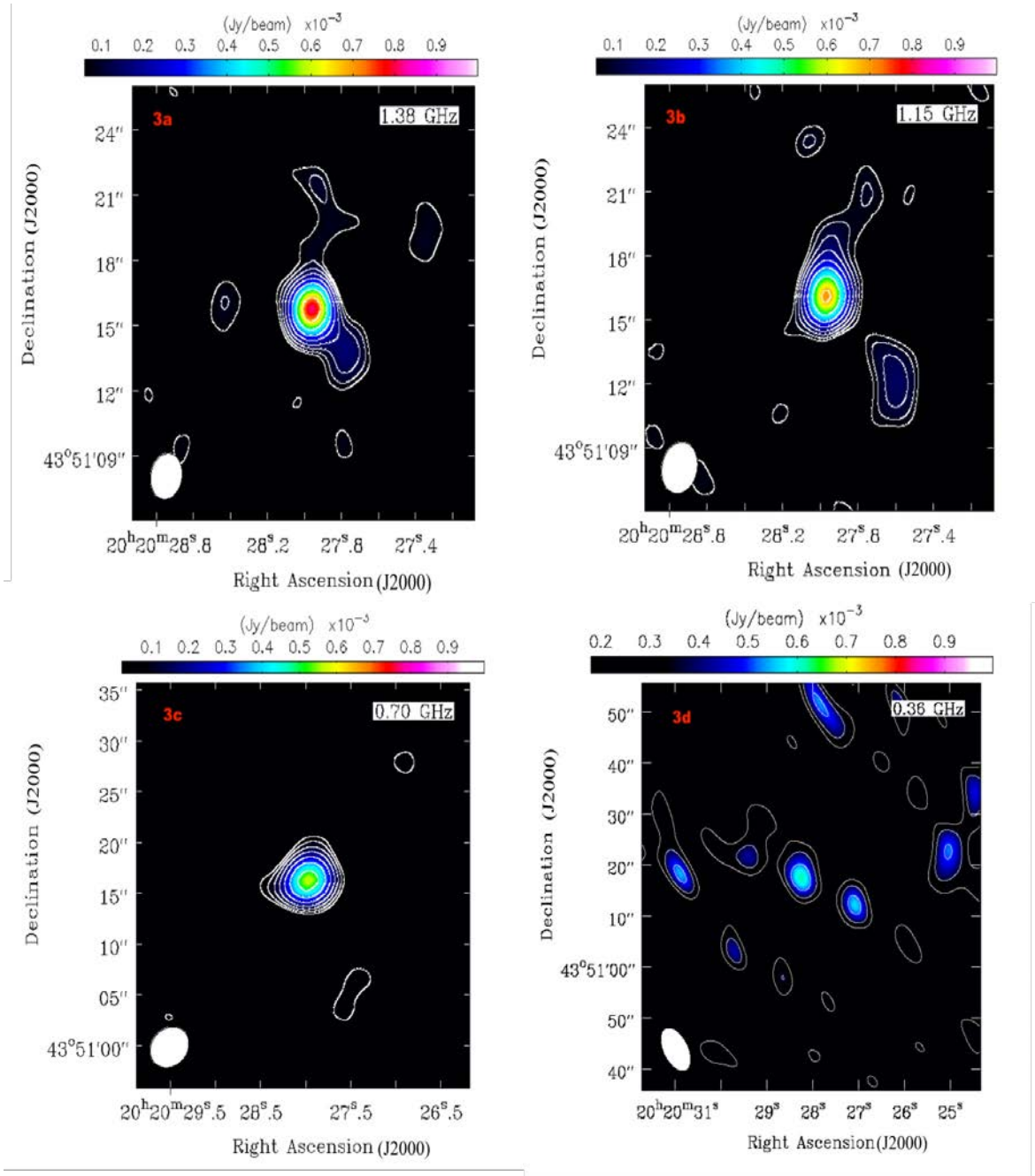

Figure 5.4: WR140 uGMRT images at 1.38, 1.15, 0.70 and 0.36 GHz. The contours for image 3a, 3b and 3d are following $-1, 1, 1.4, 2, 2.8, 4, 5.6, 8, 11.3 \times 3\sigma$ except for the image 3c at 0.70 GHz where the contour is $-1, 1, 1.4, 2, 2.8, 4, 5.6, 8, 11.3 \times \sigma$. The synthetic beam (white solid filled) were shown at the bottom left of the images. The image of WR140 at 0.36 GHz was a lot noisier with $\sim 5\sigma$ detection.

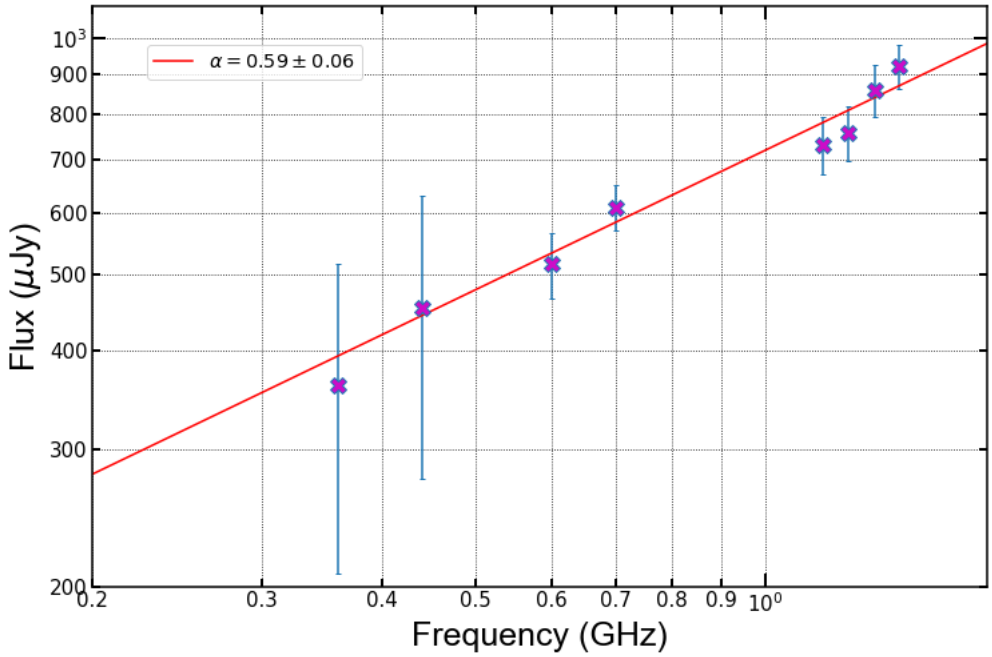

Figure 5.5: The uGMRT observations of WR140 at $\phi = 0.367$, showing the Band 3, Band 4 and Band 5 data. The best-fit power-law model is shown by the solid red line, with a slope of $\alpha = +0.59 \pm 0.06$, indicative of purely thermal free-free emission from the wind of the WR star.

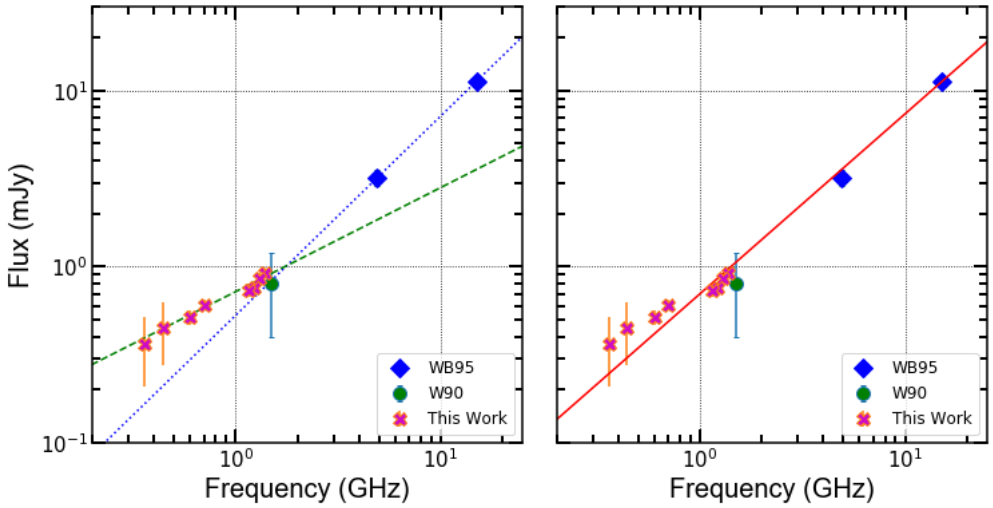

Figure 5.6: The data points of WR140 at $\phi \sim 0.4$ taken from Williams et al. (1990) and White and Becker (1995). Left panel: blue dotted line with the spectral index, $\alpha = +1.13 \pm 0.01$ compared to this uGMRT data points (green dash line, $\alpha = +0.59 \pm 0.06$). Right panel: The best-fit spectral index at $0.3 - 15$ GHz is $\alpha = +1.02 \pm 0.02$. We noted that this spectral index is steeper than the expected spectral index, $\alpha_{exp} \sim +0.6$.

from $1.5 - 22.0$ GHz, they noted that the minimum flux levels occurred around $\phi = 0.974$, is considered to be likely thermal where the non-thermal emission being absorbed by the thick WR wind and can no longer be detected- see Fig. 5.7 (please refer to Chapter 4 for more details).

We fitted Dougherty et al. (2005) thermal data at $\phi = 0.974$ observed at five frequencies ranging from 1.5 to 22.0 GHz with our recent lower frequencies uGMRT data (see Fig. 5.8). The best-fit spectral index, α for the frequencies between 0.3 and 22 GHz is $+0.64 \pm 0.02$, suggesting that the emission is thermal and closer to the expected spectral index.

5.4.1 Mass-loss rate and Effective Radius

From the observed thermal radio flux, we can calculate the value for the mass-loss rate of WR-star ($\dot{M}_{WR}$) using the Wright and Barlow (1975) mass-loss rate equation:

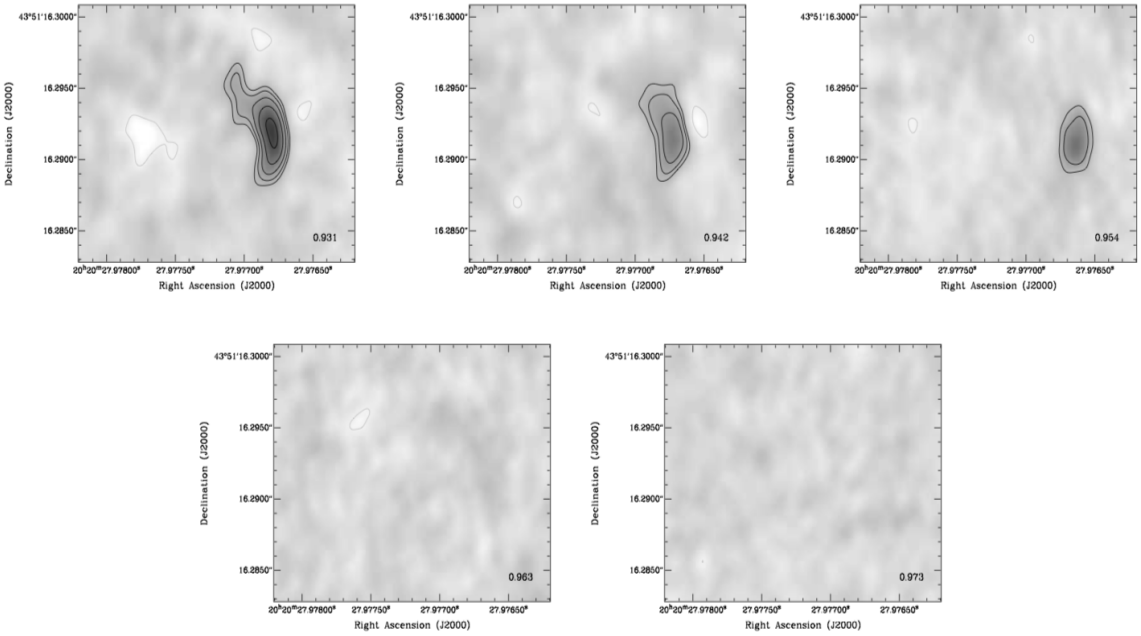

Figure 5.7: The WR140 NT emission region at $\phi = 0.931 - \phi = 0.973$ taken from Dougherty et al. (2005). The non-thermal emission being fully absorbed by the WC7 wind at $\phi \sim 0.973$ (last panel). Please refer to Chapter 4 for more details regarding the VLBA high-resolution observations.

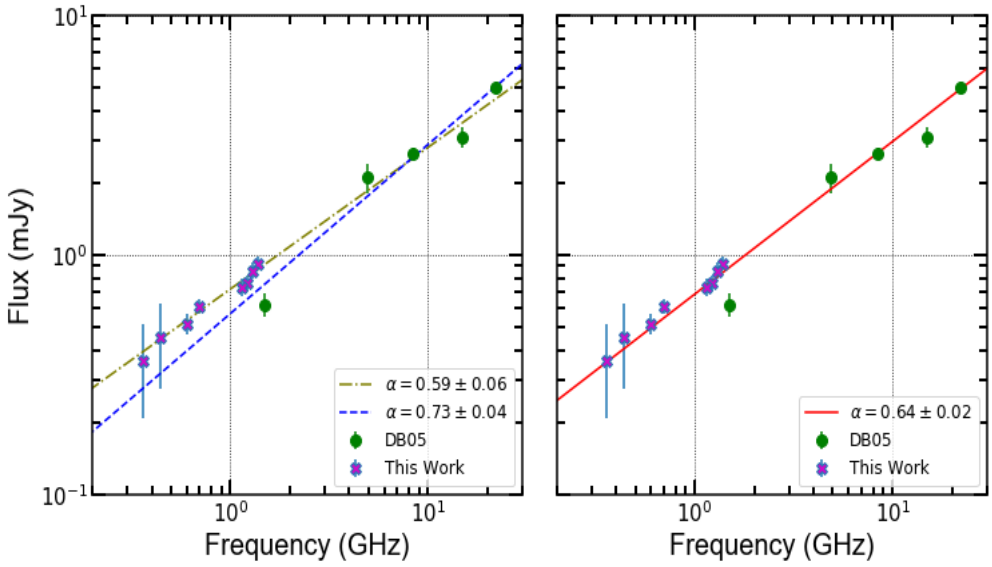

Figure 5.8: The thermal data points of WR140 where the data was taken from the high-resolution VLBA observation by Dougherty et al. (2005). Left panel: the blue dotted line ($\alpha = +0.73 \pm 0.04$) from VLBA compared to this uGMRT data points with green dotted slope ($\alpha = +0.59 \pm 0.06$). Right panel: The best-fit spectral index covering the frequencies from $0.3 - 15$ GHz is $\alpha = +0.64 \pm 0.02$, indicating that we can only see the thermal component of WR140.

$$S_\nu = 23.2 \left(\frac{\dot{M}}{\mu v_\infty} \right)^{4/3} \frac{\nu^{2/3}}{D^2} \gamma^{2/3} g_{ff}^{2/3} Z^{4/3} \mathrm{Jy} \tag{5.1}$$

where μ is the mean number of electrons per ion, Z is the mean charge per ion, γ is the ratio of electron to ion density, S_ν is in Jy, $\dot{M}$ is the mass-loss rate in $\mathrm{M}_\odot$ yr^{-1}, v_∞ is in km s^{-1} and ν is in Hz with the free-free Gaunt factor, g_{ff} (Sutherland, 1998; Van Hoof et al., 2014) estimated from Lamers and Leitherer (1993) given by:

$$g_{ff} = 9.77 \left(1 + 0.13 \log \frac{T_e^{3/2}}{Z\nu} \right). \tag{5.2}$$

Next, we adopted the wind structure from Pittard and Dougherty (2006), where C/He = 0.25 and O/He = 0.05 by number. The He is singly ionised while C and O are doubly ionised with the wind ionisation structure of H^+, He^+, C^{2+} and O^{2+}. To calculate the value of the mass-loss rate of WR-star, the value of $\gamma = 1.23$, $\mu = 6$ and $Z = 1.3$ were assumed. From Eqn. 7.5, our free-free gaunt factor, $g_{ff} = 6.09$ with the assumption of both winds to have a temperature of $T_e = 10000$ K. We also assume $v_\infty = 2860$ km s^{-1}, for the WC7 star as from Williams et al. (1990). At 0.60 GHz, we obtained the mass-loss rate of WR-star to be $\dot{M}_{WR} = 1.34 \times 10^{-4}\,\mathrm{M}_\odot$ yr^{-1}.

To estimate the mass-loss rate for O-star ($\dot{M}_O$), we used the wind momentum ratio, η as described from Pittard and Dawson (2018), such that:

$$\eta = \dot{M}_O v_O / \dot{M}_{WR} v_{WR}. \tag{5.3}$$

where v is the terminal velocity of the associated star. We used $v_{\infty,O} = 3100$ km s^{-1} from Setia Gunawan et al. (2001), $v_{\infty,WR} = 2860$ km s^{-1} from Williams et al. (1990) and the unclumped value of $\eta = 0.035$ adopted from Williams et al. (1990), and obtained the estimated value of $\dot{M}_O = 4.63 \times 10^{-6}$ $\mathrm{M}_\odot$ yr^{-1}. According to the studies by Fullerton et al. (2006), the volume-filling factor, f_v for O-star wind, is $f_v \sim 0.02 - 0.1$. So, if we assume $\eta = 0.02$ as in Pittard and Dougherty (2006) in their

Table 2, where the volume filling factor, $f_v = 0.199$, the mass-loss rate of the O-star is now $\dot{M}_O = 2.45 \times 10^{-6}$ $M_\odot$ yr^{-1}.

From Wright and Barlow (1975), the effective radius of the emitting region is given by:

$$R(\nu) = 2.8 \times 10^{28} \gamma^{1/3} g_{ff}^{1/3} Z^{2/3} T^{-1/2} \left(\frac{\dot{M}}{\mu v_\infty \nu} \right)^{2/3} \text{cm} \tag{5.4}$$

where T is in K, $\dot{M}$ is the mass-loss rate in $M_\odot$ yr^{-1} , v_∞ is in km s^{-1} and ν is in Hz. In general usage, $R(\nu)$ has been regarded as an effective radius of the radio emission. Using the mass-loss rate value obtained at 0.6 GHz from this observation and using other appropriate values from Table 5.1, we plotted the effective radius R_ν as a function of frequency from Eqn. 5.4. The effective radius of the radio emission decreases as the observing frequency increases ($R_\nu \propto \nu^{-2/3}$). From Fig. 5.9, our new uGMRT observations frequencies (shown in the cyan band) were looking at well beyond the maximum separation, which is at $\sim$ 30 AU. At 0.3 GHz to 1.5 GHz, we were looking at $R_\nu \sim 130 - 320$ AU, which can be associated with the outer wind of the system. At these radii, the NT component of the system was mostly absorbed by the thick wind from WC7. Hence, it agrees to what we observed was purely thermal, which was very close to the theoretically expected value, indicating there was no NT component in the radio emission.

5.5 WR140 Broadband Spectrum

We can extend our discussion of the thermal spectra of WR140 by including data at higher frequencies. WR140 has been observed with IRAM at 250 GHz (Altenhoff et al., 1994) and Herschel IPAC at wavelengths 70, 100 and 160μm. The fluxes and details of the observations are summarised in Table 5.4.

We performed a fitting for the data over 5 decades of frequencies and obtained a spectral index, $\alpha = +0.68 \pm 0.04$ (see Fig. 5.10) which is suggesting thermal

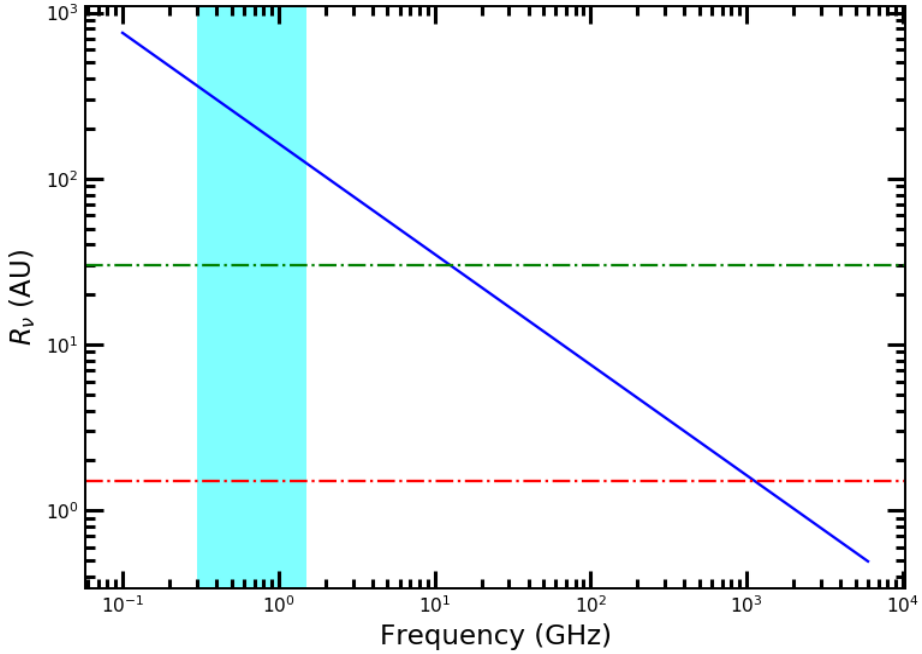

Figure 5.9: The effective radius R_ν in AU as a function of frequency in GHz. The red dotted dash line indicate the closest separation of WR140 which is at ~ 1.5 AU. The cyan region shows the range of radius which were observed in this work ($\sim 130-320$ AU) which was for a frequency range of 0.3 GHz $-$ 1.45 GHz. The green dotted dash line is the stellar separation at apastron ~ 30 AU. The new uGMRT observations may be looking at the outer wind of the system where most of the NT component suffers from absorption by the thick and dense WC7 winds.

Table 5.4: A summary of WR140 observations at higher frequencies. The data was taken from Williams et al. (1990), White and Becker (1995) and Herschel/PACS Point Source Catalogue. The table also includes the dates of observations which then were re-calculated using the recent paper by Thomas et al. (2021) to obtain the updated phase. The phases for these higher frequencies data was around $\phi \sim 0.4$ to match our uGMRT observation phase.

Frequency (GHz)	Wavelength (μm)	Flux (mJy)	Date	Phase	Telescope	Ref.
1.5		0.8 ± 0.4	27/4/1988	0.386	WSRT	W90
4.9		3.2 ± 0.32	8/3/1988	0.369	VLA	WB95
15.0		11.3 ± 0.30	8/3/1988	0.369	VLA	WB95
250.0		23.0 ± 3.0	9/3/1989	0.496	IRAM	A94
1874.0	160	97.10 ± 56.43	7/6/2012	0.428	Herschel	
3000.0	100	195.10 ± 15.10	7/6/2012	0.428	Herschel	
4283	70	201.77 ± 14.16	7/6/2012	0.428	Herschel	

* W90: Williams et al. (1990), WB95: White and Becker (1995), A94: Altenhoff et al. (1994).

emissions. Comparing this broadband spectral slope covering the frequency from 0.3 GHz to $\sim$ 4000 GHz to our uGMRT data slope (0.3–1.45 GHz), the spectral index of the broadband spectrum is slightly steeper, but still indicating thermal radio emission at $\phi \sim 0.4$ which is well away from the periastron passage.

5.6 Conclusions

In this chapter, we have successfully detected WR140 at the lowest radio frequencies (0.3-1.45 GHz) at a phase $\phi = 0.367$ using the upgraded GMRT array utilising the new broadband receivers. We presented the radio images and fitted the radio fluxes for the best-fit spectral index, α as $S_\nu \propto \nu^\alpha$ and obtained $\alpha = +0.59 \pm 0.06$, indicative of purely thermal emission from the WR star.

We estimated the mass-loss rate of the WR-star at 0.60 GHz to be $\dot{M}_{WR} = 1.45 \times 10^{-4}\,\mathrm{M}_\odot\ \mathrm{yr}^{-1}$ and from the assumed momentum ratio of $\eta = 0.035$ for the unclumped wind, we estimated the O-star's mass-loss rate to be $\dot{M}_O = 4.68 \times 10^{-6}$

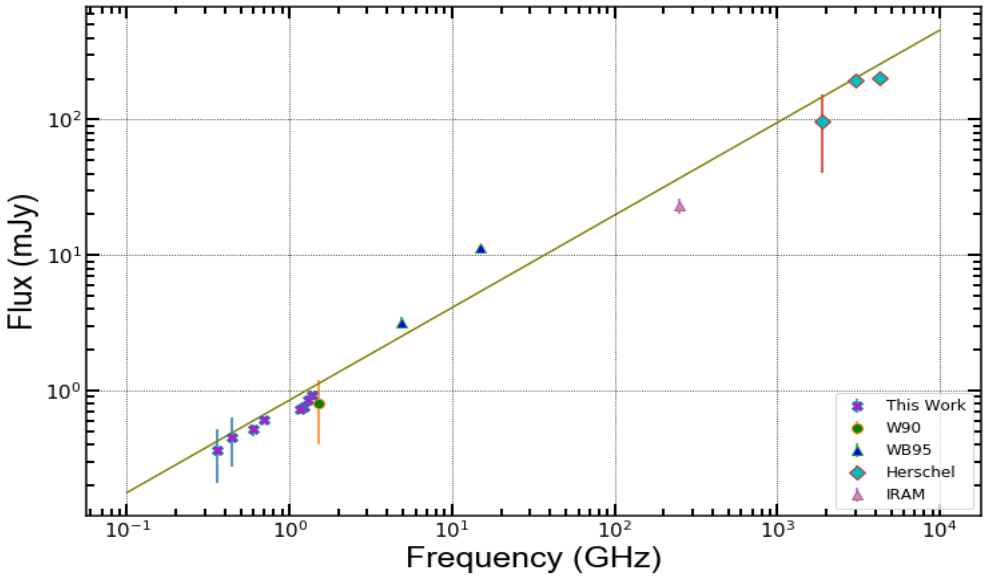

Figure 5.10: Data points expanding over 5 decades of frequencies with the slope of $\alpha = +0.68 \pm 0.04$. This slope suggesting a thermal emission from the WR-star at phase $\phi \sim 0.4$ which is well away from the periastron passage.

$M_\odot$ yr^{-1}. For the clumped wind recipe of $\eta = 0.02$ where the volume filling factor, $f_v = 0.199$ (from (Pittard and Dougherty, 2006)), the mass-loss rate of the O-star is $\dot{M}_O = 2.45 \times 10^{-6}$ $M_\odot$ yr^{-1}. These mass-loss rate values were in fair comparison with previously published values, but we noted that our values are at the higher end of the range.

Looking at the broadband spectra with the frequency ranges from 0.3 GHz to $\sim$ 4000 GHz at $\phi \sim 0.4$, the best-fit spectral index obtained was $\alpha = +0.68 \pm 0.04$, suggesting a thermal emission from the WR-star at this phase which is well away from the periastron passage.

The new uGMRT observations of WR140 at low frequencies have successfully constrained the thermal emission to give better baselines to study the non-thermal (NT) emission from WR140. In the next chapter of this thesis, we present the high-frequency observation of WR140 to study the NT emission originating from the wind collision region (WCR).

6 | High Frequency New Observation of WR140 using the EAVN

"Looking through the atmosphere is somewhat like looking through a piece of old, stained glass. The glass has defects in it, so the image is blurred from that."
–Nancy Grace Roman.

Chapter Summary

We present and discuss the new Very Long Baseline Interferometry observation using the East Asia VLBI Network (EAVN) at 22 GHz to detect the non-thermal (NT) emission region originating from the wind collision region (WCR) of WR140. The observation was performed on the 21st of March 2020, at a phase $\phi = 0.41$, closer to the apastron. The most extended baseline after the cancellation of the NSRT telescope due to Covid lockdown is 2270 km so that our angular resolution is reduced to 1.24 mas. We calculate the estimated emission measure, EM to be 2.94×10^8 cm^{-6}pc, and the corresponding optical depth, $\tau_\nu = 0.14$. We reduced and imaged the EAVN data with the phase referencing technique. No NT emission has

been detected from the WCR with an upper limit of 9 sigmas. We also outline and discuss the future capabilities of the EAVN network.

6.1 Introduction

WR140 is depicted as a textbook for the colliding wind binary (CWB) system as the orbital period is relatively short ($\sim$ 7.9 years); allowing astronomers to observe and analyse it multiple times in a lifetime. WR140 also possessed a high eccentricity orbit, $e = 0.8992$ (Thomas et al., 2021), which made it a popular choice for observing at different wavelengths such as the X- rays, infrared (IR) and radio. Despite being studied and investigated over various wavelengths throughout many epochs, there are still areas and aspects left unexplored, such as observing WR140 at high radio frequencies using the Very Long Baseline Interferometry (VLBI). High-frequency observations with the VLBI have the advantage of having a high spatial resolution, allowing us to explore physics that were unavailable at low frequencies because we can penetrate deeper into any star system.

In the case of WR140, we can see that the system's radio emission is only thermal at low frequencies. The non-thermal (NT) emission originating from the wind collision region has not been detected (WCR) as the system is not resolved (please refer to chapter 5 for more discussion on WR140 at lower frequencies). On the other hand, at high frequencies, we expected that the total radio emission from WR140 to be a composite of thermal emission and NT emission (see Fig. 6.1). The spectral index of the NT component is negative. This NT component is believed to be synchrotron emission, generated by shock accelerated electrons (De Becker, 2007). A Very Large Baseline Interferometry (VLBI) observation will resolve out the thermal emission from the WR140 system due to their high angular resolution and consequently disentangle the NT emission. Given the location of the WCR, the NT emission will be affected by the free-free absorption in the overlying wind.

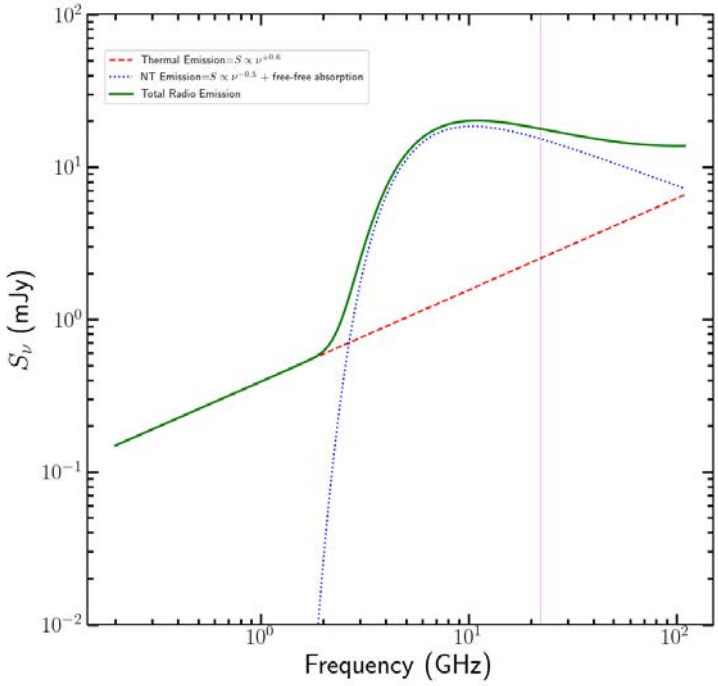

Figure 6.1: A schematic representation of the thermal and NT radio spectrum of WR140. The NT emission originating from the wind collision region (WCR) undergoes free-free absorption in the stellar winds. Observing the system at high frequency will disentangle the thermal and non-thermal components as the thermal component is mostly being resolved out at 22 GHz. The thin pink strip shows the EAVN array (KaVA + TMRT + NSRT) receiver operating at 22 GHz with a bandwidth of 32. Noted that the flux densities, S_ν used here are not from the actual observations and might be slightly different from the actual numbers.

Observing at a higher frequency, this free-free absorption will be lessened.

There was only one WR140 high-frequency observation at 22 GHz made by Dougherty et al. (2005) using the Very Large Array (VLA) located in Socorro, New Mexico while monitoring the system at lower frequencies, namely at 1.7 GHz and 8.4 GHz using the high-resolution Very Long Baseline Array (VLBA) distributed mainly across the United States, including telescopes in Hawaii and the Virgin Islands. The bow-shaped NT emission region was well detected using the high-resolution VLBA observation at both frequencies (observation at phase ϕ = 0.67 to 0.95). From the NT emission region images by Dougherty et al. (2005), we believed that

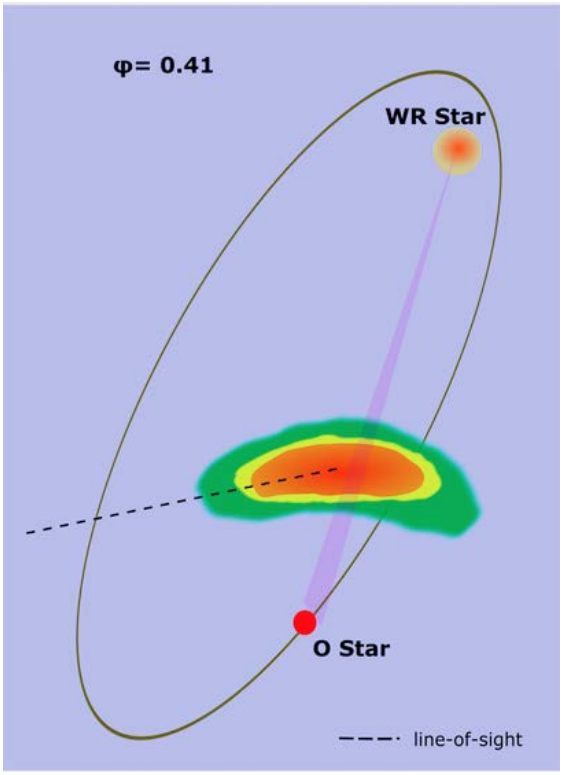

Figure 6.2: An illustration of the WR140 by the author atat $\phi = 0.41$. Based on the NT emission images from Dougherty et al. (2005), the bow-shaped NT emission region originating from the WCR is assumed to be at 0.9 of the system binary separation. The dotted line represents the observer's line of sight, which is mostly through stronger WR wind.

the NT region progresses as the orbital phase progresses. Approaching periastron, WR140 shown much interesting physical activity that can be detected by various wavelengths such as X-rays, IR and radio. On the contrary, when the system was closer to apastron, there were few observations taken; so, we need an observation as a baseline for the state of the system namely at $\phi = 0.41$ as shown in Fig. 6.2.

In section 6.2 of this chapter, the significance and motivations of new EAVN WR140 observation is discussed. We outline the EAVN data reduction in Section 6.2.1 and calculate the expected emission measure and optical depth of WR140 at 22 GHz in Section 6.3. We present the clean images, discuss the outcomes and outline EAVN's future capabilities in Section 6.4. We then conclude the chapter in Section 6.5.

6.2 High Frequency EAVN Observation of WR140

Current EAVN stations are primarily located in Korea, Japan, and China, with Korea (KJCC) serving as the primary correlator. The EAVN's open-use programme is still relatively recent, having only begun in the latter half of 2018. EAVN only has two available frequencies (22 GHz and 43 GHz) for a total of 100 hours, as well as only 9 of the 12 total stations available for use in this programme. Due to the unavailability of the 43 GHz receiver at some EAVN stations, we were awarded the telescope time at 22 GHz for our WR140 observation. The EAVN stations used for this observation are depicted in Fig. 6.3. The status of the EAVN stations on the WR140 observation and their parameters are listed in Table 6.1. The information was extracted from the EAVN 2020A status report[1] and the user support account.

This observation has three purposes:

1. A proof of concept that EAVN can see the NT emission from WR140 at high frequency and disentangle it from the thermal emission.

2. To learn the complexities of VLBI data reduction using the old package AIPS, specifically the phase referencing technique.

3. University Malaya has recently signed a Memorandum of Understanding (MoU) with the Shanghai Astronomical Observatory (SHAO) to aid Malaysia's advancement in the VLBI network (Abidin et al., 2020). This observation being the first from Malaysia, (PI: Farrah Zainol, Project Code: a2003a) would greatly improve the collaboration and encourage Malaysian radio astronomers to use the EAVN in their study.

The flux and phase calibrator used in this observation was chosen after consulting with the EAVN support officer. They recommended using these calibrators because

[1]The 2020A status report is available at `https://radio.kasi.re.kr/status_report/files/status_report_EAVN_2020A.pdf`

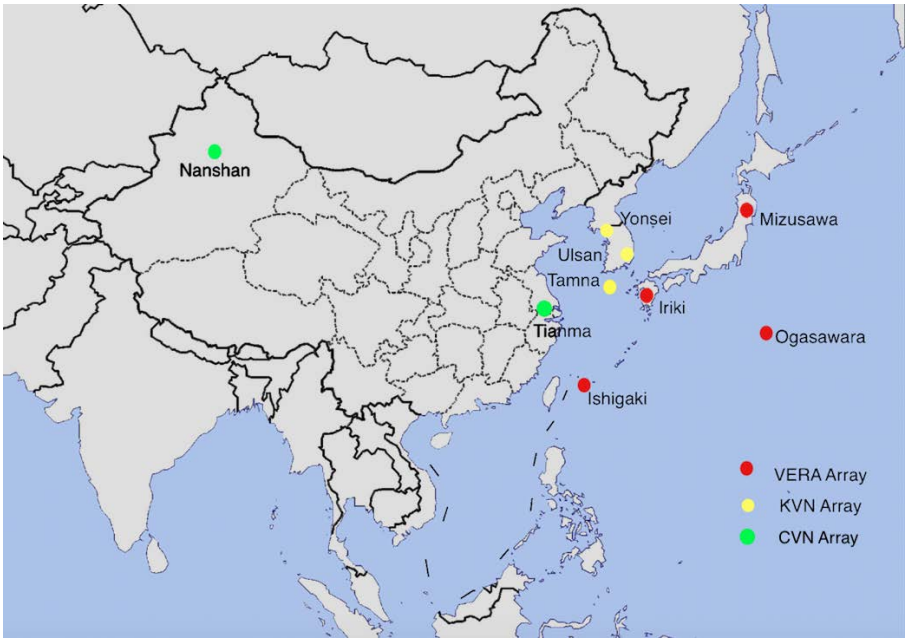

Figure 6.3: The EAVN stations used for the new WR140 observation at 22 GHz. Nanshan station provides the longest baseline of this array network which is 5078 km while the shortest baseline is from the KVN at 305 km. The details of the array specifications is shown in Table 6.3.

Table 6.1: The status of the EAVN stations on the 22 GHz WR140 observation (Project Code: a2003a, Season: 2020A).The parameters listed in the table are available in the EAVN status report[1] and the user support account. The TMRT station from the China VLBI Network (CVN) has the largest diameter, providing the highest sensitivity.

Location	Name	Network	D (m)	Lat. (degree)	Lon. (degree)	Alt. (m)	Obs. Status*
Tianma	TMRT	CVN	65	31	121	49	M
Nanshan	NSRT	CVN	26	43	87	2029	C
Mizusawa	MIZ	VERA	20	39	141	116	S
Iriki	IRK	VERA	20	32	130	574	S
Ogasawara	OGA	VERA	20	272	142	273	S
Ishigakijima	ISG	VERA	20	242	124	65	S
Tamna	KTN	KVN	21	332	126	452	S
Ulsan	KUS	KVN	21	36	129	170	S
Yonsei	KYS	KVN	21	38	127	139	S

*S:Success, M:Success with minor failures, F:Failure, C:Cancel

they are better suited for the WR140 observation. The EAVN team also has a better understanding of these calibrators, which is advantageous. The observation began on March 20th at 22:05 and ended on March 21st at 02:06, using a 32 MHz bandwidth at 22 GHz (Band K). The total observation time, including calibration, was four hours. The details of the observation was listed in Table 6.2. The observation date corresponds to a phase of $\phi = 0.41$, when the system is approaching the apastron. At the start and end of the observation, the flux calibrator, 2023+335, was scanned for 3 minutes and 8 seconds. J2012+4628, the phase calibrator, was scanned 27 seconds after the flux calibrator and kept alternating (nodding) with the source - WR140 for 385 seconds at each scan. The bandwidth used was the 32 MHz, and the data correlation was handled by the Korea-Japan Correlation Centre (KJCC), located in Korea. The correlator used in this observation was the Daejon Correlator (to correlate the KaVa and EAVN data) and the DiFX (Distributed FX) for processing the KVN data. We used the C4 mode, where the data was recorded at a data rate of 1024 Mbps with an integration time of 0.82 seconds. The 32 MHz bandwidth was recorded into 8 consecutive intermediate frequency (IF) bands with 256 channels in each IF and a 125 kHz channel separation.

The high-frequency WR140 observation was generally successful, with the exception of a minor issue caused by the coronavirus pandemic. Due to the strict lockdown in China, the NSRT station - see Fig. 6.3 for the site location - which provides the most extended baseline for this observation, has been cancelled. TMRT, another Chinese station, recorded a successful observation, but with a minor problem. Because of the cancellation by the NSRT station, our most extended baseline was reduced from about 5000 km to about 2000 km, lowering our resolution from 0.55 mas to 1.24 mas. The array specifications is listed in Table 6.3, and the *u-v* plots are depicted in Fig. 6.4.

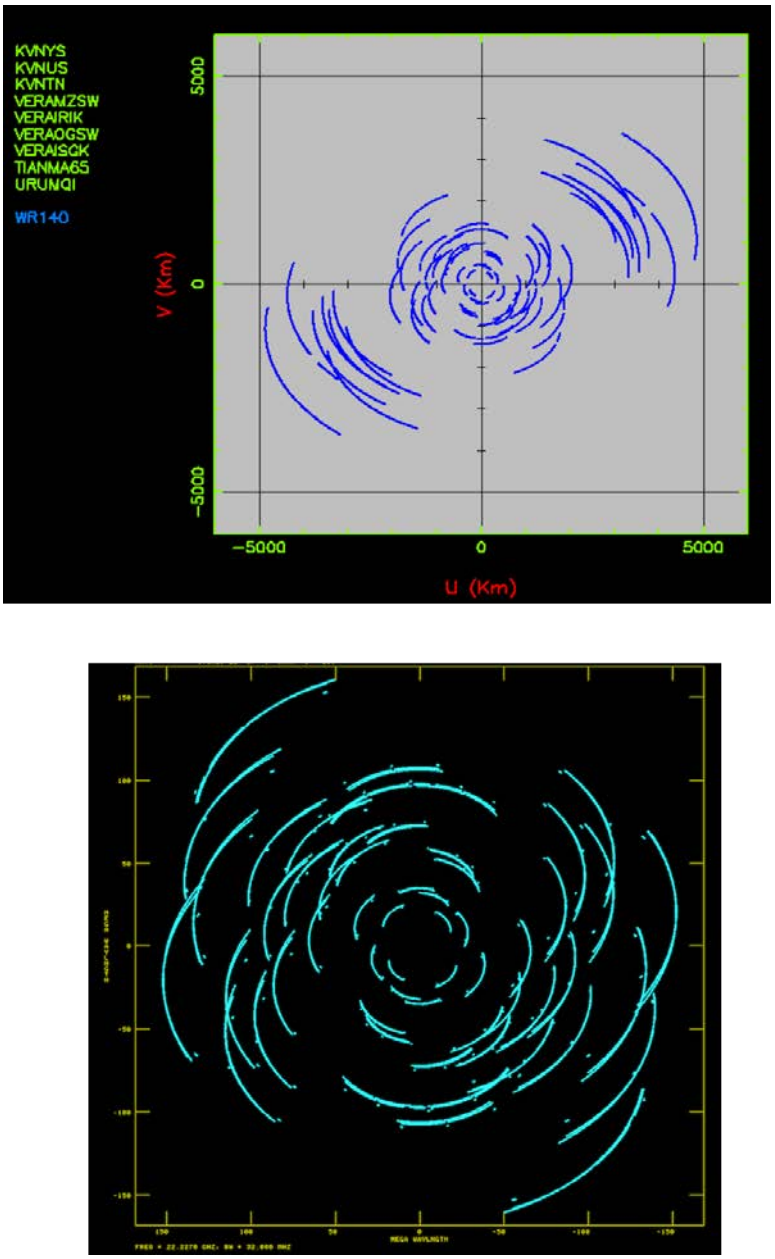

Figure 6.4: Top panel: The anticipated *uv* plot for the WR140 EAVN observation with the most extended baseline from the Nanshan Station (Urumqi), which is approximately 5000 km long. This baseline would have a resolution of 0.55 mas. Bottom panel: The *uv* plot from the actual data resulting after the cancellation of Urumqi. Noted that the unit is displayed in Mega wavelength. For an observation at 22 GHz, ($\lambda = 1.36$ cm), the longest baseline is now approximately 2270 km, which equivalent to a resolution of 1.24 mas.

Table 6.2: Details of the new EAVN observations of WR140. The observation was taken in Band K where it was the only frequency offered by the available station. The centre frequency is at 22.23 GHz.

Band	Date	Time (UTC)	BW (MHz)	Duration	Flux Cal	Phase Cal
K (22 GHz)	21-Mar-2020	22:05-02:06	32	4 hours	2023+335	J2012+4628

Table 6.3: The array specifications of the WR140 22 GHz observation. The parameters listed in the table was extracted from the EAVN 2020A status report. The parameters listed are the stations, number of antennas (N_{Ant}), number of baselines (N_{bl}), baseline length (L_{bl}) and the angular resolution (θ). The cancellation of the NSRT station changed the array specification from the expected A3 to A2 and reducing the angular resolution from 0.55 mas to 1.24 mas at 22 GHz.

Array	Stations	N_{Ant}	N_{bl}	L_{bl} (km)		θ (mas)
				min	max	22 GHz
A2	KaVA+TMRT	8	28	305	2270	1.24
A3	KaVA+TMRT+NSRT	9	36	305	5078	0.55

6.2.1 EAVN Data Reduction

Several attempts to convert the raw data from the EAVN to a CASA readable file were unsuccessful due to the way the EAVN correlator records the data. Many discussions have taken place with the EAVN support officer about the migration process. However, because of the inconsistency of each telescope station using CASA package, the only way forward is to use the old package, AIPS.

We performed a standard data reduction process, including the amplitude and phase calibration in AIPS. We generated one primary antab file with information regarding the system temperatures and gain curves provided by stations to perform the amplitude calibration. A manual phase calibration was required to align the phase among the different IFs. We first used the task FRING and CLCAL using the flux calibrator as our calibration source. We updated the new CL table by running a second FRING task with our phase calibrator as the calibration source. We transferred the solutions using the task CLCAL and combine all the IFs to increase the SNR. We used the task SPLIT on the target source and save them to

a calibrated fits file. The calibrated fits file was exported to CASA viewer for final imaging as it provides more imaging versatility and tools.

The main drawback that needed to be pointed out in using the EAVN network is the poor documentation on the data reduction process. We were assigned a support officer from Shanghai Observatory (SHAO) to assist us with the data reduction process (via email), but relying solely on an individual without proper documentation was difficult. The KJCC provided useful documentation, but it was only available in Korean.

6.3 Expected EM and Optical Depth of WR140 at 22 GHz

In this section, we estimate the expected theoretical emission measure (EM) of WR140 originating from the bow-shaped NT emission region expected for the wind collision.

The radio emission measure, EM in astronomically convenient unit cm^{-6} pc is defined as:

$$EM \equiv \int_{\rm los} n_{\rm e}^2 \, dx, \tag{6.1}$$

where $n_{\rm e}$ is the electron number density in cm^{-3} along the line of sight, x in pc. The mass density, ρ, is given by:

$$\rho = \mu_e n_e \tag{6.2}$$

where μ_e is the mean mass per electron in amu. From Pittard and Dougherty (2006), the mass-loss rate of the WR-star is $\dot{M}_{WR} = 4.3 \times 10^{-5}\,{\rm M}_\odot$ yr^{-1} with the assumed terminal velocity, $v_\infty = 2860$ km s^{-1} as in Williams et al. (1990).

Table 6.4: WR140 adopted orbital parameters.

Parameters	Value	Ref.
Period (days)	2895.0 ± 0.17	T21
eccentricity,e	0.8993 ± 0.0013	T21
Phase,ϕ	0.41	TW
Mean Anomaly,M (rad)	2.58	TW
Eccentric Anomaly,E (rad)	2.84	TW
True Anomaly, ν (rad)	3.07	TW
ω_{WR} (degrees)	227.44 ±0.52	T21
Inclination, i (degrees)	119.070	T21

* T21: Thomas et al. (2021); TW: This Work.

From this, Equation 6.1 can be expressed as:

$$EM = \int_0^\infty \left[\frac{\dot{M}}{4\pi r^2 v_\infty \mu_e}\right]^2 dx. \tag{6.3}$$

Assuming that the system is face-on to us ($i = 0°$), we have $r^2 = a^2 + x^2$ from the Pythagoras theorem (refer to Fig. 6.2). Solving the integral in Equation 6.3, the emission measure, EM is:

$$EM = \left[\frac{\dot{M}}{4\pi v_\infty \mu_e}\right]^2 \left[\frac{\pi}{4a^3}\right] \tag{6.4}$$

where a is the separation between the WR-star to the expected NT emission region at $\phi = 0.41$. Solving Kepler's Equation numerically using the orbital elements in Table 6.4, the separation is calculated to be 26.5 AU. The NT emission region is estimated to be at 0.9 × the binary separation, ρ from the WR star, and it is calculated as $a = 23.85$ AU. Referring to Fig. 6.5, we can see that at phase $\phi = 0.41$, we will see through mostly at WR wind. Assuming that the WR wind is fully ionised with the element abundance of He^{2+} and C^{2+}, the mean mass per electron, μ_e is 2. Substituting all the appropriate values to Eqn. 6.4, the value of EM at $\phi = 0.41$ is $EM = 2.94 \times 10^8$ cm^{-6}pc.

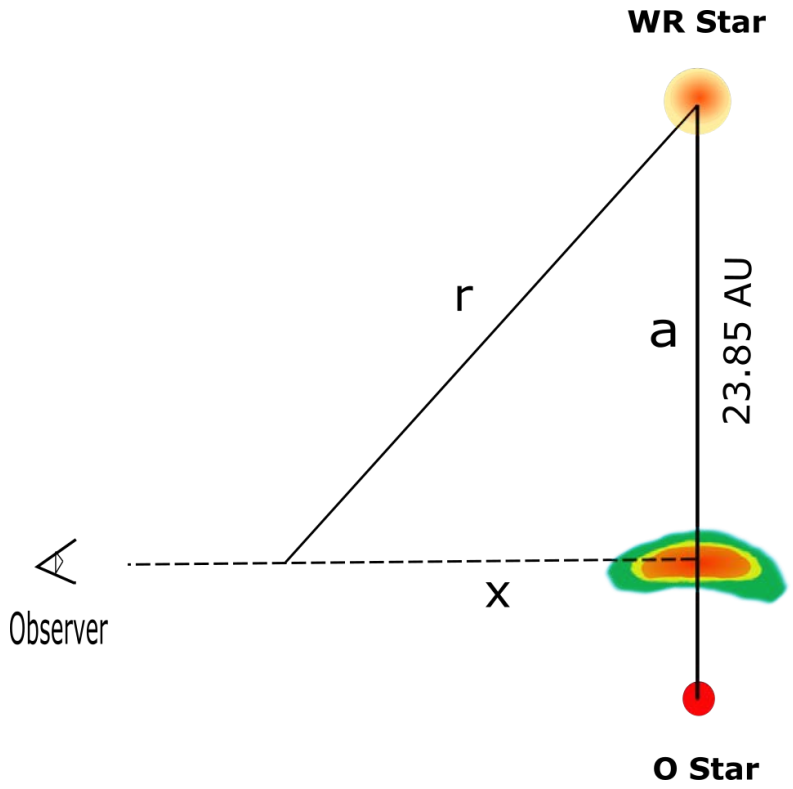

Figure 6.5: A schematic diagram of the WR140 system (not to scale). If we assume the system is face-on to us ($i = 0$) and solve Kepler's equation numerically, the distance between the WCR and the WR star is 23.85 AU. The distance of the WCR is assumed to be at 0.9 from the total binary separation. Using $\int_0^\infty n_e^2 \, dx$, the theoretical emission measure can be calculated, and the optical depth at $\phi = 0.41$ can be estimated. Please refer to the text for more details.

Remember that opacity scales as $\kappa_\nu \propto \nu^{-2.1}$ with frequency, so the optical depth is lessened at high frequency. As the wind becoming more transparent, we can detect the NT emission from the WCR. The optical depth, τ is proportional to the EM and commonly approximated in convenient astronomical unit by:

$$\tau \approx 3.014 \times 10^{-2} T^{-3/2} \nu^{-2} EM \, \langle g_{\rm ff} \rangle \, , \tag{6.5}$$

where the frequency ν is measured in GHz, the wind temperature, T is in Kelvin (K), and the EM is in cm^{-6}pc. Brussaard and Van de Hulst (1962) approximated the free-free Gaunt factor as:

$$\langle g_{\rm ff} \rangle \approx \ln \left[4.955 \times 10^{-2} \nu^{-1} \right] + 1.5 \ln T. \tag{6.6}$$

From Equation 6.5 and 6.6, the optical depth, τ_ν for our observation at 22 GHz and at phase of 0.41 is $\tau_\nu = 0.14$. As the expected $\tau_\nu < 1$, the wind is mostly transparent, and the emission from the NT region mostly will escape, and we should be able to detect them.

Note that the estimated EM value from this method assumed that the system to be face-on ($i = 0°$). The EM value will be affected if the system's inclination, $i \neq 0°$. The value of EM may go up or down depending on the distance along the line-of-sight.

6.4 Results and Discussions

The EAVN observed WR140 at JD 2458929.5 on the 20th of March 2020 at 22:05, which corresponds to a phase, $\phi = 0.41$. The beam size for this observation is 1.13×1.60 mas. Unfortunately, it seems that the source, WR140, was undetected with the upper limit of 9σ.

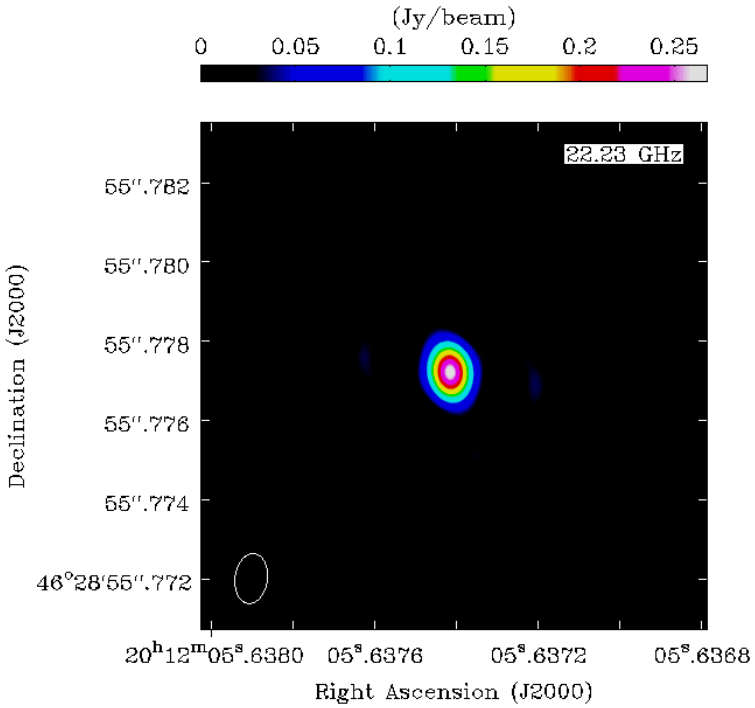

Figure 6.6: The phase calibrator, J2012+4628 was detected by the EAVN network at 22.23 GHz. The integrated flux for this source is 266.9 mJy. Assuming a spectral index of about ~ -0.2, the integrated flux obtained from the EAVN observation was approximately 50 mJy lower than the expected theoretical flux value. The position of the phase calibrator image was in the correct place up to 4.5 mas as stated by SIMBAD.

We imaged the phase calibrator, J2012+4628, again to ensure proper pointing. As shown in Fig. 6.6, the phase calibrator was well detected with an integrated flux, $S_\nu = 266.9$ mJy. We re-calibrated the data and reduced the signal-to-noise ratio (SNR) from 5 to 2. The acceptable SNR value for a point source detection from the EAVN is 5. The re-processed image revealed four bright 'blobs' as shown in Fig. 6.7.

These blobs continue to be a mystery. The brightest blob in the pack's northeast indicated a peak flux of 4.3 mJy, with an image rms of 0.5 mJy. When the SNR cut-off value during the cleaning procedure remained at 5, these artefacts were not visible. The placement of these artefacts was especially perplexing because there are no known bright objects near WR140. According to SIMBAD, which has been

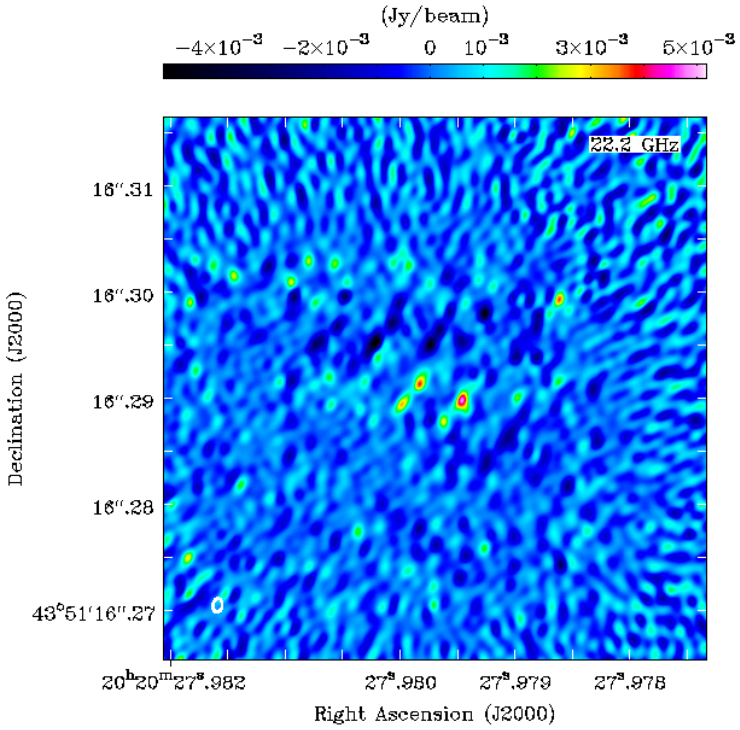

Figure 6.7: The clean image processed by CASA imaging tools centred at right ascension 20h 20m 27.9795s. Four bright blobs can be seen at the centre of the image. These artefacts only visible when the cut-off SNR was reduced to 2. The beam size for this observation is 1.13 ×1.60 mas. There are no known other bright objects around WR140 coordinates; hence, these artefacts are regarded as background noise.

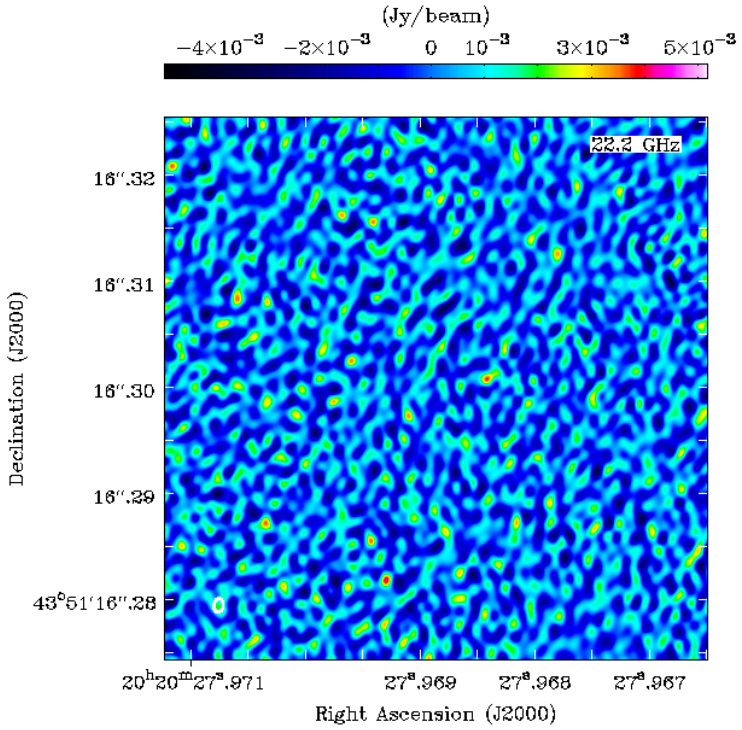

Figure 6.8: The clean image centred around the right ascension 20h 20m 27.969s with the FoV of 0.05" × 0.05". The image background noise is at 0.5 mJy. From this image, there is no apparent bright source that can be seen. Unfortunately, from this image, the NT emission from the WCR of WR140 was undetected at 22 GHz with an upper limit of 9σ.

updated with the GaiaDR2 mission, the proper motion for WR140 is $\mu_\alpha = -4.653$ mas/year. The RA should have been at 20h 20m 27.9700s at the observed time, and according to the current Gaia Early Data Release 3, (GAIAEDR3), WR140 right ascension was recorded at 20h 20m 27.9694 at J2016 epoch. As shown in Fig. 6.8, we imaged the observation around the newly recorded location by the GAIA mission with a field of view (FoV) of 0.05" × 0.05". As seen in Fig. 6.8, there is merely background noise in the FoV, with no discernible visual component. Thus, the mystery artefacts at the original target location may be due to the over-cleaning at a low SNR cutoff value.

The size of the NT emission region at 22 GHz is quite complicated to estimate because it is dependent on many factors such as array configurations, network sensitivity, array noise level, and array resolution. The NT emission region shifts from 7 mas to 3 mas as reported by Dougherty et al. (2005), peaking at 10 mas when the phase progresses from 0.74 to 0.95 at 8.4 GHz. At 1.7 GHz, the NT emission region is extended up to 27 mas with a beam size of 10×5 mas^2. Dougherty et al. (2005) estimated the upper limit for the NT emission region at 5 GHz to be < 13 mas due to the fact that WR140 was unresolved. From these numbers, we expected that at 22 GHz, the NT emission region should be small with the upper limit of < 10 mas.

Several discussions have taken place with the EAVN observation team regarding the clean image. The first probable explanation is that the angular resolution has been lowered by at least a factor of two as a result of the NSRT station's closure. Looking at our fringes on the calibrated source during the data reduction process, the SNR did not improve after a few re-processing rounds, despite adjusting the reference antenna. Additionally, according to our observation log, TMRT (Tianma telescope), which has the greatest diameter (65-m) of any other EAVN telescope station, logged a minor failure observation. Because the TMRT station did not record the weather in the observation log, the probability that this telescope was affected by adverse weather makes the actual EAVN rms considerably more significant than

the theoretical ones at a high frequency observation.

At the current stage, the EAVN network is expanding rapidly. The largest radio telescope preceding the recently demolished Arecibo, the FAST telescope, starts accepting international proposals for up to 100 hours of observation time. The observation will be expected to run from August 2021 to July 2022. The plan on expanding the China VLBI Network (CVN) is to include the FAST telescope and the newly under construction 120-metres Jingdong Radio Telescope (JRT) at Ailao Mountain (South China). In addition, the 40-m Thai National Radio Telescope (TNRT), the 32-m Jatiluhur Radio Telescope in Indonesia and the 13-m UM-XMUM-SHAO Radio Telescope in Jelebu, Malaysia, are also expected to be integrated into the EAVN network in 5 years, which will increase the sensitivity of the network significantly.

There are only a number of radio interferometer that offer high frequencies observation. It is engineeringly challenging and costly because the telescope surface needs to be precise and smooth such as the ALMA array (refer to Section 2.4.3 for more details). Other than ALMA, high frequencies observations can also be conducted by the VLBA (up to 100 GHz) and the EAVN (KaVA+TMRT+NSRT) array, up to 43 GHz. Therefore, using the EAVN network to observe the WR140 has given us insights and understanding into the EAVN especially in preparation for future observations.

6.5 Conclusion

Although we expected be able to detect the NT emission component from the estimation in Section 6.3, we concluded that we were unable to disentangle the NT emission with the EAVN rms at the phase $\phi = 0.41$ at 22 GHz. The EAVN has a promising future because many telescopes from East Asian countries will join the network, increasing the network sensitivity. As the first Malaysian P.I, the entire process, particularly the data reduction, will be invaluable, and these skills can be

transferred. This firsthand knowledge will encourage many Malaysian astronomers to begin using the EAVN in their research. We believe that the NT emission from the WR140 wind collision region will be detected and disentangled from the noise in the near future.

7 | The Low-Frequency Observation of WR146 using the Legacy GMRT

"In little localised pockets, the universe is capable of building some beautiful complexity."
–Sandra Faber.

Chapter Summary

In this chapter, we use CASA to re-analyse a low-frequency archived radio observation of another CWB system, the WR146. The observation was performed using the legacy GMRT in 2012, utilising the old dual-frequency mode at 235 MHz and 610 MHz. We present more recent WR146 radio observation data and fit our DREM model to this radio spectra. The value of the model's best-fit spectral index, $\alpha = -0.67$, is consistent with other published values. The estimated radio emission measure is then compared to the DREM model emission measure parameter. Both values are consistent, indicating that this model works.

7.1 Introduction

Massive stars usually exist in binaries or multiple systems. They have short lifetime of $\sim 1-5$ Myrs and have an incredible mass-loss (e.g. WR140 is 3×10^{-5} $M_{\odot}yr^{-1}$ (Fahed et al., 2011)) thanks to their supersonic stellar winds. Bright, hot stars such as the early-type O-B2-Wolf Rayet pairs are usually found in the massive stars formation regions such Cygnus OB2 in Cygnus X. The individual component in the massive binaries system possesses strong stellar winds, and the interaction between these two winds can form a wind collision region (WCR). These systems are well known as the colliding wind binaries (CWBs).

CWBs total radio emission are usually associated with a mixture of thermal emission and non-thermal emission (synchrotron radiation). This non-thermal emission is due to the electrons moving at a relativistic speed believed to be originated from the WCR. Many successful radio observations have been made to detect the WCR in the massive binaries such as the archetypal CWB, the WR140, discussed in Chapter 4.

This chapter focuses on one of the brightest Wolf-Rayet stars detected in the radio wavelength, the WR146. We reduced the legacy GMRT data (dual-mode) at 235 MHz and 610 MHz using CASA and presented a low-frequency radio observation image of WR146. We fit our DREM model, as discussed in Chapter 4 to the non-thermal radio spectra of WR146.

7.2 The Brightest But Not The Most Luminous WR146

The *particle-accelerating colliding-wind binaries* (PACWB) catalogue by De Becker and Raucq (2013) lists 43 identified binary systems capable of emitting synchrotron radiation. They reported that this source is a non-thermal source with the spectral

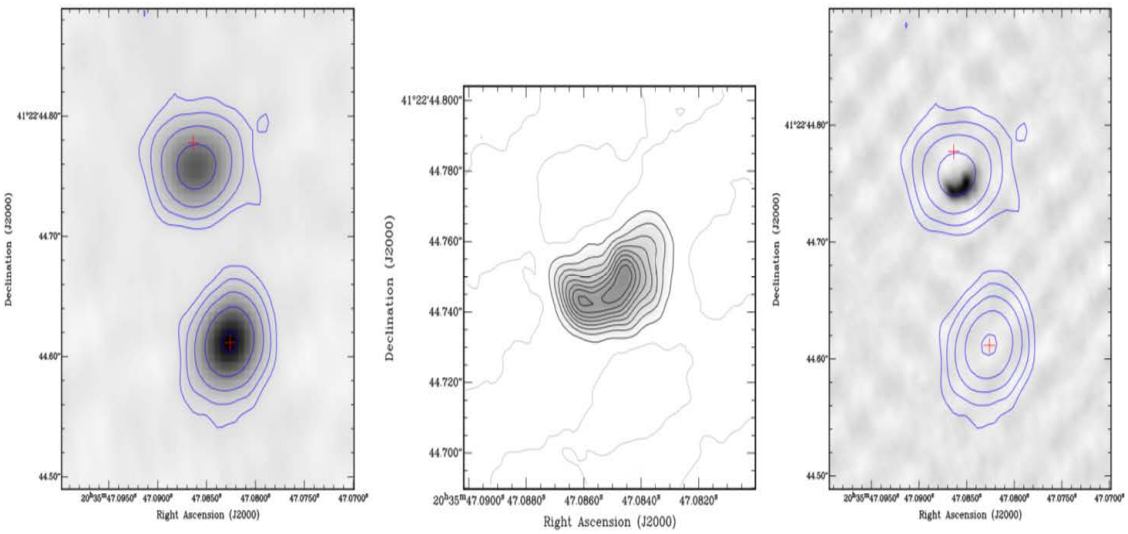

Figure 7.1: WR146 radio images from VLA + Pie Town and EVN. Left: The 43 GHz radio image from VLA + PT with 30 mas resolution. The sources are separated at 152 ± 2 mas. Centre: The source image at 5 GHz using the EVN with 9 mas resolution. The region was associated with the emission from the WCR. Right: Both of the images from VLA+PT (contours) and EVN (grey-scale) overlayed. The crosses indicate the location of the sources deduced from the HST (O'Connor et al., 2005).

index of $\alpha = -1$.

The WR146 system in J2000 coordinates (α = 20 35 47.09, δ = +41 22 44.7) from SIMBAD, is located at 1.2 kpc (Dougherty et al., 1996) and categorised as a WC6+O8 system by Niemela et al. (1998). Multi-frequency observations were made using the MERLIN array at 5 GHz and 1.6 GHz by Dougherty et al. (1996). Their 5 GHz images of WR146 show two resolved components (a bright north and weaker south). They associated the bright northern component with being a non-thermal source ($S_{(N)} = 28.5 \pm 0.2$ mJy) and the southern component as thermal ($S_{(S)} = 1.0 \pm 0.2$ mJy) with a free-free emission spectral index of $\alpha = +0.67$. WR146 has also been spatially resolved into two components (north and south) by the Hubble Space Telescope (HST) (Niemela et al., 1998).

More extensive observations of the WR146 system were performed by O'Connor et al. (2005) using the combination of VLA and the VLBA Pie Town antenna. The

high-resolution observations were carried out at 1.4 GHz to 43 GHz. They revealed two components observed at 15, 22 and 43 GHz with the sources separated by 152±2 mas at 43 GHz (see Fig. 7.1). At almost all frequencies, the northern component has a spectrum corresponding to synchrotron radiation. In contrast, the southern source has a thermal spectrum component consistent with the report from Dougherty et al. (1996, 2000) where the thermal emission is from the WC6 wind.

For over eight years, WR146 was observed using the Westerbork Synthesis Radio Telescope (WSRT) in the Netherland at 1.4 and 5.0 GHz by Setia Gunawan et al. (2000). They reported the observed period of the system is P = 3.38 yrs, which they acknowledged were too short. They also suggested a third low-mass component causes the periodic variability that modulates the O star wind. At low frequencies, specifically at 350 MHz and 1400 MHz, Gunawan et al. (2003) have performed a continuum survey of the Cygnus OB2 association which show the surrounding radio sources of WR146 (see Fig. 7.2). In recent years, Hales et al. (2017), observed the WR146 system using the Karl G. Jansky Very Large Array (JVLA) at 5 cm and 20 cm to investigate the linear polarisation of the synchrotron radiation. A handful of data spanning from 1-8 GHz was obtained, but they reported that the polarisation was absent.

WR146 distance has recently been revised using the second *Gaia* Data Release catalogue (*Gaia* DR2). The *Gaia* DR2 mission offers details on the proper motion, position and parallaxes for more than a billion stars in the Galaxy. The recent paper by Rate and Crowther (2020) measured distances from the *Gaia* DR2 catalogue using the Bayesian method for up to 383 Galactic WR stars. The distance obtained for WR146 was $d = 1.1^{+0.67}_{-0.36}$ kpc. The error listed here is exceptionally high due to the parallax measurements from *Gaia* DR2. The distance obtained for Cygnus OB2 in their second paper, (Rate et al., 2020), was $d = 1.57^{+0.08}_{-0.07}$ kpc. They indicated the distance obtained for Cygnus OB2 was in accordance with the previous distance measurements of 1.45 kpc by Wright et al. (2015) and 1.7 kpc from Massey and

Table 7.1: WR146 System parameters.

Parameters	Value	Unit	Ref.
System:			
Primary spectral type	WC6		L01
Secondary spectral type	O8		D00
Distance	$d = 1.1^{+0.67}_{-0.36}$	kpc	RC20-I
Distance (CygOB2)	$d = 1.57^{+0.08}_{-0.07}$	kpc	RC20-II
System separation	$D = 162 \pm 8$	mas	D00
Position Angle	$i = 22 \pm 4$	$\circ$	D00
Period	$P = 3.38 \pm 0.02$	yr	SG00
Period	~ 300	yr	D96
Primary Wolf-Rayet Star:			
$T_{\rm eff\,1}$	49000	K	SG00
R_1	1.5	$R_\odot$	H17
v_{∞_1} (Primary)	2900	km s^{-1}	EW94
$\dot{M}_1$	5.33×10^{-5}	$M_\odot yr^{-1}$	A19
$\dot{M}_1$	4×10^{-5}	$M_\odot yr^{-1}$	D00
$\dot{M}_1$	6.9×10^{-5}	$M_\odot yr^{-1}$	L01
Secondary O-star:			
$T_{\rm eff\,2}$	32000	K	SG00
R_2	10	$R_\odot$	H17
v_{∞_2} (Secondary)	1600 ± 480	km s^{-1}	D00
$\dot{M}_2$	8×10^{-6}	$M_\odot yr^{-1}$	D00

* SG00: Setia Gunawan et al. (2000), D00: Dougherty et al. (2000), D96: Dougherty et al. (1996), H17: Hales et al. (2017), OC05: O'Connor et al. (2005), RC20-I: Rate and Crowther (2020), RC20-II: Rate et al. (2020), L01: Lépine et al. (2001), EW94: Eenens and Williams (1994), A19:Andrews et al. (2019).

Thompson (1991) if the uncertainties were included. The basic parameters of WR146 are listed in Table 7.1.

7.3 Legacy GMRT Observation of WR146

WR146 low-frequency observations were performed with the legacy Giant Metre Radio Telescope (GMRT) located in Maharashtra, Pune, India. This radio interferometry facility consists of 30 entirely steerable parabolic dishes, each with a diameter of 45 m. The GMRT array has a standard Y-shaped configuration, with 14 antennas

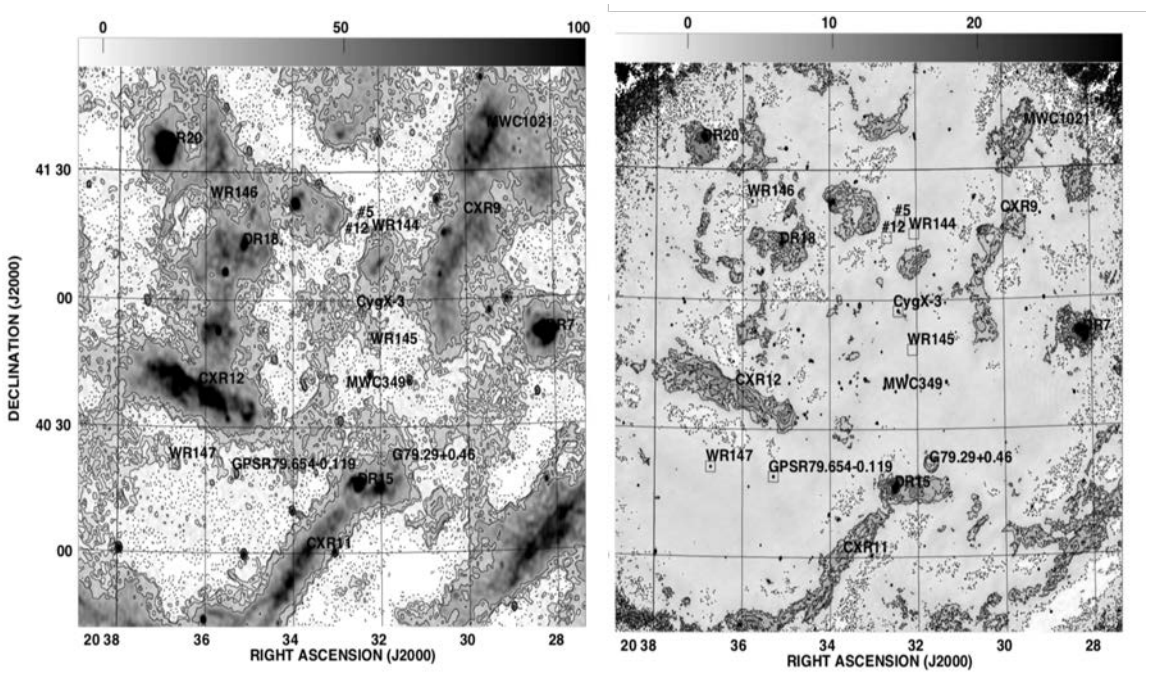

Figure 7.2: The Westerbork Synthesis Radio Telescope (WSRT) radio survey of the Cygnus OB2 association. Left: The lower frequency 350 MHz radio image of Cygnus OB2. Right: The 1400 MHz continuum image of Cygnus OB2. Both images show the surrounding radio sources of WR146 at low frequencies (Gunawan et al., 2003).

in the central core region and 16 antennas in the three arms. The shortest baseline is about 100 m, and the most extended baseline is about 25 km, (Gupta et al., 2017)). For more information about the GMRT, see section 2.4.4.

The observations were performed on November the 3rd 2012 with the legacy receivers, which were at a narrower bandwidth of 32 MHz (Gupta et al., 2017). WR146 observations were conducted using the unique dual-frequency mode setup where the receivers could perform the observation at different frequencies at the same observation time. The frequencies chosen for this study were at 610 MHz and 235 MHz to further investigate the WR146 radio spectra at lower frequencies and estimate the turnover frequencies.

WR146 observations were conducted for about 4 hours in total, including the flux and bandpass calibrator. The flux and bandpass calibrator used in the observation is the standard 3C48 and 2052+365. The flux calibrator was scanned for 30 minutes

Table 7.2: The observation was performed using the unique dual-frequency mode setup, so the observation time for both frequencies were the same.

Frequency (MHz)	Date	Time (UT)	BW (MHz)	Flux Cal	Phase Cal	Res (arcsec)
235	03-Nov-2012	$12:21-18:24$	32	3C48	2052+365	13.0
610	03-Nov-2012	$12:21-18:24$	32	3C48	2052+365	5.0

at the beginning and the end of the observation while the 2052+365 phase calibrator was scanned for 10 minutes every 30 minutes observation of WR146. The total on-source time of WR146 is about 3 hours. The summary of the observation details is shown in Table 7.2.

The data reduction was performed using the Common Astronomy Software Application (CASA) package instead of the Astronomical Image Processing System (AIPS) to produce a continuum spectra. The data reduction challenge for this observation is to perform the analysis using the new CASA on the old GMRT data, where the dual-frequency setup is still being used, and AIPS was still the primary data reduction package. Several extensive steps were implemented to the raw data so that it can be readable to CASA. The data was carefully split at the initial stage by their unutilised polarisation mode to obtain two different observation data frequencies. Each frequency band was reduced and imaged separately.

The data in each 32 MHz band was carefully flagged to remove bad spectral channels and bad baselines due to Radio Frequency Interference (RFIs). There were 26 antennas available while the other 4 were being serviced. Each band was imaged separately implementing a standard imaging routine such as spectral channels averaging, further flagging, and several iterations of self-calibrations to improve the image's quality.

Table 7.3: The integrated radio flux of WR146 observed using the dual-frequency mode setting from the legacy GMRT at 610 MHz. The flux was estimated using the CASA's Gaussian fit routine.

Frequency (MHz)	Flux (mJy)	Bandwidth (MHz)
612.59	62.8 ± 0.20	32

7.4 Results

The legacy dual-frequency mode observation was reported a successful observation, and the data was released on the National Cente for Radio Astrophysics (NCRA) archive. Unfortunately, several technical problems were detected during the data reduction process. Several private communications have been established with Ruta Kale and Ishwara Chandra (the NCRA officers) to retain the data. The 610 MHz data was successfully reduced and imaged. In contrast, the 235 MHz data has a severe problem with the calibrators which did not work properly on that band at the lowest frequency as confirmed by the GMRT centre.

The 610 MHz band integrated flux was obtained from CASA Gaussian Fit procedure, assuming the target is a point source. The flux value of the legacy GMRT observation is presented in Table 7.3, with the noted uncertainty is the rms of the image. The final image of WR146 at 612 MHz is presented in Fig. 7.3. The contours are following $-1, 1, 1.4, 2, 2.8, 4, 5.6, 8, 11.3 \times 30\sigma$. The larger field of view surrounding WR146 was also imaged and compared to the NVSS intensity map extracted from ESASky 3.7, which was imaged at 1.4 GHz as shown in Fig. 7.4 using the "postage stamp server" that return the FITS image. The FITS image was viewed and reprocessed using CASA. From Fig. 7.4, we can see that the GMRT was pointing at the correct area; hence there was no issue with the telescope's pointing. There were several SBHW sources from the Gunawan et al. (2003) catalogue that were detected surrounding WR146. Refer to Fig. 7.5 for the sources images obtained from this observation.

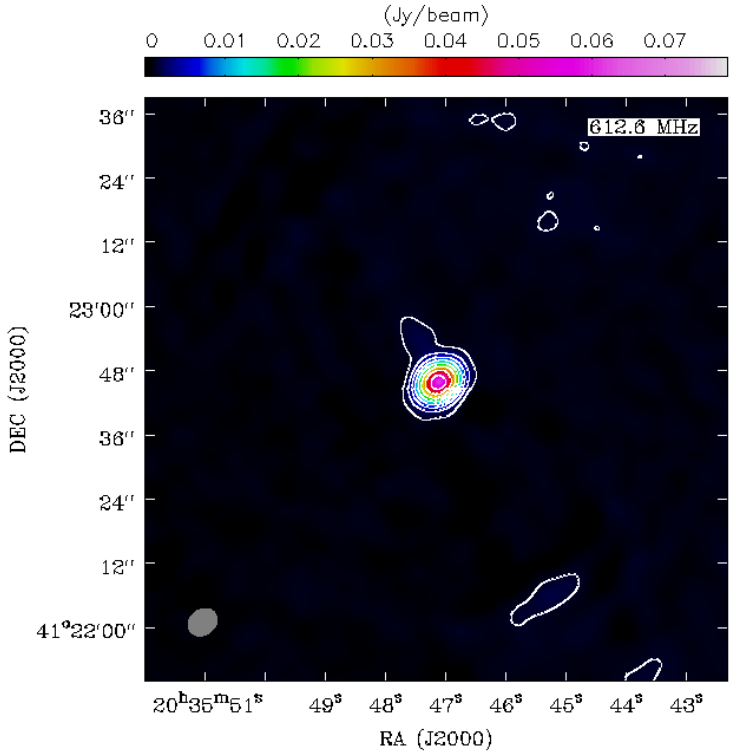

Figure 7.3: WR146 legacy GMRT images at 612 MHz. The grey circle is the synthesised beam. The contours is at $-1, 1, 1.4, 2, 2.8, 4, 5.6, 8, 11.3, 22.6, 32 \times 30\sigma$.

7.5 DREM Model Fittings

The Distributed Radio Emission Measure (DREM) model, as detailed in Section 4.5 is used to fit the non-thermal spectra of WR146 and to obtain the DREM model parameters such as the spectral index, α. The procedure used in Section 4.5 has been replicated on all the available published radio flux (see Table 7.4). The frequency of the spectra varies from 0.235 GHz up to 43 GHz. The total flux and the corresponding frequencies have been plotted, as shown in Fig. 7.6.

Dougherty et al. (1996) resolved WR146 images into two components (bright northern region and weaker southern region) at 5 GHz. Using their reported flux for the southern region ($S_{(S)} = 1.0 \pm 0.2$ mJy), which was associated with thermal emission and the corresponding free-free spectral index, $\alpha = +0.67$, we adjusted the thermal model so that the non-thermal value at the highest frequency (43 GHz) is

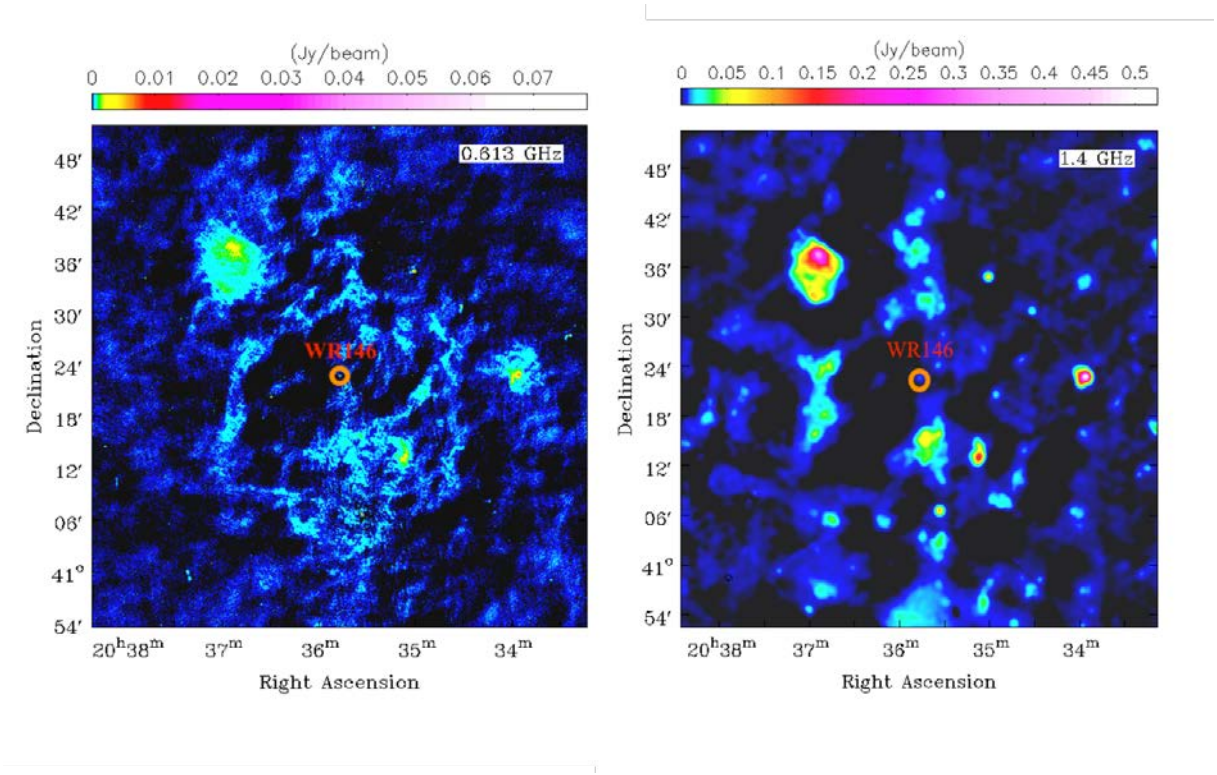

Figure 7.4: Left: The GMRT continuum image at 0.613 GHz with the image size of = 1.0° × 1.0°. Right: The similar image size from the EsaSky 3.7 (NVSS Intensity Map) at 1.4 GHz reprocessed from FITS image in CASA. (`https://sky.esa.int/?target=308.73349203249614`.). Both images were centred at WR146.

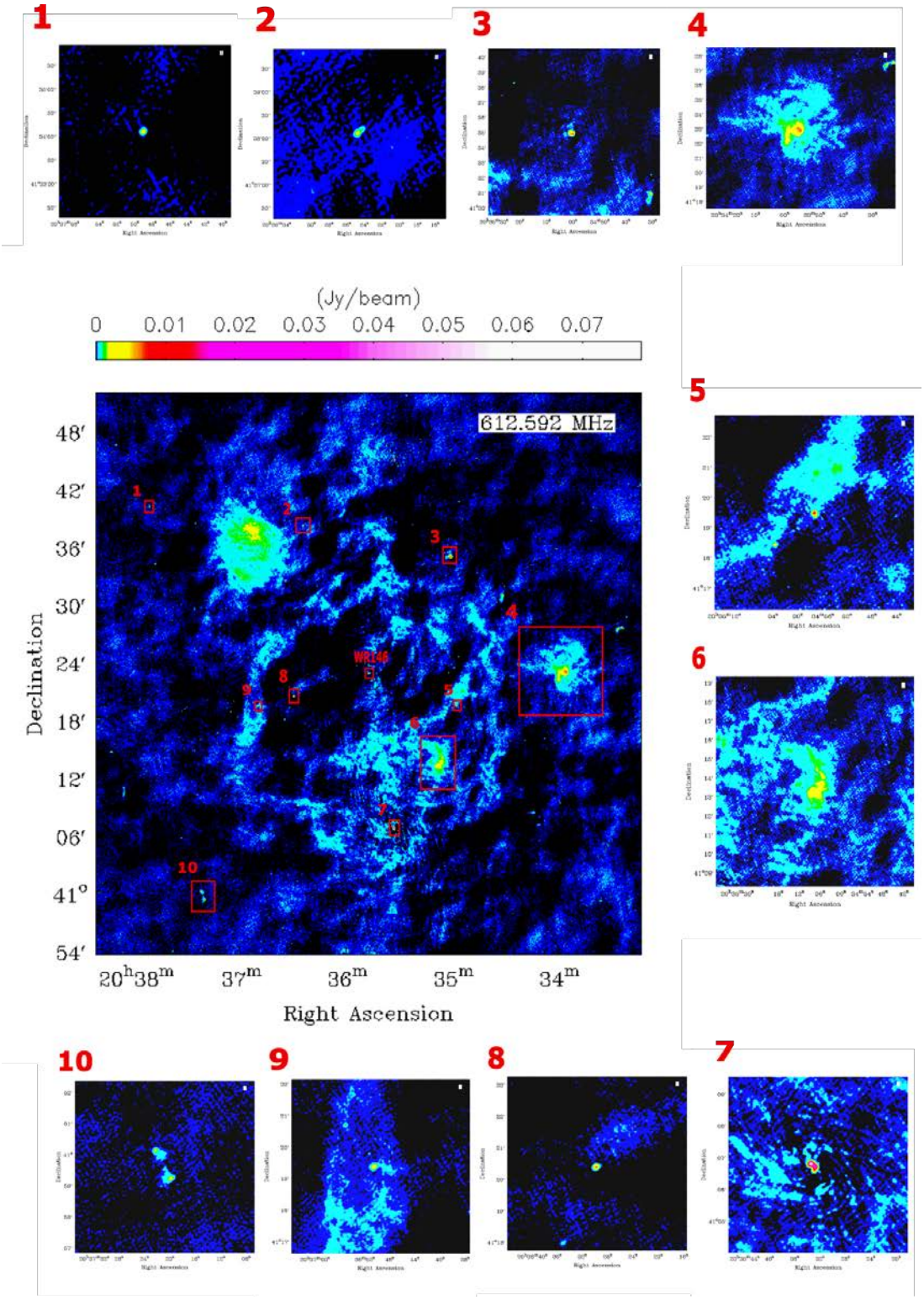

Figure 7.5: The SBHW sources detected around WR146 using the legacy GMRT at 612 MHz. The sources were cross-matched with the SBHW catalogue from Gunawan et al. (2003). 1: SBHW 193, 2: SBHW 172, 3: SBHW 141, 4: SBHW 225, 5: SBHW 140, 6: SBHW 229, 7:SBHW 156, 8: SBHW 173, 9: SBHW 179, 10: KMH 2014 (Young Stellar Object) from SIMBAD.

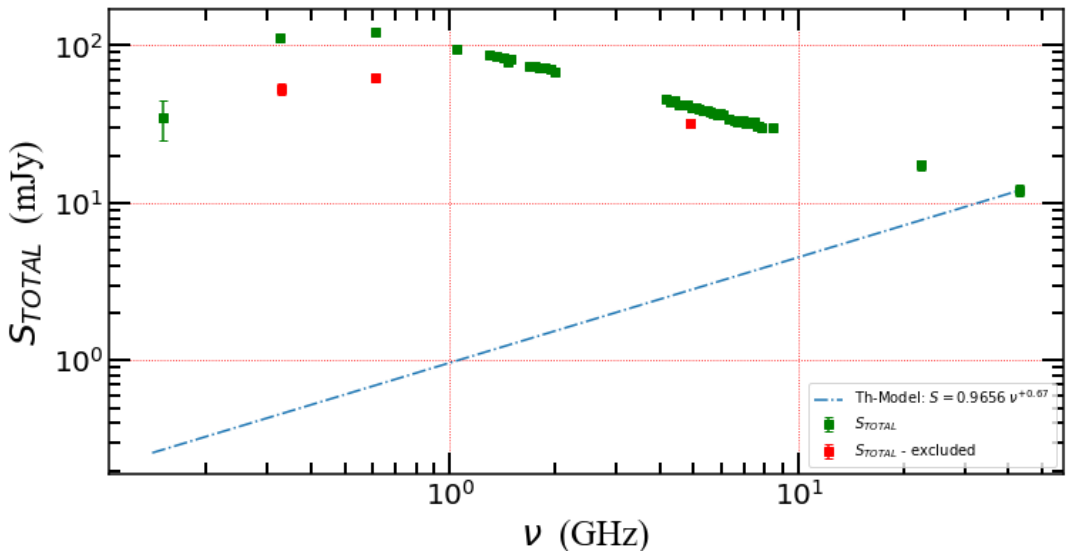

Figure 7.6: The total radio fluxes of WR146 ranges from 0.150 GHz up to 43 GHz. The dash-dot line represents the thermal model used in this work ($S_{TH} = 0.9656\ \nu^{+0.67}$) deduced from the southern thermal component from Setia Gunawan et al. (2000). The thermal model was adjusted so that the non-thermal flux at 43 GHz is zero. Note that some of the error bars are smaller than the points. The red data points plotted in the diagram are from Gunawan et al. (2003), Dougherty et al. (2000) and from this work where these points will be excluded due to the updated total flux value from recent observations. Refer to Table 7.4 for the flux values.

essentially zero. Refer to Fig. 7.6 for the power-law model used.

The thermal model used in this work is given by:

$$S_{TH} = 0.9656\ \nu^{+0.67}. \tag{7.1}$$

We subtracted the thermal component from the total radio flux simply by following $S_{NT} = S_{Total} - S_{TH}$. The non-thermal flux was recorded in Table 7.4 and plotted in Fig. 7.7. We plotted a few variations of single emission measure models against our NT WR146 radio spectra as shown in Fig. 7.8. The single EM models fail to fit the radio spectra especially at lower frequencies region.

As detailed in section 4.5, the DREM Model consists of four parameters: the radio flux when there is no absorption happen (S_0), the spectral index, (α), emission

Table 7.4: The total fluxes and the non-thermal fluxes of WR146 including their references and the telescope used. Note that the NT components were obtained by subtracting the thermal component, ($S_{TH} = 0.9656\,\nu^{+0.67}$) from the total radio flux.

Frequency (GHz)	$S_{(Total)}$ (mJy)	$S_{(NT)}$ (mJy)	Ref.	Telescope
0.150	35.0 ± 10.00	34.73 ± 10.00	B20	GMRT
0.325	111.0 ± 2.00	110.55 ± 2.00	B20	GMRT
0.327*	53.0 ± 4.00	52.55 ± 4.00	SG03	WSRT
0.610	121.0 ± 4.00	120.31 ± 4.00	B20	GMRT
0.612*	62.8 ± 0.15	62.10 ± 0.15	TW	GMRT
1.040	95.0 ± 0.45	94.00 ± 0.45	H17	VLA
1.296	86.4 ± 0.34	85.25 ± 0.34	H17	VLA
1.360	84.7 ± 0.21	83.51 ± 0.21	H17	VLA
1.424	82.7 ± 0.18	81.47 ± 0.18	H17	VLA
1.465	78.4 ± 0.20	77.15 ± 0.20	D00	MERLIN
1.488	81.6 ± 0.19	80.34 ± 0.19	H17	VLA
1.680	73.5 ± 0.22	72.13 ± 0.22	H17	VLA
1.744	73.6 ± 0.20	72.20 ± 0.20	H17	VLA
1.808	72.9 ± 0.19	71.46 ± 0.19	H17	VLA
1.872	72.0 ± 0.19	70.53 ± 0.19	H17	VLA
1.936	70.3 ± 0.29	68.80 ± 0.29	H17	VLA
2.000	68.4 ± 0.25	66.86 ± 0.25	H17	VLA
4.167	45.2 ± 0.45	42.69 ± 0.45	H17	VLA
4.295	44.0 ± 0.37	41.44 ± 0.37	H17	VLA
4.423	44.4 ± 0.39	41.79 ± 0.39	H17	VLA
4.551	42.3 ± 0.33	39.63 ± 0.33	H17	VLA
4.679	42.0 ± 0.33	39.29 ± 0.33	H17	VLA
4.807	41.6 ± 0.38	38.84 ± 0.38	H17	VLA
4.885*	32.0 ± 0.40	29.21 ± 0.40	D00	MERLIN
4.935	40.3 ± 0.37	37.49 ± 0.37	H17	VLA
5.063	40.2 ± 0.39	36.34 ± 0.39	H17	VLA
5.191	39.1 ± 0.37	35.19 ± 0.37	H17	VLA
5.319	38.3 ± 0.32	35.34 ± 0.32	H17	VLA
5.447	38.4 ± 0.35	34.39 ± 0.35	H17	VLA
5.575	37.7 ± 0.39	34.65 ± 0.39	H17	VLA
5.703	37.0 ± 0.33	33.90 ± 0.33	H17	VLA
5.831	36.3 ± 0.37	33.15 ± 0.37	H17	VLA
5.959	36.9 ± 0.43	33.70 ± 0.43	H17	VLA
6.039	36.1 ± 0.43	32.88 ± 0.43	H17	VLA
6.295	34.3 ± 0.37	30.99 ± 0.37	H17	VLA
6.551	33.3 ± 0.33	29.90 ± 0.33	H17	VLA
6.679	32.6 ± 0.34	29.15 ± 0.34	H17	VLA
6.807	32.5 ± 0.35	29.01 ± 0.35	H17	VLA
6.935	33.7 ± 0.39	30.17 ± 0.39	H17	VLA
7.063	32.1 ± 0.36	28.52 ± 0.36	H17	VLA
7.191	32.3 ± 0.35	28.68 ± 0.35	H17	VLA
7.319	32.4 ± 0.35	28.74 ± 0.35	H17	VLA
7.447	32.9 ± 0.38	29.19 ± 0.38	H17	VLA
7.575	30.7 ± 0.32	26.95 ± 0.32	H17	VLA
7.703	30.6 ± 0.30	26.81 ± 0.30	H17	VLA
7.831	30.2 ± 0.32	26.36 ± 0.32	H17	VLA
8.435	29.8 ± 0.80	25.77 ± 0.80	D00	VLA
22.46	17.4 ± 1.30	9.64 ± 1.30	D00	VLA
43	12.0 ± 1.00		OC05	VLA

[1]OC05: O'Connor et al. (2005),[2]SG03: Gunawan et al. (2003),[3]TW: This Work,[4]D00: Dougherty et al. (2000),[5]H17: Hales et al. (2017),[6]B20: Benaglia et al. (2020), * This data point was omitted at the fitting stage as the new data is made available.

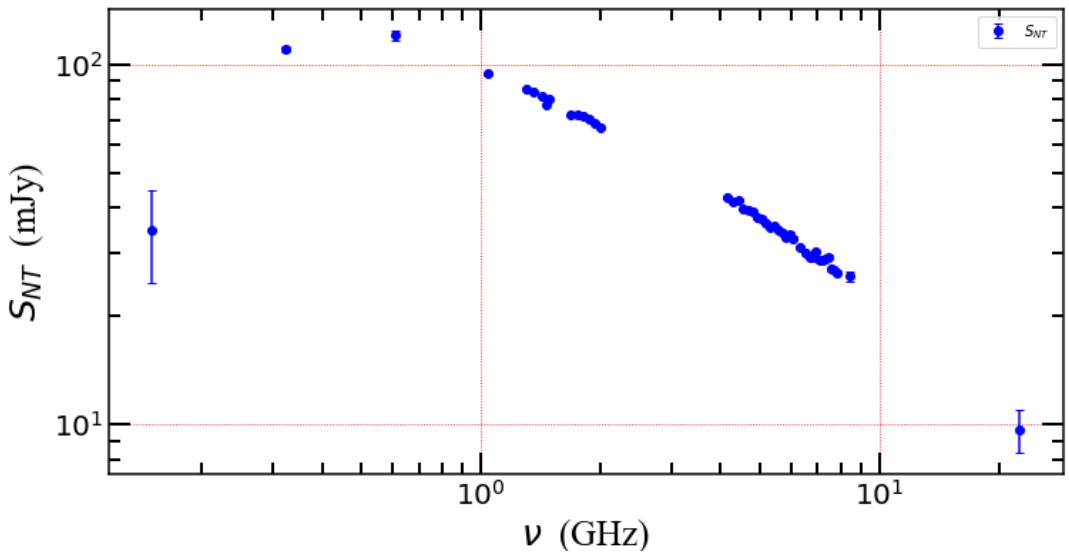

Figure 7.7: WR146 non-thermal radio spectra. The NT fluxes was obtained by subtracting the thermal component from the total radio flux following $S_{NT} = S_{Total} - S_{TH}$.

measure, (EM) and the standard deviation of the emission measure, (σEM). The DREM model can be expressed as:

$$S_0 \left(\frac{\nu}{\nu_0}\right)^{\alpha} e^{-\tau_{ff}}, \tag{7.2}$$

where the free-free opacity, τ_{ff} is given by:

$$\tau_{ff} = \left(CT^{-1.35}\right) \nu^{-2.1} EM. \tag{7.3}$$

We repeated the method in section 4.5 using several Python fittings packages, but the packages have failed. We used the Markov Chain Monte Carlo (MCMC) method as an alternative to obtain the minimum χ^2. We obtained a minimum χ^2 value of 11.3 for this radio spectra. The best-fit values for the DREM model parameters fitted for the non-thermal spectra of WR146 are displayed in Table 7.5.

We also estimated the error by calculating the χ^2 value, where only one varying parameter and the other parameters are fixed. The parabola curves in Fig. 7.9 show

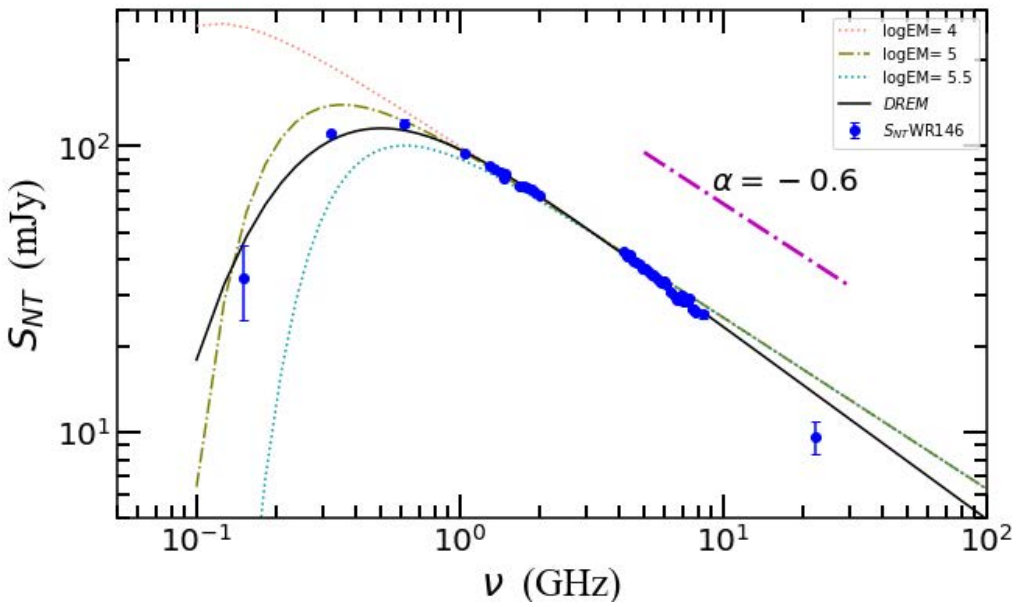

Figure 7.8: A variation of single emission measure models with $log_{10}EM$ at 4, 5, and 5.5. The magenta dash-dot line represents the slope at $\alpha = -0.6$. The solid black line represents the fittings by the DREM model. The single emission measure models fail to fit especially at the lower frequencies region. The DREM model offers better fittings to the WR146 non-thermal spectra with the spectral index of $\alpha = -0.67$. The best fit value for the parameters were recorded in Table 7.5.

Table 7.5: The best-fit values for the DREM model parameters obtained from the minimum χ^2 grid search. The minimum χ^2 obtained for WR146 NT fluxes is 11.3. The error for each parameter was estimated by plotting the parabolic curve as shown in Fig. 7.9.

DREM Parameter	Value	1σ Error
S_0 (mJy)	110.4	± 0.5
α	-0.676	± 0.01
$log_{10}\bar{EM}$	5.351	± 0.08
$\sigma log_{10}EM$	0.528	± 0.1

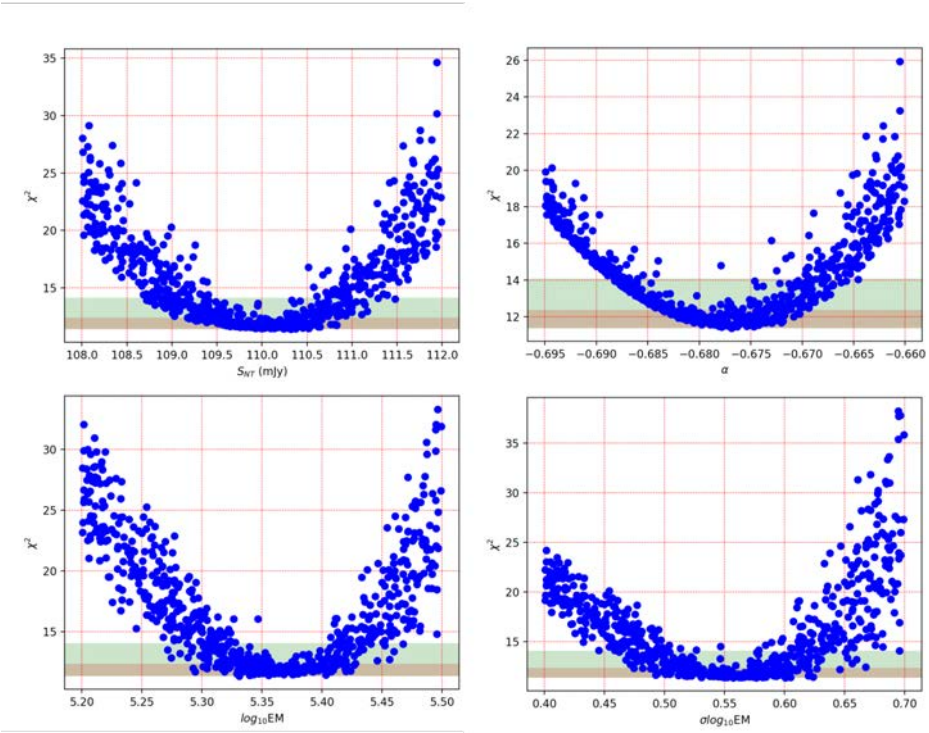

Figure 7.9: The parabola curves show the χ^2 value raising away from the optimum minimum χ^2 for each parameter in the DREM model. The brown band indicates a 1σ and the green band shows 1.6σ confidence interval.

the χ^2 value raising away from the optimum minimum χ^2 for each parameter. The best-fit value for the spectral index, $\alpha = -0.676 \pm 0.01$ from our DREM model agrees with the published value from Hales et al. (2017), which was $\alpha \approx -0.6$, indicating that the model works for another CWB, which is WR146.

7.6 Mass-loss rates of WR146

From the legacy GMRT 612 MHz radio flux, we deduced the thermal flux of WR146 and calculated the value for the mass-loss rate of WR-star ($\dot{M}_{WR}$) using Wright and Barlow (1975) mass-loss rate equation:

$$S_\nu = 23.2 \left(\frac{\dot{M}}{\mu v_\infty} \right)^{4/3} \frac{\nu^{2/3}}{D^2} \gamma^{2/3} g_{ff}^{2/3} Z^{4/3} \mathrm{Jy} \tag{7.4}$$

where γ is the mean number of electrons per ion, Z is the mean charge per ion, μ is

the ratio of electron to ion density, S_ν is in Jy, $\dot{M}$ is the mass-loss rate in $M_\odot$ yr^{-1} , v_∞ is in km s^{-1} and ν is in Hz with the free-free Gaunt factor, g_{ff}, estimated from Lamers and Leitherer (1993) given by:

$$g_{ff} = 9.77\left(1 + 0.13\log\frac{T_e^{3/2}}{Zv}\right). \tag{7.5}$$

In order to calculate the value of the mass-loss rate of WR-star, $\dot{M}_{WR}$ at 610 MHz, the value of $\gamma = 1.15$, $\mu = 5.29$ and $Z = 1.2$ were assumed as in Willis et al. (1997). We also assume $v_\infty = 2900$ km s^{-1} as in Eenens and Williams (1994) and $T_e = 49000K$ from Setia Gunawan et al. (2000). We used the recent distance, $d = 1.1$ kpc from *Gaia* DR2 as reported by Rate and Crowther (2020). We obtained the value for the Gaunt factor, $g_{ff} = 7.44$ and the mass-loss rate of WR-star, $\dot{M}_{WR} = 8.31 \times 10^{-5}\,M_\odot$ yr^{-1}. This value is in a good agreement with the previously reported mass-loss rate published by Lépine et al. (2001), $\dot{M}_{WR} = 6.9 \times 10^{-5}\,M_\odot$ yr^{-1}. Generally, the accepted 'average' mass-loss rate for WR-star is $\dot{M}_{WR} = 5.33 \times 10^{-5}\,M_\odot$ yr^{-1} (Andrews et al., 2019); thus our value is just above the average. Andrews et al. (2019) also noted that the WC sub-type was generally seen to have higher mass-loss rate values.

7.7 The Expected Emission Measure of WR146

This section estimates the theoretical emission measure of WR146 originating from the bow-shaped region expected for the wind collision. From the mass conservation equation, $\dot{M} = 4\pi r^2 \rho v_\infty$, we calculated the mass-loss rate of the WR-star to be $\dot{M}_{WR} = 8.31 \times 10^{-5}\,M_\odot$ yr^{-1} with the assumed terminal velocity, $v_\infty = 2900$ km s^{-1} as in Eenens and Williams (1994). Assuming that the system is face-on to us ($i = 0°$), we repeated the calculation of the estimated EM for WR140 in Section 6.3.

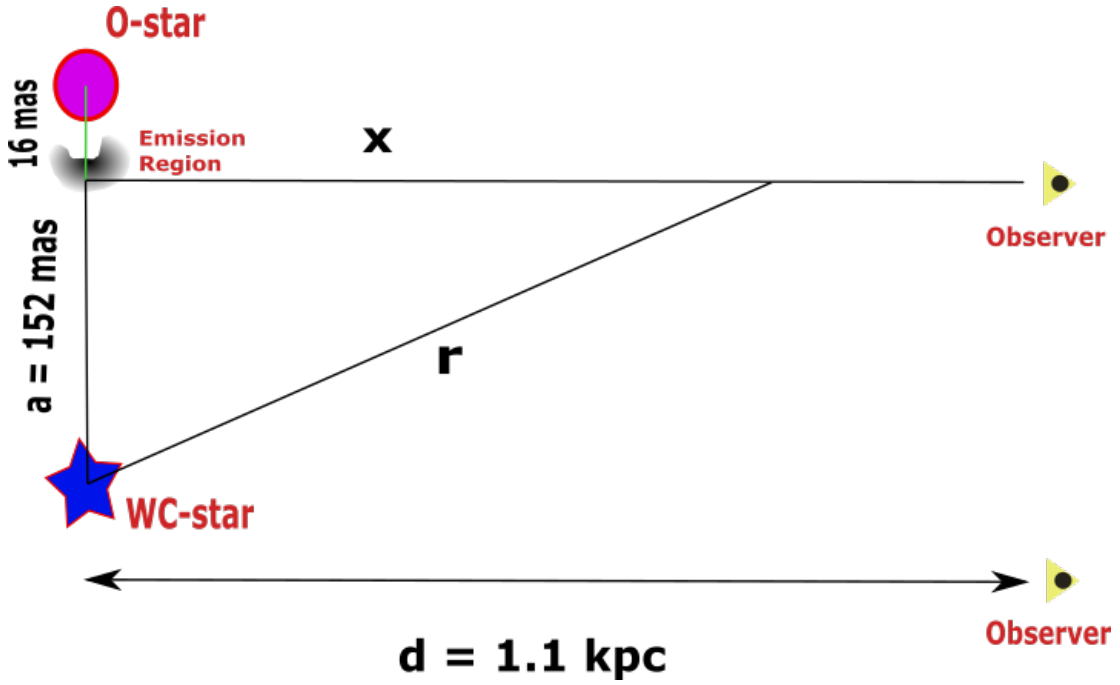

Figure 7.10: This figure shows a simple diagram (not to scale) of the WR146 system. From O'Connor et al. (2005), the separation between the WC-star to the bow-shape emission region is 152 mas, while from the HST observation (Niemela et al., 1998), the separation between the WC-star and the O-star is 168 mas. Assuming the system is face-on to us ($i = 0°$), the theoretical emission measure can be calculated using $\int_0^\infty n_e^2\, dx$. Refer to the text for details.

Remember that the emission measure, EM can be calculated using:

$$EM = \left[\frac{\dot{M}}{4\pi v_\infty \mu_e}\right]^2 \left[\frac{\pi}{4a^3}\right]. \tag{7.6}$$

So, from the Pythagoras theorem in Fig. 7.10 for WR146 system, and by substituting appropriate values into Equation 7.6, we calculated the expected value of EM using the prescription described in Section 7.6 to be EM = 4.38×10^5 cm^{-6} pc or $\log_{10}$ EM = 5.64. Note that the estimated EM value from this method assumed the system to be face-on ($i = 0°$). The EM value will be affected if the system's inclination, $i \neq 0°$. The value of EM may go up or down depending on the distance along the line-of-sight.

7.7.1 The Radio Emission Measure with Wind Clumping

In this subsection, we will define the mass-loss rate from a smooth wind as $\dot{M}_{sm}$, and from the clumped wind as $\dot{M}_{cl}$. As discussed in Section 1.6, for a given mass-loss rate, wind clumping generally raised the radio flux at all wavelengths. Remember that radio flux, S_ν scales as (from Abbott et al. (1981)):

$$S_\nu \propto \dot{M}_{sm}^{4/3} \times f_{cl}^{2/3}. \tag{7.7}$$

Assuming the observed radio flux is constant, clumping will (in effect) reduce the mass-loss rate. Hence from Eqn. 7.7, the mass-loss rate, $\dot{M}_{sm}^2$ scales as:

$$\dot{M}_{sm}^2 \propto f_{cl}^{-1}. \tag{7.8}$$

For the mass-loss rate derived from the thermal emission flux, the radio emission measure will yield higher values as $EM \equiv \int_{\rm los} n_{\rm e}^2$. So, the inhomogeneities in the wind will become more prominent in radio wavelengths. If we have a clump of materials ($f_{cl} = 2, f_V = 0.5$), and elsewhere is void, the density of the clump, (n_e/f_V), will increase by a factor of 2, and the n_e^2 terms will go up by a factor of 4. Solving the integral of the clumped emission measure, EM, scales as $EM \propto \dot{M}_{cl}^2 \times f_V^{-1}$ or $\propto \dot{M}_{cl}^2 \times f_{cl}$. Hence, in this case, clumping increase the emission measure.

Remember from previous analysis (section 7.7), $EM \propto \dot{M}_{sm}^2$. Therefore, the effect of clumping on the Emission Measure is:

$$EM \propto \dot{M}_{sm}^2 \propto f_{cl}^{-1}. \tag{7.9}$$

and

$$EM \propto \dot{M}_{cl}^2 \times f_{cl}, \tag{7.10}$$

From Eqn. 7.9 and 7.10, we can see that the effects of clumping on the emission

measure cancel out, and the EM is unaffected by clumping. Again, remember that this all depends on the mass-loss rate being determined by the observed thermal radio emission and the degree of clumping being independent of radius.

If the degree of clumping depends on the radius, then the situation becomes more complicated based on the details of how the clumping changes with radius. The value of EM may go up or down.

7.8 Discussion

The DREM model has fit the radio data well at both high and low frequencies, except the legacy GMRT observation flux at 610 MHz (this work). The flux was significantly lower than the model's expected value ($\sim$ a factor 2 lower). During the data reduction process, we noticed the 2035+365 calibrator's flux was lower than the value mentioned in the VLA calibrators catalogue. Assuming the spectral index, $\alpha = -0.45$, the expected flux for the 2052+365 calibrator at 610 MHz is $\sim$ 7.7 Jy, but we obtained 4.14 Jy from the observation data.

Several discussions have been made with the GMRT personnel (Ishwara Chandra & Ruta Kale) regarding the observation, since there was no technical problem reported after the observation. Unfortunately, few problems were detected during the data reduction process. There were some issues with the dual-frequency settings and probably the pointing issues on the unused polarisation settings, contributing to the reduced amount of flux obtained. We have been advised to send another proposal using the upgraded GMRT utilising the new broad bandwidth.

From the model, the expected value of WR146 at 612 MHz is $\sim$ 115 mJy. Benaglia et al. (2020) successfully observed WR146 at lower frequencies between 2013 and 2014 with the 32 MHz bandwidth, a few years after our observations' date. The fluxes observed by Benaglia et al. (2020) matched well with the DREM model and

shows that the turn-over frequency lies between $\sim 0.3 - 0.7$ GHz.

The spectral index from the fitting of our DREM model is $\alpha = -0.67$ which compares well with Hales et al. (2017), $\alpha = -0.62$ and the extrapolated spectral index from Setia Gunawan et al. (2000), $\alpha = -0.65$.

From two distinct methods, namely the DREM model and the calculations of the expected EM, we obtained a comparable value of the $log_{10}\ EM = 5.35$ (DREM) and $log_{10}\ EM = 5.64$ (expected). These values show that the DREM model has successfully captured the essence of the non-thermal spectral shape of the colliding wind binary WR146.

7.9 Conclusion

In this chapter, we have reduced and presented the 610 MHz legacy GMRT dual-frequency observation taken in November 2012. From the recently published radio flux for WR146, we have fitted the non-thermal radio spectra with our DREM model.

We have learned from the DREM model that our 610 MHz flux value was significantly lower than the model's expected value. Several problems contributed to the issue, such as the failure of the calibrators during the observations and the dual-frequency settings. Note that the observation was made using the legacy GMRT dual-frequency mode in 2012 where the current upgraded GMRT does not offer the setting anymore due to many technical issues. Despite the complexity of the data, we have learned that CASA has the flexibility and the capability to reduce archive data meant for AIPS.

Also, from the deduced thermal flux at 610 MHz, we calculated the mass-loss rate for the WR star to be $8.31 \times 10^{-5}\,\mathrm{M}_{\odot}\ \mathrm{yr}^{-1}$. The value is in fair comparison with the previously published values.

DREM model fitting suggests that the emission measures from the WCR of

WR146 is normally distributed with the expected turnovers varies between $\sim$ 0.3-0.7 GHz. The emission measures value from the DREM model fitting agrees well with the expected theoretical value calculated from the number density integral. From two distinctive methods, we obtained comfortably similar $log_{10}\ EM$ values that prove the DREM model works.

From Gunawan et al. (2003), the reported WSRT observation at 0.327 MHz has the flux value a factor lower than Benaglia et al. (2020)(refer Table 7.4). Although the observation was made $\sim$ 20 years apart (1994 & 2014), the difference between the fluxes is unexplainable, making the WR146 system an inevitable target to be tracked from now on. A future observation using the new upgraded GMRT at band 3, 4 and 5 covering the frequency from 0.3 - 1.5 GHz is highly recommended taking the advantage of the new broad bandwidth (200-400 MHz). The future uGMRT radio observation will vastly improve our knowledge of WR146 radio spectra at lower frequencies region.

8 | Conclusion and Future Work

"Ultimately, we actually all belong to only one tribe, to Earthlings."

–Jill Tarter.

Chapter Summary

In this final chapter of this thesis, the results obtained in the previous chapters are summarised and the overall conclusions drawn. The first part involves collecting various archival data to investigate potential relationships and models for massive stars. The second part of the thesis presents and discusses various radio interferometry observations of the CWBs focusing on data reduction and imaging. The short term future work for the radio interferometric observations focusing on colliding wind binaries is outlined, and the long term goal is discussed.

8.1 Modelling and Relations

In Chapter 3, a substantial amount of available archival massive stars radio and X-rays data was collected. This chapter investigated the possibility of a relationship between the X-ray and radio luminosities for massive stars, as has been first noted by Güdel and Benz (1993) for low mass stars. The expected Güdel-Benz relation-

ship for massive stars was derived from the known correlations between mass-loss rates, bolometric luminosities, radio luminosities, and X-ray luminosities. The radio luminosities and the X-ray luminosities scales as $L_R \propto L_X^{0.44}$.

The MCMC fittings suggest positive correlations for both Wolf-Rayet stars and OB-stars within the expected slope errors which are $\alpha = +0.38 \pm 0.23$ for WR and $\alpha = +0.38 \pm 0.14$ for OB-stars. From this analysis, we found that WR data has more intrinsic scatter and also that O-stars are X-ray brighter for the same radio luminosity than WR stars.

In Chapter 4, various archived radio data of the archetypal colliding wind binary, WR140, was collected, re-analysed and re-interpreted. As a result, the Distributed Radio Emission Measure (DREM) model is proven to capture the shape of the radio spectra better than the single emission measure model. Moreover, this simple yet effective model can fit the archived radio data and explain the radio spectra. We found that the radio Emission Measure (EM) is at its minimum just before the periastron (around $\phi = 0.88$) as at this phase, the O-star is in front of the WR star, and we look mostly through the O-star's wind. Depending on the frequency, more radio emission escapes as the density of O-star wind is smaller, revealing the NT emission region of WR140 originating from the wind collision region. As the system approaches periastron, the radio EM rises rapidly causing the NT radio emission being absorbed by the thick WC7 wind. We also compared the radio EM with the X-ray column density (N_H) and found that the radio EM begins to rise earlier than the X-ray column as the orbit progresses.

8.2 Various Radio Interferometric Observations

In Chapter 5, the new low-frequencies observations of WR140 at $\phi = 0.37$ undertaken over two days in November 2019 using the Upgraded Giant Metre Radio Telescope (uGMRT) in Maharashtra, India were reported. The radio flux of WR140

at 0.36 GHz from this observation was recorded to be at the longest wavelength ever observed. The radio data is analysed and imaged using CASA, revealing the thermal component of WR140 with the best-fit spectral index of $\alpha = +0.59 \pm 0.06$, which agrees with the theoretical spectral index of $\alpha = +0.6$. At 0.60 GHz (and at $\phi = 0.37$), we obtained the mass-loss rate of WR-star to be 1.34×10^{-4} Myr^{-1} which is within a reasonable range compared to previously published values. The broad-band spectrum of WR140 over 5 decades of frequencies suggests that the WR140 is still thermal up to at least 70μm from Hershel Telescope before the spectra start to rise due to the emission originating from the dust.

The WR140 radio observation campaign was extended in Chapter 6 to include a new high-frequency observation of WR140 at 22 GHz using the rapidly developing East Asian VLBI Network (EAVN). The observation was performed on March 20, 2020, at the phase $\phi = 0.41$, which was closer to the apastron. As a result of the Coronavirus Pandemic, the angular resolution of the network has decreased from 0.55 mas (expected) to 1.24 mas (actual) due to the NSRT station closure. The VLBI data was reduced and imaged using the older package AIPS. The expected NT emission from the wind collision region (WCR) was unfortunately not detected due to the high rms from the network, which was at 9σ. The expected radio emission measure is calculated to be $EM = 2.94 \times 10^8$ cm^{-6}pc, and the corresponding optical depth is $\tau_\nu = 0.14$ indicating that the emission from the WCR region mostly escaped at this phase.

In Chapter 7, we reduced and imaged low-frequency radio data from another CWB system, the WR146, observed in November 2012 using the legacy GMRT at 612 MHz. We applied the DREM model introduced in Chapter 4 to this radio data as well as other published WR146 values. The DREM model has successfully fit the radio data and captured the essence of the spectral shape. The calculated expected radio emission measure for the WR146 system is $log_{10}\ EM = 5.64$, which is consistent with the fitted value from the DREM model, $log_{10}\ EM = 5.35$. We

analysed the radio data and calculated the mass-loss rate to be $8.31 \times 10^{-5}\,M_{\odot}\ yr^{-1}$ which agrees with other published values. Overall, the DREM model has proven to be a simple yet effective model than expected from a single emission measure model for explaining the flatter spectral shape of CWB radio data at lower frequencies.

8.3 Future Work

This thesis is only a snapshot of the current state of the art in this topic, particularly in terms of the instrumentation displayed and discussed. In the future, new data will be collected in tandem with new and enhanced instrumentation, allowing this work to be the baselines.

In this thesis, we have added to our knowledge of WR140 in a number of ways, as described in Section 8.1 and 8.2. However, our knowledge remains incomplete and more detailed studies are still required.

At many wavelengths, WR140 is the brightest and best studied colliding wind system. Because of its extreme eccentricity, it is an excellent laboratory for studying a wide range of phenomena. The separation varies by nearly a factor of 20 between apastron and periastron, and thus the shock density varies by nearly a factor of 400.

In the short term, we recommend low-frequency observations leading up to periastron in November 2024. The observation should also run through the radio peak at phase $\phi \sim 0.8$, when the radio source is brighter to compare the orbital changes. The spectral shape from the low-frequency emission will be critical in constraining the physics of wind absorption. This work is achievable by the upgraded uGMRT, which now has a wider bandwidth.

In terms of high-frequency observations, high-resolution observations around the periastron should reveal more about the wind structure and wind absorption; thus, high-frequency observations through the periastron are desired. WR140 is a prolific

dust producer near periastron passage, and a detailed study of this dust production will be carried out with NASA's James Webb Space Telescope (JWST) near the next periastron passage in November 2024 (ERS Program No.1349 – PI Ryan Lau). The dust is formed in the WCR region, and the relationship between the X-ray, radio and dust emission is of great interest. The VLBA or the EAVN can conduct this type of observation to tie in with the JWST observation, but the EAVN's capabilities must be re-evaluated at the time. Regardless, EAVN has a promising long-term future with many new upcoming telescopes that will increase the network's sensitivity.

Unfortunately, the next premium radio telescope: the SKA, will be unable to observe WR140 as the position of the system is too far north. Nonetheless, the SKA will be able to study a plethora of interesting colliding wind systems that are currently unavailable to us due to instrumentation limitations. The SKA will have higher sensitivity and resolution; thus, these future capabilities will allow us to apply our knowledge of WR140 to other CWBs systems and enable such comparisons.

Bibliography

The Physics of Stars. 2nd Edition. Wiley, 1999.

B. P. Abbott, R. Abbott, T. Abbott, M. Abernathy, F. Acernese, K. Ackley, C. Adams, T. Adams, P. Addesso, R. Adhikari, et al. *Physical review letters*, 116(6):061102, 2016.

D. C. Abbott, J. H. Bieging, and E. Churchwell. *The Astrophysical Journal*, 250: 645–659, 1981.

D. C. Abbott, J. H. Beiging, E. Churchwell, and A. V. Torres. , 303:239–261, Apr. 1986.

R. Abbott, T. Abbott, S. Abraham, F. Acernese, K. Ackley, A. Adams, C. Adams, R. Adhikari, V. Adya, C. Affeldt, et al. *arXiv preprint arXiv:2010.14529*, 2020.

T. Abel, G. L. Bryan, and M. L. Norman. *science*, 295(5552):93–98, 2002.

Z. Z. Abidin, M. F. Asillam, and J. Y. Koay. *Nature Astronomy*, pages 1–3, 2020.

O. Agertz, A. V. Kravtsov, S. N. Leitner, and N. Y. Gnedin. *The Astrophysical Journal*, 770(1):25, 2013.

W. J. Altenhoff, C. Thum, and H. J. Wendker. , 281:161–183, Jan. 1994.

C. W. Ambruster, F. C. Fekel, and E. F. Guinan. In M. S. Giampapa and J. A. Bookbinder, editors, *Cool Stars, Stellar Systems, and the Sun*, volume 26 of *Astronomical Society of the Pacific Conference Series*, page 569, 1992.

H. Andrews, D. Fenech, R. Prinja, J. Clark, and L. Hindson. *Astronomy & Astrophysics*, 632:A38, 2019.

I. I. Antokhin, G. Rauw, J.-M. Vreux, K. A. van der Hucht, and J. C. Brown. *Astronomy & Astrophysics*, 477(2):593–609, 2008.

K. Asada, M. Kino, M. Honma, T. Hirota, R.-S. Lu, M. Inoue, B.-W. Sohn, Z.-Q. Shen, P. Ho, K. Akiyama, et al. *arXiv preprint arXiv:1705.04776*, 2017.

J. Babel and T. Montmerle. , 323:121–138, July 1997.

J. Bally and H. Zinnecker. *The Astronomical Journal*, 129(5):2281, 2005.

D. K. Bedford, K. H. Elliott, and C. J. Eyles. , 40:51–54, Feb. 1985.

P. Benaglia. In J. Martí, P. L. Luque-Escamilla, and J. A. Combi, editors, *High Energy Phenomena in Massive Stars*, volume 422 of *Astronomical Society of the Pacific Conference Series*, page 111, May 2010.

P. Benaglia, C. E. Cappa, and B. S. Koribalski. , 372:952–962, June 2001.

P. Benaglia, B. Koribalski, and J. F. Albacete Colombo. , 23:50–63, Mar. 2006.

P. Benaglia, M. De Becker, C. Ishwara-Chandra, H. Intema, and N. L. Isequilla. *arXiv preprint arXiv:2006.00867*, 2020.

H. Beuther, E. B. Churchwell, C. F. McKee, and J. C. Tan. *arXiv preprint astro-ph/0602012*, 2006.

J. H. Bieging, D. C. Abbott, and E. B. Churchwell. , 263:207–214, Dec. 1982.

J. H. Bieging, D. C. Abbott, and E. B. Churchwell. , 340:518–536, May 1989.

P. Blanchard, E. Berger, W. Fong, M. Nicholl, J. Leja, C. Conroy, K. Alexander, R. Margutti, P. Williams, Z. Doctor, et al. *The Astrophysical Journal Letters*, 848 (2):L22, 2017.

R. Blomme. *Bulletin de la Societe Royale des Sciences de Liege*, 80:67–80, Jan. 2011.

R. Blomme, G. C. van de Steene, R. K. Prinja, M. C. Runacres, and J. S. Clark. , 408:715–727, Sept. 2003.

R. Blomme, M. De Becker, D. Volpi, and G. Rauw. , 519:A111, Sept. 2010.

W. Brandner, E. K. Grebel, Y.-H. Chu, H. Dottori, B. Brandl, S. Richling, H. W. Yorke, S. D. Points, and H. Zinnecker. *The Astronomical Journal*, 119(1):292, 2000.

D. P. Brookes. *Interferometric radio observations of the interactive winds of massive stars*. PhD thesis, University of Birmingham, 2016.

J. C. Brown, J. P. Cassinelli, Q. Li, A. F. Kholtygin, and R. Ignace. , 426:323–328, Oct. 2004.

P. Brussaard and H. Van de Hulst. *Reviews of Modern Physics*, 34(3):507, 1962.

C. Cappa, W. M. Goss, and K. A. van der Hucht. , 127:2885–2897, May 2004.

J. P. Cassinelli, N. A. Miller, W. L. Waldron, J. J. MacFarlane, and D. H. Cohen. , 554:L55–L58, June 2001.

C. Cazorla, Y. Nazé, and G. Rauw. , 561:A92, Jan. 2014.

J. M. Chapman, C. Leitherer, and B. Koribalski. In K. A. van der Hucht, G. Koenigsberger, and P. R. J. Eenens, editors, *Wolf-Rayet Phenomena in Massive Stars and Starburst Galaxies*, volume 193 of *IAU Symposium*, page 59, 1999.

T. Chlebowski, F. R. Harnden, Jr., and S. Sciortino. , 341:427–455, June 1989.

D. H. Cohen, M. A. Leutenegger, E. E. Wollman, J. Zsargó, D. J. Hillier, R. H. Townsend, and S. P. Owocki. *Monthly Notices of the Royal Astronomical Society*, 405(4):2391–2405, 2010.

M. Corcoran, A. Fredericks, R. Petre, J. Swank, and S. Drake. *The Astrophysical Journal*, 545(1):420, 2000.

M. Corcoran, A. Pollock, K. Hamaguchi, and C. Russell. *arXiv preprint arXiv:1101.1422*, 2011.

M. F. Corcoran, J. Liburd, D. Morris, C. Russell, K. Hamaguchi, T. R. Gull, T. Madura, M. Teodoro, A. F. Moffat, N. Richardson, et al. *The Astrophysical Journal*, 838(1):45, 2017.

P. Crowther. *Astronomy Geophysics*, 53(4):4.30–4.36, 08 2012. ISSN 1366-8781. URL `https://doi.org/10.1111/j.1468-4004.2012.53430.x`.

S. Daley-Yates, I. R. Stevens, and T. D. Crossland. , 463:2735–2745, Dec. 2016.

M. De Becker. *The Astronomy and Astrophysics Review*, 14(3-4):171–216, 2007.

M. De Becker and F. Raucq. *Astronomy & Astrophysics*, 558:A28, 2013.

V. Dexheimer and S. Schramm. *The Astrophysical Journal*, 683(2):943, 2008.

H. R. Dickel, H. J. Habing, and R. Isaacman. , 238:L39–L41, May 1980.

S. Dougherty, P. Williams, K. Van Der Hucht, M. Bode, and R. Davis. *Monthly Notices of the Royal Astronomical Society*, 280(3):963–970, 1996.

S. M. Dougherty, P. Williams, and D. Pollacco. *Monthly Notices of the Royal Astronomical Society*, 316(1):143–151, 2000.

S. M. Dougherty, A. J. Beasley, M. J. Claussen, B. A. Zauderer, and N. J. Bolingbroke. , 623(1):447–459, Apr. 2005.

S. A. Drake, T. Simon, and J. L. Linsky. , 71:905–930, Dec. 1989.

S. A. Drake, F. M. Walter, and D. R. Florkowski. In G. Wallerstein, editor, *Cool Stars, Stellar Systems, and the Sun*, volume 9 of *Astronomical Society of the Pacific Conference Series*, pages 148–151, 1990.

S. A. Drake, T. Simon, and J. L. Linsky. , 82:311–321, Sept. 1992.

D. O. Edge, J. R. Shakeshaft, W. B. McAdam, J. E. Baldwin, and S. Archer. , 68: 37–60, 1959.

P. Eenens and P. Williams. *Monthly Notices of the Royal Astronomical Society*, 269 (4):1082–1098, 1994.

J. Eldridge. *Astronomy & Geophysics*, 61(2):2–24, 2020.

R. Fahed, A. F. Moffat, J. Zorec, T. Eversberg, A.-N. Chené, F. Alves, W. Arnold, T. Bergmann, L. G. Carreira, F. M. Dias, et al. *Bulletin de la Société Royale des Sciences de Liège*, 2011.

A. Feldmeier, J. Puls, and A. W. A. Pauldrach. , 322:878–895, June 1997.

J. Forbrich, S. J. Wolk, M. Güdel, A. Benz, R. Osten, J. L. Linsky, M. McLean, L. Loinard, and E. Berger. In C. Johns-Krull, M. K. Browning, and A. A. West, editors, *16th Cambridge Workshop on Cool Stars, Stellar Systems, and the Sun*, volume 448 of *Astronomical Society of the Pacific Conference Series*, page 455, Dec. 2011.

A. W. Fullerton, D. Massa, and R. Prinja. *The Astrophysical Journal*, 637(2):1025, 2006.

M. Gagné, G. Fehon, M. R. Savoy, D. H. Cohen, L. K. Townsley, P. S. Broos, M. S. Povich, M. F. Corcoran, N. R. Walborn, N. Remage Evans, A. F. J. Moffat, Y. Nazé, and L. M. Oskinova. , 194:5, May 2011.

S. Geen, J. Rosdahl, J. Blaizot, J. Devriendt, and A. Slyz. *Monthly Notices of the Royal Astronomical Society*, 448(4):3248–3264, 2015.

A. N. Gómez-Morán and L. Oskinova. *Astronomy & Astrophysics*, 620:A89, 2018.

J. H. Groh, G. Meynet, S. Ekström, and C. Georgy. , 564:A30, Apr. 2014.

M. Güdel. , 264:L31–L34, Oct. 1992.

M. Güdel. , 40:217–261, 2002.

M. Güdel and A. O. Benz. , 405:L63–L66, Mar. 1993.

M. Güdel, J. H. M. M. Schmitt, J. A. Bookbinder, and T. A. Fleming. , 415:236–239, Sept. 1993.

D. Y. S. Gunawan, A. G. de Bruyn, K. A. van der Hucht, and P. M. Williams. *The Astrophysical Journal Supplement Series*, 149(1):123, 2003.

Y. Gupta, B. Ajithkumar, H. Kale, S. Nayak, S. Sabhapathy, S. Sureshkumar, R. Swami, J. Chengalur, S. Ghosh, C. Ishwara-Chandra, et al. *Current Science*, pages 707–714, 2017.

C. A. Hales, P. Benaglia, S. del Palacio, G. E. Romero, and B. S. Koribalski. , 598: A42, Feb. 2017.

K. Hamaguchi, M. F. Corcoran, J. M. Pittard, N. Sharma, H. Takahashi, C. M. Russell, B. W. Grefenstette, D. R. Wik, T. R. Gull, N. D. Richardson, et al. *Nature Astronomy*, 2(9):731–736, 2018.

W.-R. Hamann, G. Gräfener, A. Liermann, R. Hainich, A. Sander, T. Shenar, V. Ramachandran, H. Todt, and L. Oskinova. *Astronomy & Astrophysics*, 625:A57, 2019.

L. Hindson, M. Thompson, J. Urquhart, A. Faimali, J. Clark, and B. Davies. *Monthly Notices of the Royal Astronomical Society*, 421(4):3418–3430, 2012.

R. M. Hjellming, C. M. Wade, and E. Webster. In *Bulletin of the American Astronomical Society*, volume 4 of , page 384, June 1972.

I. D. Howarth and R. K. Prinja. , 69:527–592, Mar. 1989.

J. R. Hurley, C. A. Tout, and O. R. Pols. *Monthly Notices of the Royal Astronomical Society*, 329(4):897–928, 2002.

R. Ignace, L. M. Oskinova, and C. Foullon. , 318:214–226, Oct. 2000.

K. G. Jansky. , 132:66, July 1933.

B. C. Kelly. , 665:1489–1506, Aug. 2007.

R. C. Kennicutt. *Proceedings of the International Astronomical Union*, 1(S227): 3–11, 2005.

J.-G. Kim, W.-T. Kim, E. C. Ostriker, and M. A. Skinner. *The Astrophysical Journal*, 851(2):93, 2017.

H. A. Kobulnicky, D. C. Kiminki, M. J. Lundquist, J. Burke, J. Chapman, E. Keller, K. Lester, E. K. Rolen, E. Topel, A. Bhattacharjee, et al. *The Astrophysical Journal Supplement Series*, 213(2):34, 2014.

J. Krtička. *Astronomy & Astrophysics*, 564:A70, 2014.

M. R. Krumholz and C. F. McKee. *The astrophysical journal*, 630(1):250, 2005.

S. Kurapati, P. Chandra, G. Wade, D. H. Cohen, A. David-Uraz, M. Gagne, J. Grunhut, M. E. Oksala, V. Petit, M. Shultz, et al. *Monthly Notices of the Royal Astronomical Society*, page stw2838, 2016.

M. Kurster, J. H. M. M. Schmitt, and T. A. Fleming. In M. S. Giampapa and J. A. Bookbinder, editors, *Cool Stars, Stellar Systems, and the Sun*, volume 26 of *Astronomical Society of the Pacific Conference Series*, page 109, 1992.

H. J. G. L. M. Lamers and C. Leitherer. , 412:771–791, Aug. 1993.

A. Laor and E. Behar. *Monthly Notices of the Royal Astronomical Society*, 390(2): 847–862, 2008.

R. M. Lau, J. Eldridge, M. J. Hankins, A. Lamberts, I. Sakon, and P. M. Williams. *The Astrophysical Journal*, 898(1):74, 2020.

C. Leitherer, J. M. Chapman, and B. Koribalski. , 450:289, Sept. 1995.

C. Leitherer, D. Schaerer, J. D. Goldader, R. M. G. Delgado, C. Robert, D. F. Kune, D. F. de Mello, D. Devost, and T. M. Heckman. , 123:3–40, July 1999.

S. Lépine, D. Wallace, M. M. Shara, A. F. Moffat, and V. S. Niemela. *The Astronomical Journal*, 122(6):3407, 2001.

D. Li and Z. Pan. *Radio Science*, 51:1060–1064, July 2016.

J. Lim. In M. S. Giampapa and J. A. Bookbinder, editors, *Cool Stars, Stellar Systems, and the Sun*, volume 26 of *Astronomical Society of the Pacific Conference Series*, page 322, 1992.

J. Lü, J.-W. Xing, Y.-C. Zou, W.-H. Lei, Q.-W. Wu, and D.-X. Wang. *Research in Astronomy and Astrophysics*, 15(5):617, 2015.

J. Marti, J. M. Paredes, C. H. C. Ishwara, and V. Bosch-Ramon. *VizieR Online Data Catalog*, art. J/A+A/472/557, Nov 2007.

F. Martins, D. Schaerer, and D. J. Hillier. , 436:1049–1065, June 2005.

P. Massey. *ArXiv Astrophysics e-prints*, July 2003.

P. Massey and A. Thompson. *The Astronomical Journal*, 101:1408–1428, 1991.

L. A. McClelland and J. Eldridge. *Monthly Notices of the Royal Astronomical Society*, 459(2):1505–1518, 2016.

G. E. McCluskey, Jr. and Y. Kondo. , 96:817–820, Oct. 1984.

C. F. McKee and J. C. Tan. *The Astrophysical Journal*, 585(2):850, 2003.

P. Mezger and A. Henderson. *The Astrophysical Journal*, 147:471, 1967.

J. D. Monnier, M. Zhao, E. Pedretti, R. Millan-Gabet, J.-P. Berger, W. Traub, F. Schloerb, T. ten Brummelaar, H. McAlister, S. Ridgway, et al. *The Astrophysical Journal Letters*, 742(1):L1, 2011.

D. C. Morton and A. E. Wright. , 182:47P–51P, Mar. 1978.

A. Murguia-Berthier, E. Ramirez-Ruiz, C. D. Kilpatrick, R. J. Foley, D. Kasen, W. H. Lee, A. L. Piro, D. A. Coulter, M. R. Drout, B. F. Madore, et al. *The Astrophysical Journal Letters*, 848(2):L34, 2017.

Y. Nazé. , 506:1055–1064, Nov. 2009.

Y. Nazé, P. S. Broos, L. Oskinova, L. K. Townsley, D. Cohen, M. F. Corcoran, N. R. Evans, M. Gagné, A. F. J. Moffat, J. M. Pittard, G. Rauw, A. ud-Doula, and N. R. Walborn. , 194:7, May 2011.

Y. Nazé, L. Mahy, Y. Damerdji, H. A. Kobulnicky, J. M. Pittard, E. R. Parkin, O. Absil, and R. Blomme. , 546:A37, Oct. 2012.

Y. Nazé, G. Rauw, and D. Hutsemékers. *Astronomy & Astrophysics*, 538:A47, 2012.

Y. Nazé, V. Petit, M. Rinbrand, D. Cohen, S. Owocki, A. ud-Doula, and G. A. Wade. , 215:10, Nov. 2014.

V. S. Niemela, M. M. Shara, D. J. Wallace, D. R. Zurek, and A. F. Moffat. *The Astronomical Journal*, 115(5):2047, 1998.

J. North, P. Tuthill, W. Tango, and J. Davis. *Monthly Notices of the Royal Astronomical Society*, 377(1):415–424, 2007.

E. O'Connor, S. Dougherty, J. Pittard, and P. Williams. *arXiv preprint astro-ph/0509231*, 2005.

L. Oskinova. *Monthly Notices of the Royal Astronomical Society*, 361(2):679–694, 2005.

L. Oskinova, W.-R. Hamann, and A. Feldmeier. *Astronomy & Astrophysics*, 476(3): 1331–1340, 2007.

L. Oskinova, W.-R. Hamann, A. Feldmeier, R. Ignace, and Y.-H. Chu. *The Astrophysical Journal Letters*, 693(1):L44, 2009.

L. M. Oskinova, R. Ignace, W.-R. Hamann, A. Pollock, and J. Brown. *Astronomy & Astrophysics*, 402(2):755–765, 2003.

S. P. Owocki, J. I. Castor, and G. B. Rybicki. , 335:914–930, Dec. 1988.

S. P. Owocki, J. O. Sundqvist, D. H. Cohen, and K. G. Gayley. *Monthly Notices of the Royal Astronomical Society*, 429(4):3379–3389, 2013.

R. Pallavicini, L. Golub, R. Rosner, G. S. Vaiana, T. Ayres, and J. L. Linsky. , 248: 279–290, Aug. 1981.

N. Panagia and M. Felli. *Astronomy and Astrophysics*, 39:1–5, 1975.

F. Panessa, X. Barcons, L. Bassani, M. Cappi, F. J. Carrera, L. Ho, and S. Pellegrini. *Astronomy & Astrophysics*, 467(2):519–527, 2007.

R. Phillips. In M. S. Giampapa and J. A. Bookbinder, editors, *Cool Stars, Stellar Systems, and the Sun*, volume 26 of *Astronomical Society of the Pacific Conference Series*, page 309, 1992.

J. Pittard and S. Dougherty. *Monthly Notices of the Royal Astronomical Society*, 372(2):801–826, 2006.

J. M. Pittard and B. Dawson. , 477(4):5640–5645, July 2018.

A. Pollock, M. Corcoran, I. Stevens, C. Russell, K. Hamaguchi, P. Williams, A. Moffat, G. Weigelt, V. Shenavrin, N. Richardson, et al. *arXiv preprint arXiv:2109.10350*, 2021.

A. M. T. Pollock, F. Haberl, and M. F. Corcoran. In K. A. van der Hucht and P. M. Williams, editors, *Wolf-Rayet Stars: Binaries; Colliding Winds; Evolution*, volume 163 of *IAU Symposium*, page 512, 1995.

W. H. Press, S. A. Teukolsky, W. T. Vetterling, and B. P. Flannery. 1992.

G. Rate and P. A. Crowther. *Monthly Notices of the Royal Astronomical Society*, 493(1):1512–1529, 2020.

G. Rate, P. A. Crowther, and R. J. Parker. , 495(1):1209–1226, June 2020.

G. Rauw and Y. Nazé. , 594:A82, Oct. 2016.

G. Rauw, Y. Nazé, N. J. Wright, J. J. Drake, M. G. Guarcello, R. K. Prinja, L. W. Peck, J. F. Albacete Colombo, A. Herrero, H. A. Kobulnicky, S. Sciortino, and J. S. Vink. , 221:1, Nov. 2015.

G. Reber. , 100:279, Nov. 1944.

B. C. Reed. *The Astronomical Journal*, 125(5):2531, 2003.

J. A. Regan, J. H. Wise, T. E. Woods, T. P. Downes, B. W. O'Shea, and M. L. Norman. *arXiv preprint arXiv:2008.08090*, 2020.

M. Renzo, C. D. Ott, S. N. Shore, and S. E. de Mink. *Astronomy & Astrophysics*, 603:A118, 2017.

N. D. Richardson, C. M. Russell, L. St-Jean, A. F. Moffat, N. St-Louis, T. Shenar, H. Pablo, G. M. Hill, T. Ramiaramanantsoa, M. Corcoran, et al. *Monthly Notices of the Royal Astronomical Society*, 471(3):2715–2729, 2017.

M. C. Runacres and S. P. Owocki. , 381:1015–1025, Jan. 2002.

M. C. Runacres and S. P. Owocki. , 429:323–333, Jan. 2005.

H. N. Russell. *Popular Astronomy*, 22:275–294, May 1914.

H. Sana, G. Rauw, Y. Nazé, E. Gosset, and J.-M. Vreux. *Monthly Notices of the Royal Astronomical Society*, 372(2):661–678, 2006.

H. Sana, S. De Mink, A. de Koter, N. Langer, C. Evans, M. Gieles, E. Gosset, R. Izzard, J.-B. Le Bouquin, and F. Schneider. *Science*, 337(6093):444–446, 2012.

R. S. Schnerr, K. L. J. Rygl, A. J. van der Horst, T. A. Oosterloo, J. C. A. Miller-Jones, H. F. Henrichs, T. A. T. Spoelstra, and A. R. Foley. , 470:1105–1109, Aug. 2007.

O. Schnurr, J. Casoli, A.-N. Chené, A. Moffat, and N. St-Louis. *Monthly Notices of the Royal Astronomical Society: Letters*, 389(1):L38–L42, 2008.

S. Scuderi, N. Panagia, C. Stanghellini, C. Trigilio, and G. Umana. , 332:251–267, Apr. 1998.

D. Setia Gunawan, A. De Bruyn, K. Van der Hucht, and P. Williams. *Astronomy and Astrophysics*, 356:676–690, 2000.

D. Y. A. Setia Gunawan, K. A. van der Hucht, P. M. Williams, H. F. Henrichs, L. Kaper, D. J. Stickland , and W. Wamsteker. , 376:460–475, Sept. 2001.

V. Shenavrin, O. Taranova, and A. Nadzhip. *Astronomy Reports*, 55(1):31–81, 2011.

S. L. Skinner, S. A. Zhekov, M. Güdel, W. Schmutz, and K. R. Sokal. , 139:825–838, Mar. 2010.

O. B. Slee, G. J. Nelson, R. T. Stewart, A. E. Wright, D. L. Jauncey, L. H. Heisler, J. D. Bunton, A. E. Vaughan, M. I. Large, W. L. Peters, and S. G. Ryan. , 227: 467–479, July 1987.

N. Smith. *Philosophical Transactions of the Royal Society A: Mathematical, Physical and Engineering Sciences*, 375(2105):20160268, 2017.

A. Stolte, W. Brandner, B. Brandl, H. Zinnecker, and E. K. Grebel. *The Astronomical Journal*, 128(2):765, 2004.

R. S. Sutherland. *Monthly Notices of the Royal Astronomical Society*, 300(2):321–330, 1998.

J. C. Tan, M. T. Beltrán, P. Caselli, F. Fontani, A. Fuente, M. R. Krumholz, C. F. McKee, and A. Stolte. *Protostars and Planets VI*, 2014. URL `http://dx.doi.org/10.2458/azu_uapress_9780816531240-ch007`.

O. G. Taranova and V. I. Shenavrin. *Astronomy Letters*, 37(1):30–39, Jan. 2011.

J. D. Thomas, N. D. Richardson, J. Eldridge, G. H. Schaefer, J. D. Monnier, H. Sana, A. F. Moffat, P. Williams, M. F. Corcoran, I. R. Stevens, et al. *Monthly Notices of the Royal Astronomical Society*, 504(4):5221–5230, 2021.

L. K. Townsley, P. S. Broos, G. P. Garmire, and M. S. Povich. *The Astrophysical Journal Supplement Series*, 244(2):28, 2019.

S. Tremaine, K. Gebhardt, R. Bender, G. Bower, A. Dressler, S. M. Faber, A. V. Filippenko, R. Green, C. Grillmair, L. C. Ho, J. Kormendy, T. R. Lauer, J. Magorrian, J. Pinkney, and D. Richstone. , 574:740–753, Aug. 2002.

A. ud-Doula and Y. Nazé. *Advances in Space Research*, 58:680–693, Sept. 2016.

G. Umana, S. Catalano, and M. Rodono. , 249:217–222, Sept. 1991.

K. A. Van Der Hucht. , 4:123–159, 1992.

K. A. Van Der Hucht. *New Astronomy Reviews*, 45(3):135–232, 2001.

P. Van Hoof, R. Williams, K. Volk, M. Chatzikos, G. J. Ferland, M. Lykins, R. Porter, and Y. Wang. *Monthly Notices of the Royal Astronomical Society*, 444(1):420–428, 2014.

S. Van Loo, M. C. Runacres, and R. Blomme. , 452:1011–1019, June 2006.

J. S. Vink, A. de Koter, and H. J. G. L. M. Lamers. , 369:574–588, Apr. 2001.

W. L. Waldron, M. F. Corcoran, S. A. Drake, and A. P. Smale. , 118:217–238, Sept. 1998.

H. J. Wendker, J. W. M. Baars, and W. J. Altenhoff. *Nature Physical Science*, 245: 118–119, Oct. 1973.

N. E. White and F. E. Marshall. , 268:L117–L120, May 1983.

R. L. White and R. H. Becker. , 451:352, Sept. 1995.

S. M. White, R. A. Duncan, J. Lim, G. J. Nelson, S. A. Drake, and M. R. Kundu. , 429:380, July 1994.

P. Williams. *arXiv preprint arXiv:1101.1046*, 2011a.

P. Williams. *Bulletin de la Societe Royale des Sciences de Liege*, 2011b.

P. Williams, K. Van Der Hucht, A. Pollock, D. Florkowski, H. Van Der Woerd, and W. Wamsteker. *Monthly Notices of the Royal Astronomical Society*, 243:662–684, 1990.

P. M. Williams, K. A. van der Hucht, and T. A. T. Spoelstra. , 291:805–810, Nov. 1994.

P. M. Williams, S. M. Dougherty, K. A. van der Hucht, M. F. Bode, and R. J. Davis. In V. Niemela, N. Morrell, P. Pismis, and S. Torres-Peimbert, editors, *Revista Mexicana de Astronomia y Astrofisica Conference Series*, volume 5 of *Revista Mexicana de Astronomia y Astrofisica Conference Series*, pages 103–105, Dec. 1996.

A. Willis, L. Dessart, P. Crowther, P. Morris, A. Maeder, P. Conti, and K. Van Der Hucht. *Monthly Notices of the Royal Astronomical Society*, 290(2):371–379, 1997.

S. Woosley. *The Astrophysical Journal*, 836(2):244, 2017.

S. E. Woosley and A. Heger. *Physics Reports*, 442(1-6):269–283, 2007.

A. E. Wright and M. J. Barlow. , 170:41–51, Jan. 1975.

N. J. Wright, J. E. Drew, and M. Mohr-Smith. *Monthly Notices of the Royal Astronomical Society*, 449(1):741–760, 2015.

H. W. Yorke and C. Sonnhalter. *The Astrophysical Journal*, 569(2):846, 2002.

N. Zacharias, C. Finch, T. Girard, A. Henden, J. Bartlett, D. Monet, and M. Zacharias. *VizieR Online Data Catalog*, pages I–322A, 2012.

S. A. Zhekov. *Monthly Notices of the Royal Astronomical Society*, 472(4):4374–4381, 2017.

H. Zinnecker and H. W. Yorke. *Annu. Rev. Astron. Astrophys.*, 45:481–563, 2007.